

Recent Advances in 2D Material Theory, Synthesis, Properties, and Applications

Yu-Chuan Lin,^{*,#} Riccardo Torsi,[#] Rehan Younas, Christopher L. Hinkle, Albert F. Rigosi, Heather M. Hill, Kunyan Zhang, Shengxi Huang, Christopher E. Shuck, Chen Chen, Yu-Hsiu Lin, Daniel Maldonado-Lopez, Jose L. Mendoza-Cortes, John Ferrier, Swastik Kar, Nadire Nayir, Siavash Rajabpour, Adri C. T. van Duin, Xiwen Liu, Deep Jariwala, Jie Jiang, Jian Shi, Wouter Mortelmans, Rafael Jaramillo, Joao Marcelo J. Lopes, Roman Engel-Herbert, Anthony Trofe, Tetyana Ignatova, Seng Huat Lee, Zhiqiang Mao, Leticia Damian, Yuanxi Wang, Megan A. Steves, Kenneth L. Knappenberger, Jr., Zhengtianye Wang, Stephanie Law, George Bepete, Da Zhou, Jiang-Xiazi Lin, Mathias S. Scheurer, Jia Li, Pengjie Wang, Guo Yu, Sanfeng Wu, Deji Akinwande, Joan M. Redwing, Mauricio Terrones, and Joshua A. Robinson^{*}



Cite This: <https://doi.org/10.1021/acsnano.2c12759>



Read Online

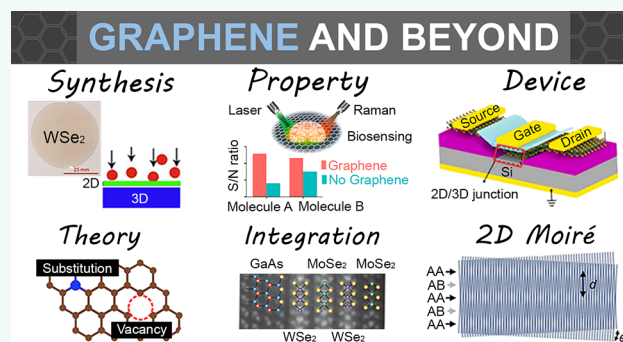
ACCESS |

Metrics & More

Article Recommendations

ABSTRACT: Two-dimensional (2D) material research is rapidly evolving to broaden the spectrum of emergent 2D systems. Here, we review recent advances in the theory, synthesis, characterization, device, and quantum physics of 2D materials and their heterostructures. First, we shed insight into modeling of defects and intercalants, focusing on their formation pathways and strategic functionalities. We also review machine learning for synthesis and sensing applications of 2D materials. In addition, we highlight important development in the synthesis, processing, and characterization of various 2D materials (e.g., MXenes, magnetic compounds, epitaxial layers, low-symmetry crystals, etc.) and discuss oxidation and strain gradient engineering in 2D materials. Next, we discuss the optical and phonon properties of 2D materials controlled by material inhomogeneity and give examples of multidimensional imaging and biosensing equipped with machine learning analysis based on 2D platforms. We then provide updates on mix-dimensional heterostructures using 2D building blocks for next-generation logic/memory devices and the quantum anomalous Hall devices of high-quality magnetic topological insulators, followed by advances in small twist-angle homojunctions and their exciting quantum transport. Finally, we provide the perspectives and future work on several topics mentioned in this review.

KEYWORDS: 2D Materials, Epitaxial Growth, Doping, Theory, Moiré Engineering, Strain Engineering, Biosensing, Machine Learning, Magnetic and Topological Properties, Multidimensional Heterostructures



INTRODUCTION

Two-dimensional materials (2D materials) are thermodynamically stable as atomically or molecularly thin layered structures and exhibit properties different from their bulk counterparts. From the seminal papers^{1,2} to current 2D materials research, it is evident that graphene, hexagonal boron nitride (hBN), 2D transition metal dichalcogenides (TMDs),³ and metal carbides and nitrides (MXenes)⁴ are currently the most common building blocks in this field. In the past decade, magnetic 2D materials,⁵ 2D metals,⁶ layered topological insulators (TIs),⁷ and 2D moiré van der Waals (vdW) heterostructures⁸ are at the

front lines of research in this material family. Additionally, more have been theoretically predicted to exist and await exploration.⁹ 2D materials and their heterostructures cover an extensive range

Received: December 25, 2022

Accepted: May 8, 2023

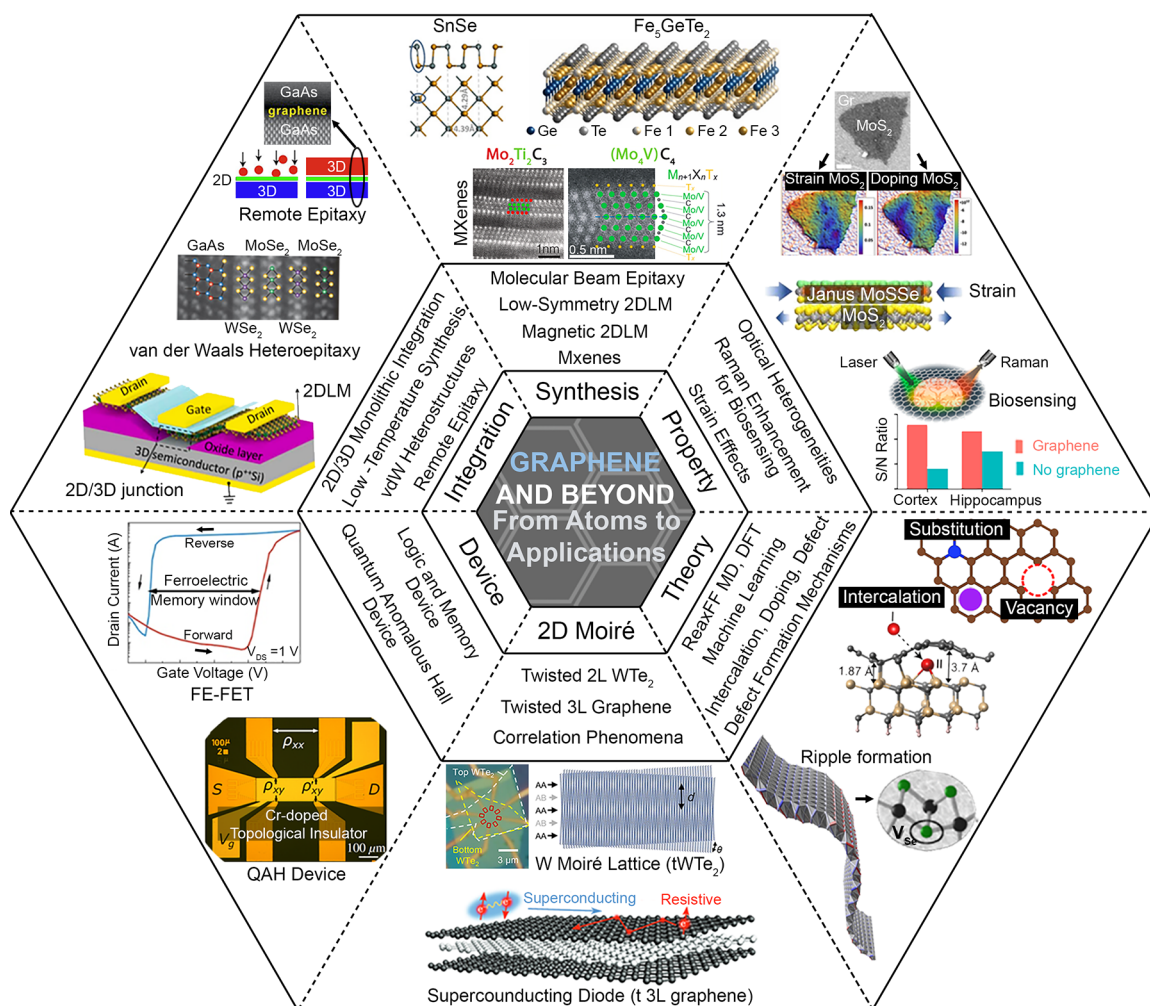


Figure 1. Overview of the scope of this review. We focus on the recent advancements in the field of two-dimensional layered materials (2DLM) learned from the Graphene and Beyond workshop at the Pennsylvania State University in 2022. The topics relevant to 2DLM in this review cover the fields of theory, synthesis and processing, material properties, material Integration, device study, and twisted 2D heterostructures.

of properties from metals to semimetals, semiconductors, insulators, and TIs that can be tailored through layer number, surface morphology, strain engineering, heterostructures, and emerging material processing. Besides their pristine form, heterogeneities such as impurities, dopants, structural defects, disorders, and interfaces may be controlled through substitutional doping and defect engineering to engineer electronic structures, induce magnetization, and trigger quantum phenomena in host materials.¹⁰ As a result, 2D materials are a rich platform for a broad spectrum of research from theory to next-generation (opto)electronics, fundamental physics, sensors, energy, and artificial intelligence and machine learning. The substantial interest in this field is reflected in the publication record: The number of publications relevant to 2D materials has increased from merely ≈ 1900 in 2004, to ≈ 9000 in 2013, and over 49,000 in 2021.^{11,12} As 2D materials science and technology expands with this spectacular pace, it is necessary to connect experts with different disciplines in conferences or workshops frequently to enhance synergy and work together toward a promising future in this field. This review reflects the views of a group of theoretical and experimental experts on advanced 2D materials interdisciplinary efforts as summarized in Figure 1.

Initially, we will discuss the theoretical aspect of 2D materials, including predicting properties introduced by defects and impurities in 2D materials, large-scale computations with reactive force field potentials to understand growth and intercalation mechanisms, and artificial intelligence (AI) and machine learning (ML) in 2D material research. Calculations and theoretical modeling are more important than ever to guide the search for 2D materials useful for energy applications and future devices and to deconvolute complicated growth and processing steps. In subsequent sections focused on material synthesis, we discuss some 2D materials that can be synthesized in large area or quantity, including MXenes prepared by chemical exfoliation of MAX-phase crystals and synthesis and doping of TIs and TMDs using molecular beam epitaxy (MBE) and metalorganic chemical vapor deposition (MOCVD). Additionally, low-symmetry SnS crystals, magnetic Fe_nGeTe_3 ($n = 3-5$) layered materials, magnetically doped TMDs, and utilization of intermediate 2D layers for remote epitaxy are discussed.

Further, we examine 2D material characterization and applications, including optical properties of asymmetric 2D materials, 2D surfaces for biosensing, and strain engineering for tuning their band structures. Thanks to Se-S ion exchange¹³ and confinement heteroepitaxy¹⁴ techniques, structurally asymmet-

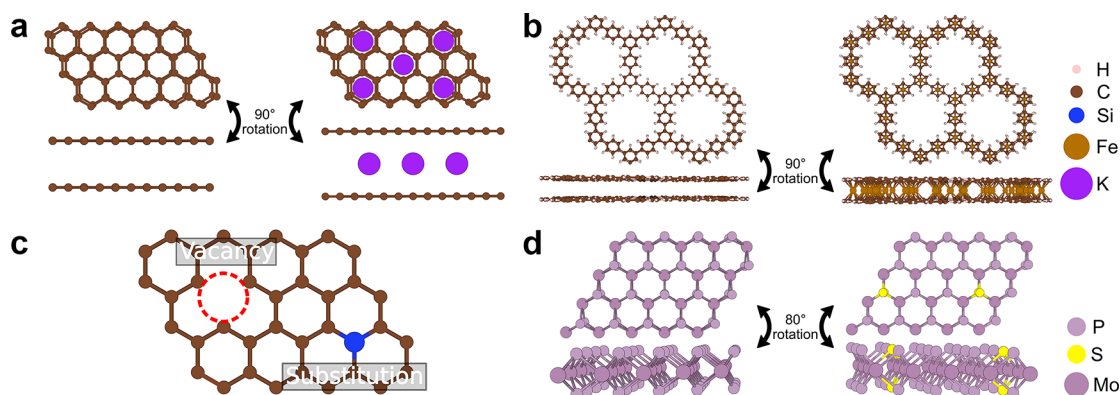


Figure 2. Modeling intercalation, defects, and doping in 2D materials. (a) Bilayer graphene before (left) and after (right) intercalation. The figure includes a top view (top) and a side view (bottom). (b) "All-benzene" 2D-COF before (left) and after (right) intercalation. Intercalated atoms are placed at the centroid of each benzene ring. The figure includes a top view (top) and a side view (bottom). (c) Defective graphene layer showing a vacancy and a silicon substitution. (d) Pristine (left) and S-doped (right) MoP. The figure includes a top view (top) and a perspective view (bottom).

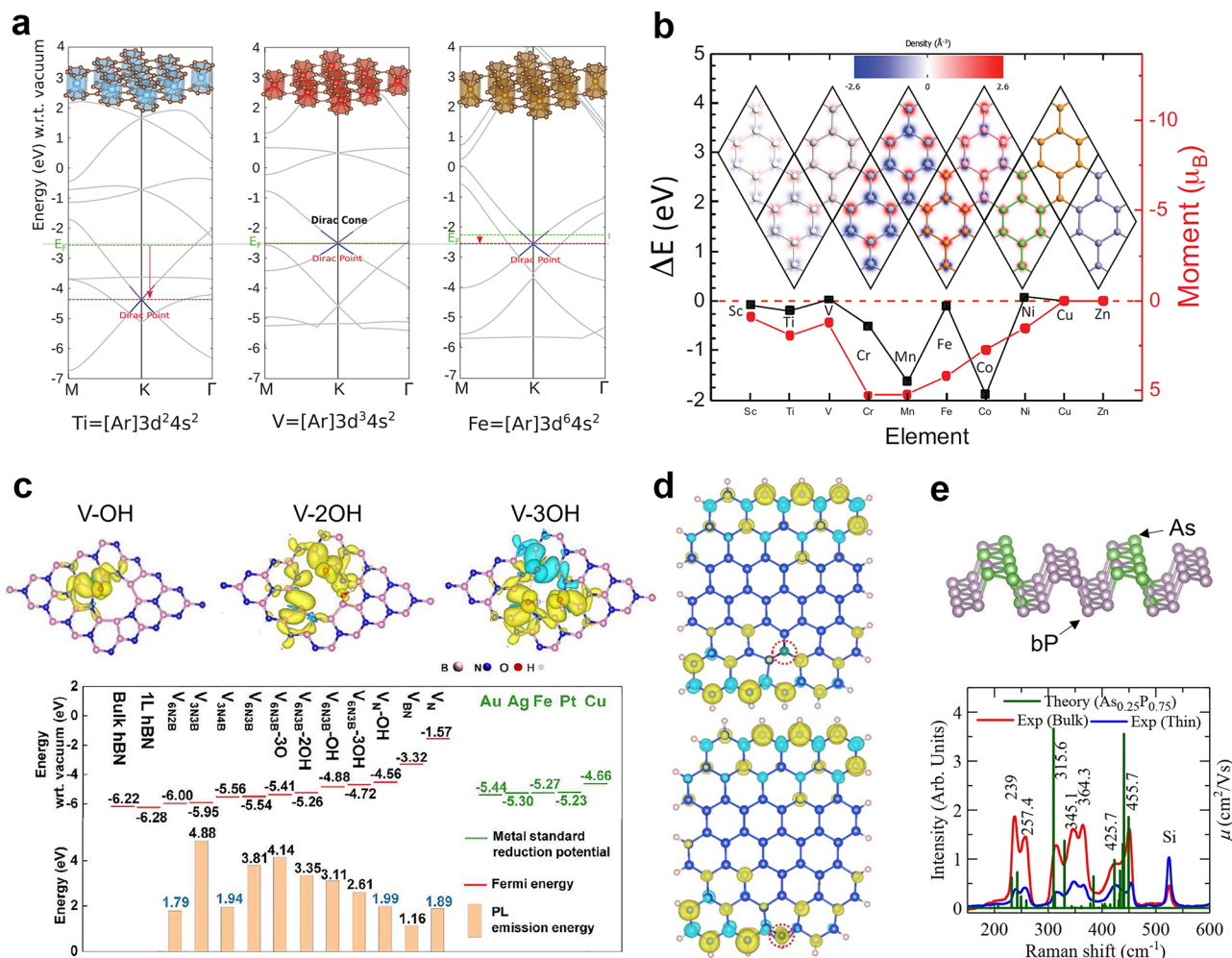


Figure 3. Theory-predicted properties of functionalized 2D materials. (a) The shifted Dirac points of BLG with Ti/V/Fe intercalants relative to pristine BLG with inserted structures. Reproduced with permission from ref 20. Copyright 2018 American Chemical Society. (b) The magnetic moment and energetic ground states of various TM-intercalated BLG. Reproduced with permission under a nonexclusive license to distribute from ref 22. Copyright 2019 arXiv. (c) The spin density of BN with functionalized vacancies, and the shifting Fermi energy of d-BNs with distinct type, size, and functional groups of the vacancies. Reproduced with permission under a Creative Commons CC-BY 4.0 License from ref 34. Copyright 2021 Elsevier. (d) The spin density relies on the position of carbon dopant(s) within MoS₂. Reproduced with permission from ref 39. Copyright 2020 American Chemical Society. (e) The distribution of As dopants within b-P and its theoretical Raman spectra relative to experimental counterpart. Reproduced with permission from ref 40. Copyright 2019 Royal Society of Chemistry.

ric 2D materials, such as Janus monolayers (e.g., SeMoS and SMoSe) and 2D metals (e.g., Ga and In) confined in graphene/SiC interface, can be realized and studied optically by Raman spectroscopy, optical measurements, second harmonic generation, etc. Because of their atomic thickness and high surface-to-volume nature, both their phonon and band structure are very sensitive to slight changes in electron doping and strain when they interface with other materials, which serve as the foundation for scalable sensing.

Finally, we summarize efforts on the physics and devices of relevant quantum materials grown via MBE and bulk crystal growth. First, we show some of recent progress in mixed-dimensional heterostructures, including 2D materials combined with single metal atoms or quantum dots (so-called zero-dimensional materials, 0D) into 0D/2D platforms for sensing and electronic doping and hybrid 2D/3D electronic material integration for logic and memory devices. Second, we highlight $\text{Mn}_2\text{Bi}_2\text{Te}_4$ —an emerging intrinsic magnetic TI—and its ferro- and antiferromagnetic properties. Third, we provide an overview on the quantum anomalous Hall effect in magnetically doped TIs and its metrological applicability without an external magnetic field. Then, we review two emerging 2D homojunctions made of and their unique moiré physics: graphene trilayer with each layer twisted by $\approx 1\text{--}2^\circ$ and $T_d\text{-WTe}_2$ bilayer with each layer twisted by $\approx 5^\circ$. Due to the rapid advancement of this field, this review only summarizes the most recent breakthroughs in 2D materials discussed at the 2022 Penn State Graphene and Beyond Workshop. At the end of the review, we provide perspectives and future works. While discussions on earlier works are not provided, they can be found in our prior reviews.^{11,12,15,16}

DISCUSSION

1. Theory and Computation. *1.1. Modeling Intercalation, Defects, and Doping in 2D Materials.* Theoretical calculations are not only tools for designing future materials but also for modifying their properties. In layered compounds, some of the most powerful engineering techniques to tailor material properties—which we will emphasize in this section—are intercalation, doping, and defects (Figure 2). In this subsection, we will give an overview on computational predictions of intercalation and defect engineering in 2D materials, highlighting their potential impact on next-generation technologies by tailoring structural, electronic, optoelectronic, magnetic, and catalytic properties.

1.1.1. Intercalation. Monolayer graphene (MLG) possesses several attractive material features; however, the lack of property tunability and limited chemical space limits its progress. By contrast, bilayer graphene (BLG), constructed by stacking two MLGs, is an effortless form to drastically expand the electronic flexibility of 2D carbon-based systems. Moreover, BLG allows for intercalation as a viable technique to perform material modification (Figure 2a). Unlike doping and adsorption, intercalation is the attempt to control material properties via taking advantage of the vdW-regulated space between BLG layers. What is more open-ended, few-layer graphene (FLG) can provide scenarios for investigating staging and cointercalation, especially in the realm of electrodes for energy storage.^{17,18}

Regarding electronic properties, graphene-based materials decorated with intercalants were found to present a controllable position of Dirac point from the Fermi level.¹⁹ This provided a way to discover candidates for various semiconductor applications, especially for interconnect technologies such as

integrated circuits. Pakhira et al.²⁰ systematically simulated 2D slab and bulk BLG systems intercalated with a series of transition metal (TM) via density functional theory (DFT) calculations. Their calculations predict high thermodynamic stability and Dirac cone tunability in the intercalated systems, as shown in Figure 3a. Since the electrons distributed near the Fermi energy can drastically affect the position of the Dirac point, distinguishing the electron density around the Fermi level becomes significant. Their results also indicate that the main electron density contributions around the Fermi level derive from the p_z subshell of carbon and $3d$ subshells of intercalated TMs. Controlling the type and concentration of TMs within BLG indeed offers an interesting approach to modulating electric properties.

Furthermore, the shift in the chemical potential of graphene caused by atomic intercalants was considered for inducing superconductivity.²¹ The intercalation of alkali and alkaline metals within few-layer graphene (FLG), whose p band crossings at the Fermi energy contribute to superconducting behavior, was well-studied. Inspired by this, Lucht et al.²² implied that the hybridization of d bands deriving from TMs could have a similar mechanism to construct superconductive systems. By comparing established superconducting systems with their theoretical results of first-row TM-intercalated BLG in the aspects of lattice constant and interlayer band energy, they found that Sc, Ti, and V are promising intercalants to promote superconductivity. The d orbital electrons of these intercalants were believed to constrain the interlayer band energies below the Fermi level via the interaction with p orbitals of graphene, inducing superconductive behavior. On the other hand, other TMs with more d orbital electrons did not present superconductivity, as they alleviated such hybridization by having more paired electrons, enlarging the interlayer distance to an inappropriate level for superconductivity. Other parameters, such as number of layers, concentration of TMs, or even cointercalation, could be starting points for sharpening the mechanism and precise property modulation in graphene and other 2D materials.

Moreover, structures that interacted with TMs were proven to display noticeable magnetic properties due to the coupling of their d orbital electrons with graphene.²³ The study by Lucht et al.²² also simulated how the magnetic features of BLG were influenced by several TM-intercalants, further defining their corresponding magnetic ground states. Briefly, in Figure 3b, Cr, Mn, and Co were found to have larger magnetic moments while Cu and Zn have moments approaching zero. These differences in their magnetic moments stem from the number of unpaired electrons. For instance, Zn has fully occupied orbitals, resulting in a lack of $d\text{-}sp^2$ hybridization when interacting with graphene. In addition, among first-row TMs, V and Ni are the only two having ferromagnetic configurations and the remaining first-row TMs are antiferromagnetic. BLG with TM intercalants is, after all, a pioneer in magnetic alteration.

Another family of materials where TM-intercalation was predicted to yield promising electronic properties is 2D covalent organic frameworks (2D-COFs), which are porous crystalline materials comprised of organic bridging linkers. The structural features of 2D-COFs are shown in Figure 2b. These compounds have become increasingly popular in the past two decades due to their porous architecture, high surface area, and unique tunability.²⁴ These properties have led to various use-cases, including catalysis,²⁵ energy storage,²⁶ molecular sensors,²⁷ and biomedical applications.²⁸ What makes 2D-COFs stand out is

that their monomers are covalently bonded in a 2D sheet, with almost perfect “eclipsed” stacking due to π - π out-of-plane interactions, generating 1D columns that are ideal for charge and exciton transport.

The electronic properties of 2D-COFs are traditionally modified by changing the organic linkers that make up the layers²⁹ or modifying the length of their chains.³⁰ However, this generally does not solve the main issue for their application as porous electronic materials: e.g., intrinsically low conductivity and charge-carrier mobility. Nevertheless, there is potential to bypass these problems by intercalating the 2D-COF layers with transition metals (see Figure 2b), which yields electronic properties that range from insulating to conducting.^{31,32} Pakhira et al.³¹ showed that the systematic addition of Fe in the centroid of the COF rings produced a drastic change to the Fermi level and band morphology of these structures. For example, they found that a pure triazine-benzene-boroxine COF's insulating behavior (2.6 eV indirect band gap) is modified to a semiconductor (1.18 eV direct band gap) with the addition of Fe atoms at the centroid of all rings in the unit cell. Furthermore, the band structures show a reversal in the conduction band curvature and a change in the relative position of the Fermi level. Intercalated 2D-COF architectures presented band gaps as small as ≈ 0.3 eV and as large as ≈ 2.6 eV, with several intermediate values. In addition, through vibrational analysis, these materials were also predicted to be thermodynamically stable. Their excellent electronic tunability and dynamic stability present an interesting opportunity to use layered COFs as nanoporous electronics and optoelectronics.

Intercalation can also be used to achieve higher reactivity during catalysis. One reaction of great interest is “water splitting” (also known as oxygen evolution reaction). Carrying out this reaction efficiently could decrease the current cost of hydrogen for fuel cells, attacking one of society's current issues: clean-energy production. A promising 2D material that stands out for this application is birnessite: a layered, ion-intercalated manganese oxide. Birnessite acts by mimicking plant's photosystem II. This natural system captures solar energy to oxidize water, a reaction that occurs in the Oxygen Evolution Center: a cubane-like structure comprised of $\text{Mn}_4\text{O}_8\text{Ca}$. Birnessite has a similar structure, composed of ion-intercalated MnO_2 tetrahedra. Birnessite intercalated with different cations was theoretically studied by Lucht et al.³³ who discovered that Sr, Ca, B and Al-intercalated birnessites have valence bands with a band alignment suitable for water splitting. In addition to its water-splitting capabilities, bulk birnessite intercalated with boron has a direct band gap of about 2 eV, which has suitable properties for light-capture. An analysis of monolayer birnessite further revealed that Mg and Sr-intercalations present an indirect-to-direct band gap transition when reducing the bulk to a slab, with direct band gap energies of 2.19 and 2.69 eV, respectively, which are also suitable for light capture. The theoretically predicted band alignments and band gaps for birnessite predict its ability to perform both oxygen evolution and light capture simultaneously, which could lead to materials that can carry out photocatalytically activated oxygen evolution, comprising a step toward achieving artificial photosynthesis.

1.1.2. Defects. Defects are generally seen as undesired, as it is usually difficult to control and predict their effect on materials' properties. However, for 2D materials, defects such as vacancies, dopants, and substitutions are effective methods to alter and fine-tune materials' properties. Vacancies, in particular, can induce an electric potential that reshapes the electron

distribution, and further changes the materials' electric and chemical properties (Figure 2c). For example, Lei et al.³⁴ activated chemically inert BN via the decoration of vacancies, which could be applied to the reduction of metal cations for the hydrogen evolution reaction (HER). Based on their DFT calculation, a high spin density, which can represent unpaired electrons or free radicals, was surrounding the vacancies; this indicates vacancy-induced reactivity. Most interestingly, the Fermi energy level of defective-BN (d-BN) could be finely shifted from -6.28 to -1.57 eV by controlling the type, size, and functional groups (functionalization) of the vacancies as shown in Figure 3c. Overall, localized free radicals and a tunable band alignment could aim to achieve several metal reductions (Fe, Cu, Au, Ag, and Pt) with different redox potentials. Aside from d-BN, other defective 2D materials that have been predicted as excellent electrocatalysts for hydrogen evolution include MoS_2 with S vacancies,³⁵ PtSe_2 with Pd/Pt substitutions,³⁶ and MoSi_2N_4 with nitrogen vacancies.³⁷ All these examples require defects to boost their electrochemical activity for hydrogen evolution, making defects essential to engineer properties of 2D materials.

On the other hand, doping is the introduction of a small amount of impurities into a material. Doping is well-known for aiding in the design of field-effect transistors (FETs), as it can help calibrate 2D materials' electric features, such as electronic transport, with dilute concentrations of dopants.³⁸ Recent studies showed that 2D materials' properties affected by the introduction of dopants were not only dependent upon the concentration of dopants (which had been widely studied in the past), but also on the atomic position of impurities in the structure. A first-principle study³⁹ in 2020 defined how the structures and properties including band gap, formation energy, and magnetism were influenced by the position of carbon dopant(s) within monolayer Si (MLS), as shown in Figure 3d. Silicon-carbon substitution at the edge sites was found to be more energetically preferable; interestingly, these substitutions generated high neighboring spin density around the doping site. Also, the authors found that reducing the distance between two dopants leads to a more distorted and unstable geometry of carbon-doped MLS. More significantly, they concluded that if a doping site breaks the symmetry of the whole structure more, more band degeneracies can be broken, inducing a larger band gap. Apart from the substitution site of a dopant, its distribution can determine advanced features for electronics as well. For instance, Pradhan et al.⁴⁰ unveiled a certain distribution of As dopants within black phosphorus (b-P) that could contribute to not only an appropriate band gap for FETs, but also an anisotropic fast carrier mobility, which can range from 300 to $600 \text{ cm}^2 \text{ V}^{-1} \text{ s}^{-1}$. In order to define such As dopant arrangements, they took advantage of theoretical techniques to compute the Raman spectra of designed models, and find the structure that agreed with their experimental Raman results, as shown in Figure 3e. To some degree, the clustering of As atoms is more stable and presents an anisotropic transport property that is gate-voltage dependent for 25% arsenic doped b-P. Finally, another doped 2D material that has shown promising properties is S-doped MoP (Figure 2d). Through theoretical and experimental results, it was found that the addition of S atoms in MoP leads to a smaller band gap (0.67 eV in S-doped MoP compared to 2.18 and 2.07 eV for pure MoS_2 and MoP, respectively), and high electron mobility near the Fermi level due to rectification of electron accumulation at the conduction and valence bands.⁴¹ These properties are highly favorable for

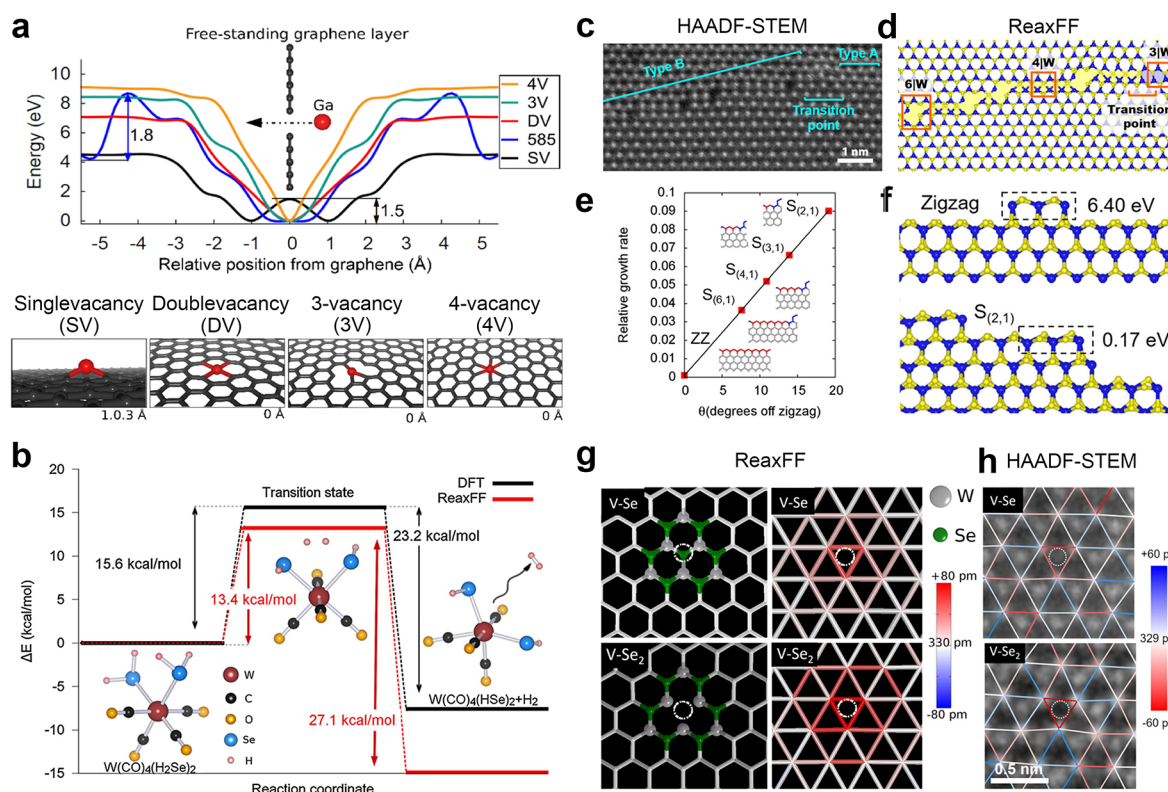


Figure 4. Examples of ReaxFF applications to 2D materials. (a) Ga diffusion through a free-standing defective graphene. The graph shows a potential energy barrier for Ga diffusion into defective graphene sites: SV, DV, S-8-S, 3 and 4 V at 0 Å. Ga diffusion realizes from right to left in the graph. The images at the bottoms show the most stable Ga adsorption on SV at 1.03 Å, DV at 0 Å, 3 V at 0 Å, and 4 V model at 0 Å, respectively. Adapted with permission from ref 46. Copyright 2022 Elsevier. (b) ReaxFF and DFT predicted reaction pathway for hydrogen release from the $\text{W}(\text{CO})_4(\text{H}_2\text{Se})_2$ molecule. Adapted with permission from ref 43. Copyright 2019 Elsevier. (c) ADF-STEM image showing type A and B GBs, as well as the transition point between them. (d) ReaxFF MD simulation equilibrated at 300 K of the structure shown in (c). (e) Computed relative growth rate of the slanted edge structures with respect to the sulfur-terminated zigzag (ZZ) edge as a function of slanted angle, θ . $S(2,1)$, $S(3,1)$, $S(4,1)$, and $S(6,1)$ are the slanted edges characterized by the translational vector $(n, 1)$ of the 2H- WS_2 lattice, where n is the number of the zigzag units along the a1 direction, and a 2-component vector contains only one zigzag unit in the GB of interest (f) Illustrations of the formation energy for adding atoms (enclosed in the dashed rectangular boxes) onto the reference sulfur terminated ZZ and $S(2,1)$ slanted edges, respectively. Adapted with permission from ref 51. Copyright 2021 American Chemical Society. (g) Ball-stick representations and W–W bond displacement maps of V-Se and V- Se_2 point defects based on ReaxFF methods. (h) HAADF-STEM images with overlaid maps of the distances between neighboring W atoms of V-Se and V- Se_2 . In (g,h) The vacancies are marked by dotted white circles. Adapted with permission from ref 44. Copyright 2020 American Chemical Society.

hydrogen evolution catalysis. Cluster model computations also elucidate the amount of dopant with the best catalytic activity. In particular, the authors found that a small percentage of S dopant (5% S) in MoP leads to a more favorable HER rate-limiting (Volmer) step during the reaction, compared to 10% S-doped MoP, pure MoS_2 , and pure MoP.

1.2. High-Speed and Large-Scale Modeling for 2D Materials Based on ReaxFF. Understanding the effect of operating conditions such as temperature, pressure, flow rate, and gas-composition on 2D material growth kinetics is challenging. Modeling and simulation can improve the atomic-level understanding of the morphology and characteristics of a resultant structure and thus enhance the ability for better control of the complex growth process of 2D materials. The ReaxFF reactive force field, originally developed by van Duin et al.,⁴² is a computationally efficient means that captures the covalent bond breaking and reforming by updating the bond order at each molecular dynamic iteration, in contrast to nonreactive potentials. Therefore, ReaxFF molecular dynamics (MD) simulations are highly effective in capturing detailed chemical events, reaction pathways, and product formation during gas-phase and gas/condensed phase simulations, for systems up to

$\sim 10^6$ atoms and for time scales not accessible to first-principles based techniques. This ReaxFF potential can simulate the nucleation and growth and intercalation of 2D materials, which involves both gas-phase and surface interactions, as a function of local chemical environment, helping in predicting effective growth protocol.^{43–46} It features vdW interactions which particularly enables the simulation of multilayer vdW hetero- and homostructures.^{44,46} Additionally, ReaxFF provides thermodynamic and kinetic insight into fundamental solid-phase phenomena observed in 2D materials such as atomic intercalation, grain boundary (GB), defect formation and diffusion, stress induced lattice distortions, morphological evolution of 2D domains as a function of local chemical environment during the growth. Also, ReaxFF differs from the so-called “first generation” reactive force fields such as Tersoff^{47,48} and Brenner⁴⁹ by applying a significantly longer-ranged bond-order relationship, which makes it possible to achieve accurate reaction kinetics. The ReaxFF framework has been successfully applied to a wide range of 2D systems^{50–52} and their defect formation, growth mechanisms and characterization, as shown in the following examples.

1.2.1. Kinetics of Ga Intercalation through Graphene. Nayir et al.^{46,52} used a combination of ReaxFF- and DFT-based simulations to study defects in graphene, which can act as pathways for Ga intercalation into the interface between graphene and SiC. The results show that the sizes of vacancy defects ranging from single carbon vacancy (SV) to multiple carbon vacancy (3 and 4 V) can affect the thermodynamic and kinetic preference of intercalant between the adsorption on graphene surface or the intercalation at the interface. For example, the diffusion of a relatively large Ga atom through small sized defects (<3 V) is kinetically hindered, where Ga encounters a kinetic barrier. However, the potential energy of the system monotonically decreases as Ga approaches to graphene with larger sized defects (>double vacancy, DV) and the diffusion through graphene layer is nearly barrierless (Figure 4a). This suggests that defect engineering provides an effective way to lower the temperature required for intercalation, by consequence, energy savings and cost reduction during 2D material intercalation.

1.2.2. MOCVD Growth of WSe₂. A combination of ReaxFF- and DFT-based chemical kinetic models developed by Xuan et al.⁴³ provides a fundamental insight into kinetic properties of elementary reaction pathways leading to the WSe₂ formation from W(CO)₆ and H₂Se precursors. During MOCVD at elevated temperatures, CO ligands will dissociate from W(CO)₆ and H₂Se will rapidly fill in the ensuing vacancies in W-carbonyl, resulting in intermediate W(CO)_x(H₂Se)_y molecules. Continuous H₂ release from the WCO_x(H₂Se)_y is a key event that could determine the growth rate of 2D WSe₂. The model in Figure 4b shows that H₂ release from W(CO)₄(H₂Se)₂ with a kinetic energy barrier of 13.4 kcal/mol at the ReaxFF results in a more stable product, W(CO)₄(HSe)₂. The reverse reaction may also occur, as pure H₂ environment is used in the process. However, for W(CO)₄(HSe)₂+H₂ → W(CO)₄(H₂Se)₂, the barrier for the reverse reaction is higher, 27.1 kcal/mol in ReaxFF. Based on simulations, these reactions are generally exothermic with a lower activation energy than their reverse reactions, indicating that H₂ release is thermodynamically favorable. After all H₂ and CO ligands are released from the intermediate molecules, stable 2D WSe₂ films can grow on substrates.

1.2.3. Grain Boundary and Defects in 2D TMDs. Hickey et al.⁵¹ uncovered invisible translational defect arrays in nearly single-orientation, coalesced monolayer WS₂ films with high-angle annular dark field (HAADF) scanning transmission electron microscopy (STEM) imaging and used ReaxFF MD simulations at 300 K to create the same irregular translational GB (Figure 4c,d). There are two types of GBs: one has vacancy line defects, and the other adopts a rectangular arrangement of W atoms, 4lW, at the boundary and is stabilized by 6lW rings that cause steps in the GB. The latter is comprised of the slanted edges with angles within the range of 0 to 30°, deviated from the zigzag edge. The ReaxFF MD calculations show that the kink concentration significantly affects the stability of slanted edges as shown in Figure 4e,f where the growth rate is linearly correlated to the kink concentration. In a Sulfur-rich environment, given the high-cost energy required for the first nucleus formation, the most stable ZZ structure, whose edge atoms are passivated by Sulfur atoms, is the slowest to grow while the slanted edge with a highest kink concentration is expected to grow fastest. The analysis in the aforementioned work indicates that growth of the S-ZZ edge requires a long time to complete its linear formation. Therefore, even though the slanted edges are less stable edge structures and should disappear quickly during the growth

process according to the growth conditions, shorter growth time or slower flow rate of the gas-phase precursors, most likely, may not allow flakes to complete their zigzag linear formation, thus, grains with the slanted edges may survive during the growth to meet at the GB.

The ReaxFF reactive potential was used to simulate point defects in a 2D WSe₂ to study their influence on local strain. Figure 4g presents the atomic configurations and the ReaxFF-based bond displacement maps of single Se vacancy (V_{Se}) and double Se vacancy (V_{Se2}) in WSe₂. The loss of Se of two defect types drives bond contraction between adjacent W atoms and reduces W–W distances by about 15 and 24%, respectively, as the unsaturated W atoms marked by red triangles radially contract toward the chalcogen vacancies in the maps. These strain effects are consistent with STEM imaging, which shows that the distances between three W atoms adjacent to the V_{Se} and V_{Se2} are contracted by approximately 10 and 18%, respectively, in good agreement with the ReaxFF results.

1.3. Artificial Intelligence and Machine Learning in 2D Materials Research. In recent years, exploiting artificial intelligence (AI), machine learning (ML), data mining, and other data-driven approaches has steadily grown its presence in various aspects of 2D materials research. With traditional materials development commonly taking 1–2 decades to develop from conception to completion,⁵³ a different approach for the creation of 2D materials research needed to be considered to reduce research time. On the one hand, the Materials Genome Initiative has provided a strong impetus for creating databases and screening methods for materials with specific functionalities. On the other hand, rapid progresses in Industry 4.0 provides matured methods for instruments and data-science to meld seamlessly to streamline manufacturing and other complex industrial processes. Given the advent of easy-to-use ML tools,⁵⁴ these emerging statistical approaches have been utilized to speed up material development processes—even reducing some experimental optimizations down to just 8 h.⁵⁵ We next describe recent developments in various aspects of 2D materials research where applications of ML can accelerate and/or enable scientific and technological advances.

1.3.1. Machine Learning in 2D Material Theory. With the availability of high-performance computing, data mining, pattern recognition, and other search algorithms are being used frequently to computationally “discover” materials, including 2D materials. These theoretical works in 2D materials have led to collaborative efforts to provide shareable DFT information using databases.⁵⁶ More importantly, such shareable resources have led to a standardization of processes for the community—effectively establishing generally accepted structures of data. These standardized data structures allow for the sharing of data across many different platforms in DFT, which is conducive to the integration of ML algorithms. Applying the data from these databases, many groups have effectively utilized ML to predict physical properties of a lattice structure,⁵⁷ replicated electron scattering in a DFT+U model,⁵⁸ and even exploited crystal graph convolutional neural networks to study nearly 45,000 2D structures to discover compositions suitable for photovoltaics.⁵⁹ Advancing this field forward, Suzuki et al.⁶⁰ have developed methods for achieving machine-learned exchange correlation (XC) functionals for time-dependent DFT (TD-DFT) calculations using neural networks. Given that XC inaccuracies have been a consistent issue in DFT, XC functionals derived from experimental data and fit through ML

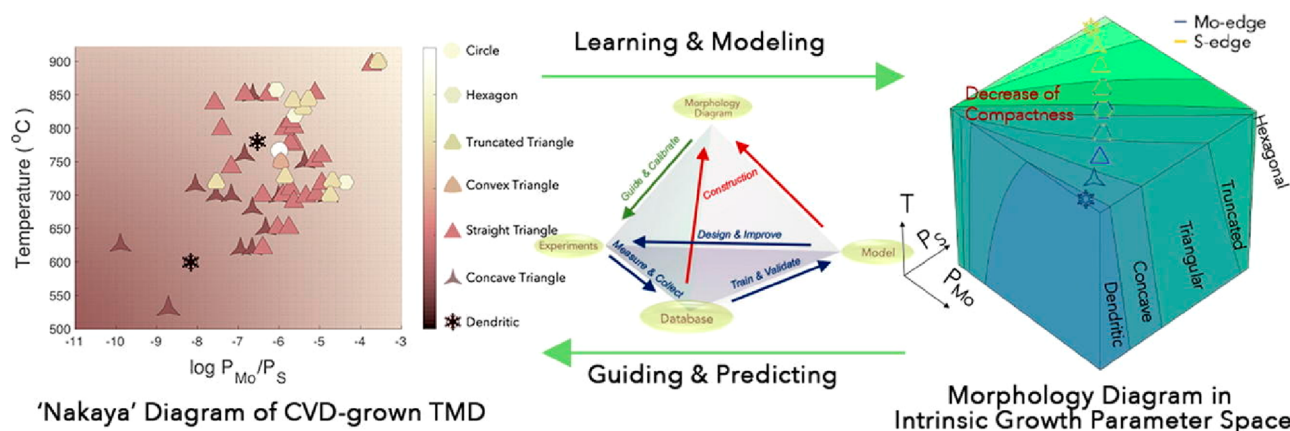


Figure 5. Proposed ML framework for understanding the correlation between the ratio of precursors in this case partial pressure of Mo versus S sources in a CVD reactor, and the resulting shape of the grown crystal. Reproduced with permission from ref 80. Copyright 2020 Elsevier.

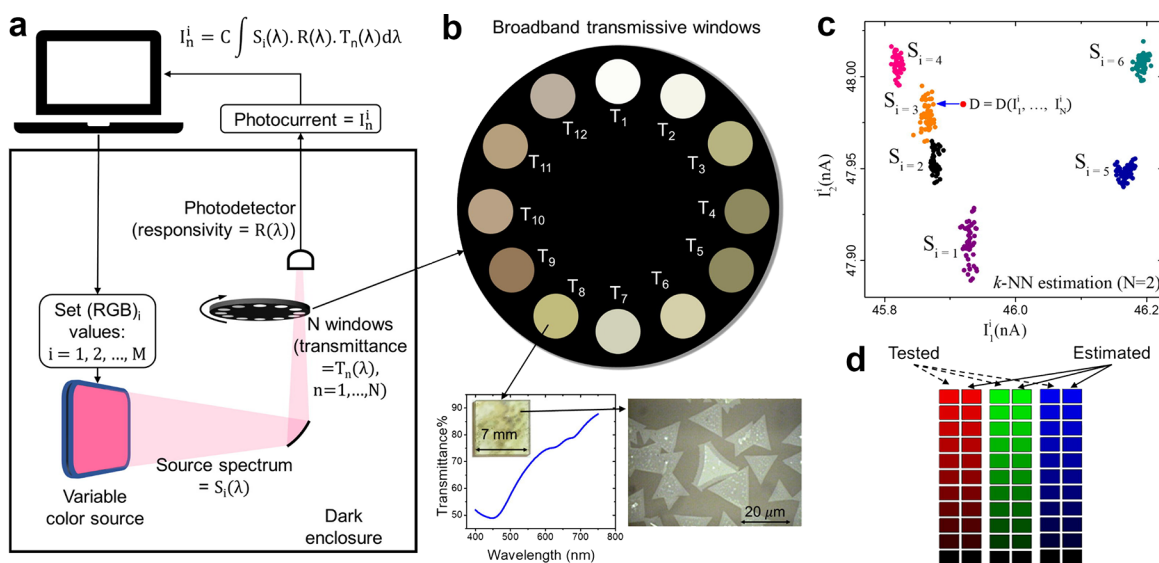


Figure 6. Artificial eye (or, A-Eye), an instrument that uses a nondispersive method for achieving accurate classification, reproduction, and spectral estimation of color by exploiting engineered variations in optical transmittances of 2D materials. (a) Schematics of data collection system in dark enclosure. The RGB colors are generated via a python code on a screen, the generated lights are allowed to pass through a set of transmissive windows, one at a time; then the transmitted lights are collected by the single photodetector. The signals are collected with the same computer. The measured photocurrent is related to the generated incident spectrum, the transmittance of the window, and the responsivity of the photodetector, via the given formulas. (b) Transmissive windows mounted on a disk (top). Transmittance curve and real-size optical image of one of a typical transmissive window made of CVD-grown TMDs, as well as microscopic image from a segment of this transmissive window (bottom). (c) Application of k -nearest neighbor (k -NN) method with $k=1$, where only two transmissive windows ($n=1, 2$ out of N) and five groups of data ($S_{i=1-5}$) are shown. For each i , an N -dimensional data point $S_i = S_i(I_1^i, I_2^i, \dots, I_N^i)$ for RGB_i is generated and stored. The data points with similar colors group together in the training set. Here, $S_i=3$ is the nearest neighbor class for the test sample $D = D(I_1^i, I_2^i, \dots, I_N^i)$. (d) A small set of tested single colors, red, green, and blue (left columns in each column pair), with their corresponding estimated colors (right columns in each column pair), using the methods outlined in panels (a)–(c). Adapted and modified with permission from ref 81. Copyright 2022 Elsevier.

algorithms stand to serve the long-standing issue of understanding unknown systems, potentially without the need for energy convergence, drastically reducing computational time while increasing accuracy of simulations. In keeping with the recent progress with magic-angle moiré superlattice engineering, ML approaches are being blended with theory and computational approaches to achieve high-throughput searches of multiply stacked, multiangle 2D materials with specific, desired properties.⁶¹ With increasing computing powers, more difficult and also more accurate calculations of functionalities will become achievable, thanks to the growing collaboration between computational physicists and data scientists.

1.3.2. Machine Learning in 2D Material Synthesis. Utilizing ML in the synthesis of 2D materials may not only be considered useful but also a requirement for future discoveries. Predictable synthesis of 2D materials depends on precise control over a combination of experimental parameters. In micromechanical exfoliation techniques, 2D flakes (e.g., graphene) are usually transferred onto a flat substrate from a bulk crystal (like graphite). In this case, the shape and size of both the bulk source and the transferred 2D layer are random. This randomness makes developing/training machine-learning algorithms that could assist fabrication of identical 2D layers a considerable challenge. In this case, ML approaches are more useful for

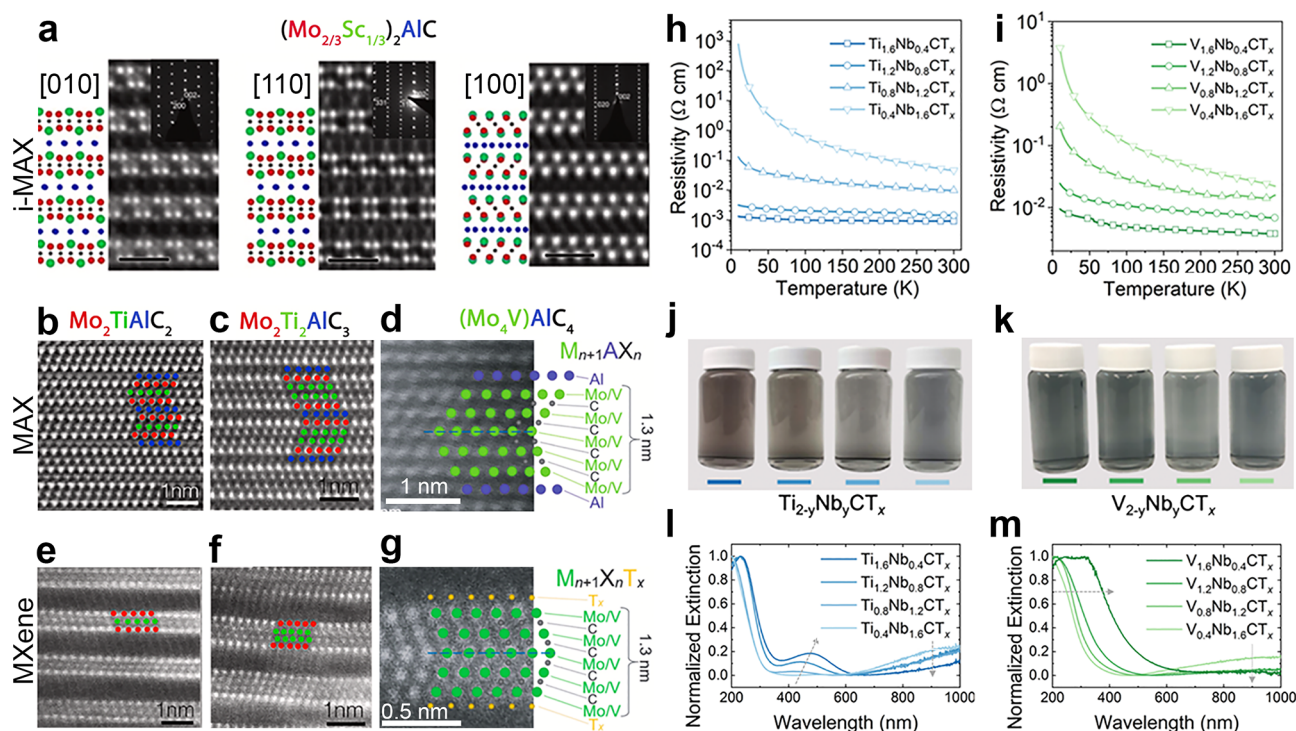


Figure 7. Structures and properties of MXenes. (a) High-resolution scanning transmission electron microscopy (HRSTEM) and corresponding selected area electron diffraction (SAED) patterns of $(\text{Mo}_{2/3}\text{Sc}_{1/3})_2\text{AlC}$ i-MAX phase along the [010], [110], and [100] crystal orientation, together with schematics based on a monoclinic $\text{C2}/c$ symmetry. The red, green, blue, and black spheres in the schematics are Mo, Sc, Al, and C, respectively. (b) HRSTEM of $\text{Mo}_2\text{TiAlC}_2$, (c) $\text{Mo}_2\text{Ti}_2\text{AlC}_3$, and (d) Mo_4VAlC_4 MAX phases. STEM images of (e) $\text{Mo}_2\text{TiC}_2\text{T}_x$, (f) $\text{Mo}_2\text{Ti}_2\text{C}_3\text{T}_x$, and (g) $\text{Mo}_4\text{VC}_4\text{T}_x$ MXenes. For the panels (b, c, e, f), the blue, red, and green spheres represent Al, Mo, and Ti, respectively. For the panels (d, g), the green, blue and orange spheres represent Mo/V, Al and surface terminations T_x . Images in (d) and (g) demonstrate a herringbone-type structure with an atomic schematic and mirror plane shown by solid circles on the right and a dashed line, respectively. Reproduced (adapted) with permission from ref 97. Copyright 2021 Elsevier. (h, i) The temperature dependent electrical properties of (h) $\text{Ti}_{2-y}\text{Nb}_y\text{CT}_x$ and (i) $\text{V}_{2-y}\text{Nb}_y\text{CT}_x$. (j, k) The optical properties of solid-solution (j) $\text{Ti}_{2-y}\text{Nb}_y\text{CT}_x$ and (k) $\text{V}_{2-y}\text{Nb}_y\text{CT}_x$ colloidal solutions in deionized water. In all three systems, the gradual change in color resulting from the different stoichiometries can be observed. (l, m) The quantitative UV-vis spectra normalized to a maximum extinction of 1 of the (l) $\text{Ti}_{2-y}\text{Nb}_y\text{CT}_x$ and (m) $\text{V}_{2-y}\text{Nb}_y\text{CT}_x$ systems. For all systems, multiple features are visible with a nonlinear shift in the absorbance with changes in the composition. Reproduced (adapted) with permission from ref 96. Copyright 2020 American Chemical Society.

automated searching specific candidates in from a dense ensemble of mixed-thickness flakes. For example, masked convolutional neural networks techniques applied to optical microscopy images can provide high-probability identification of various monolayer flakes (e.g., graphene, hBN, MoS_2 , and WTe_2) from a collection of flakes of various thicknesses exfoliated onto a flat SiO_2/Si substrate.⁶² In contrast, chemical vapor deposition (CVD), MOCVD, plasma-enhanced CVD, MBE, sputtering or other reactor-based synthesis of 2D materials can have a larger range of controllable parameters in their 2D crystal growth recipes (e.g., temperature, pressure, flow rate of carrier and reactant gases, ramp-rates, and several other design of experimental or DoE parameters). Here, trial-and-error approaches to optimize the DoE parameters for a specific type of outcome (i.e., crystal quality, yield, reproducibility, or large-area coverage, etc.) for each type of reactor can be daunting. Traditional DoE methods,^{63–65} even with Latin-hypercube sampling (LHS),⁶⁶ require a large input of samples to be useful. Because of this, Bayesian Optimization (BO)^{67–71} with Gaussian Processes (GP) tends to be the preferred method of experimental optimization of materials due to its ability to work with smaller sample sizes. While this technique has yielded promising results from previous research,^{72–77} a shortfall of this approach is the computational requirements associated with it. A

computational training cost of $O(N^3)$ with BO of GP⁷⁸ is not technically very challenging but it would be preferable to have a training cost of $O(N)$ for lower budget research groups, which will require a creative shift from BO to simpler feedforward Neural Networks (NN).⁷⁹ Since NNs typically require large data sets for training, one approach could be to simplify the problem into smaller subsets of problems. For example, the objective of one subset could be to find correlations between the ratio of precursor material P_x/P_y to the resulting shape of the flakes, i.e., triangular, polygonal, or dendritic, as was suggested in a recent perspective on 2D materials,⁸⁰ with the idea articulated in Figure 5. A second subset of machine-learning guided experiments could then aim to find correlations between the DoE parameters (precursor quantity, temperature, flow rate, ramp-rate, growth duration, etc.), and the resulting *in situ* conditions of P_x/P_y at the growth surface. Finally, a third set of ML-guided experiments will then need to find correlations between shapes of seed crystals versus their propensity for eventually growing into large-area, uniform, and/or high-quality 2D layers on a given substrate, depending on the required target outcome. A combination of these three kinds of ML-guided experiments is likely going to help provide the best correlation between DoE parameters and final 2D material outcomes.

1.3.3. Machine Learning Used with 2D Materials. In contrast to utilizing ML to discover 2D materials, 2D materials have recently been used in conjunction with, and even as, ML algorithms. It has been shown recently that the optical transmittance of TMDs can be exploited to allow for accurate light source color identification by training an ML model to identify wavelengths based off measurements from the single-cell silicon photodetector with an accuracy of 99%—effectively drastically reducing the cost of accurate color identification systems⁸¹ (Figure 6). Given that most modern cameras utilize Bayer filters over complementary metal-oxide-semiconductor (CMOS) sensors, it takes four Si photodiodes to measure the color of a single pixel in a modern camera. It is then feasible to presume that using this ML technique with TMDs filters could possibly reduce camera sensor surface area by one-quarter, while retaining similar light intensity response and color accuracy. In recent years, many researchers have also shown the viability of using 2D materials themselves to develop hardware-based neuromorphic systems.⁸² Mennel et al.⁸³ even developed an Artificial Neural Network (ANN) for identifying images—allowing for low-power training cost and ultrafast analysis—boasting some computations as fast as 50 ns. According to Mennel, this time is only limited due to the onboard clock. Given these emerging technologies, the future of ML for 2D material development may, intriguingly, be done so by 2D materials.

2. Synthesis and Processing. **2.1. MXenes with Multiple M-Elements: Composition–Structure–Property Relationships.** MXenes are an emergent, and potentially the largest, class of 2D materials discovered to date.⁸⁴ This class of transition metal carbides, nitrides, and carbonitrides has the general formula $M_{n+1}X_nT_x$ where M is an early transition metal (Ti, V, Nb, Ta, etc.), X is C and/or N, T_x represents the surface functional groups (typically O, OH, F, and Cl), and $n = 1–4$.⁸⁵ MXenes are produced by a top-down synthesis approach where $M_{n+1}AX_n$ (MAX; A is typically Al, but can be Si or Ga) phase precursors are selectively etched via wet HF-containing mixtures,⁸⁷ molten salt,⁸⁸ halogenation,⁸⁹ and others.⁹⁰ MXenes have been widely studied due to their desirable properties, such as hydrophilicity (soluble in water with no additives or surfactants),⁹¹ ease of processing (able to be used in any conventional water-based route, e.g., spray coating, dip coating, vacuum filtration),⁹¹ scalability (no change in properties as batch size is increased),^{92,93} and desirable optical (tunable plasmon resonance, optical response in visible region, electrochromic nature),^{94–96} electrical ($>20,000$ S/cm conductivity, metallic-like response to cryogenic temperatures, magnetic transitions),^{94,96,97} and mechanical properties (around 0.4 TPa Young's modulus from solution processed materials).^{97,98} Due to these properties, MXenes have found widespread use in a variety of fields, including electrochemical energy storage,⁹⁹ electromagnetic interference shielding,¹⁰⁰ medicine,^{101,102} environmental remediation,^{103,104} additives to composites, etc.^{105,106} To date, more than 30 stoichiometric MXenes have been discovered, in addition to a theoretical infinite number of solid-solution MXenes. In addition to single-M MXenes, there are broadly three classes of multi-M MXenes: i-MXenes (in-plane ordered divacancy MXenes; Figure 7a), ordered double transition metal MXenes (out-of-plane ordered MXenes; Figure 7b,c,e,f), and solid-solution MXenes (Figure 7d,g).

2.1.1. In-Plane Ordered MXenes (I-MXenes). I-MXenes are synthesized from $(M'_{2/3}M''_{1/3})_2AlC$ I-MAX phases, where M' is Mo, W, V, Cr, and M'' is Sc, Zr or Y, or some lanthanides. These

structures occur due to the difference in atomic size between M' and M'' . The most common i-MAX phases are $(Mo_{2/3}Sc_{1/3})_2AlC$ (Figure 4a)¹⁰⁷ or $(Mo_{2/3}Y_{1/3})_2AlC$,¹⁰⁸ but there a number of others have also been produced.^{109,110} These materials, when etched, can lead to two different structures, either $(Mo_{2/3}Sc_{1/3})_2CT_x$ or $Mo_{4/3}CT_x$ depending on the etchant time and concentration.¹¹¹ This leads to a benefit, where the effect of controlled defects in MXenes can be studied. The i-MXenes have positive and negative properties—due to the highly defective nature, these MXenes tend to be more chemically active, especially for catalysis.¹¹⁰ However, due to their defective nature, they also tend to be less stable.¹¹² For example, $Mo_{4/3}CT_x$ has a volumetric (gravimetric) capacitance of 1153 F cm^{-3} (339 F g^{-1}),¹⁰⁷ which is $\approx 65\%$ higher than Mo_2CT_x . Further studies have shown that the enhanced capacitance and energy density of $Mo_{4/3}CT_x$ comes at the expense of lower stability and a faster discharge rate.¹¹³

2.1.2. Out-of-Plane Ordered MXenes. Out-of-plane ordered MXenes have two elements that do not intermix in the M layers (Figure 7b,c,e,f), such as $Mo_2Ti_2C_3T_x$, $Mo_2TiC_2T_x$, $Mo_2ScC_2T_x$,¹¹⁴ or $Cr_2TiC_2T_x$.⁴ For these, the Cr (or Mo) is on the outer layer with Ti (or Sc) on the inner layer. These MXenes are beneficial because they offer unique chemistries that cannot be easily attained in single-M MXenes.^{115,116} Moreover, it was shown that the inner layer affects the electronic properties of the outer layer transition metal.¹¹⁷ This class of MXenes also has different properties than single-M MXenes, such as modified plasmon resonance.⁹⁵ $Mo_2TiC_2T_x$ has a transverse surface plasmon resonance at 476 nm, whereas $Ti_3C_2T_x$ is at 780 nm. Based on this, $Mo_2TiC_2T_x$ should have a higher free electron density, but experimentally this has not been confirmed, electrical conductivity points to the opposite (≈ 1500 S/cm for $Mo_2TiC_2T_x$ against $>20,000$ S/cm for $Ti_3C_2T_x$),¹¹⁸ $Cr_2TiC_2T_x$ was also shown to be unique among MXenes; it is the only MXene that was experimentally shown to have a magnetic transition resulting from the MXene itself.¹¹⁶

2.1.3. Solid-Solution MXenes. Solid-solution MXenes have uniform, random mixing of the two M elements within their entire structure (Figure 7d,g). There have been a number of solid-solution MXenes synthesized already, including $Ti_{2-y}Nb_yT_x$,⁹⁶ $Nb_{2-y}V_yT_x$,⁹⁶ $Ti_{2-y}V_yT_x$,⁹⁶ $Ti_{3-y}Ta_yT_x$,¹¹⁹ $Mo_{4-y}V_yT_x$,¹²⁰ $Nb_{4-y}Zr_yT_x$,¹²¹ $Nb_{4-y}Ti_yT_x$,¹²¹ and $Mo_4VC_4T_x$.⁸⁵ It is noteworthy that this class of MXenes is the only one that spans $n = 1–4$ to date. This is noteworthy: for MXenes, the only case where $n = 4$ observed to date was a solid-solution MXene, $Mo_4VC_4T_x$.⁸⁵ This MXene is stable only at a narrow compositional range, a variance of 5% in either direction of the M element causes impurity MAX phases to form. It also has a structure unlike other MAX/MXene—it is twinned at the middle M-site, a structural motif that has never been observed before. Moreover, in terms of properties it is also exceptional, it has a higher thermal stability than any other MXene, is resistant to the electron-withdrawing effect of organic intercalants, and has low optical absorbance over the entire studied range (out to near-infrared).⁸⁵

In solid-solution MXenes, some properties appear to be linearly related to the chemistry, while others are nonlinear. The conductivity is one property that monotonically varies with the chemistry. Typically, Nb_2CT_x has a low conductivity (≈ 25 S/cm), while V_2CT_x and Ti_2CT_x are substantially higher (>1000 S/cm).^{95,122,123} As the Nb content in $Ti_{2-y}Nb_yCT_x$ and $V_{2-y}Nb_yCT_x$ increases, the conductivity correspondingly decreases (Figure 7h,i).^{96,123} This trend continues over the

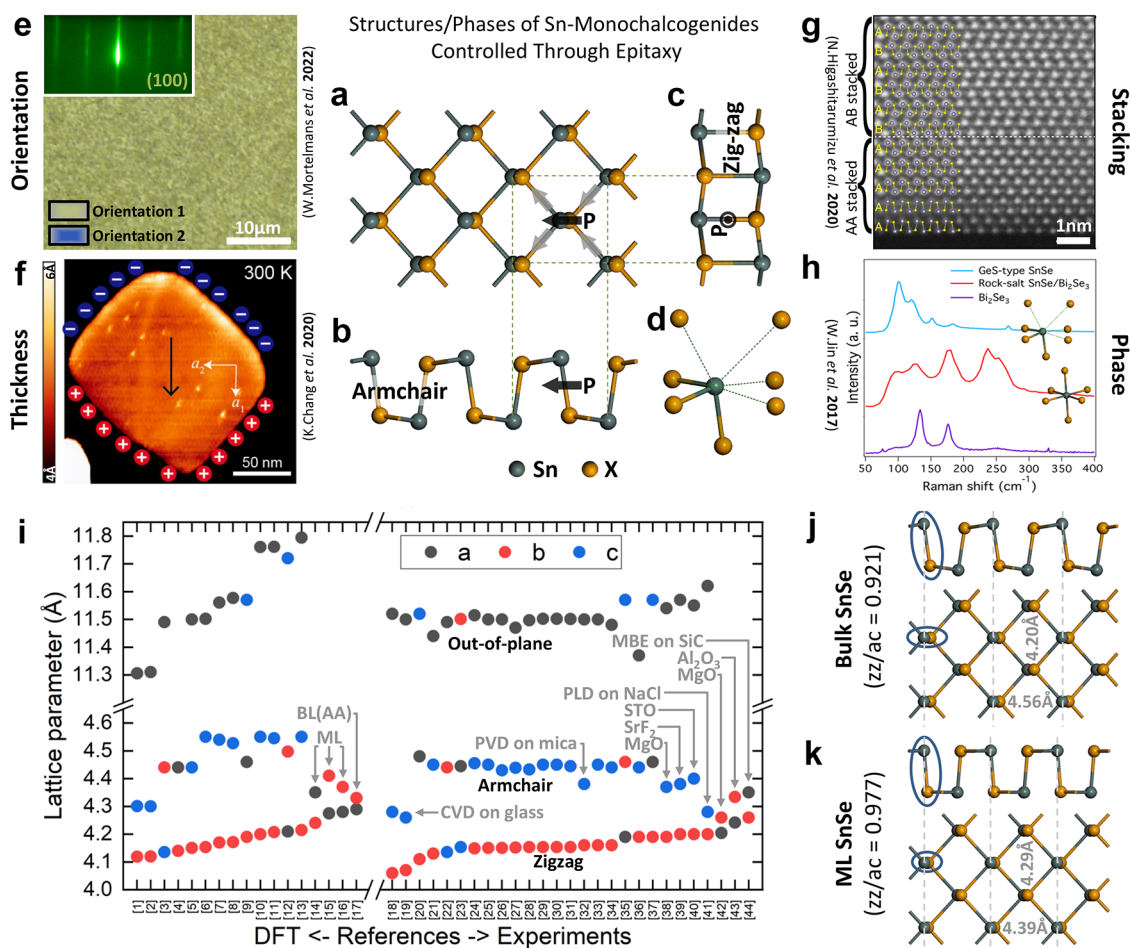


Figure 8. Controlling the structure and phase of Sn monochalcogenides through epitaxy. (a) Top view showing the in-plane unit cell in dashed lines, orientation of the polar bonds, and the net in-plane polarization within a single sheet. (b, c) Visualizing the in-plane armchair and zigzag directions. (d) The SnSe_7 coordination polyhedron. Reproduced with permission from ref 134. Copyright 2022 American Chemical Society. (e–h) Demonstrations of structure and phase control through epitaxy: (e) eliminating twin domains. Reproduced with permission from ref 134. Copyright 2022 American Chemical Society. (f) realizing ferroelectricity in monolayers. Reproduced with permission from ref 135. Copyright 2020 American Chemical Society. (g) making a multilayer, polar crystal with metastable layer stacking. Reproduced with permission under a Creative Commons CC-BY 4.0 License from ref 136. Copyright 2020 Springer Nature. (h) Making a topological crystalline insulator by stabilizing the rock-salt phase. Reproduced with permission under a Creative Commons Attribution 4.0 International license from ref 137. Copyright 2017 American Physical Society. (i) Reported lattice constants ordered from smallest to largest along the armchair direction and separated into results reported by theory (left) and experiments (right). Gray arrows give more information on the simulated/measured samples. (j, k) Cross-section and plan-view images of SnSe simulated by DFT for the case of (j) bulk and (k) monolayer. The armchair lattice constants are visualized using gray dashed lines, and the reduced in-plane anisotropy in the monolayer case is highlighted using blue ovals. Note that there is no consensus in the literature on crystal indexing.

entire compositional range, and all films show similar temperature response. But, interestingly there are a variety of properties that are not linearly related to the composition. For single-M MXenes, there is a single plasmon resonance peak that is related to the free electron density of the MXene, and is affected by the etching/delamination approach.⁹⁶ While, for solid-solution MXenes (Figure 7j,k), there are instead two plasmon resonance peaks (Figure 7l,m). Using $\text{Ti}_{2-y}\text{Nb}_y\text{CT}_x$ as an example, there is one peak around 550 nm (similar to Ti_2CT_x) and a second in the near IR region (similar to Nb_2CT_x), but both are slightly shifted, due to the interactions of the metals with each other.⁹⁷ This is due to the modification of the electronic states of the metals due to the other metal, as was recently shown with electron energy loss spectroscopy (EELS)¹²⁴ in addition to computational predictions.⁹⁷ Interestingly, the same trend with EELS does not occur with $\text{Nb}_{2-y}\text{V}_y\text{CT}_x$, meaning that the interactions depend on the specific metals themselves. Thus, to fully understand and

predict the specific properties that solid-solution MXenes will have, it is imperative to continue fundamental studies.

The electrochemical performance of solid-solution MXenes also benefits from the multiple chemistries.^{120,125} For certain MXenes, such as Ti_2CT_x and V_2CT_x , they have high capacitance, but are unstable. Nb_2CT_x is highly stable but has lower capacitance. Thus, combining the two can alleviate the negatives of both chemistries. For $\text{Ti}_{2-y}\text{Nb}_y\text{CT}_x$ and $\text{V}_{2-y}\text{Nb}_y\text{CT}_x$, the cyclic voltammograms (CVs) are directly related to the MXene chemistry. Depending on the specific chemistry, the volumetric (gravimetric) capacitance ranged from 680 to 1070 F cm^{-3} ($245\text{--}490 \text{ F g}^{-1}$) in 3 M H_2SO_4 .¹²⁵ Interestingly, in some cases, middle compositions outperformed both extremes in capacitance: $\text{V}_{1.2}\text{Nb}_{0.8}\text{CT}_x$ and $\text{Ti}_{1.6}\text{Nb}_{0.4}\text{CT}_x$ outperformed Ti_2CT_x , V_2CT_x , or Nb_2CT_x in these studies. This implies that some synergistic effect is occurring within solid-solution MXenes, giving them enhanced performance. A similar case where a

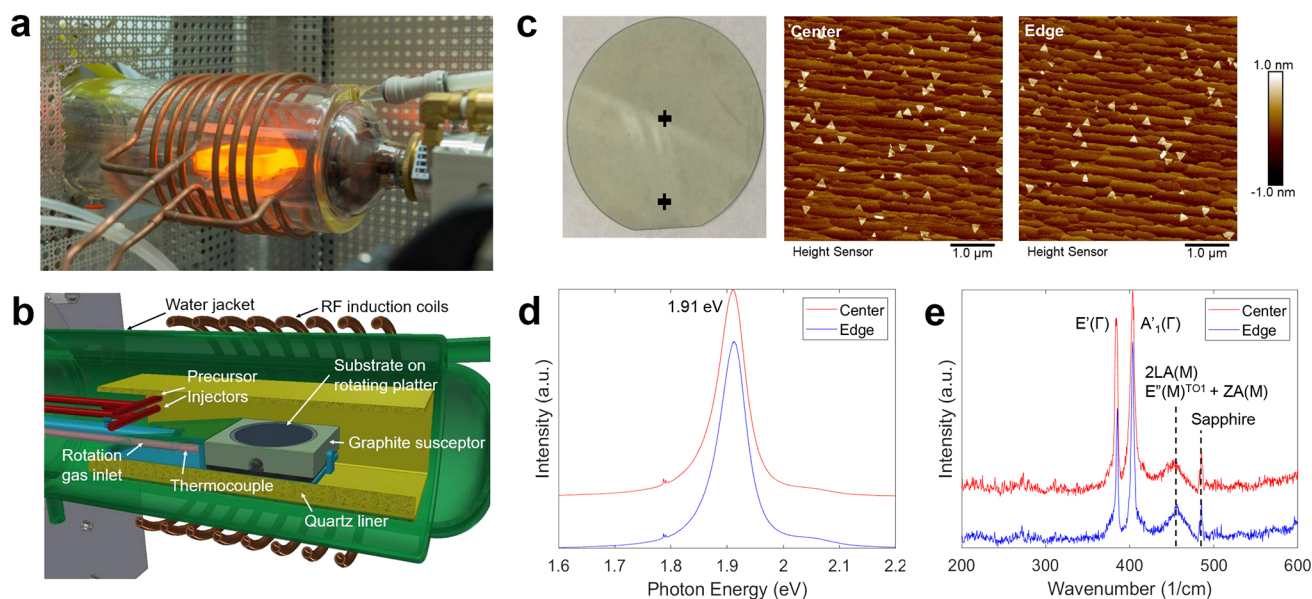


Figure 9. MOCVD for epitaxial 2D TMD semiconductors. (a) photo and (b) schematic of horizontal cold wall MOCVD reactor used for TMD growth. (c) Surface morphology of MoS₂ monolayer grown on 2" c-plane sapphire at center and edge of the wafer (locations indicated by + in photo). Room temperature (d) PL and (e) Raman spectra obtained at the center and edge of the wafer show spatially uniform monolayer thickness across the wafer.

middle composition outperforms other extremes was also observed in Mo_{4-y}V_yC₃T_x.¹²⁰

2.2. Controlling the Structure and Phase of Low-Symmetry 2D Materials. Low-symmetry 2D materials with in-plane anisotropic crystal structures possess a distinct functionality because of their in-plane direction-dependent properties. Low-symmetry 2D materials include black phosphorus, certain TMDs including rhenium disulfide (ReS₂) and diselenide (ReSe₂), and monochalcogenides of the group IV elements Ge and Sn.^{126,127} Here, we focus on the Sn monochalcogenide semiconductors SnSe and SnS. Their crystal structure resembles a perturbed rock-salt, with ferroelectric and ferroelastic distortions and substantial phonon anharmonicity, which make these materials interesting for ferroelectrics, thermoelectrics, and photonics.^{128–130} The orthorhombic, ground state crystal structure is thermodynamically adjacent to different phases with higher symmetry and distinct properties, suggesting the possibility of facile phase control and phase-change functionality.¹³¹

We visualize the crystal structure in Figure 8a–d. The top view (Figure 8a) illustrates the shape and symmetry of the in-plane unit cell. The in-plane unit cell is a rectangle with dissimilar lattice constants ranging from 3.9 to 4.5 Å, depending on the chalcogen and crystal thickness. Each 2D sheet in the crystal structure contains two layers of atoms (Figure 8j,k), and the out-of-plane lattice constant is perpendicular to the layers, forming the overall orthorhombic crystal structure. The arrangement of Sn–Se bonds, distorted from the high-symmetry rock-salt structure (Figure 8j), results in net polarization along the longer in-plane armchair direction.¹³² The unit cell contains two sheets with opposing polarity (called AB stacking), so that the crystal is antiferroelectric and centrosymmetric (i.e., nonpolar). In Figure 8d we visualize the SnSe₇ coordination polyhedron, with both short-bonds and long-bonds within each 2D sheet, and longer bonds linking the sheets.¹³³

The properties and functionality exclusive to these low-symmetry 2D materials can be accessed by controlling the

structure and phase through epitaxial growth (Figure 8e–h). The ferroelastic distortion that creates the distinction between armchair and zigzag directions leads to a system of 90° twin boundaries, across which these directions (and their associated anisotropic properties) exchange. Mortelmans et al.¹³⁴ showed that these 90° twins in SnSe can be eliminated by epitaxial growth on a substrate with a rectangular and lattice-matched in-plane unit cell (Figure 8e), making possible large-area thin films with uniform in-plane anisotropy. Chang et al.¹³⁵ demonstrated through epitaxial growth on 6H-SiC(0001) that monolayers of SnSe are indeed polar (Figure 8f), and exhibit in-plane ferroelectricity at room temperature. The antiferroelectric, AB-stacked crystal structure implies that polar crystals can only be achieved in the monolayer limit. However, Higashitarumizu et al.¹³⁶ observed AA stacking in multilayer SnS crystals grown on mica, thereby realizing polar and ferroelectric SnS beyond the monolayer limit, with intriguing possibilities for the optical and optoelectronic properties (Figure 8g). Jin et al.¹³⁷ demonstrated that this nonequilibrium rock-salt phase can be stabilized through epitaxial film growth (Figure 8h). These results highlight that a multitude of structures and phases can be accessed through epitaxy, creating possibilities for fundamental study and device technology.

Within the orthorhombic ground state structure, the in-plane lattice constants and the measure of in-plane anisotropy are remarkably sensitive to crystal thickness and likely also growth conditions. A review of SnSe lattice constants reported by theory (left) and experiments (right) is provided in Figure 8i. The data are ordered from smallest (4.12 Å for theory, 4.06 Å for experiment) to largest (4.29 Å for theory, 4.26 Å for experiment) lattice constant along the zigzag direction. From the presented theoretical work, we see that the lattice constants in the zigzag and armchair directions approach closer to each other in monolayer and bilayer SnSe, compared to the bulk.^{138,139} In other words, on decreasing the crystal thickness, the in-plane symmetry approaches square, bringing the crystal closer to the rock-salt structure. This trend is confirmed by experimental

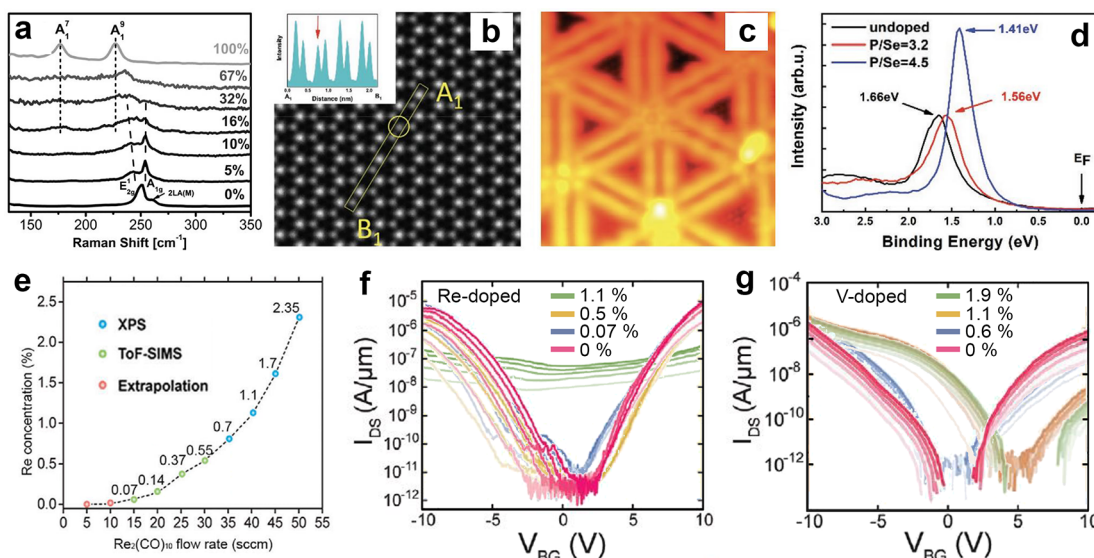


Figure 10. Doping and alloying 2D materials for electrical applications. (a) Raman spectra of $\text{WSe}_{2(2-x)}\text{Te}_x$ alloys showing a transition from the semiconducting 2H phase to the semimetallic 1T' phase as a function of increasing Te concentration. Adapted from ref 161. Copyright 2019 IOP Publishing Ltd. (b) ADF-STEM image and corresponding intensity profiles along the boxed region showing a P atom sitting at a Se site. (c) STM image of P-doped MoSe_2 (sample bias: -1.0 V, size: 10×10 nm²). The hexagonal structure of MoSe_2 remained intact after doping. (d) UPS of the undoped, lightly doped (P/Se flux ratio ≈ 3.2), and heavily doped (P/Se ≈ 4.5)-doped MoSe_2 , showing a p-type behavior. Panels (b)–(d) were adapted with permission from ref 162. Copyright 2020 John Wiley & Sons, Inc. (e) The doping concentration of Re in WSe_2 from X-ray photoemission spectroscopy (XPS), secondary ion mass spectrometry (SIMS), and extrapolated points are plotted as a function of $\text{Re}_2(\text{CO})_{10}$ flow rate during WSe_2 growth. (f) Transfer characteristics of pristine and Redoped WSe_2 field-effect transistors. While ambipolar conduction in the pristine and lightly Redoped WSe_2 films is demonstrated, at higher Re concentrations device performance is degraded due to the increasing impurity scattering. Panels (e) and (f) were adapted and modified with permission from ref 164. Copyright 2020, Wiley-VCH. (g) Transfer characteristics of the pristine WSe_2 film at different drain voltages (1–5 V) display ambipolar conduction. However, the n-branch degrades as V concentration increases and transistors gradually become p-type. All transistors were on 50 nm ALD Al_2O_3 . Reproduced with permission from ref 165. Copyright 2021, Wiley-VCH.

observations on thin films grown using CVD and physical vapor deposition (PVD), compared to measurements on thicker films and bulk crystals.^{140,141} The out-of-plane lattice constant generally increases along with increasing in-plane lattice constants.

In Figure 8j,k we present DFT simulations that illustrate and quantify the tendency of SnSe to have reduced in-plane anisotropy for thinner crystals. Bulk SnSe has in-plane lattice constants of 4.20 and 4.56 Å, in a ratio of 0.921; results for 2D SnSe are 4.29 and 4.39 Å, in a ratio of 0.977. This approach toward square symmetry manifests as a reduced staggering, and Sn – Se out-of-plane bonds that approach perpendicular relative to the layers (highlighted by blue ovals), which reduces the in-plane polarization (Figure 8a) control of SnX structure and phase through epitaxy may enable a range of useful applications. The in-plane ferroelastic distortion of single-crystal thin films can be used for “domain change” applications, whereby the armchair and zigzag directions are switched (exchange of short- and long-bonds within the plane) on a picosecond time scale by pulsed light, leveraging the dielectric anisotropy to realize a diffusionless, martensitic, nonthermal, nonresonant switching process.¹⁴² Such “domain change” functionality could be useful for low-injection-loss optical phase control in photonic integrated circuits.¹⁴³ Ferroelectric monolayer and AA-stacked multilayer crystals could be used for electro-optic phase modulation, nonlinear optics, and concepts in ferroelectric nonvolatile memory.¹⁴⁴ The topological crystalline insulator phases could enable high-responsivity infrared optical detectors.¹⁴⁵ Control of crystal anisotropy could also enable

fundamental understanding and applications of thermoelectricity in SnX materials, for waste heat energy harvesting.¹⁴⁶

2.3. Epitaxial Growth of Wafer-Scale TMD Monolayers by MOCVD. Epitaxial TMD monolayers (MoS_2 , WS_2 , WSe_2) at the wafer scale is of significant interest for device applications. MOCVD is a promising approach for TMD growth as it enables the use of high substrate temperatures (700–1000 °C) and chalcogen/metal ratios (10^3 – 10^5)^{147,148} that are beneficial for epitaxy. In addition, the flow rate of precursors can be modulated during growth to enhance the surface diffusion of metal-containing species and control the lateral growth rate of TMD domains.¹⁴⁷ C-plane sapphire has emerged as a promising substrate for TMD epitaxy due to its crystallographic compatibility and good chemical stability in the CVD environment. In addition, steps on the sapphire surface can be used to induce a preferred alignment of TMD domains resulting in a significant reduction in inversion domains in the films.^{149,150}

MOCVD growth of wafer-scale TMDs has been carried out using a cold-wall horizontal quartz tube reactor that includes an induction-heated rotating SiC-coated graphite susceptor as shown in Figure 9a,b, which is available in the Penn State 2D Crystal Consortium facility.¹⁵¹ The precursors used include metal hexacarbonyls ($\text{Mo}(\text{CO})_6$ and $\text{W}(\text{CO})_6$) and hydrides (H_2Se and H_2S) with H_2 as the carrier gas. The cold wall geometry, reduced reactor pressure (50–200 Torr) and separate gas injectors are beneficial to reduce the extent of gas phase prereactions that occur between the carbonyls and hydrides.⁴³ Epitaxial growth of monolayer MoS_2 ,¹⁵² WS_2 ,¹⁵³ and WSe_2 ¹⁵⁴ on 2° c-plane sapphire miscut $\pm 0.2^\circ$ toward the m-axis has been demonstrated at growth temperatures in the range of 800–1000

°C. For example, epitaxial MoS₂ films grown under these conditions consist of a uniform monolayer across the entire 2" diameter wafer with small triangular bilayers at a surface coverage of <15% (Figure 9c). Undulations in the surface morphology of the monolayer arise from the steps on the sapphire surface. Room temperature photoluminescence (PL) spectra (Figure 9d) obtained at the center and the edge of the 2" sapphire contain an emission peak at 1.91 eV associated with the A exciton of 1L MoS₂.¹⁵⁵ Raman spectra (Figure 9e) obtained at the center and edge of the wafer show the characteristic modes for 1L MoS₂. All of these results indicate the quality and monolayer thickness can be uniform across the entire wafer.

The availability of wafer-scale MOCVD-grown epitaxial TMD monolayers films has enabled a variety of studies that benefit from high quality large area films that can be readily transferred off the growth substrates for device fabrication and testing. This includes benchmarking studies of FET performance,¹⁵⁶ 2D memtransistors for Bayesian networks,^{157,158} large area vdW superlattices,¹⁵⁹ localized quantum emitters,¹⁵⁹ and 2D photo-detectors for biomimetic sensing platforms.¹⁶⁰

2.4. Substitutional Doping and Alloying 2D Materials for Device Applications. Ion implantation is a standard semiconducting technique to achieve small-depth channel post-growth electronic doping on Si using energetic ion beams. However, the high energy beams in traditional ion implantation techniques will lead to significant damage for 2D materials and would require postimplantation thermal annealing to recover crystallinity. Bottom-up doping or alloying of 2D materials can be achieved through MBE and MOCVD in a homogeneous and repeatable fashion by codelivery and control of multiple source materials and their flux ratios. First, in an attempt to demonstrate the potential of MBE to grow TMD alloys at back-end-of-line (BEOL) temperatures (≤ 550 °C) and highlight relevant challenges, Barton et al.¹⁶¹ reported WSe_(2-x)Te_x alloys grown at $T = 250$ °C. For $\text{Te} < 14\%$, a stable alloy in the semiconducting 2H phase was achieved while for $\text{Te} > 79\%$ a semimetallic 1T' phase was found to be stable. Interestingly, for Te in the range of 14 to 79% a miscibility gap was observed which resulted in a phase separation between two different alloys having different crystal structures and composition, as shown by Raman data in Figure 10a. The metallic alloys can be very useful to make low resistance contacts by increasing the film conductivity significantly.

Recently, substitutional doping of TMDs has been gaining popularity for a variety of applications. Xia et al.¹⁶² demonstrated phosphorus (P) doping in a monolayer of MoSe₂ by codepositing P, Mo, and Se on a variety of substrates to tune the electrical conductivity. As shown in Figure 10b, P substitution at the Se sites was confirmed through annual dark field scanning transmission electron microscopy (ADF-STEM).¹⁶² The cluster setup of the MBE system, combining scanning tunneling microscopy (STM) and ultraviolet photoelectron spectroscopy (UPS), allowed them to perform in-depth characterization without exposing the samples to air. As confirmed by STM (Figure 10c), P doping did not affect the hexagonal structure or inversion domain boundaries of the MoSe₂, nor generated any apparent P clusters within or on the surface of the MoSe₂. In contrast to other reports where dopants prefer to segregate at domain boundaries,¹⁶³ very uniform doping was achieved. UPS measurements showed a clear p-type behavior where the valence band maxima gradually moved closer to the Fermi level (E_F) as a function of P doping (Figure 10d).¹⁶² To have such fine control over tuning the electrical

conductivity and E_F through doping is highly desirable to control the threshold voltages and ON-current density in TMD-based transistors.

Recently, controllable substitutional doping of TMDs with transition metal elements during MOCVD for modulating TMDs-based transistors has been demonstrated. Kozhakhmetov et al.^{164,165} introduced Re₂(CO)₁₀ and V₂(C₅H₅)₂ during WSe₂ growth to substitute W with Re and V for n- and p-type doping, respectively. Furthermore, by controlling carrier gas flow going through the bubblers of precursors that provide dopants, dopant concentrations can be tuned the parts per million to the percentage level in WSe₂ (Figure 10e). Furthermore, to understand the impact of dopant types and concentrations on the transport of 2D WSe₂, Kozhakhmetov et al.^{164,165} established the relationship between dopant concentration and transfer characteristics for both Re- and V-doped WSe₂ using back-gate-FET (BGFET). The pristine WSe₂ BGFETs exhibit ambipolar transfer characteristics and remain the same until both Re and V concentrations exceed 1%. While standard semiconductor doping level for Si is at the ppm level (<0.1%), the doping for 2D semiconductors is relatively ineffective due to the quantum confinement effect and reduced dielectric screening.¹⁶⁶ This could be alleviated by encapsulation with high- κ dielectric materials,¹⁶⁶ alloying TMDs with high dopant concentrations,¹⁶⁷ or few-layer thick TMDs. Nevertheless, contrary to high energy ions or high temperature diffusion processes normally used in the CMOS-compatible processes, *in situ* substitutional doping during MBE and MOCVD can maintain the highest crystallinity of TMDs and control dopant concentration well.

2.5. Native Oxide Formation of Semiconducting TMDs. Like most metals in the galvanic series, and nearly all well-developed semiconductors, the surfaces of TMDs are prone to oxidation. Oxidation of TMDs is a long-appreciated and still outstanding challenge in present-day applications of TMDs for solid-state lubrication and desulfurization catalysis. In general, the TMD surface is more easily oxidized as the chalcogen decreases in electronegativity (descending in the periodic table) from S, to Se, to Te.¹⁶⁸ Group VI compounds containing Mo and W have a larger formation energy of sulfur vacancies and are more stable compared to nongroup IV compounds containing Hf, Zr, Ti, and Nb.¹⁶⁸ The oxidation of synthetic thin films is more pronounced than that of bulk single crystals, due to accelerated oxidation at random GBs, twin boundaries, and other crystallographic defects.¹⁶⁹ Control over oxidation is therefore a further reason to address the challenges of nucleation and growth in TMD thin film crystal growth, for future applications in microelectronics, optoelectronics, and photonics.¹⁷⁰

In particular, for microelectronics, the sustained academic research activity and the increasing attention from industry increase the urgency of understanding and controlling the processing and properties of TMD native oxides. In some situations, such as applications of monolayer crystals of highly oxygen-sensitive compounds (e.g., MoTe₂, TiS₂), oxidation must be avoided entirely, and therefore oxidation rates even in nominally oxygen-free environments should be quantified.^{171,172} In other situations, such as applications of multilayer crystals of less-oxygen-sensitive compounds (e.g., WS₂ field effect transistors), controlled oxidation could be beneficial, and research is ongoing into oxidation methods including thermal, UV/ozone, and plasma-assisted.^{173–176} The processes of TMD native oxidation are quite different, on the atomic scale, from the long-

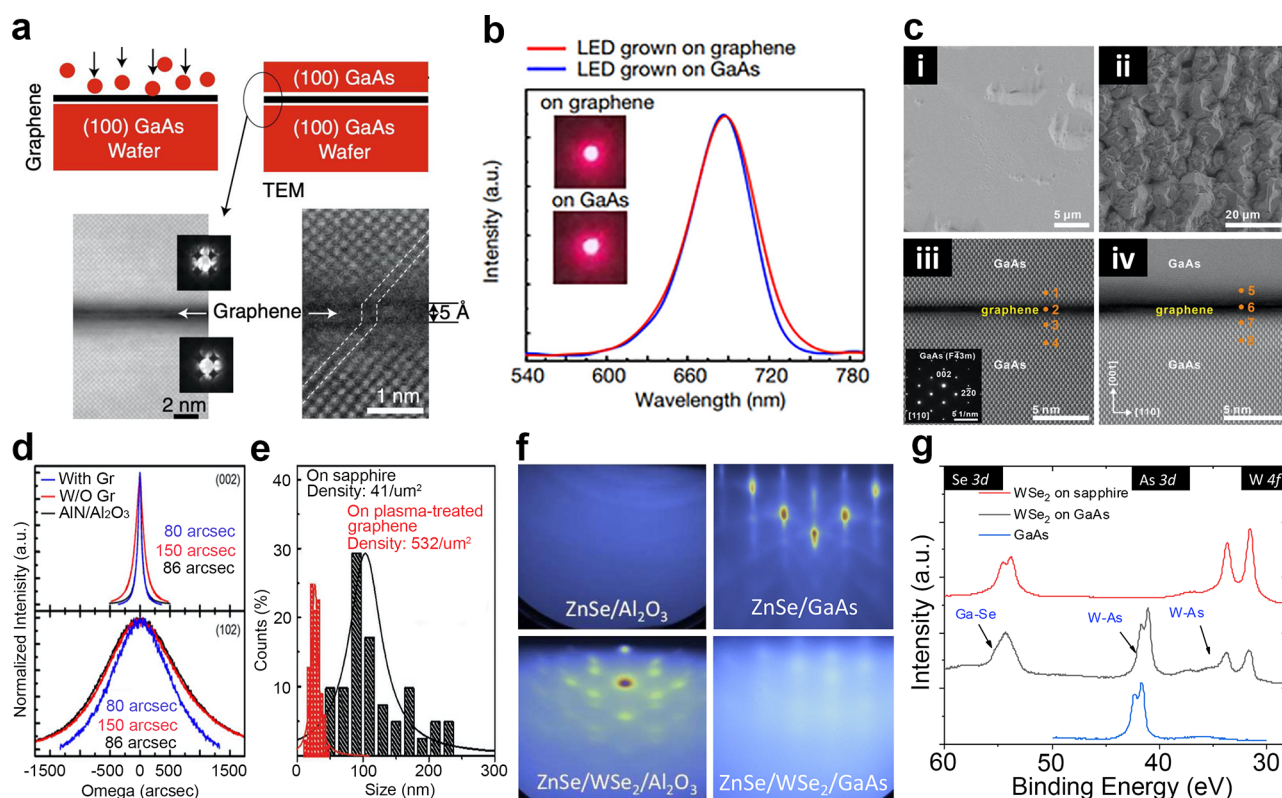


Figure 11. 2D materials as the intermediate layer of remote epitaxy. (a) Illustration of remote epitaxy of GaAs and cross-sectional TEM at GaAs/graphene/GaAs interface. Adapted with permission from ref 178. Copyright 2019 Springer Nature. (b) Electroluminescence spectra of GaAs LEDs prepared directly on GaAs (red curve) and graphene through remote epitaxy on GaAs (blue curve). Inset shows pictures of working LEDs grown on both substrates. Adapted and modified with permission from ref 179. Copyright 2022 AIP Publishing LLC. (c) Scanning electron microscopy (SEM) (i, ii) and STEM (iii, iv) comparison of GaAs epitaxy using dry (i, iii) and wet (ii, iv) transferred graphene as an intermediate layer. The quality is significantly better on dry transferred graphene. Adapted and modified with permission from ref 180. Copyright 2021 AIP Publishing LLC. (d) X-ray diffraction rocking curves of the (002) and (102) planes for the aluminum nitride (AlN) growth on different templates. Quality is improved on the graphene template. (e) AlN nucleation and grain size comparison for direct growth on sapphire and remote epitaxy using plasma-treated graphene. Larger grain sizes on graphene enabled higher quality growth of the AlN film. (d, e) Adapted with permission from ref 181. Copyright 2020 AIP Publishing LLC. (f) Improvement in growth quality of MBE grown ZnSe by using an MBE grown 2D WSe₂ as a template. The reflection high-energy electron diffraction pattern transitions from Debye rings to streaky dots confirming better quality of the film when grown on WSe₂. (g) A comparison of ZnSe grown directly on GaAs with one grown using WSe₂ as an intermediate layer. (h) XPS comparison of ZnSe shown in panel (g). A reaction between the WSe₂ and the GaAs substrate can be clearly observed in the form of W-As and Ga-Se chemical states in the XPS. (f–h) Adapted with permission from ref 187. Copyright 2021 IEEE.

studied native oxidation processes in legacy semiconductors, Si chief among them. Some of the oxides in question are volatile, such as MoO₃ that evaporates more readily than either Mo or MoS₂. The oxides of Mo and W can form with wide variations in oxygen content, leading to wide variations in electronic conductivity, which is detrimental for dielectric functionality but may be useful for resistive switching. Further, TMD oxidation is accompanied by chalcogen loss. The expelled chalcogen may leave the system as a volatile gas (e.g., SO₂), or segregate as an additional (and likely unwanted) solid phase.

A lesson learned from Si microelectronics is that, if at all possible, we should make use of semiconductor native oxides. Particularly for semiconducting TMDs for which the native oxides may be useful dielectrics (or even ferroelectrics), there is opportunity in better understanding the processing–property relationships that control dielectric response, leakage, and interface quality. For TMDs for which the native oxides have easily varied conductivity, there is opportunity in developing resistive switching functionality for memory and neuromorphic computing, or in developing native oxide electrodes. It took decades to develop SiO₂ as a reliable dielectric for Si CMOS

technology. With the much wider processing and property space for TMD native oxides than for traditional semiconductors, we look forward to many years of productive research and development.

2.6. Remote Epitaxy Using 2D Materials as an Intermediate Layer. Remote epitaxy, utilizing a 2D/3D heterostructure, is an emerging technology that uses 2D materials as an intermediate layer to grow and later isolate single-crystal, free-standing 3D thin films in a nondestructive manner. In 2017, Kim et al.¹⁷⁷ revealed that thin films of different properties/functionalities can be grown, exfoliated, and heterogeneously stacked as required.¹⁷⁸ As shown in Figure 11a, a thin layer of graphene was used to partially screen the electrostatic potential fluctuations from the GaAs (100) substrate for homoepitaxial growth of GaAs (100).¹⁷⁷ Since the surface fluctuations of the substrate were not fully suppressed, adatoms on graphene were still able to interact with the substrate lattice to grow in an epitaxial manner with the same crystal orientation as the substrate. Additionally, unlike traditional epitaxy in which a strong bond exists between the epilayer and the substrate, the dangling bond free inert surface of graphene facilitated an easy

detachment of the epilayer. An advantage of remote epitaxy is that adding a graphene intermediate layer between a grown film and its host wafer does not degrade the device performance of grown films (Figure 11b).¹⁷⁹ This area that had originally started from homoepitaxy of GaAs with graphene as an intermediate layer has now expanded to a variety of epitaxial materials (e.g., GaAs,¹⁸⁰ III-N,¹⁸¹ and oxide ultrathin films¹⁸²) and intermediate 2D layers (e.g., hBN¹⁸³ and TMDs¹⁸⁴).

Since remote epitaxy is facilitated by the intermediate 2D film, the quality of this layer is one of the most important variables dictating the crystallinity of the grown epilayer. As shown in Figure 11c for remote epitaxy of GaAs, oxide formation at the substrate and interface of wet transferred graphene altered the effective distance between GaAs and the substrate to compromise the growth quality. In contrast, when GaAs was grown on dry-transferred graphene, which is less susceptible to oxidation, better quality was achieved. In a different report on remote epitaxy of GaN microcrystals, Jeong et al.¹⁸⁵ reported that when the 2D film is defective or has pinholes in it, a fraction of the grown structures could not be exfoliated and remained stuck on the substrate because of a direct covalent epitaxy through the defective region which made it difficult to reuse the substrate as well. Moreover, when there is an irregularity in the thickness of the 2D layer, such that there are regions where the thickness is greater than the critical thickness for remote interaction, epitaxy in those areas will not take place.¹⁸⁶ All these reports, consistently stress the elimination of transferred vdW layers and highlight the importance of contamination-free, uniformly grown 2D layers as the ideal pathway for reliable remote epitaxy.¹⁸⁷

Though remote epitaxy is still in its early stage of development, it is already showing potential for a variety of applications such as the growth of free-standing devices, flexible electronics, and light-emitting diodes (LEDs).¹⁷⁸ In addition to this, remote epitaxy can help improve the overall growth quality of a material as well. An increase in the crystallinity and grain size of the epi-film have been observed when an intermediate 2D layer is used (Figure 11d,e).¹⁸¹ Zhou et al.^{184,187} used a MBE grown intermediate WSe₂ layer to improve the growth quality of zinc selenide (ZnSe) on sapphire at BEOL compatible temperatures (Figure 11f). ZnSe is a promising p-type semiconductor and is sought after as a channel material for BEOL transistors. The atomically thin, inert surface of WSe₂ enabled the long-range diffusion of adatoms at relatively lower temperatures to improve the crystallinity of the film. It is important to mention here that not only the quality of the intermediate layer, but the inertness of the substrate is also a critical factor to grow high quality epilayers. In contrast with the relatively chemically inert substrate sapphire, ZnSe growth on GaAs with a WSe₂ intermediate layer resulted in a degraded quality of the epilayer. Although GaAs and ZnSe are lattice matched (Figure 11g), the WSe₂ growth process reacted with the GaAs substrate, formed unwanted Ge–Se (Figure 11h), and failed to provide a pristine, dangling bond-free template for the epilayer to grow with high quality.

2.7. Challenges for Growing High-Quality 2D Materials on 3D Substrates by Thin-Film Deposition. Among the bottom-up approaches of fabricating 2D materials and structures, CVD and PVD are commonly used, as they generally produce high quality thin films with relatively simple equipment and low maintenance costs. However, for some layered materials such as TIs, MBE is preferred for its extremely high purity,¹⁸⁸ precise control on doping,¹⁸⁹ and capability of creating atomically sharp inter-

faces¹⁹⁰ in heterostructures. Chalcogenide-based TIs like Bi₂Se₃ have hexagonal in-plane crystal structure with vdW bonds between each layer. They are of interest because their band structure comprises a bulk band gap and linear-dispersed surface states crossed within.¹⁹¹ To exploit these surface states, we need wafer-scale thin films that are atomically smooth with few defects, similar to the needs for other layered materials. Unlike a conventional 3D semiconductor system, synthesis of these layered materials proceeds by vdW epitaxy in which a vdW gap exists between the material and the substrate, relaxing the lattice-matching constraint. However, the substrate still must be properly treated and growth conditions (substrate temperature, flux ratios, etc.) must be carefully chosen such that the material grows in the expected orientation.¹⁹²

Here, we will take the growth of Bi₂Se₃ by MBE as an example; however, many of the problems and solutions we discuss are applicable to other layered materials. Bi₂Se₃ has a crystal structure comprising sequentially covalently bonded quintuple layers (QL) of Se(1)-Bi-Se(2)-Bi-Se(1); the QLs are connected to each other by vdW bonds. Bi₂Se₃ has been successfully grown on sapphire,¹⁹³ GaAs,¹⁹⁴ Si,¹⁹⁵ and other substrates,^{196,197} even with considerable lattice mismatch. However, these films tend to suffer from three major types of structural defects, all of which increase electron scattering and reduce TI device quality. The first step is the formation of twin defects. Because Bi₂Se₃ has a hexagonal in-plan crystal structure, it can nucleate in two different orientations rotated by 60 degrees with respect to each other with equal probability. When these domains coalesce, dislocations arise which can lead to electron scattering. Twin defects can be mitigated by selecting more lattice-matched substrates with pregrowth treatment to align substrate step edges,^{198,199} or by using vicinal substrates with regular step edges to promote step-flow growth mode.²⁰⁰ However, vicinal substrates lead to additional difficulties as described below.

The second structural defect is terraced growth, in which a second or third layer begins to grow before the first layer has finished leading to a “wedding cake” morphology. This arises due to the presence of Ehrlich-Schwoebel (ES) barriers.^{201,202} The ES barrier is the energy barrier for an adatom to cross an atomic step to a lower terrace.²⁰³ If the ES barrier is large compared to the in-plane diffusion barrier, adatoms are more likely to form a “daughter” island on incomplete “parent” island rather than move downward to fill the gap and smooth the film.²⁰⁴ The typical way to reduce the ES barrier is by using a surfactant such as Bi, In, or Sb.²⁰⁵ However, all three of these metals will incorporate into chalcogenide-based materials rather than acting as a surfactant. We instead take an alternative approach to reducing the root-mean square roughness of the film: reducing in-plane adatom diffusion. Nucleating the film at a low temperature, then growing the rest of the film at a higher temperature and/or by increasing growth rates both reduce in-plane diffusion and thereby reduce the film roughness. It is possible that other materials could be used as surfactants to further improve film morphology.

Another unwelcome morphology often witnessed in TI films is the spiral growth. In conventional materials, spiral growth almost always originates from screw dislocations.²⁰⁶ For vdW materials, these types of dislocations should be mitigated by the vdW gaps. However, when the growth front of a TI domain encounters the step edge of the substrate, it can “pin” the domain. The six sides of the hexagonal in-plane Bi₂Se₃ crystal structure are not equivalent. One set of three sides grows faster than the other set due to a higher density of dangling bonds. If

the domain encounters a step at the wrong angle, this difference in edge growth rate will result in spiral growth.²⁰⁷ It is possible that substrates with step heights equal to the thickness of a QL would reduce the spiral formation. These defects can also be mitigated by pretreating the substrate such that all the atomic steps are aligned, though challenges will still arise when domains coalesce if the substrate step height does not equal the *c*-axis lattice constant of the film.

In addition to these structural defects, Bi₂Se₃ films are often *n*-type doped due to selenium vacancies, surface oxidation, and/or band bending at the top and bottom interfaces. These unwanted carriers can pin the Fermi level above the Dirac point into the bulk conduction band, obscuring the signal from the surface states. There are several ways to mitigate the doping. A cracker source can be deployed to promote incorporation of the selenium atoms.²⁰⁸ A capping layer such as elemental selenium²⁰⁹ or other materials including oxides and polymers can be deposited on the Bi₂Se₃ surface to suppress oxygen exchange or contaminant adsorption. In addition, one can also introduce a lattice-matched trivially insulating buffer layer (e.g., (Bi_{1-x}In_x)₂Se₃) between the substrate and the Bi₂Se₃ film to reduce defects and band bending at the interface.²¹⁰ Through a combination of these efforts, background doping in Bi₂Se₃ films has steadily decreased such that the Fermi energy is often found in the bulk band gap. As noted above, vdW epitaxy has been widely adopted for other 2D material synthesis such as elemental 2D materials like silicene,²¹¹ stanene,²¹² antimonene,²¹³ and TMDs.^{214,215} With the extremely accurate control over material flux, MBE is also capable of creating functional heterostructures and superlattices based on 2D materials for optic and electronic applications, especially when the interface plays a critical role as in the 2D system.^{216,217} Overall, MBE growth of layered materials has progressed significantly over the past decade. Using a detailed understanding of the unique challenges and opportunities presented by vdW epitaxy, the future for MBE growth of functional vdW devices is bright.

2.8. Ternary Magnetic Layered Compounds Grown by MBE. The quest for layered ferromagnets, one of the functionalities more recently pursued within the class of 2D materials, is to demonstrate a robust ferromagnetic order at room temperature. The initial question was if indeed ferromagnetism can be stabilized in the single atomic layer limit at finite temperatures. This presence of magnetic order would represent a violation of the Mermin-Wagner theorem,²¹⁸ i.e. the inability to establish any long-range magnetic order if an isotropic and finite-range Heisenberg exchange interaction is present. An alternative interpretation would be that 2D materials are simply not well captured by this theorem, and rather the highly anisotropic bond geometry inherent to 2D materials along with a finite thickness even in the single 2D layer limit would be enough to stabilize magnetic order, rendering a rigorous application of the theorem as not suitable. In any case, it is to be expected that magnetic order in 2D materials will not be very robust and potentially limited to a regime significantly lower than room temperature.

The experimental confirmation of ferromagnetism in atomically thin layers of the layered magnetic materials CrI₃²¹⁹ and Cr₂Ge₂Te₆²²⁰ in 2017 were widely considered fundamental breakthroughs, which led to an intensification of activities aimed at the further exploration of the field of 2D magnetism. Pioneering research activities have identified several vdW ferromagnets exhibiting insulating, semiconducting, and metallic ground states, both in the form of bulk single crystals as well

as atomically thin flakes and films.²²¹ This is particularly exciting because vdW materials are considered an ideal playground for fundamental exploration of magnetic spin-on-lattice phenomena in the 2D limit, including the study of exotic magnetic ground states and magnetic phase transitions,²²² and they are also host of topologically nontrivial spin configurations (skyrmions).²²³ Aside from the exciting possibilities to explore fundamental physics questions, therefore pushing the horizon of our understanding of magnetism in 2D systems, research on these materials is also anticipated to stir up perspectives and avenues toward realization of ultracompact magnetic devices with relevance in spintronics and emerging quantum technologies. Here, one fascinating aspect is the fabrication of multifunctional vdW heterostructures by combining them and other 2D crystals like graphene and TMDs into vdW stacks, in which proximity-induced coupling effects across atomically smooth interfaces of layered materials can tailor magnetism by heterostructure design.²²⁴

Most 2D ferromagnets experimentally realized and investigated so far have Curie temperatures (*T*_C) well below 300 K even in the bulk regime,²²⁵ a constraint that hinders their practical applications. Hence, there is an urgency in finding materials that can furnish long-range ferromagnetic order in a robust fashion above room temperature and within a thickness range from a few nanometers down to the single layer limit. Additionally, the 2D material of choice should allow for a straightforward, easy to control, and high-quality wafer-scale synthesis that should be stable in ambient conditions. Hence, beyond the growth of bulk single crystals and subsequent exfoliation, the utilization of thin film synthesis methods, such as MBE and CVD, is highly desirable.

The development of a precise deposition route with atomic level control is also key for assessing fundamental phenomena in these materials. This thickness range of interest, namely from few layers down to the single layer limit, seems to be difficult to access via standard exfoliation schemes in various 2D crystals including some vdW magnets. The structural and chemical stability is an additional, important aspect to advance the field toward technological realization. For example, the fast degradation commonly observed in chromium halides upon air exposure²²⁶ presents a great challenge for the development of reliable device fabrication routes. To be compatible with the envisioned device application, it is necessary to find magnetic 2D materials with superior chemical stability and robust magnetic order well above room temperature that will facilitate their realistic exploration for future technologies.

TMDs with sizable free carrier concentrations, such as 1T-VSe₂,²²⁷ 1T-CrTe₂,²²⁸ and Fe_{*n*}GeTe₂ (*n* ≥ 5),²²⁹ show excellent prospect for the envisioned applications as they can exhibit ferromagnetic order around or even above 300 K. Recently, unique insights have been reported on the origin of magnetism in 1T-VSe₂.²³⁰ It has been shown for 2D VSe₂ synthesized via MBE on MoS₂ that postgrowth anneals promoted Se desorption, which induced the formation of a reconstructed surface. Since the magnetic signal was absent in pristine, i.e. unreconstructed, layers, the formation of 1D line defects were assumed to originate a ferromagnetic response at 300 K. This suggests that alternative methods offering local control, such as focused ion beam,²³¹ could be utilized to introduce magnetic defects in a controlled fashion and with high spatial precision in the 2D lattice of 1T-VSe₂. These recent reports indicate that the development of reproducible protocols for scalable synthesis and defect creation are indeed challenging.

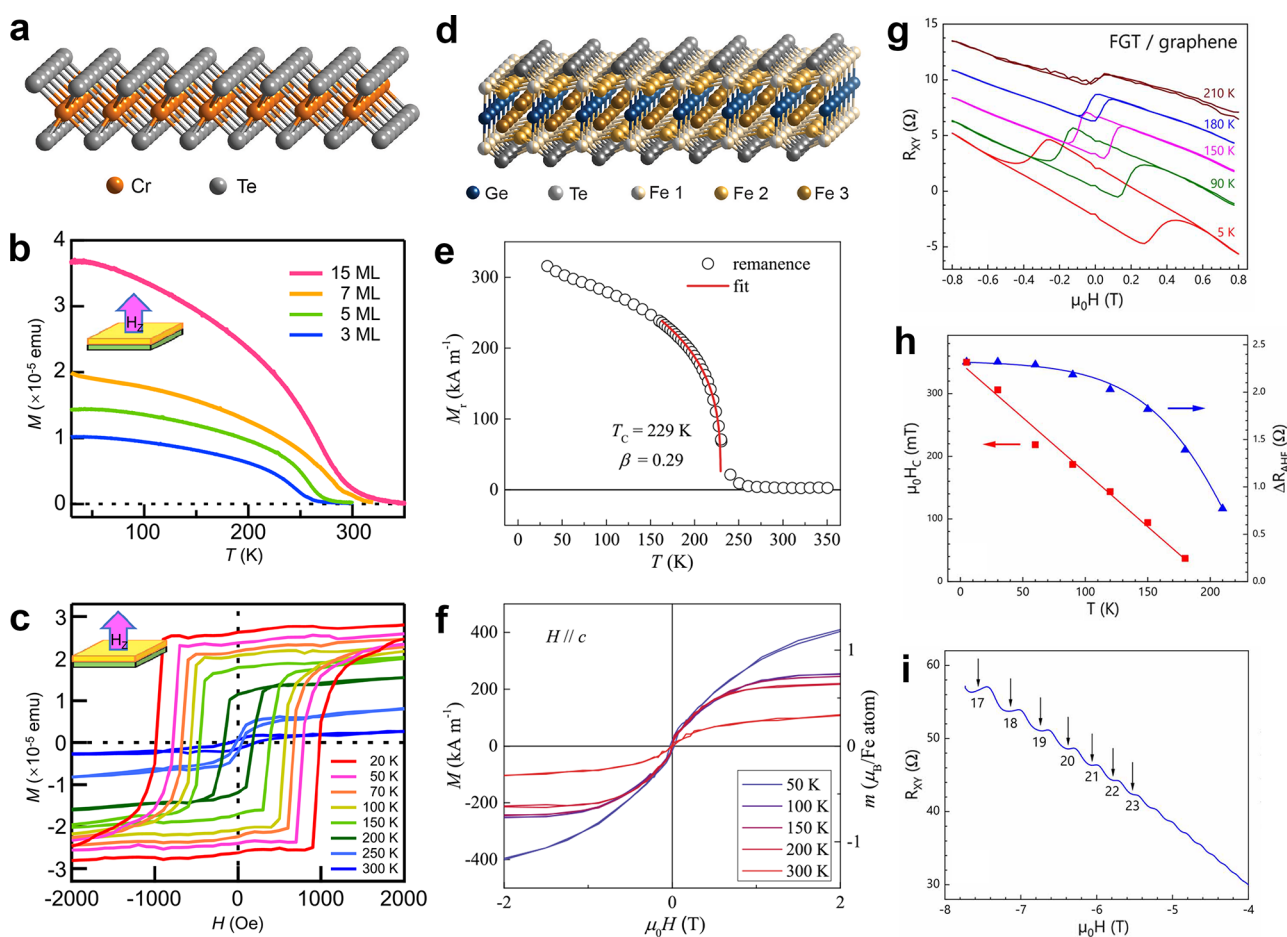


Figure 12. Properties of layered magnetic compounds. (a) Schematic depiction of a single layer of 1T-CrTe₂. (b) Temperature-dependent magnetization curves of CrTe₂ films with different thicknesses in a magnetic field of 1 kOe oriented along the out-of-plane direction. A high T_C close to room temperature was found for a trilayer. (c) Temperature-dependent magnetic hysteresis loops for a 7-layer-thick film with a magnetic field applied along the film normal. Panels (b) and (c) were reproduced with permission under a Creative Commons CC-BY 4.0 License from ref 234. Copyright 2021 Springer Nature. (d) Schematic depiction of a single layer of Fe₃GeTe₂. Temperature-dependent (e) remanent magnetization and (f) magnetic hysteresis loops of bilayer Fe₃GeTe₂ grown on c-plane sapphire by MBE. Panels (e) and (f) were reproduced with permission under a Creative Commons CC-BY 4.0 License from ref 229. Copyright 2022 Springer Nature. (g) The anomalous Hall effect (AHE) measured for Fe₃GeTe₂/Gr at different temperatures. For clarity, the resistance curves are successively shifted up by 2.5 Ω for temperatures ≥ 5 K. The square hysteresis loop of the AHE contribution in the Hall resistance R_{XY} is due to a strong out-of-plane magnetic anisotropy and superimposed onto the negative linear slope arising from the ordinary Hall response of the free carriers in Fe₃GeTe₂/Gr. (h) Coercive field $\mu_0 H_C$ and saturation resistance ΔR_{AHE} from the AHE contribution as a function of temperature for Fe₃GeTe₂/Gr. (i) Hall resistance R_{XY} in the high field limit of the Fe₃GeTe₂/Gr heterostructure showing Quantum Hall effect plateaus, indicating a high carrier mobility in Gr and thus the ability to preserve the functionality of the vdW templates after the growth of Fe₃GeTe₂ by MBE.²³⁸ The Landau level index is assigned to every plateau. Reproduced with permission under a Creative Commons Attribution 4.0 license from ref 238. Copyright 2021 IOP Publishing.

On the one hand it represents a critical roadblock that needs to be overcome for the future exploration of vdW magnets, while at the same time this research area offers fertile grounds to make further ground-breaking discoveries in magnetic 2D materials.

Capping layers were required to prevent unintentional oxidation and to avoid inactivation of magnetic defects.²³² Interestingly, degradation of magnetic properties upon air exposure was found less critical for 1T-CrTe₂,²³³ although for long-term operation the use of capping layers seems inevitable as well. Like VSe₂, CrTe₂ assumes the conventional configuration of TMDs, schematically depicted in Figure 12a. Importantly, 1T-CrTe₂ crystals were reported to exhibit Curie temperatures around 300 K in the bulk form, which remained close to room temperature for exfoliated flakes as thin as 8 nm.²²⁸ Interestingly, Zhang et al.²³⁴ observed room-temperature ferromagnetism of few-layer-thick CrTe₂ films grown by MBE on bilayer epitaxial

graphene on SiC, while T_C decreases to about 200 K when the thickness is reduced to a single layer, shown in Figure 12b,c. An intriguing aspect in the available reports is that a robust out-of-plane anisotropy was usually observed for epitaxially grown material. This is in marked difference from bulk crystals and corresponding ultrathin flakes, which always displayed an in-plane magnetic anisotropy. Specifically, Meng et al.²³⁵ reported a transition from an in-plane to an out-of-plane magnetocrystalline easy axis in CVD-grown 1T-CrTe₂ islands for thicknesses ≤ 10 nm. The origin of an out-of-plane anisotropy, which has not been observed in exfoliated flakes, has been associated with an enhanced magnetic anisotropic energy in the 2D limit, which can better resist thermal fluctuations and therefore help mediating a long-range ferromagnetic order. Further investigations are required to understand these peculiar observations and existing discrepancies. Considering the rich phase diagram

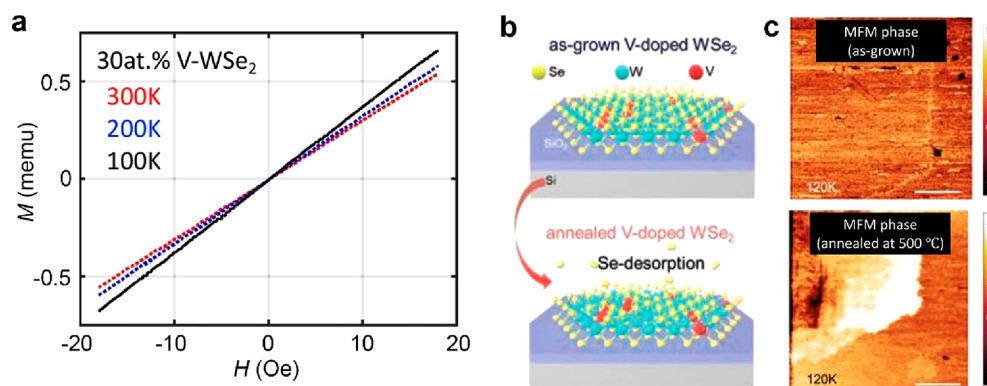


Figure 13. Quality versus magnetism in 2D TMDs. (a) Temperature dependent M versus H loops for a MBE grown, 30% V-doped 2D WSe_2 on sapphire showing the absence of any ferromagnetism at 100 K. (b) As-grown V-doped 2D WSe_2 sample grown on SiO_2/Si was intentionally annealed to create Se vacancies. (c) Magnetic force microscopy (MFM) phase images measured at 120 K for as-grown and 500 °C annealed 0.5% V-doped WSe_2 are compared: The as-grown WSe_2 exhibits a negligible MFM phase contrast with respect to the SiO_2/Si . In contrast, the annealed WSe_2 exhibits a distinct magnetic domain contrast, confirming ferromagnetism in the annealed sample. Panels (b) and (c) were adapted and modified with permission from ref 256. Copyright 2022 John Wiley & Sons, Inc.

of the Cr-Te system, which also includes the existence of stable phases with Cr atoms intercalated between chromium telluride layers,²³⁶ the existence of intermixed phases and/or thickness-dependent phase transitions occurring during epitaxial growth could possibly explain the differences in the magnetic properties observed so far.

The ferromagnetic metal Fe_nGeTe_2 is yet another very relevant contender as a 2D material with an above room temperature ferromagnetic order. This is not only because of the high transition temperatures it can exhibit, but also due to the flexibility it offers to tailor magnetic properties via structural and chemical design within the individual vdW layers. As proposed by Seo et al.,²³⁷ a single layer of Fe_nGeTe_2 can be considered as a specific material representation of a more general layered structure, in which a mechanical backbone is formed from a nonmagnetic and a chalcogen element—here Ge and Te with the chemical composition of a dichalcogen crystal—that is “filled” with magnetic elements—here Fe—that mediate the exchange interaction and ultimately originate the long-range magnet order. A schematic of the atomic arrangement is shown in Figure 12d. A 3D-like network of magnetic elements confined within a 2D layer is formed in such a way that only vdW interaction are present for the interlayer interaction. Tuning the Fe content within the layers has been experimentally realized, and until now, Fe_nGeTe_2 with n values ranging from 3 to 5 was experimentally demonstrated.^{229,237,238}

Recently, changes in the magnetic properties as a function of thickness have been assessed. The general trend confirmed by several studies is a decrease in T_C when the 2D limit is reached.^{239,240} For monolayer-thick Fe_3GeTe_2 , T_C values ranging from 20 to 126 K have been reported, depending on the measurement technique and method utilized for synthesis (either MBE growth on $\text{Ge}(111)$ ²³⁹ or mechanical exfoliation²⁴⁰). A bilayer of Fe_3GeTe_2 grown epitaxially on c-plane sapphire exhibited a record-high T_C of around 230 K (Figure 12e,f).²²⁹ Systematic studies are needed to unambiguously identify the critical thickness for T_C reduction for the different Fe_nGeTe_2 structures, as well as other contributing factors such as substrate type and capping layers. Such insights into Fe_nGeTe_2 become even more desirable, since it exhibits good stability in air. Furthermore, electrostatic gating of Fe_3GeTe_2 using ionic liquids has demonstrated that Curie temperatures can be further

increased up to room temperature.²⁴⁰ One promising path to engineer the intrinsic magnetic properties of Fe_nGeTe_2 is by substituting Fe with transition metal elements possessing a strong magnetic moment as well. Co- and Ni-doping in $\text{Fe}_{5-x}\text{GeTe}_2$ bulk crystals²⁴¹ allowed for a rich variety of modifications in magnetism depending on the dopant content and type, from ferromagnetic-antiferromagnetic exchange to T_C boosting well above room temperature (Chen et al.²⁴¹ recently reported a T_C around 476 K for Ni-doped Fe_3GeTe_2 crystals). Further efforts should now be put on the realization atomically thin layers of doped Fe_nGeTe_2 with uniform intra- and interlayer dopant distribution.

Progress has also been made in large-scale bottom-up growth of Fe_nGeTe_2 . MBE has so far been the method of choice for the epitaxial growth of continuous, large-area films utilizing the “3D” substrates.^{229,238,239,242} For example, c-plane sapphire has been used for the growth of Fe_3GeTe_2 epitaxial films.²²⁹ A Curie temperature of 300 K was reported, in good agreement with values obtained for bulk crystals.²⁴³ Fe_nGeTe_2 synthesized directly on a 2D material surface has also been realized.²³⁸ A robust out-of-plane magnetic anisotropy and T_C around 220 K were measured for Fe_3GeTe_2 films grown on epitaxial graphene on SiC at relatively low growth temperatures around 300 °C. The high structural and electronic quality of the heterostructures was also confirmed by the observation of the quantum Hall effect in graphene, see Figure 12g–i. This is a key step toward the realization of epitaxial vdW heterostructures with pure and sharp interfaces, where proximity-induced phenomena can be used as a tool for tailoring magnetism. In this regard it remains of particular interest to develop synthesis of atomically thin, all-epitaxial heterostructures combining Fe_nGeTe_2 not only with graphene but also with wafer-scale 2D crystals such as TMDs and hBN to realize the vision of highly functional vdW heterostructures, in which proximity-induced coupling across atomically smooth interfaces of layered materials with different properties enable unique functionalities²²⁴ that can be further tuned by external applied fields.

2.9. 2D Magnets and Controversies. Magnetism in the 2D limit is a desired property to build an all 2D-integrated chip capable of performing logic operations as well as storing the information.²⁴⁴ Although, a variety of 2D materials have been predicted and experimentally realized as room temperature

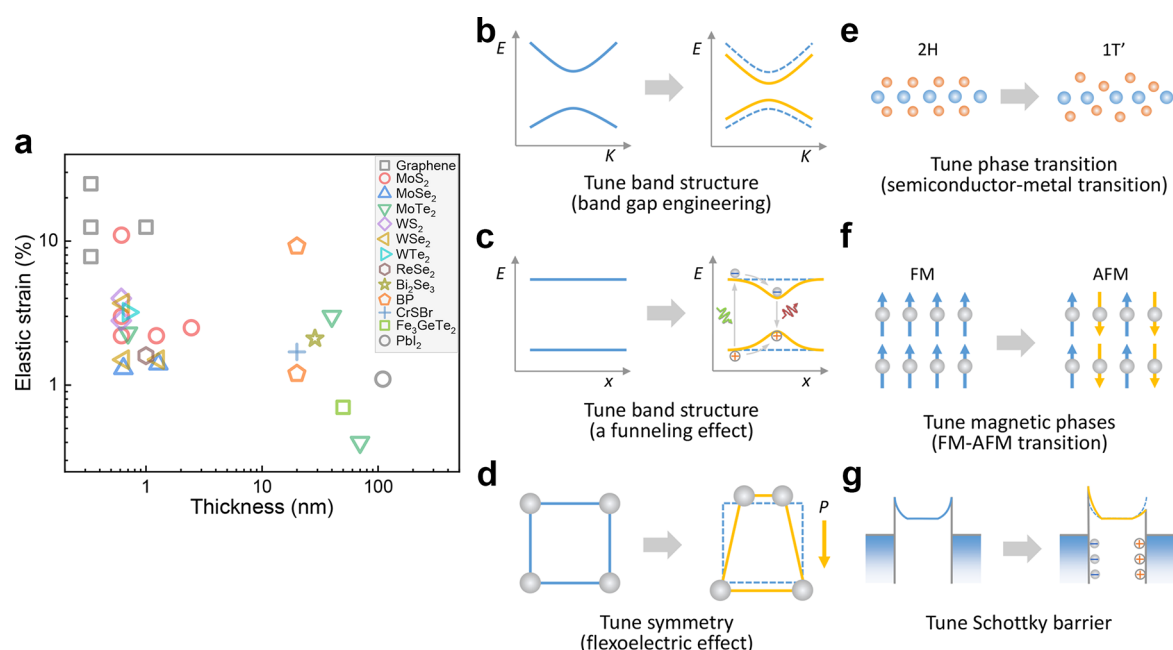


Figure 14. Large elastic strains and strain gradients in 2D materials. (a) Experimental measured elastic strains in representative 2D materials as a function of thickness. Here 2D materials include graphene,^{261,262,266} MoS₂,^{263,265,267,289} MoSe₂,^{268,269} MoTe₂,^{270–272} WS₂,^{273,274} WSe₂,^{268,275,276} WTe₂,²⁷⁷ ReSe₂,²⁷⁸ Bi₂Se₃,²⁷⁹ BP,^{280,281} CrSBr,²⁸² Fe₃GeTe₂,²⁸³ and PbI₂.²⁹⁵ Strain and strain gradient engineering in 2D materials. (b) Schematics of band structures (K for crystal momentum) before (left) and after (right) applying a strain (band gap engineering). Blue dashed curves represent the original bands. (c) Schematics of band structures (x for distance) before (left) and after (right) applying a strain (a funneling effect). (d) Schematics of symmetries before (left) and after (right) applying a strain gradient. The strain gradient induces a spontaneous electrical polarization (P) (flexoelectric effect). (e) Atomic structures of transition metal dichalcogenides before (2H semiconducting phase, left) and after (1T' metallic phase, right) applying a strain (semiconductor–metal transition). (f) Schematics of magnetic phases before (FM, left) and after (AFM, right) applying a strain (FM–AFM transition). (g) Schematics of band diagrams before (left) after (right) applying a strain. (g) Schottky barrier heights formed at contacts are tuned by strain due to strain-induced polarization in piezoelectric materials.

magnets, the origin of this magnetism is under intense debate in the community.^{245,246} The case of VSe₂ is one such example. Bonilla²⁴⁷ and Duvjir²⁴⁸ independently report magnetism in MBE grown VSe₂ monolayers on a variety of substrates, where magnetometry characterization using vibrating sample magnetometer (VSM) and superconducting quantum interference device (SQUID) showed magnetic hysteresis at room temperature suggesting ferromagnetic order. However, later investigations by Batzill's group reported that pristine VSe₂ did not show magnetism. Instead, the magnetism arose following postgrowth annealing and Se vacancy formation in the film.^{245,249} This was confirmed in studies on pristine VSe₂ using a different characterization technique of X-ray magnetic circular dichroism (XMCD), which indicate the absence of any magnetic moments on the V atoms in pristine 2D VSe₂.^{250,251} Further evidence comes from angle-resolved photoemission spectroscopy (ARPES) measurements where no spin-polarized bands are found in 2D VSe₂.^{251,252} Lastly, the reported observation of a charge density wave (CDW) in monolayer VSe₂, which competes with the ferromagnetic ground state of the system to suppress it, supports the claim of the nonmagnetic nature of pristine VSe₂.^{252,253} Thus, many reports demonstrate that the pristine VSe₂ is nonmagnetic. It is important to mention here that such a lack of intrinsic ferromagnetism is reported for other systems as well, where different artifacts such as edge states, surface adsorbates, and point defects were responsible for the magnetic effects.^{254,255}

Magnetic impurity-doped semiconductors, commonly known as dilute magnetic semiconductors (DMS), have also been

suggested as another platform to search for RT 2D magnetism. Once again, the literature on 2D DMS is similarly filled with controversies and inconsistencies, in both theory and experiments. For example, Tiwari et al.²⁵⁷ used first-principles calculations to predict that >18% atomic substitution of vanadium for W in a monolayer of WSe₂ should give an out-of-plane RT ferromagnet. However, MBE grown 2D WSe₂ with about 30 atomic % V substitution does not show any magnetism for temperatures as low as 100 K (Figure 13a). In contrast, several other groups have observed RT ferromagnetism for V doping levels in the range of 0.1–1% that are far below what DFT predicts for RT Curie temperatures.^{258,259} On the other hand, recently, point defects in the form of Se vacancies in CVD grown V-doped WSe₂ created by thermal annealing were found to be responsible for magnetism in this system (Figure 13b,c).²⁵⁶ As the MBE growth is usually performed in a high chalcogen flux environment, Se vacancy concentrations are likely too low to show any vacancy induced magnetism and may explain why MBE V-doped WSe₂ films do not exhibit ferromagnetism. In short, while RT 2D magnets are coveted elements for memory and spintronic devices, the literature is rife with inconsistent and sometimes contradicting observations.

3. Strain Engineering, Symmetry Breaking, and Biosensing. **3.1. Strain and Strain Gradient Engineering in 2D Materials.** Strain engineering has been shown as a neat and effective approach in tuning or engineering the physical properties of 2D materials. The ability to reach large elastic strain in 2D materials has led to various scientific progresses in materials science, which include the editing of Berry

connection/curvature and topological Dirac states, tuning of metal–insulator and magnetic phase transition, direct–indirect electronic band structure evolution, and the realization of the flexo-photovoltaic effect, with details discussed in the paragraphs below.

3.1.1. Colossal Strains and Strain Gradients in 2D Materials. In bulk materials, an elastic strain $\ll 1\%$ can be sustained due to a large number of intrinsic defects (e.g., cracks and dislocations) either on the surface or inside the material.²⁶⁰ These defects multiply rapidly once deformation occurs (e.g., dislocation multiplied by Frank–Read source). However, in low dimensional nanoscale materials, thermodynamic equilibrium shape can be easily reached and less defects are expected to be formed during the crystal growth. When deformed, for example, defect creation is largely dominated by surface dislocation nucleation, not by growth and propagation as the case of bulk crystals, making them much stronger than their bulk counterparts. Large elastic strains of above 1% have been widely demonstrated in low dimensional ceramic materials.

Figure 14a shows the experimental measured elastic strains in representative 2D materials such as graphene, transition metal dichalcogenides, and other layered materials. Lee et al.²⁶¹ and Pérez Garza et al.²⁶² reported elastic strains of above 10% in graphene or few-layer graphene by nanoindentation and a tensile microelectromechanical system, respectively. Similarly, Bertolazzi et al.²⁶³ reported that elastic strains in MoS₂ monolayer reaches above 10% by nanoindentation using an atomic force microscope (AFM) tip. Researchers have reported many other methods, such as bending,²⁶⁴ bulking,²⁶⁵ and using substrates with grating²⁶⁶ and nanocones,²⁶⁷ to generate elastic strains in graphene and MoS₂. Large elastic strains have been reported in other TMDs (MoSe₂,^{268,269} MoTe₂,^{270–272} WS₂,^{273,274} WSe₂,^{268,275,276} WTe₂,²⁷⁷ ReSe₂,²⁷⁸ and Bi₂Se₃²⁷⁹), black phosphorus (BP),^{280,281} layered magnets (CrSBr,²⁸² Fe₃GeTe₂,²⁸³), and layered halide (PbI₂,²⁸⁴), as plotted in Figure 14a as a function of thickness. In general, the measured elastic strain limits increase with decreasing thicknesses of samples.

Although elastic strain has been studied widely in most 2D materials, the strain gradient has received much less attention. In bulk crystals, the strain gradient can normally only reach below 0.1 m^{−1}, which is often induced by mechanical bending.²⁶⁴ However, with reducing the sample thickness, a large elastic strain gradient can be created. Incredibly, large strain gradients of up to $\approx 10^6$ m^{−1} and $\approx 10^5$ m^{−1} are possible in MoS₂²⁸⁵ and freestanding film of BiFeO₃,²⁸⁶ respectively, whereas a bulk crystal such as MAPbBr₃²⁶⁴ can only manage strain gradients of < 0.1 m^{−1}. Normally, when strains are generated in local regions in 2D materials (such as nanoindentation and buckling), strain gradients are formed simultaneously. These strain gradients should not be ignored and may play an important role on some physical properties. For example, strain gradient can break the inversion symmetry of a material and induce a spontaneous electrical polarization (flexoelectric effect), leading to intriguing phenomena such as flexo-photovoltaic effect (bulk photovoltaic effect coupled with flexoelectric effect).^{285–287} Therefore, relevant studies on strain gradient–property relations on 2D materials are highly desired.

By introducing strain in a material, one can modify the lattice constant, atom position, symmetry, and space group. All these parameters determine the Hamiltonian of the system and thus can be used to design or tune its electronic structure. For example, by introducing compressive strain, a smaller lattice constant could increase orbital overlapping, thus leading to a

larger band gap. The tensor form of strain can be used to design or lower the symmetry of the system while symmetry breaking is sometimes accompanied by the emergence of interesting physical properties. Strain gradient naturally breaks the inversion symmetry of materials and could be used to design polarization or Berry connection.²⁸⁸ When spin–orbit coupling is considered, by tuning the symmetry of the crystal, strain or strain engineering could be used to design the topological properties of material. In 2D materials, strain and strain gradient have been demonstrated to be able to tune the electron–lattice interactions, band structure, phonon behaviors, magnetic ordering, spin–momentum coupling, and topological parameters.

The strain–band gap relation is one of the most widely investigated topics in 2D materials.^{265,274,280,289} By applying a uniaxial tensile mechanical strain ε in a monolayer MoS₂ (Figure 14b), Conley et al.²⁸⁹ reported a nearly linear decrease of around 45 meV/% in the optical band gap of the monolayer. A pronounced decrease in the PL intensity with increasing tensile strain suggests a possible direct-to-indirect transition in this material. If strain is applied at a local region, e.g., by nanoindentation using an AFM tip, a funneling effect can be induced (Figure 14c),²⁹⁰ where photoexcited electron and holes can migrate to the center and then they may recombine or they can be collected by electrodes. Based on this funneling effect, Li et al.²⁶⁷ designed and fabricated a 2D MoS₂ strained crystal by transferring MoS₂ monolayer onto a SiO₂ nanocone array. The authors demonstrated broadband light absorption and efficient funneling effect at maximum strain points in this strained crystal.²⁶⁷ Finally, this effect can lead to efficient funneling of excitons to generate single photon emission in nonuniformly strained monolayer WSe₂,^{291,292} and trions in nonuniformly strained monolayer WS₂.²⁷³ Strain gradients can also tune the point group of a material (flexoelectric effect, Figure 14d). By using this method, Jiang et al.²⁸⁵ reported a large strain gradient of up to 10^{−6} m^{−1} in a strain gradient-engineered MoS₂ sheet, leading to a flexo-photovoltaic effect. The 2D materials with nonuniform strains induced by nanoindentation, buckling and substrate with nanocones reported previously, also have strain gradients. The flexoelectric effect in these 2D materials may play an important role on some intriguing phenomena. By modifying the thermodynamic energy landscape, strain can tune phase transition temperature in 2D materials, such as a structural 2H–1T' phase transition (Figure 14e) with a proper strain in TMDs. It is suggested that the activation energy for 2H–1T' phase transition can be modulated by strain: tensile strain lowers the energy barrier height.²⁹³ The structural phase transition is often accompanied by electronic phase transition–metal–semiconductor transition, important for the development of fast-switching transistors.²⁹³ By using strain-tuned phase transition in MoTe₂, Hou et al.²⁷¹ fabricated MoTe₂ phase change transistor and achieved nonvolatile conductivity change $G_{\text{on}}/G_{\text{off}}$ of near 10⁷. Through tuning the interlayer or intralayer magnetic exchange interaction, strain can control magnetic phases in 2D materials, including a ferromagnetic (FM) to antiferromagnetic (AFM) phase transition (Figure 14f).²⁸² As a final example of how strain impacts electronic properties, strain in piezoelectric 2D materials can also be used to tune the Schottky barrier heights when Schottky contacts are formed (Figure 14g). Wu et al.²⁹⁴ reported the piezoelectricity in 2D MoS₂ and demonstrated an asymmetric carrier transport under strains in this device indicating a piezotronic effect in 2D MoS₂. Besides, strain can tune Dirac surface states and control exciton–phonon

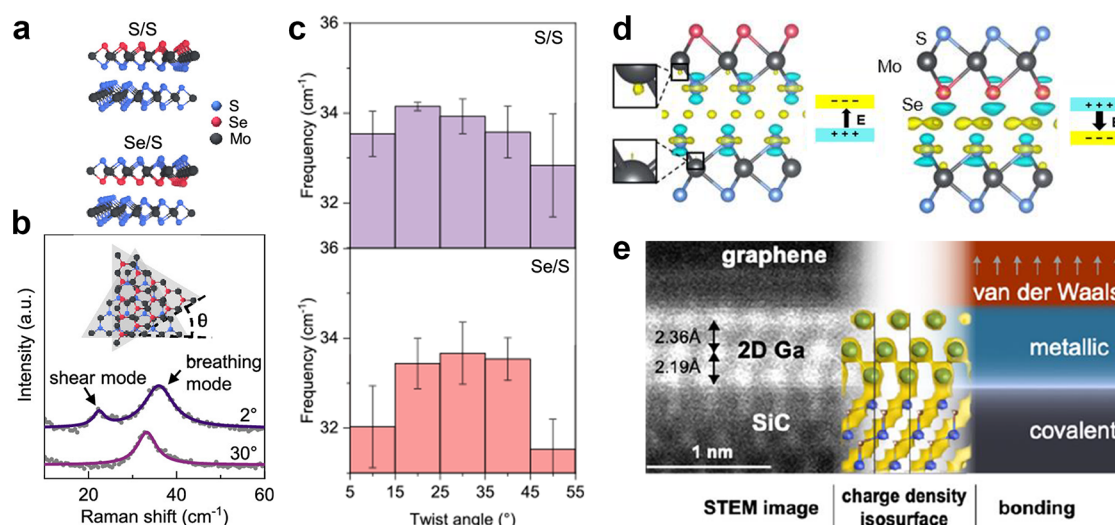


Figure 15. Emerging optical phenomena of asymmetric 2D materials. (a) Illustration of SeMoS/MoS₂ (SS) and SMOSe/MoS₂ (Se/S) heterobilayers. (b) The shear and breathing mode frequencies of interlayer shear and breathing modes of S/S heterobilayer at two twisted angles (θ), which is defined as the angle between the zigzag directions of SeMoS and MoS₂. (c) The breathing mode frequencies of S/S and Se/S heterobilayers fabricated by transfer stacking. (d) The charge density difference of the above Janus heterostructures with S/S and Se/S interfaces predicted by DFT calculations shows the direction of the interfacial electric field. Panels (a)–(d) were reproduced with permission from ref 317. Copyright 2021 American Chemical Society. (e) STEM image depicting the structure of 2D Ga PMet, consisting of three atomic layers of gallium on a SiC substrate capped with bilayer graphene, along with calculated charge density and schematic of bonding character. Reproduced with permission from ref 312. Copyright 2020 American Chemical Society.

coupling in Bi₂Se₃ films, as reported by Flötotto et al.²⁷⁹ Strain can control exciton–phonon coupling in monolayer transition metal dichalcogenides, as reported by Niehues et al.²⁶⁸

3.2. Second Harmonic Generation in 2D Materials. Here, we discuss recent research progress and challenges in the second harmonic generation (SHG) of 2D materials. For a more comprehensive review of nonlinear properties, the readers are referred to several excellent previous reviews on 3D bulk²⁹⁶ and 2D materials.²⁹⁷ SHG describes a coherent frequency-doubling process when intense light passes through a material. As a higher-order process compared with linear optical response, SHG involves more complexities in interpreting experimental measurements and theoretical calculations. However, the initial appeal of studying SHG in 2D materials was simple: SHG relies on inversion asymmetry, commonly found in monolayers and not their bulk layered parents.²⁹⁸ Within a monolayer with inversion asymmetry, any local disruptions to the lattice will also modulate $\chi^{(2)}$,^{299–301} promoting SHG to be a defect characterization method that is more efficient and less destructive than transmission electron microscopy methods.³⁰⁰ One experimental difficulty is that there is no direct readout of $\chi^{(2)}$ from experiments: the extraction of $\chi^{(2)}$ from experimental measurements of SHG requires a model of the second harmonic radiation field driven by the polarization of the material. One common “bulk” model originating from Boyd’s classic text is to treat a monolayer as a bulk material with a thickness (e.g., 0.65 nm per layer for MoS₂), as has been done for MoS₂,³⁰² GaSe,³⁰³ and InSe.³⁰⁴ This bulk model has been shown to severely overestimate $\chi^{(2)}$ compared with a more careful treatment using a “sheet” model.³⁰⁵ For example, $\chi^{(2)}$ for MoS₂ was overestimated to be 10⁵ pm/V using the bulk model, while the sheet model yields 6 pm/V (static³⁰⁶) or 40–100 pm/V (on resonance).³⁰⁶ Fortunately, Clark et al.³⁰⁶ also prescribes how to convert the bulk-model-derived $\chi^{(2)}$ to sheet-model-derived ones. Applying this conversion to GaSe, and InSe has achieved better agreement with theory results.³⁰⁷ Other methods were

reported too: a model based on the Green’s function of a sheet source has estimated $\chi^{(2)}$ to be around 10⁴ pm/V for 2D TMDs³⁰⁸ at 800 nm excitation,³⁰⁹ 2 orders of magnitude larger than the on-resonance $\chi^{(2)}$ for TMDs extracted from the sheet model. At present it is not clear why these models yield $\chi^{(2)}$ values that appear inconsistent with both the bulk and sheet models.

The initial successful characterizations of SHG in 2D materials also brought focus to maximizing $\chi^{(2)}$ for potential applications in frequency doubling. Typically, measured $\chi^{(2)}$ were compared with that of industry-standard nonlinear crystals like barium borate (BBO) or potassium dihydrogen phosphate (KDP). However, $\chi^{(2)}$ is not the only metric of an ideal nonlinear crystal. A sufficiently large bandgap is required to ensure transparency and withstand laser-induced damage; adequate birefringence is necessary for phase matching; a crystal growth protocol that minimizes defect population is needed to reduce defect absorption. Even if one only considers two metrics— $\chi^{(2)}$ and bandgap—the known trade-off relationship³¹⁰ between them means that large $\chi^{(2)}$ values reported in the literature are frequently obtained at the implicit cost of a smaller bandgap.

A fairer metric should therefore be how far $\chi^{(2)}$ exceeds the $\chi^{(2)}$ -bandgap trade-off. One way to quantify this is to report $\chi^{(2)}$ normalized by the bandgap, as is done in Taghizadeh et al.³¹¹ Overall, we recommend that future research compare $\chi^{(2)}$ in the context of the material’s bandgap. For example, in the case of 2D metals, in-plane $\chi^{(2)}$ components of 4.8 and 3.8 nm²/V were measured for 2D Ga and In intercalated between a SiC substrate and a graphene cap.³¹² These values, in a fair comparison with other zero-gap materials systems, are larger than the in-plane $\chi^{(2)}$ of metal surfaces such as Al(111), estimated to be 0.2 nm²/V. For the case of metal thiophosphates, He et al.³¹³ demonstrated that the bulk layered compound SnP₂S₆ achieves a large $\chi^{(2)}$ for its bandgap (2.3 eV). Its $\chi^{(2)}$ is on the order of 53 pm/V, larger than other common infrared nonlinear crystals with similar bandgaps, such as AgGaS₂ and AgGaSe₂. SnP₂S₆ also has a high

laser-induced damage threshold, three times greater than that in ZnGeP_2 , a commercially available nonlinear optical crystal.³¹³ Along with a large bandgap and laser damage threshold, the synthetic method is also important when considering 2D crystals for frequency doubling and other nonlinear optical applications. For example, it has recently been shown that few-layer MoS_2 exfoliated through a solution-phase redox process can exhibit saturable SHG and multiphoton absorption up to 10th order.³¹⁴ Polyoxometalate clusters which are formed during the redox exfoliation process and adsorb onto the 2D material flakes were implicated in the unusual nonlinear optical properties. Saturable SHG and multiphoton absorption were not observed in MoS_2 prepared by CVD, demonstrating that the choice of synthesis method can not only enhance or suppress the magnitude of existing nonlinear optical properties in 2D materials but also enable interesting phenomena.

3.3. Symmetry Breaking in 2D Materials. Symmetry reduction can introduce exotic physical and chemical properties. For instance, the breaking of inversion symmetry in twisted BLG led to strongly correlated states due to moiré superlattice formation.³¹⁵ While low-symmetry 2D materials exist (e.g., SnS , PdSe_2 , and WTe_2), there was a lack of 2D materials with mirror symmetry breaking because they were metastable. Thanks to recent advancement in synthesis methods for 2D materials, researchers can break the mirror symmetry of monolayers and unleash functionalities that cannot be achieved by traditional thin film techniques. This section covers two examples of 2D materials with structural symmetry breaking and their properties. First, Janus TMDs (e.g., SWSe , SeMoS) are one example of structural asymmetry enabled by surface treatments such as annealing with sulfur vapor³¹⁶ or low-energy selenium implantation¹³ performed on WSe_2 or MoS_2 . The mirror symmetry breaking in Janus TMDs leads to an intrinsic vertical dipole moment that induces a wealth of unique properties that are not normally accessible and enhance the vdW coupling in heterostructures.³¹⁶ Second, air-stable 2D polar metals (e.g., Ga and In) in between epitaxial graphene and SiC with one side covalently binding to SiC and the other side that interacts with graphene by vdW forces are made possible by confined heteroepitaxy (CHet).⁵⁰ Due to different bond environments on both surfaces of half-vdW 2D metals, the out-of-plane metal–metal bond changes by near 10%,³¹² resulting in symmetry breaking and a large nonlinear optical response. Both cases demonstrate the optical and photonic properties can be controlled precisely at the submonolayer level.

3.3.1. Janus TMD Heterostructures. Janus TMDs is an example of broken mirror symmetry enabled by surface modification. It is a type of TMD material in which the transition metal is sandwiched between two different species of chalcogen. When Janus TMDs are assembled with other 2D materials into heterobilayers, different interfaces can be formed because of the structural asymmetry (Figure 15a). Zhang et al.³¹⁶ demonstrated that the dipole moment of Janus SeMoS enhanced the vdW coupling in a $\text{SeMoS}/\text{MoS}_2$ heterostructure synthesized by thermal selenization of bilayer MoS_2 . The interlayer force constant of $\text{SeMoS}/\text{MoS}_2$ related to the interlayer shear and breathing modes was larger by 13.2% than that of as-grown bilayer MoS_2 due to the intrinsic dipole moment.³¹⁶ As the intrinsic dipole is perpendicular to the basal plane, the same group showed that this vdW coupling is dependent on which side of Janus TMDs was interacting with their pristine counterparts as well as their twisted angles (Figure 15b).³¹⁷ For a Janus TMD transferred onto a pristine TMD, the

MoS_2 exhibited a better vdW interaction with the sulfur side of SeMoS , as shown by the higher interlayer phonon frequencies in Figure 15c, due to a shorter interlayer spacing. DFT calculations also revealed that the intrinsic dipole led to an interfacial electric field (Figure 15d), promoting charge transfer between layers when MoS_2 was in contact with the sulfur side of MoSSe .³¹⁷ The modulated vdW coupling and charge transfer of Janus TMDs showcase the great potential for manipulation of electron dynamics in a variety of optoelectronic devices. Besides the experimentally probed optical properties, the intrinsic dipole moment was predicted to contribute to robust Rashba spin splitting independent of the applied electric field and strain,³¹⁸ which is important for spintronic devices, such as spin filters, spin FETs, and spin-resolved photodetectors. Theoretical predictions also suggested that Janus TMDs displayed great potential for applications including photocatalytic water-splitting, hydrogen evolution reaction, and gas sensing.

3.3.2. 2D Polar Metal Heterostructures. While nanostructured metals are ubiquitous in technologies for sensing, catalysis, and nonlinear optics, 2D elemental metals are understudied compared to other 2D materials. The reduced dimensionality of 2D metals may offer advantages for highly tunable plasmonics,³¹⁹ photocatalysis,⁶ enhanced magnetism,⁵ and superconductivity.³²⁰ However, unlike other materials which are well-known in both 2D and 3D forms, traditional metals do not have an intrinsically layered bulk structure. Therefore, 2D metals are difficult to synthesize and often unstable, which has limited them to small lateral dimensions and high vacuum environments, hindering their applicability.³²¹ Epitaxial graphene grown on SiC can be physically decoupled from the SiC by intercalating atoms, such as F, O, and H,³²² to the graphene/SiC interface. Although this interface can improve the stability of intercalated ultrathin metals,¹⁴ metal intercalation has not been studied actively.

Recently, atomically thin, air-stable metals have been realized through CHet.⁵⁰ These 2D polar metal heterostructures (2D-PMets) consist of a few atomic layers of metal that are epitaxial to a SiC substrate and capped with bilayer graphene (Figure 15e). The components of the heterostructure are crucial to the properties of the 2D metals: registry to the SiC substrate results in the metal layers adopting a strained hexagonal lattice, while the graphene protects the metal from oxidation. As a result, 2D-PMets offer opportunities for both fundamental studies of the properties of crystalline metals in lattice configurations not achievable in bulk and expanded studies of 2D metals beyond gold under ambient conditions. Since the introduction of 2D-PMets, their properties including superconductivity,⁵⁰ nonlinear optical phenomena,³¹² potential epsilon-near-zero modes,³²³ and tunable optical resonances and energy dissipation have been reported.³²⁴ 2D-PMets, such as Ga and In, exhibit extremely efficient nonlinear optical transduction, with $\chi^{(2)}$ of 3 to 5 nm/V.³¹² 2D-Ga and -In also outperform other metal SHG sources like gold nanorods and graphene-coated gold films (1000 and 100× higher $\chi^{(2)}$, respectively) and industry standards like LiNbO_3 (100× higher $\chi^{(2)}$).³²⁵ Nonlinear optical microscopy has revealed in-plane and out-of-plane symmetry breaking in 2D-PMets which allows the large second-order response and determines the polarization plane of the emission.³¹²

As the family of 2D-PMets grows to include more elements, nonlinear optical microscopy will continue to enable fast, noninvasive characterization of the quality and crystal structure of intercalated metals. The structural information obtained through polarization-resolved SHG microscopy may be

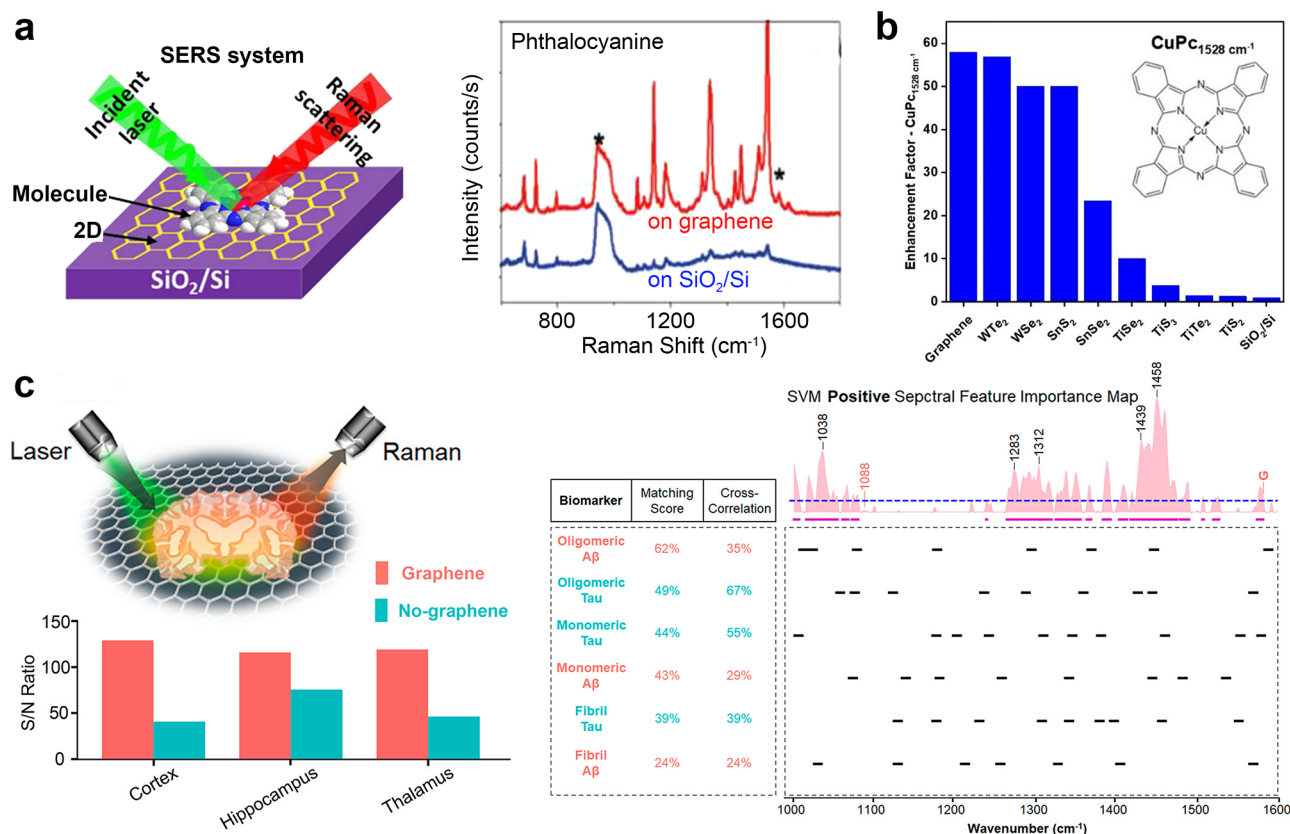


Figure 16. Biosensing based on Raman enhancement through 2D materials. (a) GERS of Phthalocyanine. Adapted and modified with permission from ref 333. Copyright 2015 American Chemical Society. (b) Raman enhancement of CuPc using different 2D materials. Adapted and modified with permission from ref 335. Copyright 2019 American Chemical Society. (c) The Raman signals obtained from different brain regions showed a better signal-to-noise ratio when graphene was in contact with the brain slice. Different ML classifiers showed higher accuracy in distinguishing mice with and without Alzheimer's disease. Adapted and modified with permission from ref 338. Copyright 2022 American Chemical Society.

complemented by wide-field hyperspectral nonlinear imaging, which can be performed with diffraction-limited and subdiffraction spatial resolution through Fourier transform nonlinear optical microscopy.^{326,327} These combined modalities may address further remaining questions about 2D-PMets, such as the influence of metal thickness on the properties of the 2D metal heterostructures and the possibility of enhancing the intrinsically strong light–matter interactions of 2D-PMets through the formation of hybrid resonances.

3.4. Biosensing Applications. 2D materials' surfaces have low roughness and are dangling bond-free, which are more desirable than 3D substrates to host small molecules and biological materials to avoid unnecessary material binding and improve surface adsorption. Additionally, 2D materials exhibit characteristic Raman peaks (e.g., G band and 2D band of graphene and E_{2g} band and A_{1g} band of 2D MoS₂) whose position and width are very sensitive to changes in doping, strain, environment effects, and materials heterogeneity (e.g., substitutional doping, alloying, and vdW heterostructure formation). Therefore, Raman peaks of 2D materials and in some cases PL of 2D semiconductors are used as indicators in nondestructive sensing including photodetectors, strain sensors, and biosensing. In the following, we discuss biosensing of small molecules and biomolecules on 2D surfaces using Raman characterization³²⁸ and learn from Ignatova et al.³²⁹ about using multi-imaging techniques to understand the nonuniformities in MoS₂/graphene bilayers. Since 2D materials are scalable, transferrable,

and air-stable thanks to the continuous improvement of their manufacturing, it is possible to realize them as large-area biosensors in the near future.

3.4.1. Raman Enhancement through 2D Surfaces. 2D materials have attracted substantial interest in the field of biological sensing because of their large surface-to-volume ratio, superior electrical transport, strong surface adsorption, and biocompatibility.³³⁰ These excellent attributes meet the demands of rapid and accurate biomolecular sensing, which requires high multiplexity and specificity. For the detection of infectious diseases, the challenge is to detect rapidly and remotely to minimize unnecessary contacts and reduce the transmission rate.³³¹ While for other diseases with unknown origin, Alzheimer's disease, for instance, it is challenging to provide additional information that pinpoints reliable disease biomarkers for early detection.³³² However, realizing such sensing functionality needs a reliable technique tool to obtain fingerprinting signals of biological samples and efficient interaction between the sensing media and biomolecules. Facing these challenges, Raman enhancement through 2D materials offers an effective approach for chemical sensing of biomolecules with high multiplexity, specificity, and signal-to-noise ratios.³²⁸ An example of Raman enhancement through 2D materials is the surface-enhanced Raman scattering (SERS),³³³ in which the Raman signals of analyte molecules can be significantly enhanced by contacting graphene and other 2D crystals (Figure 16a). This sensing mechanism relies on the dipole–dipole

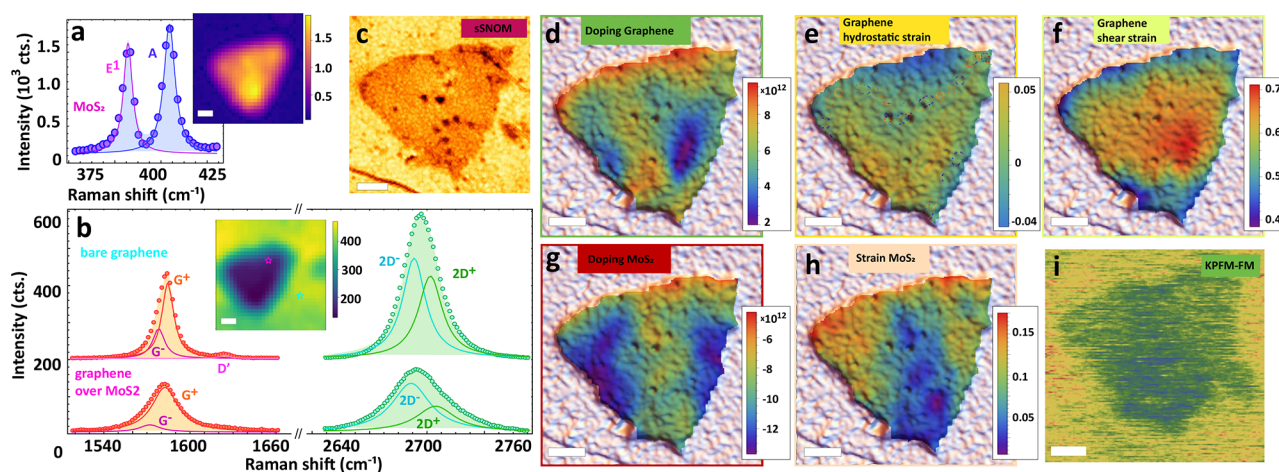


Figure 17. Multidimensional imaging on MoS₂/graphene. (a) MoS₂ Raman spectrum, fitted with E1 and A-bands, (inset) A-band intensity map; (b) Raman spectra for graphene off/on MoS₂ island, fitted by G (orange), D' (pink) and 2D (green) bands, (inset) Raman map of 2D-amplitude showing the island location; (c) KPFM image; (d–f) calculated graphene doping, hydrostatic and shear strain maps, overlaid with scanning electron microscopy image; (g, h) doping and strain for MoS₂ layer overlaid with SEM image; (i) sSNOM phase image of the same area. All scale bars are 1 μ m. Reproduced with permission from ref 329. Copyright 2022 American Chemical Society.

interaction and charge transfer between 2D materials and molecules.³³⁴ Since the discovery of graphene-enhanced Raman scattering (GERS), a plethora of 2D materials including graphene and TMDs (WSe₂, SnS₂, and WTe₂) have exhibited the capability to strengthen the Raman signals of a wide range of small molecules (Figure 16b).^{330,328,335,336}

The application of Raman enhancement through 2D materials is not limited to small molecules. It can be widely applied to a range of biological samples, such as macromolecules,³³⁷ tissues,³³⁸ and cerebrospinal fluid.³³⁹ Huang et al. demonstrated the enhancement of blood constituent proteins, including hemoglobin and albumin based on their unique structures and oxidation states.³⁴⁰ Wang et al.³³⁸ showed that 2D materials can also be used to enhance the signal-to-noise ratio of Raman signals in mouse brains with Alzheimer's disease (Figure 16c). The accuracy of machine learning (ML) classification for brain tissues with and without Alzheimer's disease was also increased from 77 to 98% by applying graphene.³³⁸ Moreover, this work identified biomarkers specific to Alzheimer's disease, including Amyloid- β and Tau, and other potential biomarkers that have been confirmed by other biochemical studies. Equipped with ML analysis,³³⁸ enhanced Raman response can accelerate the understanding of disease pathology, the control of viral transmission, and the development of therapeutics. Aside from being applied to biochemical sensing, 2D materials have been extensively explored in the landscape of other biomedical applications, such as bioimaging,³⁴¹ tissue engineering,³⁴² and drug delivery,³⁴³ continuing to attract interdisciplinary research interest.

3.4.2. The Role of Optical Nonuniformities in vdW Heterostructures for Multidimensional Imaging. 2D heterostructures were shown to operate in a multimodal regime—producing several signals in response to a single analyte, allowing for reporting the analyte in a complex media.¹⁰ Multiplexed sensing of doxorubicin, a common cancer drug, was demonstrated by Ignatova et al.³²⁹ using a 2D material vertical heterostructure. A biosensor composed of monolayer MoS₂ coated with graphene utilized GERS, MoS₂ photoluminescence (PL), and graphene Raman shift signals to report drug molecules with a 60 nM threshold. A multiplexing approach has enabled reporting the drug in the mixed solution with a “contaminant”

organic molecule.³⁴⁴ However, this method could suffer from the above-mentioned local fluctuations of material properties at the nanoscale. The nonuniformities that influence device performance can be divided in two groups: inherited during synthesis (intrinsic) and acquired during device fabrication process. Intrinsic nonuniformities include atomic impurities, lattice defects,^{46,52,345} GBs, wrinkles and ruptures that result in strain, doping and/or charge transfer, often possessing variation at the nanometer scale. Acquired nonuniformities that come from the transfer process and nanofabrication can be partially eliminated by post-transfer cleaning procedures (annealing) or by using Soxhlet extractor³⁴⁶ for improving quality of transfer. Despite efforts to remove contaminants, typical resultant materials are not perfect, leading to variability in optical signaling and high noise in biosensors.

Ignatova et al.³²⁹ applied multidimensional imaging analysis to unveil mechanisms of the local fluctuations of optical response (PL, Raman) of a biosensor. Typical Raman spectra of graphene-MoS₂ heterostructure are shown in Figure 17a,b (insets show maps of a MoS₂ island and locations of single-point spectra of the main plot). Advanced fitting procedure described previously^{347,348} was used to determine the local values of strain and doping for graphene and MoS₂ materials across the whole heterostructure. Furthermore, the splitting of the G- and 2D-Raman bands of graphene yields the shear (nonisotropic) component of the strain (Figure 17b). Generated maps in Figure 17d–h show correlation between the sources of local optical fluctuation and morphology of the sample, as determined by high resolution infrared scattering scanning near-field optical microscopy (sSNOM) image (Figure 17c). Charge doping and components of graphene strain clearly vary across the MoS₂ island, consistent with the Kelvin probe force microscopy (KPFM) results (Figure 17i) and sSNOM (not shown). The cross-correlation of KPFM and sSNOM data allows quantification of the variation of in Fermi level of graphene above the MoS₂ island at nanoscale resolution impossible for KPFM or Raman microscopy along. The presented study suggests that to improve the performance of devices and sensors based on 2D heterostructures, nonuniformity of doping and strain—two major mechanisms for optical signal variation—must be

addressed. Strain-free and doping-free transfer methods are also needed.

4. Multidimensional Heterostructures. **4.1. 0D/2D Heterostructures.** Mixed-dimensional 0D/2D heterostructures formed by the stacking of 2D materials with 0D nanoparticles constitute a class of nanomaterials that offers multifunctionality that goes beyond those of 2D heterostructure systems.³⁴⁹ The class of 0D materials that can be stacked on 2D materials primarily consist of fullerenes, organic molecules, quantum dots (QD), atomic clusters, and atoms.³⁵⁰ In principle, due to the lack of lattice matching and processing compatibility limitations, a large panel of radically different materials can be stacked to form mixed-dimensional 0D/2D heterostructures with diverse properties.³⁴⁹ Mixed-dimensional 0D/2D heterostructures have attracted attention in the fields of catalysis, molecular sensing, quantum information, optoelectronics, and energy conversion and storage due to their unique properties.^{351,352}

The recent work by Kolli et al.³⁵³ is a typical example representing a mixed-dimensional 0D/2D heterostructure between SnS_2 QDs and 2D MoS_2 . The SnS_2 -QDs prepared using solution-processing method were spin coated on MoS_2 monolayers grown on SiO_2/Si by the CVD technique, to form the mixed-dimensional 0D/2D SnS_2 -QDs/ MoS_2 heterostructure. The 0D/2D heterostructure of SnS_2 -QDs/monolayer MoS_2 was fabricated for high-performance and broadband (UV–visible–near-infrared (NIR)) photodetector, with photoresponsivity for UV, visible, and NIR regions of ~ 278 , ~ 435 , and ~ 189 A/W, respectively. Monolayer MoS_2 is visible- and NIR-light-sensitive, and discretely distributed SnS_2 -QDs extends the photodetection range to the UV region, thus broadening the photodetection range of SnS_2 -QDs/ MoS_2 from UV to NIR. The excellent performance of the fabricated SnS_2 -QDs/monolayer MoS_2 hybrid photodetector is attributed to the band bending and built-in potential created at the junction of SnS_2 -QDs and MoS_2 (Figure 18a), which enhances the injection and separation efficiency of the photoexcited charge carriers.

Metallic nanoclusters and/or atomically dispersed metal atoms confined on 2D materials is also a promising avenue for mixed dimensional heterostructures for catalysis, molecular sensing, and energy storage due to their highly efficient metal utilization.³⁵⁴ Reducing the metallic particle size to metallic nanoclusters and single metal atoms increases the exposed surface atoms, modifies the surface electronic and atomic structure, and creates defects.³⁵⁵ The strong metal–2D material support interaction and quantum size effects can lead to exceptionally distinct chemical, physical and electronic properties relative to nanoparticles and bulk metals. Lei et al.³⁴ showed a typical example of a mixed-dimensional 0D/2D heterostructure based on metallic nanoclusters and atomically dispersed metal atoms confined on 2D materials between hexagonal boron nitride (hBN) and various metals including, Fe, Cu, Au, Ag, and Pt. In this report, the hBN/AgPt nanoclusters (Figure 18b) demonstrated excellent hydrogen evolution reaction (HER) activity, with an onset potential better than all other heterostructures (87 mV) due to the robust anchoring of atomically dispersed Pt atoms, improved electrical conductivity from the Ag, and the synergetic effects between hBN and AgPt.

Single metal atom sites attached on a 2D material matrix in a mixed-dimensional 0D/2D heterostructure can also be used to tune the electronic structure of the 2D material host matrix. A typical example representing a 0D/2D heterostructure in which attaching single metal atoms are attached onto a 2D matrix to

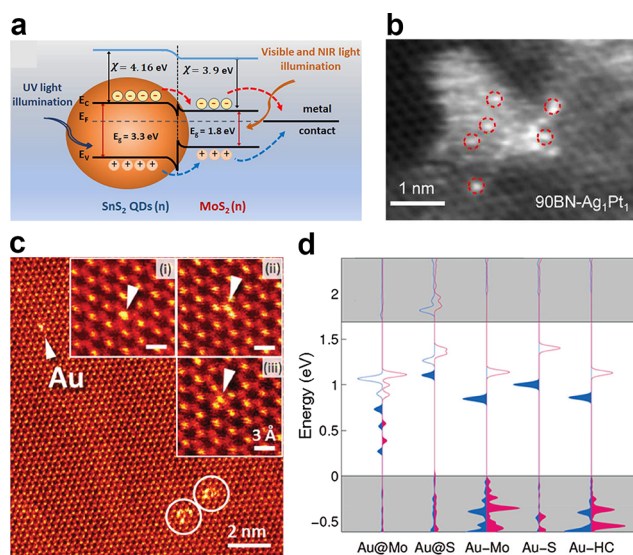


Figure 18. Mixed-dimensional 0D/2D heterostructures. (a) Schematic illustration of SnS_2 -QDs and monolayer MoS_2 band structure after the formation of heterojunction with proposed e–h pair separation. Reproduced with permission from ref 353. Copyright 2022 American Chemical Society. (b) Representative high magnifications STEM-ADF images of hBN-AgPt where the atomically dispersed Pt atoms in the Ag-Pt cluster are highlighted with red dashed circles. Reproduced with permission under a Creative Commons Attribution 4.0 International license (CC BY 4.0) from ref 34. Copyright 2021 Elsevier. (c) An annular dark-field TEM image of a ~ 0.6 at. % Au-doped MoS_2 monolayer. Au adatom (indicated by arrows) were found to be located on top of the Mo (i), S (ii), and hollow-center site (iii), respectively. (d) LDOS of the Au dopant atoms at their considered atomic structures. The blue and red plots are for the spin up and spin down components, respectively. The filled curves indicate occupied states. Panels (c) and (d) were adapted and modified with permission from ref 356. Copyright 2014 John Wiley & Sons, Inc.

tune the electronic structure of the host matrix is an Au single atom/monolayer MoS_2 hybrid.^{356,357} For example, Lin et al. prepared Au dopants on the surface of a MoS_2 monolayer and confirmed the position of Au adatoms can be on top of the Mo, S, and hollow-centers (HC) of MoS_2 in the TEM image (Figure 18c). To investigate the impact of Au adatoms on the electronic structure of 2D MoS_2 , the authors simulated local density of states (LDOS) around Au adatoms on MoS_2 (Figure 18d). The LDOS around Au adatoms at the Mo, S, and HC sites exhibit the gap states inside the bandgap of MoS_2 , which can act as p-type doping sources to compensate the n-type nature of MoS_2 . Recently, Liu et al.³⁵⁷ reported a spontaneous defect-free functionalization method consisting of attaching Au single atoms to monolayers of semiconducting MoS_2 by using S-Au-Cl coordination complexes and confirmed the doping effect of Au single atoms with MoS_2 FETs. The output characteristics of the Au- MoS_2 BGFETs showed that the Au single atoms led to the transfer of electrons from MoS_2 to Au, as the threshold voltage was shifted toward negative voltages with Au dopants, which introduced p-type doping to the functionalized MoS_2 monolayers.³⁵⁷ Moreover, the degree of n- and p-type doping in the MoS_2 matrix can be finetuned by choosing the transition metal single atom attached and by varying their concentrations, thus controlling the electronic band structure of MoS_2 .³⁵⁸

4.2. 2D/3D Heterojunction Devices. The advent of 2D materials has attracted considerable attention in design

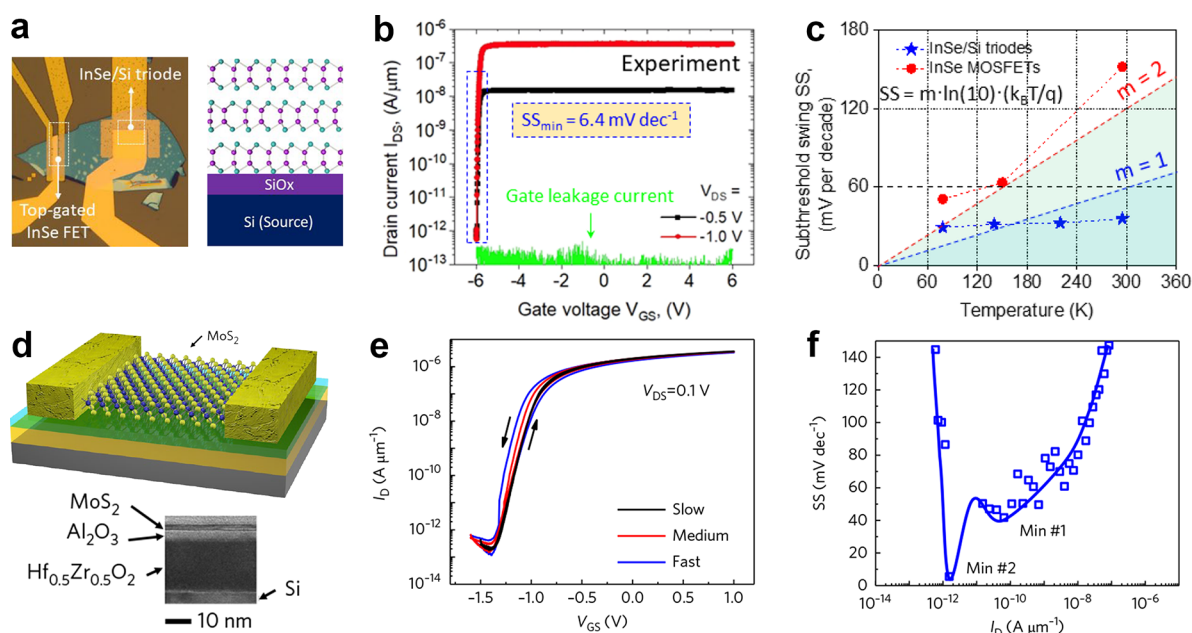


Figure 19. 2D/3D heterojunctions for logic devices. (a) 3D schematic of a 2D/3D TFET based on 2D n-type InSe and 3D p++ Si. (b) the 2D/3D heterojunction TFET was observed to have as an average SS of 34 mV/decade over four decades of drain current with a minimum SS of as low as 6.4 mV/decade. (c) Extracted SS versus temperature in InSe/Si 2D/3D heterojunction TFET. Panels (a)–(c) were reproduced with permission from ref 366. Copyright 2022 Springer Nature. (d) Schematic view of HZO/MoS₂ NCFET. (e) Transfer characteristics of the HZO/MoS₂ NCFET measured at room temperature and at drain voltage of 0.1 V at different gate voltage sweep speeds. (f) Extracted SS versus drain current in the HZO/MoS₂ NCFET. Panels (d)–(f) were reproduced with permission from ref 369. Copyright 2018 Springer Nature.

exploration for highly scaled FETs, thanks to the enhanced electrostatic control over bulk 3D semiconductors due to their atomically thin bodies and self-passivated surfaces.^{359,360} However, introduction of 2D materials is quite challenging since high material quality, stable, complementary doping are not readily available for them, while Si and III-V technology is very much established in terms of doping type and doping density control.^{361,362} Hence, it is natural to explore 2D semiconductors and 3D bulk semiconductors as complementary counterparts in next-generation logic device architectures. In this regard there have been considerable efforts by the community for the exploration of 2D/3D heterojunctions for next-generation logic and memory devices.

4.2.1. Logic Devices. A fundamental thermionic limit defined by the so-called Boltzmann tyranny of the subthreshold slope (SS) at 60 mV dec^{−1} in single band transport devices such as metal-oxide-semiconductor FET (MOSFETs) not only precludes further scaling down the supply voltage but also increases overall power density and consumption in MOSFET-based circuits.³⁶³ Tunneling field-effect transistors (TFETs) is the primary approach to overcome the fundamental thermionic limits, in which the current conducts through band-to-band tunneling (BTBT) rather than the thermionic emission in single band transport devices.³⁶⁴ To allow strong direct BTBT transport, TFET devices are normally made of p-i-n homo or heterojunctions in which the intrinsic layer should have superior tunability subject to electrostatic modulation and ease of miniaturization in lateral dimensions.³⁶⁵ 2D semiconductors have great electrostatic control due to their ultrathin body and low static dielectric constants, which makes them ideal candidates for the intrinsic region of the TFET devices. However, unlike 3D semiconductors, the lack of stable and complementary doping in 2D materials makes the “all-2D” vdW heterojunction not compelling for the TFET device config-

uration. Hence, it is natural to combine 2D semiconductors with 3D bulk semiconductors for exploring next-generation TFET architectures, in which 2D semiconductors work as the intrinsic region and the heavily doped regions are made of 3D bulk semiconductors. Miao et al.³⁶⁶ recently reported a 2D/3D heterojunction TFET as shown in Figure 19a, in which the heterojunction was made of unintentionally n-doped 2D-InSe and heavily doped (p++) Si. As shown in Figure 19b, the 2D/3D heterojunction TFET was observed to have as an average SS of 34 mV/decade over four decades of drain current with a minimum SS of as low as 6.4 mV/decade, which are both below the fundamental thermionic limit at 60 mV/decade. Further, the devices showed a high current on/off ratio of 10⁵ for sub-60 mV/decade and a high on-state current density of 0.3 μA/μm, while most other TFETs including ones made using 2D/3D junctions have long been limited by low on/off ratios for sub-60 mV/decade operation and low on-current density.^{367,368} The extracted SS slope in Miao et al. is nearly independent of temperature (Figure 19c),³⁶⁶ which unambiguously confirmed that the observed transport in the InSe/Si heterojunction TFETs was dominated by BTBT.

Another mechanism for inducing steep SS (<60 mV/dec) switching is by adding a ferroelectric thin layer to the gate stack of a MOSFET, which is so-called negative-capacitance FET (NCFET).³⁷⁰ In a NCFET, the semiconductor channel surface potential can be amplified more than the gate voltage as the ferroelectric thin layer contributes a negative capacitance, which leads to a SS < 60 mV dec^{−1} at room temperature in the device.^{369,370} However, it remains challenging to design a stable NCFET by proper design of capacitance matching to simultaneously achieve the steep SS and the nonhysteretic *I*–*V* characteristics. 2D semiconductors may offer a promising solution to those challenges, thanks to their low static dielectric constants, flatness of the body capacitance, and compatibility to

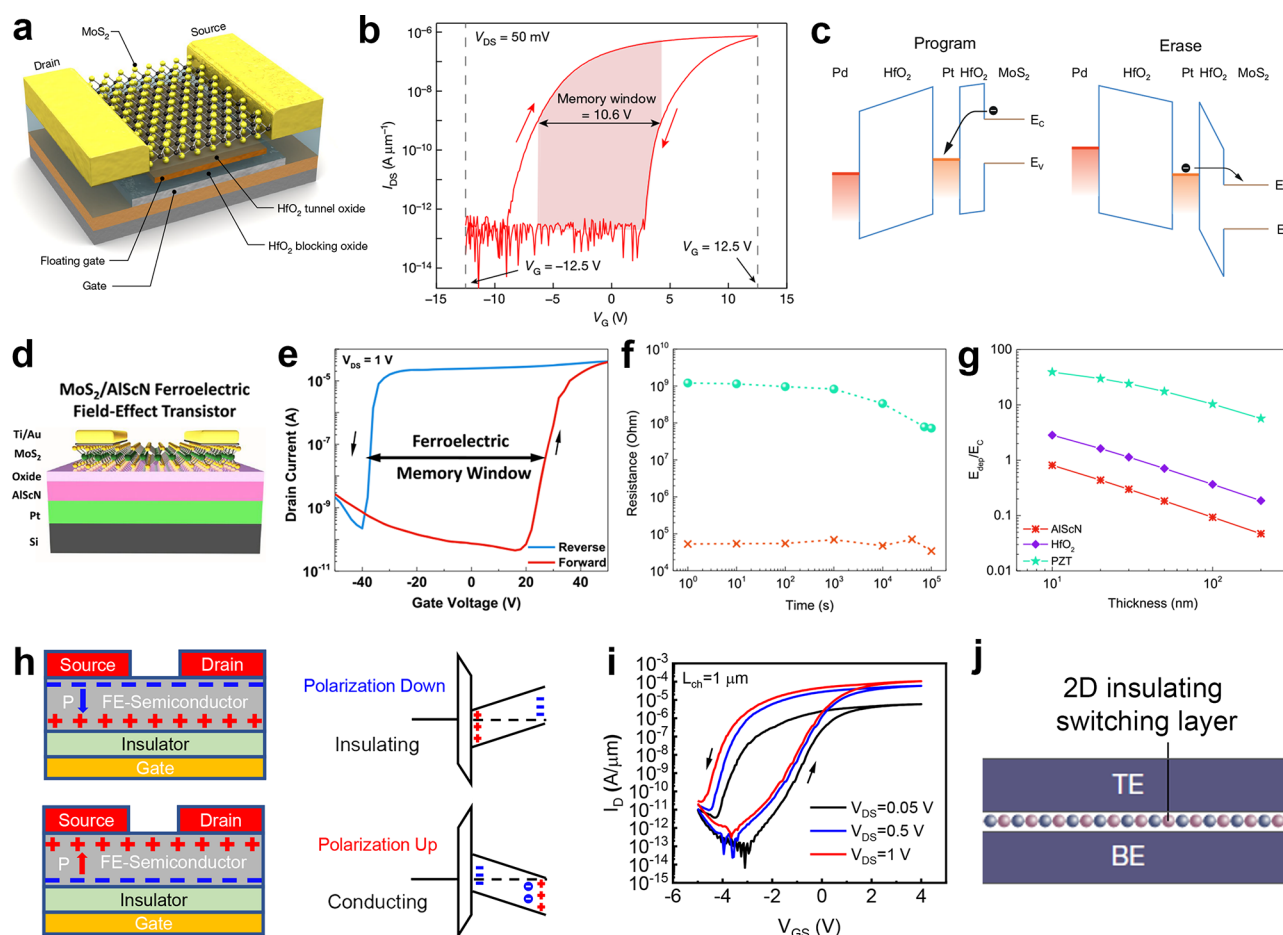


Figure 20. 2D/3D heterojunctions for memory devices. (a) 3D schematic of a FGFETs device based on MOCVD-grown monolayer MoS₂. (b) Transfer characteristic of the FGFET acquired for two different gate voltage sweep directions, showing a memory window of 10.6 V when observing at 1 nA constant current. (c) Simplified band diagrams of MoS₂ FGFETs for both programming (left panel) and erasing (right panel). Reproduced with permission from ref 374. Copyright 2020 Springer Nature. (d) Schematic view of a AlScN/MoS₂ FE-FET. (e) Transfer characteristic of the AlScN/MoS₂ FE-FET acquired for two different gate voltage sweep directions, showing a memory window more than 4 MV/cm. (f) Retention measurement on AlScN/MoS₂ FE-FET by monitoring the drain current for varying time intervals up to 10⁵ s. (g) Calculated ratio of depolarization field over coercive field in three different MoS₂ FE-FET cases: (1) AlScN/MoS₂; (2) HfO₂/MoS₂; (3) PZT/MoS₂. Reproduced with permission from ref 375. Copyright 2020 American Chemical Society. (h) Polarization charges distribution (left) and band diagram (right) in a FeS-FET in polarization down and polarization up states. (i) The demonstrated FeS-FETs showed a high on/off ratio of over 10⁸ and a large memory window of over 1 MV/cm. Reproduced with permission from ref 376. Copyright 2019 Springer Nature. (j) Illustration of an atomristor consisting of a mono or few layer TMD or h-BN sandwiched between conducting electrodes. The structure can produce nonvolatile memory effect. Reproduced with permission from ref 377. Copyright 2019 Springer Nature.

the junction-less transistor architecture. Recently, Si et al.³⁶⁹ reported a 2D steep-slope transistor by using MoS₂ as a semiconductor channel and a 2D ferroelectric hafnium zirconium oxide layer (HZO) in the gate dielectric stack (Figure 19d). As shown in Figure 19e, the demonstrated MoS₂ NCFET showed a steep-slope in both forward sweep and reverse sweep and it was also observed to exhibit near hysteresis-free transfer characteristics, which indicates a good capacitance matching by using an atomic thin channel in a NCFET. The SS was extracted for both forward sweep (average SS \approx 52.3 mV dec⁻¹) and reverse sweep (average SS \approx 57.6 mV dec⁻¹) and those two values <60 mV dec⁻¹ indicated subthermionic subthreshold slope has been overcome and provided strong evidence that the observed steep SS is the result of a NC effect (Figure 19f).

4.2.2. Memory Devices. The discussed advantages of 2D semiconductors not only manifest themselves in highly scaled and energy efficient logic devices and circuits but also make them appealing for transistor-backed emerging memory

technologies such as Static Random-Access Memory (SRAM), Dynamic RAM (DRAM), and Floating-Gate FET (FGFET).^{371–373} Marega et al.³⁷⁴ reported a floating-gate memory device based on a junction-less transistor architecture with wafer-scale 2D MoS₂ as the channel and an additional metal gate as the floating gate in the gate stack, as shown in Figure 20a. The gate stack (from the bottom to the top) was comprising of a bottom control gate, a 30 nm-thick 3D HfO₂ blocking oxide layer, the floating gate, a 7 nm-thick HfO₂ tunnel oxide layer, and the MoS₂ channel. The distinguishable memory states in FGFET memory are achieved by the programmable transistor threshold voltage controlled by the amount of charge stored in the 3D charge trap layer. The total shift of the memory threshold voltage was estimated to be a memory window of 10.6 V, when observed at 1 nA (Figure 20b). Further, the authors also demonstrated that various logic operations can be directly performed using the reconfigurable memory elements. Programming of the FGFETs (positive shift in the threshold

voltage) is achieved by injecting electrons into the floating gate with the application of a positive voltage pulse on the gate; erase of the FG-FETs (negative shift in the threshold voltage) is achieved by extracting electrons from the floating gate with the application of a negative voltage pulse on the gate (Figure 20c).

The ferroelectric FET (FE-FET) is another emerging memory technology that could take advantage of the 2D semiconductor-based junction-less transistor architecture when integrated with 3D crystalline ferroelectric dielectrics. In FE-FETs, the information is stored by the amount of remnant polarization in a ferroelectric layer, which controls the transistor threshold voltage in the device.³⁷⁸ Despite their emergence in 1963, subsequent efforts to produce a practical, compact FE-FET have been plagued by poor retention due to large depolarization fields and incompatibility with CMOS process integration.³⁷⁹ By implementing 2D semiconductors as the channel to the FE-FETs, the depolarization fields can be minimized because of their low dielectric constants, fully depleted ultrathin bodies, and the flatness of the body capacitance. In addition, due to the absence of the surface dangling bonds, vdW 2D semiconductors such as MoS₂ can be transferred via wet- or dry-transfer schemes onto arbitrary substrates at room temperature, which makes them a great candidate for transistor channel in CMOS front end of line (FEOL) and BEOL process compatible technology. Among 2D/3D FE-FETs, Liu et al.³⁷⁵ has recently reported high-performance devices that integrates an atomically thin MoS₂ channel on top of a 3D wurtzite structure AlScN ferroelectric (Figure 20d). The devices showed a normalized memory window of 3 MV/cm and concurrently a current on/off ratio of near 10⁶, stable memory states up to 10⁴ cycles and state retention up to 10⁵ s as shown in Figure 20e,f. 2D semiconductor channel combined with large coercive field 3D ferroelectrics^{380,381} can present as an ideal scenario for long retention in FE-FETs, as shown by the calculated ratio of depolarization field over coercive field in three different FE-FET cases in Figure 20g. By theoretical simulations, Liu et al.³⁷⁵ also show that the ratio of the depolarization field over the coercive field can be less than 1, while keeping a wide and stable memory window, even the AlScN ferroelectric layer is scaled down to 10 nm, which makes them ideal also for high voltage scaled devices.

As discussed above, the depolarization field combined with cycling endurance are two of the main issues slowing down the commercialization of FE-FETs in nonvolatile memory applications. Another option to potentially minimize the effects of the depolarization field is by using ultrathin ferroelectric semiconductors as the channel material in the ferroelectric transistor rather than using ferroelectric dielectric as gate material. Si et al.³⁷⁶ reported a ferroelectric semiconductor FET (FeS-FET), in which the polarization that stores the information in the FeS-FETs exists in the α -In₂Se₃ ferroelectric semiconductor. Although FE-FET and FeS-FET have similar counter-clock hysteresis loops in their transfer curve, the operation mechanism of a FeS-FET (Figure 20h) fundamentally differs from a FE-FET: in a FeS-FET, the polarization charges accumulate at both the bottom- and top-surface of the 2D ferroelectric semiconductor, and they simultaneously determine the drain current due to the ultrathin body of the 2D ferroelectrics semiconductor, while only the polarization charges at the ferroelectric/semiconductor interface play a role in the electrostatics. The demonstrated FeS-FETs showed a high on/off ratio of over 10⁸ and a large memory window of over 1 MV/cm with a low operation voltage as shown in Figure 20i.

In addition, 2D materials such as TMDs and h-BN are suitable to realize vertical memristors consisting of one or more layers sandwiched between 3D conductive electrodes.^{382–384} These memristors are sometimes referred to as atomristors (Figure 20j), a colloquial term to describe resistance switching effect in an atomically thin material, with monolayer h-BN representing the thinnest memristor active layer.³⁸⁵ Since the initial atomristor report in 2017,³⁸² there have been much progress in advancing the understanding, performance, and applications of these memory devices. Atomic-resolution studies reveal that metal ion adsorption into native vacancy defects in 2D monolayers are responsible for nonvolatile resistance switching effect, arising from a phenomenon termed virtual conductive point effect,³⁸⁶ an atomic scale version of conductive bridge effect in conductive bridging random access memory (CBRAM) devices. Hence, the atomristor effect can be considered an application of defect, otherwise known as defectronics, where defect engineering can be utilized to optimize device performance.³⁸⁷ It is likely alternative mechanisms could also result in a memristor effect including conductive-bridge formation from metal diffusion along GBs in few-layer 2D materials to more exotic atomic distortions that can trigger resistance switching.^{388–391}

The performance of 2D memristors has similarly progressed over the past years with demonstrations of low switching energies, low switching voltages, and low switching currents suitable for diverse applications.^{384,392–394} In terms of reliability, a months-long retention has been demonstrated with the potential for indefinite retention with engineered devices and interfaces.³⁹⁵ The endurance of 2D memristors is still at a nascent stage with current cyclability in the 100 to 1000 s of switching cycles for mono or few layers.³⁹² Thicker films of TMDs with partial oxidation have afforded more than a million cycles.³⁹⁶ For applications, wafer-scale demonstration of cross-bar arrays for artificial neural networks for neuromorphic computing have been reported with character recognition approaching the accuracy limit.³⁹² Likewise, nonvolatile switches for high-frequency applications in the 5G and 6G communication spectrum with a bandwidth up to around 500 GHz and data transmission of 100 Gb/s has been reported.^{395,397}

5. Magnetic Topological Insulators and Twisted vdW Heterostructures. **5.1. *MnBi₂Te₄: An Intrinsic Magnetic Topological Insulator.*** Research on quantum materials has been at the frontiers of materials science and condensed matter physics since exotic functional properties of quantum materials are not only fundamentally important but also have wide prospects for applications in information and energy technologies. Magnetic topological insulators are a type of recently discovered quantum materials in which a combination of magnetism and nontrivial band topology can create a variety of topological quantum states, such as a quantum anomalous Hall insulator (QAH) and an axion insulator.³⁹⁸ Since QAH can support dissipationless charge transport without an external magnetic field, it carries great promise for applications in energy-saving electronic and spintronic devices. Although magnetic doping into topological insulators (TIs) and the interface magnetic proximity effect in heterostructures have been employed to demonstrate the QAH, the chemical inhomogeneity of magnetic doping leads to small exchange gaps,^{399,400} thus limiting the working temperature of the quantum anomalous Hall state. This disadvantage has inspired the search for topological materials with intrinsic magnetism.

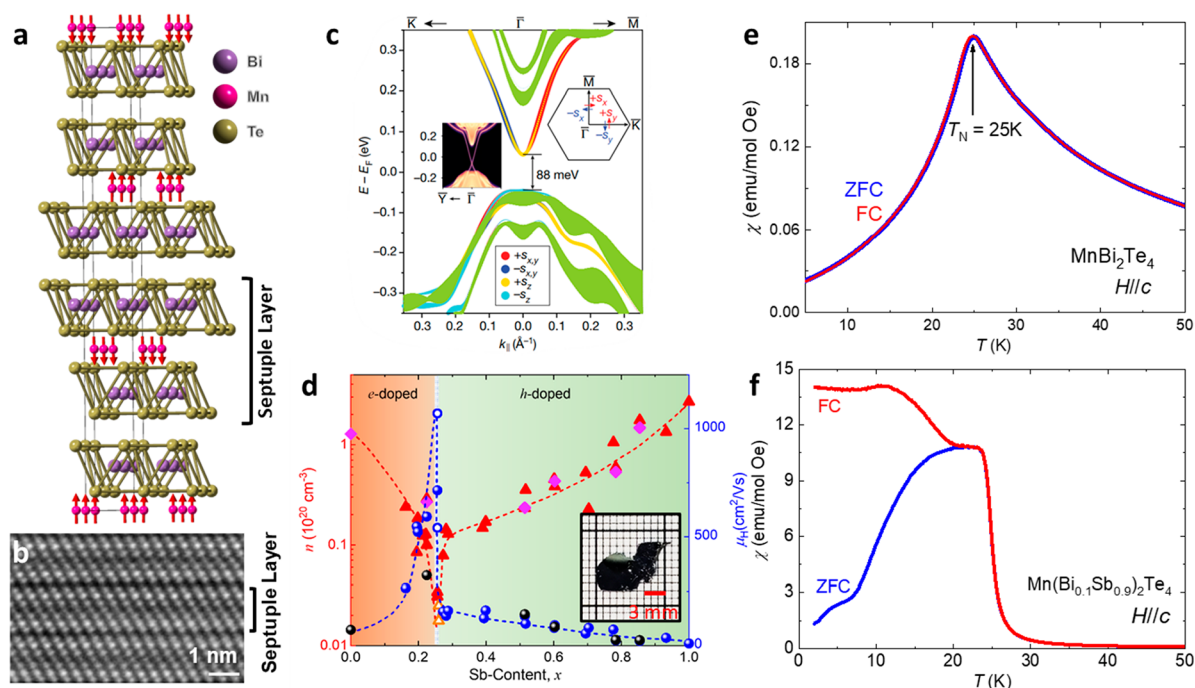


Figure 21. Crystal and magnetic properties of magnetic TIs. (a) Crystal and magnetic structure of MnBi_2Te_4 . (b) HAADF-STEM image taken from the $[100]$ zone axis of MnBi_2Te_4 . Reproduced with permission under a Creative Commons Attribution 4.0 International license from ref 404. Copyright 2019 American Physical Society. (c) Spin-resolved electronic structure of the MnBi_2Te_4 (0001) surface. Reproduced with permission from ref 401. Copyright 2019 Springer Nature. (d) Composition dependence of carrier density n and transport mobility μ_H of $\text{Mn}(\text{Bi}_{1-x}\text{Sb}_x)_2\text{Te}_4$. Inset: Flux-grown crystals' image. Reproduced with permission under a Creative Commons Attribution 4.0 International license from ref 410. Copyright 2021 American Physical Society (e, f) Field-cooled (FC) and zero-field-cooled (ZFC) temperature dependences of magnetic susceptibility χ with magnetic field aligned parallel to the c -axis ($H//c$) for (e) MnBi_2Te_4 ⁴⁰⁴ and (f) $\text{Mn}(\text{Bi}_{0.1}\text{Sb}_{0.9})_2\text{Te}_4$, respectively. Panel (f) was reproduced with permission from ref 411. Copyright 2020 American Physical Society.

MnBi_2Te_4 has recently been investigated as an emerging intrinsic magnetic TI.^{401–403} It is a layered ternary tetradyte compound, crystallizing in a rhombohedral structure with the space group $R\bar{3}m$, and its structure is built of the stacking of Te-Bi-Te-Mn-Te-Bi-Te septuple layers (SLs) along the c -axis (Figure 21a,b). Given that the SLs are coupled through the vdW force, MnBi_2Te_4 can be easily exfoliated into thin flakes. This material exhibits an antiferromagnetic (AFM) order below $T_N = 25$ K (Figure 21e), with in-plane ferromagnetic (FM) coupling and out-of-plane AFM coupling.⁴⁰⁴ Such a magnetic order is intimately coupled with band topology, which was predicted to yield a large exchange gap (Figure 21c) and various topological quantum states, as discussed below. Since MnBi_2Te_4 is a metastable phase, its crystal can be obtained only by quenching the crystals grown in the slowly cooling down process of the melt with a stoichiometric composition.^{401,404} However, single crystals grown using this method are small and thin. The other problem with this method is the presence of intergrowth between MnBi_2Te_4 and Bi_2Te_3 . Soon after, Yan et al.⁴⁰⁵ developed an effective growth protocol for growing large MnBi_2Te_4 crystals. They used Bi_2Te_3 as a flux to grow MnBi_2Te_4 crystals. Crystals grown using this flux method have significantly larger lateral dimensions (up to a few millimeters) and can be easily exfoliated, which is critical to nanodevice fabrications and exploration of emerging topological quantum states in its 2D limit. The availability of such high-quality crystals has enabled observation of various topological quantum states in MnBi_2Te_4 , including the QAHI, the axion insulator, the high number of Chern insulators ($C = 2$), as well as the layer Hall effect.^{406–409}

In addition to the 2D topological states noted above, MnBi_2Te_4 is also predicted to host a long-sought, ideal time-reversal symmetry breaking Weyl semimetal (WSM) with one pair of Weyl nodes in bulk when its AFM order is coerced into FM order by a magnetic field parallel to the c -axis.^{402,403} Zhang et al.⁴⁰² suggest that this FM WSM can be either type-I or type-II, depending on the lattice parameters. Recent theoretical studies further predict that such a Weyl state can be tuned by the field orientation but disappears as the field is rotated to the in-plane direction.⁴¹² However, there has been no experimental evidence that supports the presence of the Weyl state in the FM phase driven by the c -axis magnetic field in MnBi_2Te_4 . This is because the Weyl nodes are far from the Fermi surface due to self-doping effects in pristine MnBi_2Te_4 .^{404,405}

Several groups have shown that it is possible to tune the chemical potential of MnBi_2Te_4 by doping Sb to the Bi site, similar to the $(\text{Bi,Sb})_2\text{Te}_3$ system.^{410,413–415} Lee et al.⁴¹⁰ have shown that single crystals of $\text{Mn}(\text{Bi}_{1-x}\text{Sb}_x)_2\text{Te}_4$ (MBST, $0 \leq x \leq 1$) with controlled chemical potentials can be grown using Sb_2Te_3 - Bi_2Te_3 as a flux, similar to the growth protocol reported by Yan et al.⁴¹⁴ To achieve a desired chemical potential, the Sb concentration and the temperature for centrifuging need to be tuned to appropriate values. Empirically, large MBST single crystals with lateral dimensions being up to 10 mm can be grown using the molar ratio of Mn:Sb:Bi:Te in $1:5x:5(1-x):16$.^{410,413} Carefully tuning of the centrifugation temperatures for each x is critically important since the melting points of both fluxes and $\text{Mn}(\text{Bi}_{1-x}\text{Sb}_x)_2\text{Te}_4$ are very close. Given that the melting points of Bi_2Te_3 and Sb_2Te_3 are 585 and 620 °C, respectively, the excessive flux is separated by centrifuging in the range of 585 to

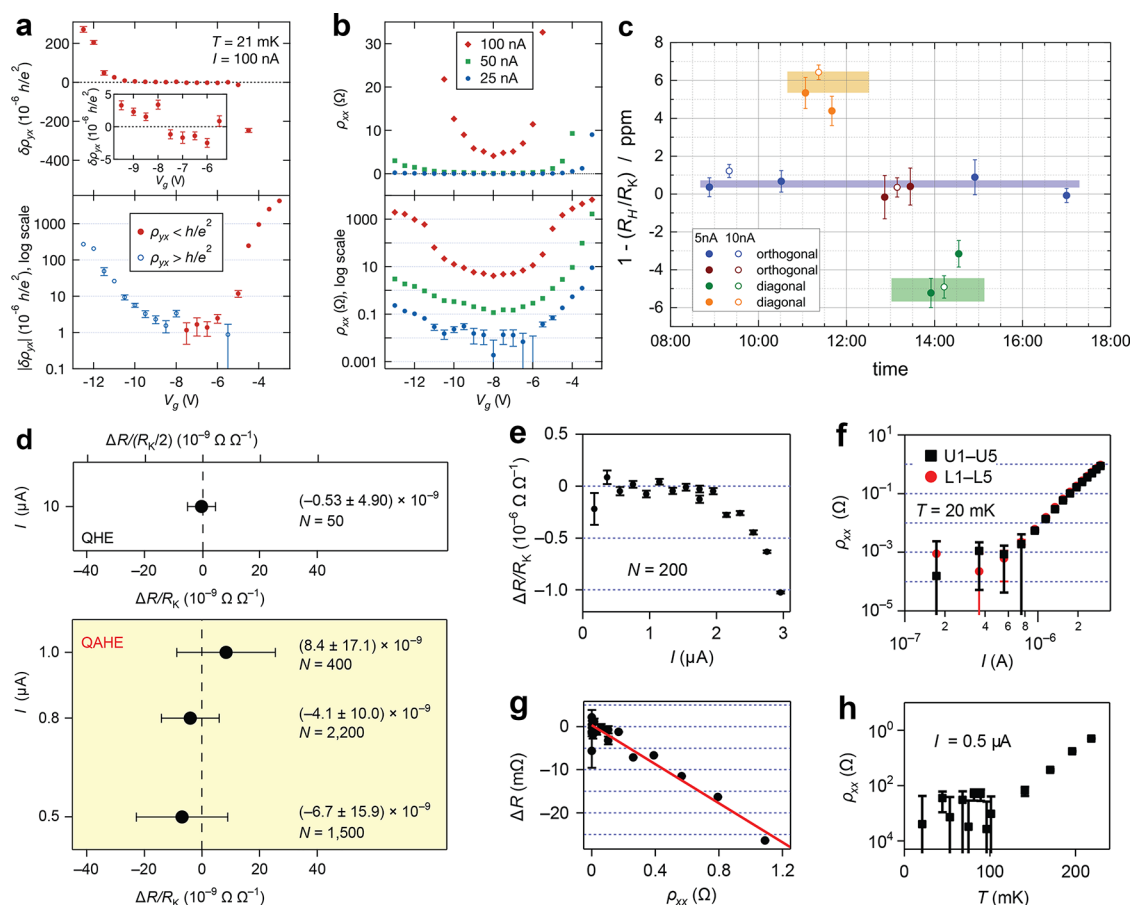


Figure 22. Summary of QAHE measurements of MTI-based films. (a) Cryogenic current comparator data are shown for Hall measurements in an example device using a 100 nA current at 21 mK. The plateau in the upper panel shows the deviation from R_K . The inset shows a magnified view of the Hall resistance deviations in the center of the plateau ($\nu = 1$). The bottom panel shows the logarithmic behavior of the deviations as one departs from the optimal gate voltage. (b) The longitudinal resistivity for the same device. Data are displayed on a linear and log scale in the top and bottom panels, respectively. All error bars show the standard uncertainty and are omitted when they are smaller than the data point. Reproduced with permission from ref 425. Copyright 2018 by the American Physical Society. (c) Topological insulator at the $\nu = 1$ plateau data. Currents of 5 and 10 nA were used in both orthogonal and diagonal configurations. The colored rectangles represent the weighted average and standard deviation of the data from those configurations. Reproduced from ref 423 with the permission of AIP Publishing. (d–h) Quantization accuracy of the QAHE-based resistance standard. (d) The normalized deviation $\Delta R/R_K$ are shown (top panel shows conventional quantum Hall effect). The error bars correspond to the combined standard uncertainty and N denotes the number of data points used for averaging. (e) The dependence of $\Delta R/R_K$ on the source-drain current (I) is shown, with the error bars corresponding to the standard deviation of $N = 200$ measurements. (f) The current dependence of the longitudinal resistance (ρ_{xx}) is shown at a temperature of 20 mK. The longitudinal resistivity was measured by using the upper (U1–U5) and lower (L1–L5) pairs of voltage contacts. The error bars are the standard deviation of $N = 20$ measurements. (g) The relationship between ΔR and ρ_{xx} shown with a red line as the linear fitting result. (h) Temperature dependence of ρ_{xx} measured at 0.5 μ A using the upper pair of voltage contacts (U1–U5). The error bars are the standard deviation of $N = 20$ measurements. Reproduced with permission from ref 424. Copyright 2022 Springer Nature.

620 °C, depending on x . Higher centrifugation temperatures are used for the samples with higher Sb content. It is worth noting that ramping down quickly below the solidification temperatures and then ramping up to the desired centrifugation temperature in higher Sb-content alloy can lead to high density of Mn occupation at the Sb sites (e.g., antisite defects), which favors a ferromagnetic exchange between Mn layers.^{411,416–418}

While MnBi_2Te_4 is electron-doped, as the Sb concentration increases, the chemical potential of $\text{Mn}(\text{Bi}_{1-x}\text{Sb}_x)_2\text{Te}_4$ is tuned from the bulk conduction band to the bulk valence band passing through the charge neutral point near x equal to 0.3. Through fine-tuning of chemical potential by Sb substitution for Bi, Lee et al.⁴¹⁰ observed transport hallmarks of the predicted ideal Weyl state in the lightly hole-doped samples with $x = 0.26$ (Figure 21d), including a large intrinsic anomalous Hall effect and chiral anomaly. The Weyl state in $\text{Mn}(\text{Bi}_{1-x}\text{Sb}_x)_2\text{Te}_4$ is of particular

interest because it is the least complicated possible manifestation of a Weyl phase, hosting only one pair of Weyl nodes at the Fermi level and having no interference from other trivial bands near the Fermi level. Therefore, it is an ideal model system for further study of Weyl Fermion physics. The magnetic phase of $\text{Mn}(\text{Bi}_{1-x}\text{Sb}_x)_2\text{Te}_4$ is also dependent on Sb concentration. For $x < 0.9$, the systems exhibit an A-type AFM order similar to that seen in the pristine compound MnBi_2Te_4 . However, for $0.9 \leq x \leq 1.0$, an FM phase with $T_c = 26\text{--}46$ K (Figure 21f) is accessible due to the Mn-Sb antisite defect-mediated layered FM coupling, as noted above.^{416–418} The realization of the FM phase in MBST is an important step toward understanding intrinsic ferromagnetic topological insulators, which opens up opportunities for engineering topological states in this vdW ferromagnet and related family members $\text{MnBi}_{2n}\text{Te}_{3n+1}$.

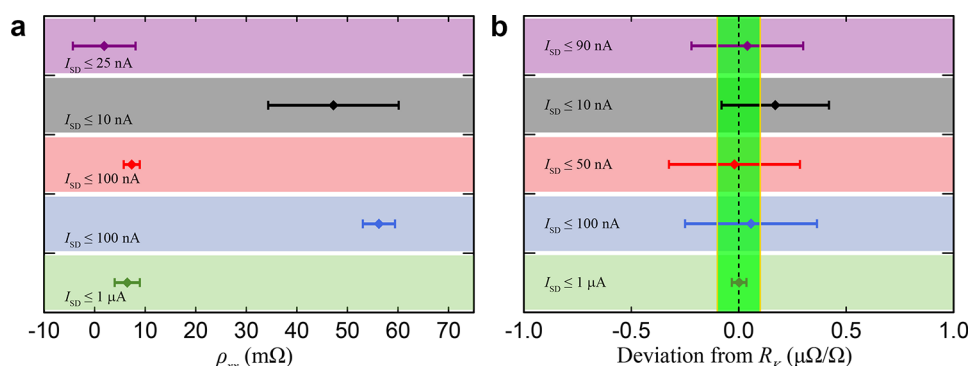


Figure 23. Summary of the precision measurements of (a) ρ_{xx} and (b) the QAHE over the previous few years. Applied currents vary, and the following MTI measurements are represented: 2018 NIST/Stanford (purple),⁴²⁵ PTB/UW (black),⁴²³ 2022 NIST/Stanford (red and blue),⁴²⁸ and 2022 NMIJ and partners (olive).⁴²⁴ The light green region in panel (b) marks the boundary for data points going beneath one part in 10^7 . All error bars represent $k = 1$ type A and B combined uncertainties. Adapted with permission under Creative Commons Attribution 4.0 International license from ref 428. Copyright 2022 American Physical Society.

5.2. Quantum Anomalous Hall Effect in Magnetically Doped Topological Insulators. The quantum Hall effect has been in the eye of the scientific community for nearly half a century, and materials hosting a 2D electron system could exhibit it. Graphene and gallium arsenide heterostructures were among the more popular material systems for performing quantum Hall research. Many applications of the quantum Hall effect, notably electrical metrology, have required strong magnetic fields for the quantized plateaus to be exhibited in a robust way.⁴¹⁹ This requirement has limited the extent to which an experimental apparatus may be simplified, namely in the necessity of an electromagnet. Emerging thin materials, like magnetically doped topological insulators (MTIs), are known to exhibit the quantum Hall effect at zero magnetic field. This phenomenon, known as the quantum anomalous Hall effect (QAHE), is linked to the breaking of time-reversal symmetry and the opening of an energy gap that can accommodate the existence of topological surface states.^{420–422}

Under typical circumstances, the formed energy gap closes in physical locations where the component of the magnetization normal to the surface changes direction. This implies that for material systems nearing the 2D limit, assuming they have relatively uniform out-of-plane magnetization, this transition occurs at the edges of the material system. Therefore, the edges of a suitable material system would then enable the QAHE to be exhibited and observed. Electrically, its longitudinal transport would be ideally dissipationless given that its corresponding quantization conditions are $\sigma_{xy} = e^2/h$ and $\sigma_{xx} = 0$. Thus, in the context of metrology, the QAHE could become the basis for a future resistance standard, at most needing only a small permanent magnet to activate a quantized resistance value.^{423–425} Ultimately, such metrologically suitable devices could operate at zero-field for measurements, making the dissemination of the ohm more economical and portable.

The details of how the QAHE arises are obviously more nuanced when compared with the conventional integer quantum Hall effect. As summarized by Kou et al.,⁴²⁶ there are two main approaches for introducing magnetic exchange that allows one to break surface states' time-reversal symmetry. The first approach is by means of magnetic proximity, typically achieved by adding in a topologically trivial magnetic material, which locally aligns the relevant electrons' spin moments out of plane. The second approach involves the incorporation of magnetic ions into the host material system.⁴²⁰ Currently, MTIs

that are used in electrical metrology have been grown by MBE,⁴²⁷ presumably due to the method's advantages vis-à-vis its nonequilibrium physical deposition, accurate layer thickness and doping control, and wafer-scale growth capability.

As mentioned earlier, most quantum Hall applications based on graphene devices will generally need a sufficiently strong magnetic field to observe any robust quantum behavior. This limitation is inherently tied to the band structure of graphene. However, with the QAHE, one may observe a physical manifestation of a material's topologically nontrivial electronic structure without needing an electromagnet to break time-reversal symmetry. There are several types of materials that exhibit the QAHE, with some being classified among the following categories: doped MTIs, intrinsic MTIs, and twisted vdW layered systems. Some key recent results involve materials that display a quantized resistance plateau at zero-field suitable for metrology measurements, with some recent work already mentioned.^{423,425}

Recent work by Fox et al.⁴²⁵ explored the metrological applicability of the QAHE in a MTI-based thin film. Using a cryogenic current comparator, or an apparatus that allows for the precise comparison of two electrical currents (and thus, two resistances), the group measured the quantization of the Hall resistance to within one part per million and, at smaller electrical currents, measured the longitudinal resistivity to be under 10 mΩ at zero magnetic field. Some of these acquired data are shown in Figure 22a,b. A breakdown of the quantized state was induced by gradually increasing the current density past a critical value. It was thought that this effect was due to electron heating in parallel bulk current flow. This work furthered the understanding of MTIs by gaining comprehension for the physical mechanisms that ultimately contribute to these devices' limitations, including thermal activation, bulk dissipation, and variable-range hopping. Gotz et al.⁴²³ also sought to present a metrologically comprehensive measurement at zero-field of a MTI (in this case, it was V-doped $(\text{Bi,Sb})_2\text{Te}_3$). When the difference of the QAHE resistance was measured as compared to the von Klitzing constant (R_K), a value of $0.176 \mu\Omega/\Omega \pm 0.25 \mu\Omega/\Omega$ was obtained. Some of these data are shown in Figure 22c.

Two other recent works surrounding MTIs and the quality of their exhibited QAHE plateaus come from Okazaki et al. and Rodenbach et al.^{424,428} In the former, the group demonstrates a precision of 10 nΩ/Ω for the $\nu = 1$ plateau of the QAHE.

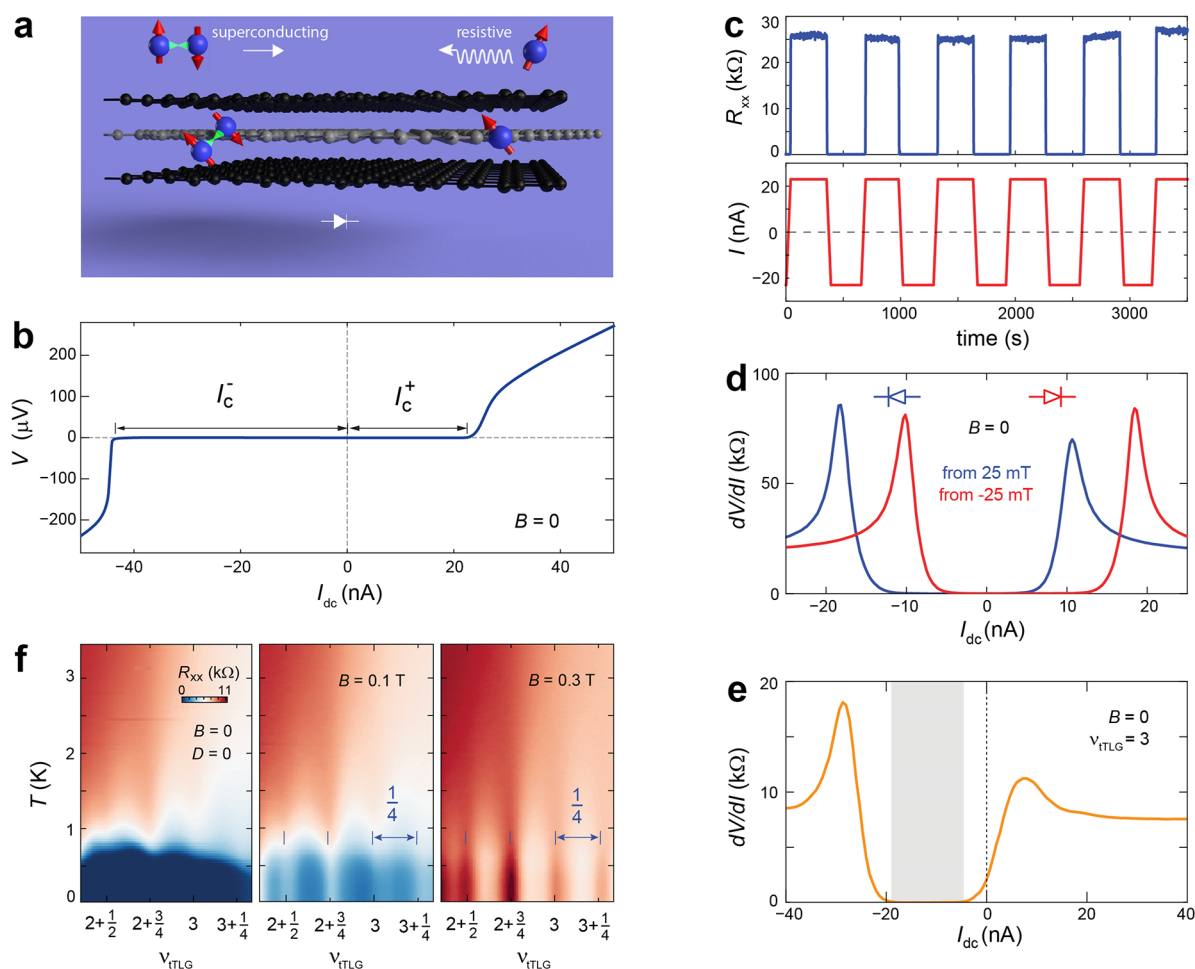


Figure 24. Nonreciprocity and superconducting diode effect. (a) Schematic diagram showing the superconducting diode effect. Cooper pairing is only stable when current flows from left to right. As a result, the transport response across the sample is dissipationless when current flows from left to right, whereas a resistive behavior is observed when current direction is reversed. (b) Differential resistance as a function of DC current bias of the superconducting phase at $B = 0$. I_c^+ and I_c^- are the critical current with positive and negative DC current bias, respectively. The asymmetry in I_c^+ and I_c^- shows the nonreciprocity. (c) Demonstration of robust zero-field superconducting diode effect. (d, e) Field-training of the superconducting diode: (d) After a positive (negative) field training, the superconducting diode remains as a reverse (forward) diode as shown in the blue (red) curve. (e) Extremely high diode efficiency at large doping, as the zero-resistance regime (shaded part) has shifted totally to the negative current side. (f) Interplay between superconductivity and density-wave state. Longitudinal resistance as a function of temperature and doping, at different magnetic fields. As the magnetic field increases, superconductivity is suppressed and density-wave state (resistance oscillations with $1/4$ periodicity) takes over at the low temperature range. Adapted with permission from ref 441. Copyright 2022 Springer Nature.

Furthermore, they directly compared both the QAHE and QHE from a conventional device to confirm their observations. These results are shown in Figure 22d–h. In Rodenbach et al.,⁴²⁸ extensive analyses on the surrounding elements of metrological measurements, namely noise measurements, are summarized and shown in Figure 23. These works are crucial to understand for eventually realizing a zero-field quantum resistance standard. One of the last remaining limitations to be lifted are the stringent temperature requirements, which are currently in the 10 to 100 mK range. Fijalkowski et al.⁴²⁹ show that the chiral edge channels associated with the QAHE continue to exist without applied magnetic field up to the Curie temperature (about 20 K) of bulk ferromagnetism in their TI system. This conclusion was reached through a careful analysis of nonlocal voltages in Corbino-type devices. It was also found that thermally activated bulk conductance was mostly responsible for quantization breakdown.⁴²⁹ These results show promise on the availability of

topological protection from MTI edge channels for developing a resistance standard.

5.3. Superconducting Diode Effect in Twisted Trilayer-Graphene Heterojunctions. Within BCS theory and for most known superconductors, time-reversal symmetry is a key ingredient to the formation of Cooper pairs.^{430,431} Nonetheless, superconductivity can survive moderate time-reversal symmetry breaking perturbations, e.g., resulting from the proximity to a ferromagnet or from an applied external magnetic field. The microscopic coexistence between superconductivity and ferromagnetism in a single electron liquid, however, is very rare in nature.^{432–434} Time-reversal symmetry also implies that the critical current for forward, I_c^+ , and backward direct current (DC) bias, I_c^- , are identical. If, however, it is broken in the superconductor along with inversion symmetry, $I_c^+ \neq I_c^-$ becomes possible. In that case, applying a DC current I_{DC} with $|I_{DC}|$ between I_c^- and I_c^+ , will lead to dissipationless superconducting transport for one sign of I_{DC} and resistive behavior for the other.

Such “superconducting diode” behavior has been reported in previous works where time-reversal symmetry is explicitly broken by applying an external magnetic field or proximitizing with a magnetic material.^{435–437} Alternatively, diode effect has been demonstrated in Josephson junctions.^{438–440} Notably, the superconducting diode effect at zero-field in a uniform, junction-free sample would be a strong indication of the microscopic coexistence between superconductivity and spontaneous time-reversal symmetry breaking. Such a zero-field superconducting diode effect was recently observed in small twisted angle trilayer graphene,⁴⁴¹ where the authors demonstrated a prominent diode effect that was intrinsic to the superconducting phase and could reach reasonably large current asymmetries, with $|I_c^+ - I_c^-|/(I_c^+ + I_c^-)$ approaching 1.

In the mirror-symmetric twisted trilayer graphene (tTLG) sample (Figure 24a), the middle graphene layer is rotationally misaligned with the outer layers by an angle of $\theta = 1.25^\circ$, which is detuned from the magic angle of 1.55° .⁴⁴¹ The zero-field superconducting diode is evidenced by the nonreciprocal current–voltage characteristic, as shown in Figure 24b. At $B = 0$, the superconducting critical current, defined as the peak position in the differential resistance dV/dI , is around 10 nA with forward biased current flow but increases dramatically to around 90 nA when the current flow is reversed. Such nonreciprocity enables a diode-like switching between dissipationless and resistive transport behaviors, when a DC current of 22 nA alternates between forward and reverse bias directions, as shown in Figure 24c. Notably, the alternating behavior remains robust for more than an hour, indicating that the zero-field superconducting diode effect is nonvolatile.

As shown in Figure 24d, the sign of nonreciprocity at zero-field can be reversed by training with an external magnetic field. After training with a negative magnetic field of -25 mT, which is then set to zero, the superconducting phase behaves like a forward diode, with the critical current being larger with a positive DC current bias. Conversely, a reverse diode behavior is observed after training with a positive magnetic field of 25 mT. The dependence on the magnetic field history offers unambiguous evidence for an underlying spontaneous time-reversal symmetry breaking. Moreover, a prominent diode effect is observed throughout the density regime of the superconducting phase, indicating an origin that is intrinsic to the moiré system.⁴⁴¹ An extreme nonreciprocal behavior can be achieved by tuning the carrier concentration of the system by electrostatic doping. As shown in Figure 24e, the sample is resistive at zero current bias but becomes superconducting in the presence of a negative DC current bias.

Since the presence of either time-reversal or 2-fold rotation/inversion symmetry guarantees reciprocal superconducting transport, the zero-field superconducting diode effect implies that both time-reversal and 2-fold rotation symmetry are broken in the superconducting state of the tTLG sample. The mechanism underlying the superconducting diode effect is therefore constrained by these broken symmetries, which can be understood by considering the possible symmetry-breaking instabilities of moiré electrons.⁴⁴¹ The simplest possible scenario is that the system spontaneously develops an imbalance of its two valleys, which breaks both of the aforementioned symmetries. Then, a superconducting phase emerging from a valley-imbalanced Fermi surface will exhibit a zero-field superconducting diode effect. Due to the multitude of internal “flavor” degrees of freedom—resulting from the spin, valley, and conduction-valence-band quantum numbers of the band

structure—there is a whole plethora of such possible candidate instabilities in tTLG.^{441,442} A careful consideration of the trainability of the observed diode effect⁴⁴¹ leaves only a single candidate phase that is symmetry-equivalent to the valley-imbalance case discussed above.

The zero-field superconducting diode effect is observed in the so-called small twisted angle regime. In stark contrast with the magic-angle regime, the phenomenon of Dirac revival is mostly absent in the small twist angle regime. Instead of correlated insulators appearing at every integer moiré filling, the moiré band is populated with density wave states that exhibit a density modulation of $1/2$ and $1/4$ moiré fillings. This gives rise to an interesting coexistence between the superconducting and density wave states. As superconductivity is suppressed by the application of an external magnetic field, a series of density wave states are evidenced by the observation of resistance peaks appearing at integer multiple of $1/4$ moiré filling,⁴⁴¹ as shown in Figure 24f. The onset temperature of these resistance peaks, which defines the melting transition of the underlying density wave order, coincides with the transition temperature of the superconducting phase. It is argued that these density-wave states likely compete against the superconducting state, since the critical temperature of the superconducting phase do not show the same density modulation as the density wave order. Nevertheless, the simultaneous presence of the density wave order and the superconducting phase in the phase space of the small-angle tTLG provides more constraints for theoretical models aiming to understand the origin of superconductivity in a graphene moiré band.

In summary, the intrinsic zero-field superconducting diode effect in small-angle tTLG demonstrates the microscopic coexistence of superconductivity and spontaneous time-reversal symmetry breaking. This discovery not only provides a platform with superconducting diode effect for potential applications but also draws our attention to the unique behavior of the superconductivity in this system and hopefully brings us closer to deciphering the nature of strongly correlated moiré physics.

5.4. Moiré Luttinger Liquids in Twisted WTe_2 Bilayers. The Luttinger liquid (LL) model^{443,444} offers a powerful tool to study interacting electrons in 1D metals, which are distinct from 2D or 3D metals that are typically captured by the Fermi liquid theory. An interesting question is whether the LL physics could be stabilized down to the lowest temperature in some strongly correlated 2D or 3D systems, as investigated by Philip W. Anderson.⁴⁴⁵ Approaches based on coupled-wire models,⁴⁴⁶ which consist of a 2D array of 1D LLs, have been developed to investigate this fundamental question theoretically.^{446–450} The experimental realization of high-quality arrays of 1D wires necessary for investigating various coupled wire models remains challenging as they require many identical wires to be strictly arranged with crystalline quality at both nano and microscopic scales. Experimental tests of many interesting ideas^{451–453} along this direction remain uncharted.

Significant experimental progress has been made recently based on 2D moiré quantum engineering. The study utilizes a unique moiré material consisting of twisted bilayer WTe_2 (t WTe_2).⁴⁵⁴ With an elongated rectangular unit cell, monolayer WTe_2 is known to exhibit rich physics including topology,^{455–457} superconductivity,^{458,459} and strong correlations.^{460,461} As shown in Figure 25a, 2D WTe_2 has a sandwiched structure, in which the middle layer hosts the W atoms that form 1D zigzag chains. Figure 25b illustrates the moiré superlattice of the t WTe_2 twisted at a small angle of near 5° (for simplicity, only

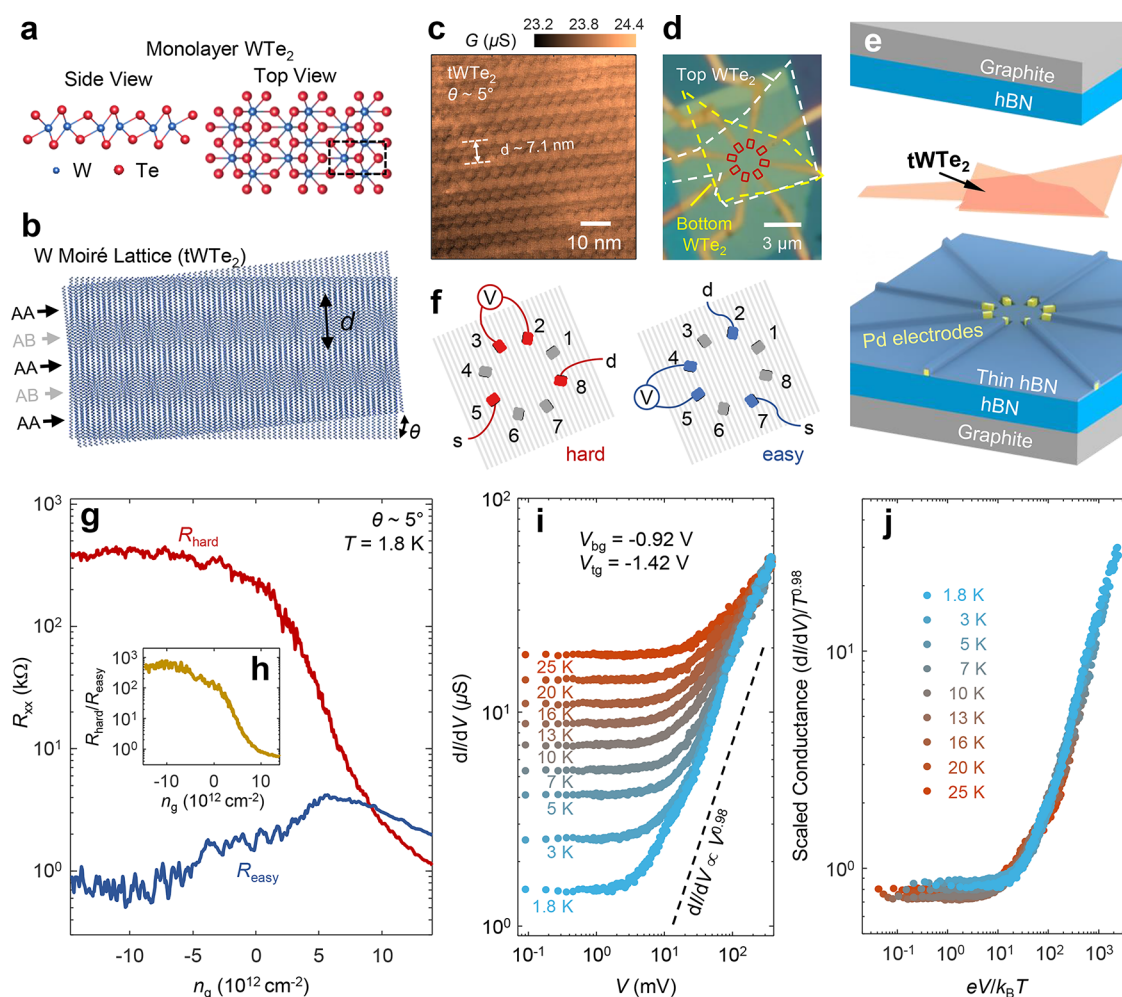


Figure 25. Luttinger liquid behavior in tWTe₂ moiré system. (a) The crystal structure for monolayer WTe₂. The W atoms are sandwiched by two Te atom layers. From the top view, the W atoms (blue) form zigzag chains. The dashed square denotes the unit cell. (b) Moiré superlattice of tWTe₂, where only the W atoms are shown. The alternating AA and AB 1D stripes are illustrated. (c) conductive AFM image of a tWTe₂ sample. (d) Optical image of a typical device, with the contact regions marked with red solid lines and the two layers of WTe₂ with yellow and white dashed lines, respectively. (e) Cartoon illustration of the device structure. From bottom to top: bottom graphite, bottom hBN, electrodes, thin hBN, tWTe₂, top hBN, and top graphite. (f) Measurement configuration for the hard and easy directions. The squares denote the contacts, and the gray lines indicate the moiré stripes. s, source; d, drain. (g) Four-probe resistance of the hard and easy direction shown in panel (f), measured at 1.8 K, as a function of the gate-induced doping density n_g of the device. (h) The anisotropy ratio, $R_{\text{hard}}/R_{\text{easy}}$ with R_{hard} and R_{easy} in g, versus n_g . (i) The across-wire differential conductance dI/dV measured under different d.c. bias and temperature, with the doping fixed on the hole side. (j) Scaled differential conductance $(dI/dV)/T^\alpha$, plot against $eV/k_B T$ (same data in panel (i)), showing that all the data collapse into one curve. Adapted with permission from ref 454. Copyright 2022 Springer Nature.

the two layers of W atoms of tWTe₂ are shown). Clearly, the moiré supercell is an enlarged rectangle, with a size tunable by twist angles. Figure 25c confirms the formation of such an anisotropic moiré pattern via a conductive atomic force microscopy image. Transport studies indeed revealed a highly anisotropic phase and LL behaviors in the hole-rich state of tWTe₂ devices near this twist angle.⁴⁵⁴ With carefully designed and fabricated devices (Figure 25d,e), Wang et al.⁴⁵⁴ showed that an exceptionally large transport anisotropy with a four-probe resistance ratio of close to 10^3 along the two orthogonal directions (Figure 25f) was observed in the hole-doped regime (Figure 25g,h) but not in the electron-doped regime. Moreover, the across-wire conductance obeys power-law dependence on temperature down to 1.8 K, and the differential conductance under varying applied d.c. bias and temperature shows the universal power-law scaling behavior (Figure 25i,j) expected for LL physics.⁴⁴³ Both the anisotropy and the interaction strength

are highly tunable in the tWTe₂ moiré structure, by knobs, e.g., doping density and twisted angle.⁴⁵⁴ The tWTe₂ system offers a high-quality, high-controllable platform for studying the intriguing physics related to various coupled-LL models.

An immediate question from the moiré LLs in the tWTe₂ is whether such a 2D anisotropic LL behavior could be stabilized down to millikelvin temperature, one crucial question in the study of non-Fermi liquid physics.^{447–449} An exciting future direction is to search for unconventional quantum oscillations and quantum Hall states in such a non-Fermi liquid system.^{450–452} The physics of spin-charge separation^{443,444} is another interesting direction to pursue here in such a 2D setting. Other predictions in coupled wire models, including topological phases⁴⁶² and quantum spin liquids,⁴⁶³ are also of potential future interest. On the material side, ventures in other rectangular moiré lattices, such as twisted GeSe,⁴⁶⁴ twisted T_d-MoTe₂, twisted phosphorene, T_d-MoTe₂/T_d-WTe₂ hetero-

structure, also deserve careful studies as they may develop similar phenomena.

PERSPECTIVES AND FUTURE WORK

This review provides the recent progress of theory, synthesis, heterostructures, characterization, sensing, devices, and physical properties of 2D materials. There continue to be many interesting breakthroughs in recent months and years, including MD simulations and machine learning for 2D materials synthesis and applications. Theory is becoming inseparable from experimental studies and is now key to design materials, predict device performances, and optimize processing. Additionally, remote epitaxy using 2D materials as the intermediate layer and wafer-scale synthesis of 2D TMDs by MOCVD also established their own fields and continue to emerge. However, as we are moving forward in 2D materials' science and technology, many challenges still require interdisciplinary efforts and collaborations to be addressed. For examples, some challenges regarding synthesis of high-quality 2D films and introduction of magnetic properties into TMDs have been mentioned in sections 2.7 and 2.9, respectively. Here, we provide perspectives on the future research directions that we may pursue.

Material Theory. Computationally we find that intercalation, doping, and defects provide an efficient platform for tailoring 2D materials' properties. However, for intercalation, there are still open questions about staging and cointercalation in common materials such as multilayer graphene, which could potentially provide further property control. Defects, on the other hand, can be difficult to simulate at the atomic level, especially when working with charged point defects, where long-range artificial interactions occur. There are several schemes that have been proposed to correct for this; however, it is still an unanswered question and requires continuous investigation.

Artificial Intelligence and Machine Learning for 2D Materials. While many solutions have been devised in the 2D material world with the utilization of ML, the field of condensed matter still has a lot of room to grow with these mathematical tools. As demonstrated in recent publications,⁵⁸ it becomes apparent that ML algorithms could conceivably be trained to refine potential energies in DFT calculations, suggesting a feasibility to derive a generalized exchange correlations through ML—arguably the holy grail of DFT work—thus reducing computational load and greatly increasing accuracy. In synthesis, Bayesian optimization (BO) seems to be the prevailing technique. Though, it could be noted that—with a high computational cost—it would be beneficial to migrate away from BO and toward neural networks. Unfortunately, without any training data or a large quantity of pre-existing samples, this is not possible. Therefore, a proposed solution could be to mimic the theoretical community in devising an open, centralized, and normalized database structure. In case of applications, availability of diverse ML tools on 2D materials and devices provides the exciting possibility that not only will we be able to improve traditional applications but also explore autonomous material synthesis and processing.

Optimizing ReaxFF Parameters with Guidance from Machine Learning. Developing the ReaxFF force field, like other empirical potentials, has been challenging due to the many-body character of the potential energy function and the high dimensionality of the force field parametrization. Obtaining an accurate, transferable, and efficient ReaxFF is therefore critical to atomic scale simulations. Molecular dynamics simulations are an effective method to test the performance of

a force field at hand. In the future, a data-driven approach that combines ML, DFT, *ab initio*, and classic MD simulations needs to be developed for active learning of force field. Besides the ML algorithm, inclusion of *ab initio* MD simulations to this framework will significantly accelerate the force field development process, particularly for gas-phase reactions. ML will automate the force field training work flow which consists of the evaluation of models taken from MD simulations in comparison with DFT and the identification of the non-DFT matched data, followed by the generation of DFT data and their addition to training set in order to reoptimize force field parameters. Thus, it is necessary to enhance the accuracy and quality of force field parameters by active learning.

Automatic Analysis of ReaxFF Simulations with Machine Learning. Studies using MD simulations usually require large-size and long-time runs that generate large amounts of data. Their postprocessing, especially when the investigation is coupled with rare events of interest like chemical reactions, costs significant efforts. Machine learning methods can automate analysis of ReaxFF simulations, helping with extracting and classifying outliers and unique features in simulations of materials. Our future work will focus on ML automated postprocessing of ReaxFF simulations to better manage and interpret our data, then connecting them to experimental efforts.

Continuous Exploration of MXenes Properties. In section 2.1, we learn that the family of MXenes is enormously large. There is still significant work to be done to understand the relationship between their chemistry and properties. While more than 30 stoichiometric MXenes have been discovered, in addition to a variety of solid-solution MXenes, there is still ample room for exploring MXenes. Computationally it is expected that there will be more ordered and solid-solution MXenes discovered for each structure: $M_2X_2T_x$, $M_3X_2T_x$, $M_4X_3T_x$, and $M_5X_4T_x$.^{465,466} For some specific chemistries, there are predictions of ferromagnetism, topological semiconductors, and others, depending on the specific chemistry and surface chemistry.^{467,468} Additional effort must be placed on the synthesis and discovery of these materials. Generally, multiple-M chemistry represents the future of MXenes with desired properties. Thus, additional systematic studies are needed to determine the specific relationships and effects different chemistries have on MXene properties and need incorporated into computational models to further guide experimental studies.

Making Magnetic Layered Compounds with High Curie Temperatures. Adding more Fe into Fe_nGeTe_2 is expected to enhance the strength of the exchange interaction present and consequently allows one to push toward higher Curie temperatures (T_C). Indeed, from Fe_3GeTe_2 to Fe_5GeTe_2 with thicknesses around 10 nm or thicker, T_C was found to generally increase from about 220 K to about 300 K. These promising T_C values are expected to further increase with increasing Fe content to values up to and even beyond 500 K.⁴⁶⁹ Recent theoretical studies also predicted that Fe_6GeTe_2 and Fe_7GeTe_2 are stable 2D phases.⁴⁶⁹ However, experimental validation is lacking. In-depth studies that correlate structure, specifically the precise atomic arrangement of nearest neighbor Fe facilitating the magnetic coupling, and the resulting magnetic properties at the mesoscopic scale, in particular T_C , magneto-crystalline anisotropy, coercive fields, remanence and magnetic domain structure, will establish the structure–property relationship in these material systems and help form a comprehensive

understanding of magnetic phenomena in these material systems.

Strain Engineering for 2D Materials. To tune the structural or electronic phases of materials, strain is as important as temperature. The six independent strain components and 18 independent strain gradients provide a vast design space to explore or engineer the thermodynamic landscape of materials and their properties. So far, most strain engineering or strain gradient engineering studies have been focused on utilizing one or two independent components. There are a plenty of uncharted spaces yet to be explored. Experimental challenges exist in realizing a multistrain or multistrain gradient tuned system. While both mechanical bending/stretching and epitaxial growth can lead to the design of one or two independent strain or strain gradient components, there is no reliable experimental approach to realize a complex designed strain or strain gradient pattern. Further, the vdW or quasi vdW bonding nature of these 2D materials makes it difficult to introduce long-lasting strain without delamination subject to thermal or mechanical cycling.

To reproduce the technical successes of strain engineering in Si transistors or III-V quantum well layers, one also must be able to produce the strain and strain gradients at the large or wafer scale. For this, mechanical stretching or similar local approaches involving the use of a sharp mechanical tip or structure may be replaced by large scale strain engineering approaches such as epitaxy using lattice mismatched substrates that are widely used in commercial III-V quantum well systems. Most works on the epilayer–substrate interaction in 2D materials have been focused on graphene or MoS₂. When the interlayer interactions in 2D materials become strong, it has been found that some epitaxial 2D layers may take epitaxial strains as high as a few percent.^{470,471} However, it is unclear how and why such large strain even exists. Further efforts are needed to understand the materials chemistry and epitaxy science of 2D materials for strain engineering. Though strain, in theory, can be produced at a large scale for 2D systems, the strain gradient, by its nature, prevents its development beyond the nanometer scale. Due to this reason, works on strain gradient engineering of 2D materials have been focused on the small scale. A potential strategy in the mass production of the strain gradient is to separate a large piece of 2D materials into many nanoscale pieces with each serving as an active component carrying a large enough strain gradient. This approach, though, may bring complexity in devices fabrication, especially if the out-of-plane dimension is needed in designing the strain gradient.

SHG in 2D Materials. One future challenge is seeking a rational design principle for materials with large $\chi^{(2)}$ that could exceed the current apparent upper boundaries of the $\chi^{(2)}$ -bandgap trade-off, with initial efforts focusing on cataloging materials data for $\chi^{(2)}$ and bandgap through high-throughput computation, as has been carried out for 3D bulk materials in Naccarato et al.⁴⁷² One empirical observation related to dimensionality is that, among materials with similar bandgaps, $\chi^{(2)}$ tend to be larger for lower-dimensional materials since they host more pronounced singularities in their low-energy excitation spectra that contribute to a nonresonant nonlinear response.⁴⁷³ It is unclear to what degree this strategy would apply since, by extrapolation, one may expect molecular systems to achieve the largest $\chi^{(2)}$, yet there have been no reports demonstrating this.

2D/3D Electronic Devices. The marriage of 2D semiconductors with crystalline 3D materials is a rich area of exploration not just from the perspective of basic interface

physics but also in terms of high-performance device applications. In terms of logic devices, the appeal of TFETs with a steep SS concurrently with a high on/off current ratio and a high on-current density is a worthy and impactful goal. Further studies and investigations are warranted to scale the devices and optimize contact, junction, and dielectric–semiconductor interfaces in addition to pursuing high quality, near-intrinsic, phase pure and scalable growth of 2D semiconductors. From the perspective of memory devices, the appeal of low-depolarization fields in atomically thin bodies combined with transferrable, high quality layered semiconductors makes it worthwhile to pursue interfaces between 2D semiconductors and 3D ferroelectrics. Additionally, 3D ferroelectrics that have low-static dielectric constants and high remnant polarizations that can be integrated with the 2D semiconductors are equally important to attain long retention. The grand challenges in this area, pertain once again to scaling the 2D materials to wafer scales as well as retaining device performance for highly voltage and area-scaled devices. Finally, 2D ferroelectric semiconductors are another very promising class of materials, and their junctions with 3D semiconductors and 3D ferroelectric dielectrics will be beneficial to device design and applications.

MTI Devices. In the ideal case, MTI-based devices will make disseminating the ohm more economical and portable and will, more importantly, serve as a basis for a compact quantum ampere, an electrical standard that has been even more limited in its versatility than resistance or voltage standards, primarily because they are based on single electron transistors. For instance, at present, the global accessibility of the quantum ampere is constrained to mostly National Metrology Institutes.⁴⁷⁴ Other limitations that may possibly be overcome by using MTIs include the sub-nA currents typically associated from the aforementioned single electron transistors and the Josephson voltage standard's aversion to magnetism, which would complicate its integration with a graphene-based resistance standard in a single cryostat. The work that comes from MTIs and any other 2D material system that exhibits the QAHE will help to move forward the realization of the quantum SI in terms of electrical standards. The realization of a compact quantum ampere through integration of devices operable in a zero-field environment will impact how calibration services are provided for industry.

Going forward, three research directions can emerge from among following efforts: (1) Identification of the physical limitations of the many promising materials, both through experimental and theoretical means. For instance, computing the defect behavior and the impact of disorder on Hall quantization would provide invaluable knowledge to materials growers. (2) Optimization of the best QAHE materials for device applications. In theory, knowledge from the first listed research direction (1) would provide a feedback loop with which one could narrow down the list of systems with immediate promise, allowing researchers the ability to determine dominant sources of nonideal behavior (e.g., point defects, magnetic order inhomogeneity such as domain walls, etc.). (3) Testing of applied QAHE technologies. Although the QAHE has been understood much more in recent times, there are still vast amounts of interdisciplinary work required to harness the effect in a way that enables the adoption of relevant 2D material systems for future technological advances.

AUTHOR INFORMATION

Corresponding Authors

Yu-Chuan Lin – Department of Materials Science and Engineering, The Pennsylvania State University, University Park, Pennsylvania 16802, United States; Department of Materials Science and Engineering, National Yang Ming Chiao Tung University, Hsinchu 300, Taiwan; orcid.org/0000-0003-4958-5073; Email: ycl194@nycu.edu.tw

Joshua A. Robinson – Department of Materials Science and Engineering, Department of Chemistry, Department of Physics, Center for 2-Dimensional and Layered Materials, and Center for Atomically Thin Multifunctional Coatings, The Pennsylvania State University, University Park, Pennsylvania 16802, United States; Two-Dimensional Crystal Consortium, The Pennsylvania State University, University Park, Pennsylvania 16802, United States; orcid.org/0000-0002-1513-7187; Email: jrobinson@psu.edu

Authors

Riccardo Torsi – Department of Materials Science and Engineering, The Pennsylvania State University, University Park, Pennsylvania 16802, United States; orcid.org/0000-0001-7748-1074

Rehan Younas – Department of Electrical Engineering, University of Notre Dame, Notre Dame, Indiana 46556, United States

Christopher L. Hinkle – Department of Electrical Engineering, University of Notre Dame, Notre Dame, Indiana 46556, United States; orcid.org/0000-0002-5485-6600

Albert F. Rigosi – National Institute of Standards and Technology, Gaithersburg, Maryland 20899, United States

Heather M. Hill – National Institute of Standards and Technology, Gaithersburg, Maryland 20899, United States

Kunyan Zhang – Department of Electrical and Computer Engineering, Rice University, Houston, Texas 77005, United States; Department of Electrical Engineering, The Pennsylvania State University, University Park, Pennsylvania 16802, United States; orcid.org/0000-0002-6830-409X

Shengxi Huang – Department of Electrical and Computer Engineering, Rice University, Houston, Texas 77005, United States; Department of Electrical Engineering, The Pennsylvania State University, University Park, Pennsylvania 16802, United States; orcid.org/0000-0002-3618-9074

Christopher E. Shuck – A.J. Drexel Nanomaterials Institute and Department of Materials Science and Engineering, Drexel University, Philadelphia, Pennsylvania 19104, United States; orcid.org/0000-0002-1274-8484

Chen Chen – Two-Dimensional Crystal Consortium, The Pennsylvania State University, University Park, Pennsylvania 16802, United States

Yu-Hsiu Lin – Department of Chemical Engineering & Materials Science, Michigan State University, East Lansing, Michigan 48824, United States; orcid.org/0000-0002-3599-9032

Daniel Maldonado-Lopez – Department of Chemical Engineering & Materials Science, Michigan State University, East Lansing, Michigan 48824, United States

Jose L. Mendoza-Cortes – Department of Chemical Engineering & Materials Science, Michigan State University, East Lansing, Michigan 48824, United States; orcid.org/0000-0001-5184-1406

John Ferrier – Department of Physics and Chemical Engineering, Northeastern University, Boston, Massachusetts 02115, United States

Swastik Kar – Department of Physics and Chemical Engineering, Northeastern University, Boston, Massachusetts 02115, United States

Nadire Nayir – Two-Dimensional Crystal Consortium, The Pennsylvania State University, University Park, Pennsylvania 16802, United States; Department of Mechanical Engineering, The Pennsylvania State University, University Park, Pennsylvania 16802, United States; Department of Physics, Karamanoglu Mehmet University, Karaman 70100, Turkey; orcid.org/0000-0002-3621-2481

Siavash Rajabpour – Department of Materials Science and Engineering, The Pennsylvania State University, University Park, Pennsylvania 16802, United States; orcid.org/0000-0002-1686-065X

Adri C. T. van Duin – Department of Materials Science and Engineering, Department of Mechanical Engineering, Department of Chemical Engineering, and Department of Chemistry, The Pennsylvania State University, University Park, Pennsylvania 16802, United States; Two-Dimensional Crystal Consortium, The Pennsylvania State University, University Park, Pennsylvania 16802, United States; orcid.org/0000-0002-3478-4945

Xiwen Liu – Department of Electrical and Systems Engineering, University of Pennsylvania, Philadelphia, Pennsylvania 19104, United States

Deep Jariwala – Department of Electrical and Systems Engineering, University of Pennsylvania, Philadelphia, Pennsylvania 19104, United States; orcid.org/0000-0002-3570-8768

Jie Jiang – Department of Materials Science and Engineering, Rensselaer Polytechnic Institute, Troy, New York 12180, United States

Jian Shi – Department of Materials Science and Engineering, Rensselaer Polytechnic Institute, Troy, New York 12180, United States; orcid.org/0000-0003-2115-2225

Wouter Mortelmans – Department of Materials Science and Engineering, Massachusetts Institute of Technology, Cambridge, Massachusetts 02142, United States

Rafael Jaramillo – Department of Materials Science and Engineering, Massachusetts Institute of Technology, Cambridge, Massachusetts 02142, United States; orcid.org/0000-0003-3116-6719

Joao Marcelo J. Lopes – Paul-Drude-Institut für Festkörperelektronik, Leibniz-Institut im Forschungsverbund Berlin e.V., 10117 Berlin, Germany; orcid.org/0000-0001-5268-1862

Roman Engel-Herbert – Paul-Drude-Institut für Festkörperelektronik, Leibniz-Institut im Forschungsverbund Berlin e.V., 10117 Berlin, Germany

Anthony Trofe – Department of Nanoscience, Joint School of Nanoscience & Nanoengineering, University of North Carolina at Greensboro, Greensboro, North Carolina 27401, United States; orcid.org/0000-0002-2579-6979

Tetyana Ignatova – Department of Nanoscience, Joint School of Nanoscience & Nanoengineering, University of North Carolina at Greensboro, Greensboro, North Carolina 27401, United States; orcid.org/0000-0003-3859-6367

Seng Huat Lee – Two-Dimensional Crystal Consortium, The Pennsylvania State University, University Park, Pennsylvania 16802, United States; Department of Physics, The

- Pennsylvania State University, University Park, Pennsylvania 16802, United States
- Zhiqiang Mao** – Two-Dimensional Crystal Consortium, The Pennsylvania State University, University Park, Pennsylvania 16802, United States; Department of Physics, The Pennsylvania State University, University Park, Pennsylvania 16802, United States; orcid.org/0000-0002-4920-3293
- Leticia Damian** – Department of Physics, University of North Texas, Denton, Texas 76203, United States
- Yuanxi Wang** – Department of Physics, University of North Texas, Denton, Texas 76203, United States
- Megan A. Steves** – Institute for Quantitative Biosciences, University of California Berkeley, Berkeley, California 94720, United States; orcid.org/0000-0002-1410-5650
- Kenneth L. Knappenberger, Jr.** – Department of Chemistry, The Pennsylvania State University, University Park, Pennsylvania 16802, United States; orcid.org/0000-0003-4123-3663
- Zhengtianye Wang** – Two-Dimensional Crystal Consortium, The Pennsylvania State University, University Park, Pennsylvania 16802, United States; Department of Materials Science and Engineering, University of Delaware, Newark, Delaware 19716, United States
- Stephanie Law** – Department of Materials Science and Engineering, The Pennsylvania State University, University Park, Pennsylvania 16802, United States; Two-Dimensional Crystal Consortium, The Pennsylvania State University, University Park, Pennsylvania 16802, United States; Department of Materials Science and Engineering, University of Delaware, Newark, Delaware 19716, United States; orcid.org/0000-0002-5087-6663
- George Bepete** – Department of Chemistry, Department of Physics, Center for 2-Dimensional and Layered Materials, and Center for Atomically Thin Multifunctional Coatings, The Pennsylvania State University, University Park, Pennsylvania 16802, United States; orcid.org/0000-0002-5562-1125
- Da Zhou** – Department of Physics and Center for 2-Dimensional and Layered Materials, The Pennsylvania State University, University Park, Pennsylvania 16802, United States; orcid.org/0000-0002-7189-5222
- Jiang-Xiazi Lin** – Department of Physics, Brown University, Providence, Rhode Island 02906, United States
- Mathias S. Scheurer** – Institute for Theoretical Physics, University of Innsbruck, Innsbruck A-6020, Austria; orcid.org/0000-0002-9439-5159
- Jia Li** – Department of Physics, Brown University, Providence, Rhode Island 02906, United States
- Pengjie Wang** – Department of Physics, Princeton University, Princeton, New Jersey 08540, United States; orcid.org/0000-0002-1427-6599
- Guo Yu** – Department of Physics and Department of Electrical and Computer Engineering, Princeton University, Princeton, New Jersey 08540, United States; orcid.org/0000-0003-1812-9825
- Sanfeng Wu** – Department of Physics, Princeton University, Princeton, New Jersey 08540, United States; orcid.org/0000-0002-6227-6286
- Deji Akinwande** – Department of Electrical and Computer Engineering, The University of Texas at Austin, Austin, Texas 78712, United States; Microelectronics Research Center, The University of Texas, Austin, Texas 78758, United States; orcid.org/0000-0001-7133-5586

Joan M. Redwing – Department of Materials Science and Engineering and Department of Electrical Engineering, The Pennsylvania State University, University Park, Pennsylvania 16802, United States; Two-Dimensional Crystal Consortium, The Pennsylvania State University, University Park, Pennsylvania 16802, United States; orcid.org/0000-0002-7906-452X

Mauricio Terrones – Department of Materials Science and Engineering, Department of Chemistry, Department of Physics, Center for 2-Dimensional and Layered Materials, and Center for Atomically Thin Multifunctional Coatings, The Pennsylvania State University, University Park, Pennsylvania 16802, United States; Research Initiative for Supra-Materials and Global Aqua Innovation Center, Shinshu University, Nagano 380-8553, Japan; orcid.org/0000-0003-0010-2851

Complete contact information is available at:
<https://pubs.acs.org/10.1021/acsnano.2c12759>

Author Contributions

*Y.-C.L. and R.T. contributed equally.

Notes

The authors declare no competing financial interest.

ACKNOWLEDGMENTS

Y.-C.L., R.T., R.Y., C.L.H., and J.A.R. acknowledge funding from NEWLIMITS, a center in nCORE, a Semiconductor Research Corporation (SRC) program sponsored by NIST through award number 70NANB17H041. Y.-C.L. also appreciates the support from the Department of Materials Science and Engineering at NYCU. R.Y. and C.L.H. were also supported by the SRC through the Global Research Collaboration (GRC) Program. This work was also supported in part by the National Science Foundation (NSF) through the Division of Materials Research (DMR) award number 1921818. Work presented herein was performed, for a subset of the authors (A.F.R. and H.M.H.), as part of their official duties for the United States Government. Funding is hence appropriated by the United States Congress directly. Commercial equipment, instruments, and materials are identified in this paper in order to specify the experimental procedure adequately. Such identification is not intended to imply recommendation or endorsement by the National Institute of Standards and Technology or the United States government, nor is it intended to imply that the materials or equipment identified are necessarily the best available for the purpose. D.J. and X.L. acknowledge support from Intel Rising Star Award and AFOSR GHz-THz program award FA9550-21-1-0035. K.Z. and S.H. acknowledge the support from NSF under Grant No. ECCS-2246564 and ECCS-1943895. S.H. also acknowledges the support from Johnson & Johnson WiS-TEM2D Award and the National Institutes of Health under Grant No. 1R01AG077016-01. K.Z. also acknowledges the Harold K. Schilling Dean's Graduate Scholarship. Y.-H.L., D.M.-L., and J.L.M.-C. acknowledge startup funds from Michigan State University. J.J. and J.S. thank NSF for the financial support under award no. of 2031692 and 2024972. S.K. acknowledges support from the Massachusetts Technology Collaborative award number 22032 and J.F. acknowledges support from the NSF under GRFP award No. 1938052. M.A.S. and K.L.K. acknowledge funding from the Airforce Office of Scientific Research (FA-9550-18-1-0347) and the National Science Foundation, DMR-2011839. M.A.S. acknowledges support

from the NSF Graduate Research Fellowship Program under grant no. DGE1255832. Z.W. and S.L. acknowledge funding from U.S. Department of Energy, Office of Science, Office of Basic Energy Sciences, under Award No. DE-SC0017801. D.A. acknowledges support from Office of Naval Research (ONR). G.B., D.Z., and M.T. thank the National Science Foundation- I/UCRC Phase II the Pennsylvania State University: Center for Atomically Thin Multifunctional Coatings (ATOMIC); grant No. 2113864 for partial support. G.B., D.Z., and M.T. also thank the NSF for Grants DMR-1420620 and DMR-2011839, and the NSF for the Early concept Grants for Exploratory Research OIA-2030857. S.H.L., C.C., Z.M., J.M.R., and J.A.R. acknowledge financial support from the 2D Crystal Consortium—Materials Innovation Platform (2DCC-MIP) facility at the Pennsylvania State University, which is funded by the National Science Foundation under cooperative agreement DMR-2039351.

VOCABULARY

2D materials: A class of crystalline solids consisting of a single layer of atoms or molecules that are covalently bonded within the 2D plane and held together by weak van der Waals forces between adjacent layers.

ReaxFF: The reactive force-field (ReaxFF) interatomic potential is a computational method used to study chemical reactions in large-scale systems over long time scales bridging together the accuracy of *ab initio* methods with the computational efficiency of classical force field methods.

van der Waals Epitaxy: A heteroepitaxy method for growth of high-quality 2D materials that relies on van der Waals forces between the substrate and the epilayer, thereby lifting lattice mismatch and thermal mismatch constraints of traditional heteroepitaxy.

MXenes: A family of 2D materials composed of transition metal carbides, nitrides, and carbonitrides with the general formula $M_{n+1}X_nT_x$, where M is an early transition metal, X is either C and/or N, $n = 1-4$, and T_x represents surface functional groups such as -OH, -O, -F, and -Cl.

Strain Engineering: A method to tune the structural, electronic, and optical properties of 2D materials by applying a mechanical stress.

Multidimensional Heterostructures: Systems in which materials of mixed dimensionality are placed in contact to take advantage of rich interface physics. This review will focus on examples of 2D crystals integrated with materials of different dimensionality to realize mixed-dimensional vdW heterostructures of the form $2D + nD$ ($n = 0, 1$, and 3).

MTIs: Magnetic topological insulators (MTIs) are a recently discovered quantum materials class in which a combination of magnetism and nontrivial band topology can create a variety of topological phenomena such as the quantum anomalous Hall effect and topological axion insulating states.

REFERENCES

- (1) Novoselov, K. S.; Geim, A. K.; Morozov, S. V.; Jiang, D.; Zhang, Y.; Dubonos, S. V.; Grigorieva, I. V.; Firsov, A. A. Electric Field Effect in Atomically Thin Carbon Films. *Science* **2004**, *306*, 666–669.
- (2) Geim, A. K.; Novoselov, K. S. The Rise of Graphene. *Nat. Mater.* **2007**, *6*, 183–191.
- (3) Manzeli, S.; Ovchinnikov, D.; Pasquier, D.; Yazyev, O. V.; Kis, A. 2D Transition Metal Dichalcogenides. *Nat. Rev. Mater.* **2017**, *2*, 17033.
- (4) Anasori, B.; Xie, Y.; Beidaghi, M.; Lu, J.; Hosler, B. C.; Hultman, L.; Kent, P. R. C.; Gogotsi, Y.; Barsoum, M. W. Two-Dimensional, Ordered, Double Transition Metals Carbides (MXenes). *ACS Nano* **2015**, *9*, 9507–9516.
- (5) Gibertini, M.; Koperski, M.; Morpurgo, A. F.; Novoselov, K. S. Magnetic 2D Materials and Heterostructures. *Nat. Nanotechnol.* **2019**, *14*, 408–419.
- (6) Chen, Y.; Fan, Z.; Zhang, Z.; Niu, W.; Li, C.; Yang, N.; Chen, B.; Zhang, H. Two-Dimensional Metal Nanomaterials: Synthesis, Properties, and Applications. *Chem. Rev.* **2018**, *118*, 6409–6455.
- (7) Li, J.; Li, Y.; Du, S.; Wang, Z.; Gu, B. L.; Zhang, S. C.; He, K.; Duan, W.; Xu, Y. Intrinsic Magnetic Topological Insulators in van Der Waals Layered $MnBi_2Te_4$ -Family Materials. *Sci. Adv.* **2019**, *5*, eaaw5685.
- (8) Novoselov, K. S.; Mishchenko, A.; Carvalho, A.; Castro Neto, A. H. 2D Materials and van Der Waals Heterostructures. *Science* **2016**, *353*, 461–472.
- (9) Mounet, N.; Gibertini, M.; Schwaller, P.; Campi, D.; Merkys, A.; Marrazzo, A.; Sohler, T.; Castelli, I. E.; Cepellotti, A.; Pizzi, G.; Marzari, N. Two-Dimensional Materials from High-Throughput Computational Exfoliation of Experimentally Known Compounds. *Nat. Nanotechnol.* **2018**, *13*, 246–252.
- (10) Ko, W.; Gai, Z.; Puzos, A. A.; Liang, L.; Berlijn, T.; Hachtel, J. A.; Xiao, K.; Ganesh, P.; Yoon, M.; Li, A.-P. Understanding Heterogeneities in Quantum Materials. *Adv. Mater.* **2022**, 2106909.
- (11) Bhimanapati, G. R.; Lin, Z.; Meunier, V.; Jung, Y.; Cha, J.; Das, S.; Xiao, D.; Son, Y.; Strano, M. S.; Cooper, V. R.; Liang, L.; Louie, S. G.; Ringe, E.; Zhou, W.; Kim, S. S.; Nair, R. R.; Sumpter, B. G.; Terrones, H.; Xia, F.; Wang, Y.; Zhu, J.; Akinwande, D.; Alem, N.; Schuller, J. A.; Schaak, R. E.; Terrones, M.; Robinson, J. A. Recent Advances in Two-Dimensional Materials Beyond Graphene. *ACS Nano* **2015**, *9*, 11509–11539.
- (12) Lei, Y.; Zhang, T.; Lin, Y.-C.; Granzier-Nakajima, T.; Bepete, G.; Kowalczyk, D. A.; Lin, Z.; Zhou, D.; Schranghamer, T. F.; Dodda, A.; Sebastian, A.; Chen, Y.; Liu, Y.; Pourtois, G.; Kempa, T. J.; Schuler, B.; Edmonds, M. T.; Quek, S. Y.; Wurstbauer, U.; Wu, S. M.; Glavin, N. R.; Das, S.; Dash, S. P.; Redwing, J. M.; Robinson, J. A.; Terrones, M. Graphene and Beyond: Recent Advances in Two-Dimensional Materials Synthesis, Properties, and Devices. *ACS Nanosci. Au* **2022**, *2*, 450–485.
- (13) Lin, Y.-C.; Liu, C.; Yu, Y.; Zarkadoulas, E.; Yoon, M.; Puzos, A. A.; Liang, L.; Kong, X.; Gu, Y.; Strasser, A.; Meyer, H. M.; Lorenz, M.; Chisholm, M. F.; Ivanov, I. N.; Rouleau, C. M.; Duscher, G.; Xiao, K.; Geoegean, D. B. Low Energy Implantation into Transition Metal Dichalcogenide Monolayers to Form Janus Structures. *ACS Nano* **2020**, *14*, 3896–3906.
- (14) Briggs, N.; Gebeyehu, Z. M.; Vera, A.; Zhao, T.; Wang, K.; De La Fuente Duran, A.; Bersch, B.; Bowen, T.; Knappenberger, K. L.; Robinson, J. A. Epitaxial Graphene/Silicon Carbide Intercalation: A Minireview on Graphene Modulation and Unique 2D Materials. *Nanoscale* **2019**, *11*, 15440–15447.
- (15) Lin, Z.; McCreary, A.; Briggs, N.; Subramanian, S.; Zhang, K.; Sun, Y.; Li, X.; Borys, N. J.; Yuan, H.; Fullerton-Shirey, S. K.; Chernikov, A.; Zhao, H.; McDonnell, S.; Lindenberg, A. M.; Xiao, K.; LeRoy, B. J.; Drndić, M.; Hwang, J.; Park, J.; Chhowalla, M.; Schaak, R. E.; Javey, A.; Hersam, M. C.; Robinson, J.; Terrones, M. 2D Materials Advances: From Large Scale Synthesis and Controlled Heterostructures to Improved Characterization Techniques, Defects and Applications. *2d Mater.* **2016**, *3*, 042001.
- (16) Lin, Z.; Lei, Y.; Subramanian, S.; Briggs, N.; Wang, Y.; Lo, C. L.; Yalon, E.; Lloyd, D.; Wu, S.; Koski, K.; Clark, R.; Das, S.; Wallace, R. M.; Kuech, T.; Bunch, J. S.; Li, X.; Chen, Z.; Pop, E.; Crespi, V. H.; Robinson, J. A.; Terrones, M. Research Update: Recent Progress on 2D Materials beyond Graphene: From Ripples, Defects, Intercalation, and Valley Dynamics to Straintronics and Power Dissipation. *APL Mater.* **2018**, *6*, 080701.
- (17) Hui, J.; Schorr, N. B.; Pakhira, S.; Qu, Z.; Mendoza-Cortes, J. L.; Rodríguez-López, J. Achieving Fast and Efficient K^+ Intercalation on Ultrathin Graphene Electrodes Modified by a Li^+ Based Solid-Electrolyte Interphase. *J. Am. Chem. Soc.* **2018**, *140*, 13599–13603.

- (18) Hui, J.; Nijamudheen, A.; Sarbapalli, D.; Xia, C.; Qu, Z.; Mendoza-Cortes, J. L.; Rodríguez-López, J. Nernstian Li^+ Intercalation into Few-Layer Graphene and Its Use for the Determination of K⁺ Co-Intercalation Processes. *Chem. Sci.* **2021**, *12*, 559–568.
- (19) Jiang, J.; Kang, J.; Cao, W.; Xie, X.; Zhang, H.; Chu, J. H.; Liu, W.; Banerjee, K. Intercalation Doped Multilayer-Graphene-Nanoribbons for Next-Generation Interconnects. *Nano Lett.* **2017**, *17*, 1482–1488.
- (20) Pakhira, S.; Mendoza-Cortes, J. L. Tuning the Dirac Cone of Bilayer and Bulk Structure Graphene by Intercalating First Row Transition Metals Using First-Principles Calculations. *J. Phys. Chem. C* **2018**, *122*, 4768–4782.
- (21) Csányi, G.; Littlewood, P. B.; Nevidomskyy, A. H.; Pickard, C. J.; Simons, B. D. The Role of the Interlayer State in the Electronic Structure of Superconducting Graphite Intercalated Compounds. *Nat. Phys.* **2005**, *1*, 42–45.
- (22) Lucht, K. P.; Mahabir, A. D.; Alcantara, A.; Balatsky, A. v.; Mendoza-Cortes, J. L.; Haraldsen, J. T. Designing a Path towards Superconductivity through Magnetic Exchange in Transition-Metal Intercalated Bilayer Graphene. *arXiv*. 2019, 1903.10112. <https://arxiv.org/abs/1903.10112> (accessed March 1, 2023).
- (23) Mao, Y.; Yuan, J.; Zhong, J. Density Functional Calculation of Transition Metal Adatom Adsorption on Graphene. *J. Phys.: Condens. Matter* **2008**, *20*, 115209.
- (24) Li, X.; Yadav, P.; Loh, K. P. Function-Oriented Synthesis of Two-Dimensional (2D) Covalent Organic Frameworks - from 3D Solids to 2D Sheets. *Chem. Soc. Rev.* **2020**, *49*, 4835–4866.
- (25) Li, Y.; Chen, W.; Gao, R.; Zhao, Z.; Zhang, T.; Xing, G.; Chen, L. 2D Covalent Organic Frameworks with Built-in Amide Active Sites for Efficient Heterogeneous Catalysis. *Chem. Commun.* **2019**, *55*, 14538–14541.
- (26) Mandal, A. K.; Mahmood, J.; Baek, J. B. Two-Dimensional Covalent Organic Frameworks for Optoelectronics and Energy Storage. *ChemNanoMat* **2017**, *3*, 373–391.
- (27) Evans, A. M.; Bradshaw, N. P.; Litchfield, B.; Strauss, M. J.; Seckman, B.; Ryder, M. R.; Castano, I.; Gilmore, C.; Gianneschi, N. C.; Mulzer, C. R.; Hersam, M. C.; Dichtel, W. R. High-Sensitivity Acoustic Molecular Sensors Based on Large-Area, Spray-Coated 2D Covalent Organic Frameworks. *Adv. Mater.* **2020**, *32*, 2004205.
- (28) Bhunia, S.; Deo, K. A.; Gaharwar, A. K. 2D Covalent Organic Frameworks for Biomedical Applications. *Adv. Funct. Mater.* **2020**, *30*, 2002046.
- (29) Alahakoon, S. B.; Thompson, C. M.; Occhialini, G.; Smaldone, R. A. Design Principles for Covalent Organic Frameworks in Energy Storage Applications. *ChemSusChem* **2017**, *10*, 2116–2129.
- (30) Zhu, P.; Meunier, V. Electronic Properties of Two-Dimensional Covalent Organic Frameworks. *J. Chem. Phys.* **2012**, *137*, 244703.
- (31) Pakhira, S.; Lucht, K. P.; Mendoza-Cortes, J. L. Iron Intercalation in Covalent-Organic Frameworks: A Promising Approach for Semiconductors. *J. Phys. Chem. C* **2017**, *121*, 21160–21170.
- (32) Pakhira, S.; Mendoza-Cortes, J. L. Intercalation of First Row Transition Metals inside Covalent-Organic Frameworks (COFs): A Strategy to Fine Tune the Electronic Properties of Porous Crystalline Materials. *Physical chemistry chemical physics* **2019**, *21*, 8785–8796.
- (33) Lucht, K. P.; Mendoza-Cortes, J. L. Birnessite: A Layered Manganese Oxide to Capture Sunlight for Water-Splitting Catalysis. *J. Phys. Chem. C* **2015**, *119*, 22838–22846.
- (34) Lei, Y.; Pakhira, S.; Fujisawa, K.; Liu, H.; Guerrero-Bermea, C.; Zhang, T.; Dasgupta, A.; Martinez, L. M.; Rao Singamaneni, S.; Wang, K.; Shallenberger, J.; Elías, A. L.; Cruz-Silva, R.; Endo, M.; Mendoza-Cortes, J. L.; Terrones, M. Low Temperature Activation of Inert Hexagonal Boron Nitride for Metal Deposition and Single Atom Catalysis. *Mater. Today* **2021**, *51*, 108–116.
- (35) Tsai, C.; Li, H.; Park, S.; Park, J.; Han, H. S.; Nørskov, J. K.; Zheng, X.; Abild-Pedersen, F. Electrochemical Generation of Sulfur Vacancies in the Basal Plane of MoS_2 for Hydrogen Evolution. *Nat. Commun.* **2017**, *8*, 15113.
- (36) Ma, L. J.; Shen, H. Activating PtSe_2 Monolayer for Hydrogen Evolution Reaction by Defect Engineering and Pd Doping. *Appl. Surf. Sci.* **2021**, *545*, 149013.
- (37) Qian, W.; Chen, Z.; Zhang, J.; Yin, L. Monolayer $\text{MoSi}_2\text{N}_{4-x}$ as Promising Electrocatalyst for Hydrogen Evolution Reaction: A DFT Prediction. *J. Mater. Sci. Technol.* **2022**, *99*, 215–222.
- (38) Zhao, J.; Liu, H.; Yu, Z.; Quhe, R.; Zhou, S.; Wang, Y.; Liu, C. C.; Zhong, H.; Han, N.; Lu, J.; Yao, Y.; Wu, K. Rise of Silicene: A Competitive 2D Material. *Prog. Mater. Sci.* **2016**, *83*, 24–151.
- (39) Pablo-Pedro, R.; Magaña-Fuentes, M. A.; Videa, M.; Kong, J.; Li, M.; Mendoza-Cortes, J. L.; van Voorhis, T. Understanding Disorder in 2D Materials: The Case of Carbon Doping of Silicene. *Nano Lett.* **2020**, *20*, 6336–6343.
- (40) Pradhan, N. R.; Garcia, C.; Lucking, M. C.; Pakhira, S.; Martinez, J.; Rosenmann, D.; Divan, R.; Sumant, A. v.; Terrones, H.; Mendoza-Cortes, J. L.; McGill, S. A.; Zhigadlo, N. D.; Balicas, L. Raman and Electrical Transport Properties of Few-Layered Arsenic-Doped Black Phosphorus. *Nanoscale* **2019**, *11*, 18449–18463.
- (41) Liang, K.; Pakhira, S.; Yang, Z.; Nijamudheen, A.; Ju, L.; Wang, M.; Aguirre-Velez, C. I.; Sterbinsky, G. E.; Du, Y.; Feng, Z.; Mendoza-Cortes, J. L.; Yang, Y. S-Doped MoP Nanoporous Layer Toward High-Efficiency Hydrogen Evolution in PH-Universal Electrolyte. *ACS Catal.* **2019**, *9*, 651–659.
- (42) van Duin, A. C. T.; Dasgupta, S.; Lorant, F.; Goddard, W. A. ReaxFF: A Reactive Force Field for Hydrocarbons. *J. Phys. Chem. A* **2001**, *105*, 9396–9409.
- (43) Xuan, Y.; Jain, A.; Zafar, S.; Lotfi, R.; Nayir, N.; Wang, Y.; Choudhury, T. H.; Wright, S.; Feraca, J.; Rosenbaum, L.; Redwing, J. M.; Crespi, V.; van Duin, A. C. T. Multi-Scale Modeling of Gas-Phase Reactions in Metal-Organic Chemical Vapor Deposition Growth of WSe_2 . *J. Cryst. Growth* **2019**, *527*, 125247.
- (44) Nayir, N.; Wang, Y.; Shabnam, S.; Hickey, D. R.; Miao, L.; Zhang, X.; Bachu, S.; Alem, N.; Redwing, J.; Crespi, V. H.; van Duin, A. C. T. Modeling for Structural Engineering and Synthesis of Two-Dimensional WSe_2 Using a Newly Developed Reaxff Reactive Force Field. *J. Phys. Chem. C* **2020**, *124*, 28285–28297.
- (45) Nayir, N.; Shin, Y. K.; Wang, Y.; Sengul, M. Y.; Hickey, D. R.; Chubarov, M.; Choudhury, T. H.; Alem, N.; Redwing, J.; Crespi, V. H.; van Duin, A. C. T. A ReaxFF Force Field for 2D- WS_2 and Its Interaction with Sapphire. *J. Phys. Chem. C* **2021**, *125*, 17950–17961.
- (46) Nayir, N.; Sengul, M. Y.; Costine, A. L.; Reinke, P.; Rajabpour, S.; Bansal, A.; Kozhakhmetov, A.; Robinson, J.; Redwing, J. M.; van Duin, A. Atomic-Scale Probing of Defect-Assisted Ga Intercalation through Graphene Using ReaxFF Molecular Dynamics Simulations. *Carbon* **2022**, *190*, 276–290.
- (47) Tersoff, J. New Empirical Approach for the Structure and Energy of Covalent Systems. *Phys. Rev. B* **1988**, *37*, 6991.
- (48) Tersoff, J. Empirical Interatomic Potential for Carbon, with Applications to Amorphous Carbon. *Phys. Rev. Lett.* **1988**, *61*, 2879.
- (49) Brenner, D. W. Empirical Potential for Hydrocarbons for Use in Simulating the Chemical Vapor Deposition of Diamond Films. *Phys. Rev. B* **1990**, *42*, 9458.
- (50) Briggs, N.; Bersch, B.; Wang, Y.; Jiang, J.; Koch, R. J.; Nayir, N.; Wang, K.; Kolmer, M.; Ko, W.; de La Fuente Duran, A.; Subramanian, S.; Dong, C.; Shallenberger, J.; Fu, M.; Zou, Q.; Chuang, Y. W.; Gai, Z.; Li, A. P.; Bostwick, A.; Jozwiak, C.; Chang, C. Z.; Rotenberg, E.; Zhu, J.; van Duin, A. C. T.; Crespi, V.; Robinson, J. A. Atomically Thin Half-van Der Waals Metals Enabled by Confinement Heteroepitaxy. *Nat. Mater.* **2020**, *19*, 637–643.
- (51) Reifsnnyder Hickey, D.; Nayir, N.; Chubarov, M.; Choudhury, T. H.; achu, S.; Miao, L.; Wang, Y.; Qian, C.; Crespi, V. H.; Redwing, J. M.; van Duin, A. C. T.; Alem, N. Illuminating Invisible Grain Boundaries in Coalesced Single-Orientation WS_2 Monolayer Films. *Nano Lett.* **2021**, *21*, 6487–6495.
- (52) Nayir, N. Density Functional Study of Ga Intercalation at Graphene/ SiC Heterointerface. *J. Mater. Res.* **2022**, *37*, 1172–1182.
- (53) White, A. The Materials Genome Initiative: One Year On. *MRS Bull.* **2012**, *37*, 715–716.
- (54) Ward, L.; Dunn, A.; Faghaninia, A.; Zimmermann, N. E. R.; Bajaj, S.; Wang, Q.; Montoya, J.; Chen, J.; Bystrom, K.; Dylla, M.; Chard, K.; Asta, M.; Persson, K. A.; Snyder, G. J.; Foster, I.; Jain, A. Matminer: An

Open Source Toolkit for Materials Data Mining. *Comput. Mater. Sci.* **2018**, *152*, 60–69.

(55) Chang, J.; Nikolaev, P.; Carpena-Núñez, J.; Rao, R.; Decker, K.; Islam, A. E.; Kim, J.; Pitt, M. A.; Myung, J. I.; Maruyama, B. Efficient Closed-Loop Maximization of Carbon Nanotube Growth Rate Using Bayesian Optimization. *Sci. Rep.* **2020**, *10*, 9040.

(56) Kirklin, S.; Saal, J. E.; Meredig, B.; Thompson, A.; Doak, J. W.; Aykol, M.; Rühl, S.; Wolverton, C. The Open Quantum Materials Database (OQMD): Assessing the Accuracy of DFT Formation Energies. *NPJ. Comput. Mater.* **2015**, *1*, 15010.

(57) Frey, N. C.; Akinwande, D.; Jariwala, D.; Shenoy, V. B. Machine Learning-Enabled Design of Point Defects in 2D Materials for Quantum and Neuromorphic Information Processing. *ACS Nano* **2020**, *14*, 13406–13417.

(58) Yu, M.; Yang, S.; Wu, C.; Marom, N. Machine Learning the Hubbard U Parameter in DFT+U Using Bayesian Optimization. *NPJ. Comput. Mater.* **2020**, *6*, 180.

(59) Venturi, V.; Parks, H. L.; Ahmad, Z.; Viswanathan, V. Machine Learning Enabled Discovery of Application Dependent Design Principles for Two-Dimensional Materials. *Mach. Learn. Sci. Technol.* **2020**, *1*, 035015.

(60) Suzuki, Y.; Nagai, R.; Haruyama, J. Machine Learning Exchange-Correlation Potential in Time-Dependent Density-Functional Theory. *Phys. Rev. A* **2020**, *101*, 050501.

(61) Tritsarlis, G. A.; Carr, S.; Schleder, G. R. Computational Design of Moiré Assemblies Aided by Artificial Intelligence. *Appl. Phys. Rev.* **2021**, *8*, 031401.

(62) Masubuchi, S.; Watanabe, E.; Seo, Y.; Okazaki, S.; Sasagawa, T.; Watanabe, K.; Taniguchi, T.; Machida, T. Deep-Learning-Based Image Segmentation Integrated with Optical Microscopy for Automatically Searching for Two-Dimensional Materials. *NPJ. 2D Mater. Appl.* **2020**, *4*, 3.

(63) Enderlein, G.; Fisher, R. A. The Design of Experiments. Eighth Edition. Oliver and Boyd, Edinburgh 1966. XVI + 248 S., 5 Abb., 39 Tab., Brosch. Preis s 15. *Biom. Sci.* **1969**, *11*, 139–139.

(64) Montgomery, D. C. *Design and Analysis of Experiments*; John Wiley & Sons: Hoboken, NJ, 2017.

(65) Gray, C. T. Introduction to Quality Engineering: Designing Quality into Products and Processes, G. Taguchi, Asian Productivity Organization, 1986. Number of Pages: 191. Price: \$29 (U.K.). *Qual. Reliab. Eng. Int.* **1988**, *4*, 198–198.

(66) Park, J.-S. Optimal Latin-Hypercube Designs for Computer Experiments. *J. Stat. Plan. Inference* **1994**, *39*, 95–111.

(67) Shahriari, B.; Swersky, K.; Wang, Z.; Adams, R. P.; de Freitas, N. Taking the Human Out of the Loop: A Review of Bayesian Optimization. *Proceedings of the IEEE* **2016**, *104*, 148–175.

(68) Snoek, J.; Larochelle, H.; Adams, R. P. Practical Bayesian Optimization of Machine Learning Algorithms. *Advances in neural information processing systems* **2012**, *25*, 2122–2130.

(69) Brochu, E.; Cora, V. M.; de Freitas, N. A Tutorial on Bayesian Optimization of Expensive Cost Functions, with Application to Active User Modeling and Hierarchical Reinforcement Learning. *arXiv* **2010**, 1012.2599. DOI: [10.48550/arXiv.1012.2599](https://doi.org/10.48550/arXiv.1012.2599) (accessed March 1, 2023).

(70) Kandasamy, K.; Schneider, J.; Póczos, B. High Dimensional Bayesian Optimisation and Bandits via Additive Models. In *Proceedings of the 32nd International Conference on Machine Learning*; Association for Computing Machinery, 2015; pp 295–304.

(71) Gelbart, M. A.; Snoek, J.; Adams, R. P. Bayesian Optimization with Unknown Constraints. *arXiv* **2014**, 1403.5607. DOI: [10.48550/arXiv.1403.5607](https://doi.org/10.48550/arXiv.1403.5607) (accessed March 1, 2023).

(72) Zhang, Y.; Apley, D. W.; Chen, W. Bayesian Optimization for Materials Design with Mixed Quantitative and Qualitative Variables. *Sci. Rep.* **2020**, *10*, 4924.

(73) Deshwal, A.; Simon, C. M.; Doppa, J. R. Bayesian Optimization of Nanoporous Materials. *Mol. Syst. Des. Eng.* **2021**, *6*, 1066–1086.

(74) Wahab, H.; Jain, V.; Tyrrell, A. S.; Seas, M. A.; Kotthoff, L.; Johnson, P. A. Machine-Learning-Assisted Fabrication: Bayesian

Optimization of Laser-Induced Graphene Patterning Using in-Situ Raman Analysis. *Carbon* **2020**, *167*, 609–619.

(75) Li, C.; Rubin de Celis Leal, D.; Rana, S.; Gupta, S.; Sutti, A.; Greenhill, S.; Slezak, T.; Height, M.; Venkatesh, S. Rapid Bayesian Optimisation for Synthesis of Short Polymer Fiber Materials. *Sci. Rep.* **2017**, *7*, 5683.

(76) Langner, S.; Häse, F.; Perea, J. D.; Stubhan, T.; Hauch, J.; Roch, L. M.; Heumüller, T.; Aspuru-Guzik, A.; Brabec, C. J. Beyond Ternary OPV: High-Throughput Experimentation and Self-Driving Laboratories Optimize Multicomponent Systems. *Adv. Mater.* **2020**, *32*, 1907801.

(77) MacLeod, B. P.; Parlange, F. G. L.; Morrissey, T. D.; Häse, F.; Roch, L. M.; Dettelbach, K. E.; Moreira, R.; Yunker, L. P. E.; Rooney, M. B.; Deeth, J. R.; Lai, V.; Ng, G. J.; Situ, H.; Zhang, R. H.; Elliott, M. S.; Haley, T. H.; Dvorak, D. J.; Aspuru-Guzik, A.; Hein, J. E.; Berlinguette, C. P. Self-Driving Laboratory for Accelerated Discovery of Thin-Film Materials. *Sci. Adv.* **2020**, *6*, eaaz8867.

(78) Liu, H.; Ong, Y.-S.; Shen, X.; Cai, J. When Gaussian Process Meets Big Data: A Review of Scalable GPs. *IEEE Trans. Neural Netw. Learn. Syst.* **2020**, *31*, 4405–4423.

(79) Sejnowski, T. J. The Unreasonable Effectiveness of Deep Learning in Artificial Intelligence. *Proc. Natl. Acad. Sci. U. S. A.* **2020**, *117*, 30033–30038.

(80) Zhang, J.; Wang, F.; Shenoy, V. B.; Tang, M.; Lou, J. Towards Controlled Synthesis of 2D Crystals by Chemical Vapor Deposition (CVD). *Mater. Today* **2020**, *40*, 132–139.

(81) Hejazi, D.; Kari Rezapour, N.; Ferrier, J.; Ostadabbas, S.; Kar, S. Dispersion-Free Highly Accurate Color Recognition Using Excitonic 2D Materials and Machine Learning. *Mater. Today* **2022**, *59*, 18–24.

(82) Tong, L.; Peng, Z.; Lin, R.; Li, Z.; Wang, Y.; Huang, X.; Xue, K.-H.; Xu, H.; Liu, F.; Xia, H.; Wang, P.; Xu, M.; Xiong, W.; Hu, W.; Xu, J.; Zhang, X.; Ye, L.; Miao, X. 2D Materials-Based Homogeneous Transistor-Memory Architecture for Neuromorphic Hardware. *Science* **2021**, *373*, 1353–1358.

(83) Mennel, L.; Symonowicz, J.; Wachter, S.; Polyushkin, D. K.; Molina-Mendoza, A. J.; Mueller, T. Ultrafast Machine Vision with 2D Material Neural Network Image Sensors. *Nature* **2020**, *579*, 62–66.

(84) Naguib, M.; Kurtoglu, M.; Presser, V.; Lu, J.; Niu, J.; Heon, M.; Hultman, L.; Gogotsi, Y.; Barsoum, M. W. Two-Dimensional Nanocrystals Produced by Exfoliation of Ti_3AlC_2 . *Adv. Mater.* **2011**, *23*, 4248–4253.

(85) Deysh, G.; Shuck, C. E.; Hantanasirisakul, K.; Frey, N. C.; Foucher, A. C.; Maleski, K.; Sarycheva, A.; Shenoy, V. B.; Stach, E. A.; Anasori, B.; Gogotsi, Y. Synthesis of $\text{Mo}_4\text{VAlC}_4\text{MAX}$ Phase and Two-Dimensional Mo_4VC_4 MXene with Five Atomic Layers of Transition Metals. *ACS Nano* **2020**, *14*, 204–217.

(86) Sokol, M.; Natu, V.; Kota, S.; Barsoum, M. W. On the Chemical Diversity of the MAX Phases. *Trends Chem.* **2019**, *1*, 210–223.

(87) Verger, L.; Xu, C.; Natu, V.; Cheng, H. M.; Ren, W.; Barsoum, M. W. Overview of the Synthesis of MXenes and Other Ultrathin 2D Transition Metal Carbides and Nitrides. *Curr. Opin. Solid State Mater. Sci.* **2019**, *23*, 149–163.

(88) Li, Y.; Shao, H.; Lin, Z.; Lu, J.; Liu, L.; Duployer, B.; Persson, P. O. Å.; Eklund, P.; Hultman, L.; Li, M.; Chen, K.; Zha, X. H.; Du, S.; Rozier, P.; Chai, Z.; Raymundo-Piñero, E.; Taberna, P. L.; Simon, P.; Huang, Q. A General Lewis Acidic Etching Route for Preparing MXenes with Enhanced Electrochemical Performance in Non-Aqueous Electrolyte. *Nat. Mater.* **2020**, *19*, 894–899.

(89) Jawaid, A.; Hassan, A.; Neher, G.; Nepal, D.; Pachter, R.; Kennedy, W. J.; Ramakrishnan, S.; Vaia, R. A. Halogen Etch of $\text{Ti}_3\text{AlC}_2\text{MAX}$ Phase for Mxene Fabrication. *ACS Nano* **2021**, *15*, 2771–2777.

(90) Li, T.; Yao, L.; Liu, Q.; Gu, J.; Luo, R.; Li, J.; Yan, X.; Wang, W.; Liu, P.; Chen, B.; Zhang, W.; Abbas, W.; Naz, R.; Zhang, D. Fluorine-Free Synthesis of High-Purity $\text{Ti}_3\text{C}_2\text{T}_x$ ($T = \text{OH}, \text{O}$) via Alkali Treatment. *Angew. Chem., Int. Ed.* **2018**, *57*, 6115–6119.

(91) Akuzum, B.; Maleski, K.; Anasori, B.; Lelyukh, P.; Alvarez, N. J.; Kumbur, E. C.; Gogotsi, Y. Rheological Characteristics of 2D Titanium

Carbide (MXene) Dispersions: A Guide for Processing MXenes. *ACS Nano* **2018**, *12*, 2685–2694.

(92) Shuck, C. E.; Sarycheva, A.; Anayee, M.; Levitt, A.; Zhu, Y.; Uzun, S.; Balitskiy, V.; Zahorodna, V.; Gogotsi, O.; Gogotsi, Y. Scalable Synthesis of $\text{Ti}_3\text{C}_2\text{T}_x$ MXene. *Adv. Eng. Mater.* **2020**, *22*, 1901241.

(93) Shuck, C. E.; Gogotsi, Y. Taking MXenes from the Lab to Commercial Products. *Chemical Engineering Journal* **2020**, *401*, 125786.

(94) Hantanasirisakul, K.; Gogotsi, Y. Electronic and Optical Properties of 2D Transition Metal Carbides and Nitrides (MXenes). *Adv. Mater.* **2018**, *30*, 1804779.

(95) Maleski, K.; Shuck, C. E.; Fafarman, A. T.; Gogotsi, Y. The Broad Chromatic Range of Two-Dimensional Transition Metal Carbides. *Adv. Opt. Mater.* **2021**, *9*, 2001563.

(96) Han, M.; Maleski, K.; Shuck, C. E.; Yang, Y.; Glazar, J. T.; Foucher, A. C.; Hantanasirisakul, K.; Sarycheva, A.; Frey, N. C.; May, S. J.; Shenoy, V. B.; Stach, E. A.; Gogotsi, Y. Tailoring Electronic and Optical Properties of MXenes through Forming Solid Solutions. *J. Am. Chem. Soc.* **2020**, *142*, 19110–19118.

(97) Shekhirev, M.; Shuck, C. E.; Sarycheva, A.; Gogotsi, Y. Characterization of MXenes at Every Step, from Their Precursors to Single Flakes and Assembled Films. *Prog. Mater. Sci.* **2021**, *120*, 100757.

(98) Lipatov, A.; Alhabebe, M.; Lu, H.; Zhao, S.; Loes, M. J.; Vorobeve, N. S.; Dall'Agnese, Y.; Gao, Y.; Gruverman, A.; Gogotsi, Y.; Sinitskii, A. Electrical and Elastic Properties of Individual Single-Layer $\text{Nb}_4\text{C}_3\text{T}_x$ MXene Flakes. *Adv. Electron. Mater.* **2020**, *6*, 1901382.

(99) Li, X.; Huang, Z.; Shuck, C. E.; Liang, G.; Gogotsi, Y.; Zhi, C. MXene Chemistry, Electrochemistry and Energy Storage Applications. *Nat. Rev. Chem.* **2022**, *6*, 389–404.

(100) Shahzad, F.; Alhabebe, M.; Hatter, C. B.; Anasori, B.; Hong, S. M.; Koo, C. M.; Gogotsi, Y. Electromagnetic Interference Shielding with 2D Transition Metal Carbides (MXenes). *Science* **2016**, *353*, 1137–1140.

(101) Huang, K.; Li, Z.; Lin, J.; Han, G.; Huang, P. Two-Dimensional Transition Metal Carbides and Nitrides (MXenes) for Biomedical Applications. *Chem. Soc. Rev.* **2018**, *47*, 5109–5124.

(102) Unal, M. A.; Bayrakdar, F.; Fusco, L.; Besbinar, O.; Shuck, C. E.; Yalcin, S.; Erken, M. T.; Ozkul, A.; Gurcan, C.; Panatli, O.; Summak, G. Y.; Gokce, C.; Orecchioni, M.; Gazzi, A.; Vitale, F.; Somers, J.; Demir, E.; Yildiz, S. S.; Nazir, H.; Grivel, J. C.; Bedognetti, D.; Crisanti, A.; Akcali, K. C.; Gogotsi, Y.; Delogu, L. G.; Yilmazer, A. 2D MXenes with Antiviral and Immunomodulatory Properties: A Pilot Study against SARS-CoV-2. *Nano Today* **2021**, *38*, 101136.

(103) Zhang, Y.; Wang, L.; Zhang, N.; Zhou, Z. Adsorptive Environmental Applications of MXene Nanomaterials: A Review. *RSC Adv.* **2018**, *8*, 19895–19905.

(104) Mansoor, N. E.; Diaz, L. A.; Shuck, C. E.; Gogotsi, Y.; Lister, T. E.; Estrada, D. Removal and Recovery of Ammonia from Simulated Wastewater Using $\text{Ti}_3\text{C}_2\text{T}_x$ MXene in Flow Electrode Capacitive Deionization. *NPJ. Clean Water* **2022**, *5*, 26.

(105) Lee, K. H.; Zhang, Y. Z.; Jiang, Q.; Kim, H.; Alkenawi, A. A.; Alshareef, H. N. Ultrasound-Driven Two-Dimensional $\text{Ti}_3\text{C}_2\text{T}_x$ MXene Hydrogel Generator. *ACS Nano* **2020**, *14*, 3199–3207.

(106) Tu, S.; Jiang, Q.; Zhang, X.; Alshareef, H. N. Large Dielectric Constant Enhancement in MXene Percolative Polymer Composites. *ACS Nano* **2018**, *12*, 3369–3377.

(107) Tao, Q.; Dahlqvist, M.; Lu, J.; Kota, S.; Meshkian, R.; Halim, J.; Palisaitis, J.; Hultman, L.; Barsoum, M. W.; Persson, P. O. Å.; Rosen, J. Two-Dimensional $\text{Mo}_{1.33}\text{C}$ MXene with Divacancy Ordering Prepared from Parent 3D Laminate with in-Plane Chemical Ordering. *Nat. Commun.* **2017**, *8*, 14949.

(108) Dahlqvist, M.; Lu, J.; Meshkian, R.; Tao, Q.; Hultman, L.; Rosen, J. Prediction and Synthesis of a Family of Atomic Laminate Phases with Kagomé-like and in-Plane Chemical Ordering. *Sci. Adv.* **2017**, *3*, e1700642.

(109) Meshkian, R.; Dahlqvist, M.; Lu, J.; Wickman, B.; Halim, J.; Thörnberg, J.; Tao, Q.; Li, S.; Intikhab, S.; Snyder, J.; Barsoum, M. W.; Yildizhan, M.; Palisaitis, J.; Hultman, L.; Persson, P. O. Å.; Rosen, J. W-Based Atomic Laminates and Their 2D Derivative $\text{W}_{1.33}\text{C}$ MXene with Vacancy Ordering. *Adv. Mater.* **2018**, *30*, 1706409.

(110) Ahmed, B.; El Ghazaly, A.; Rosen, J. i-MXenes for Energy Storage and Catalysis. *Adv. Funct. Mater.* **2020**, *30*, 2000894.

(111) Persson, I.; El Ghazaly, A.; Tao, Q.; Halim, J.; Kota, S.; Darakchieva, V.; Palisaitis, J.; Barsoum, M. W.; Rosen, J.; Persson, P. O. Å. Tailoring Structure, Composition, and Energy Storage Properties of MXenes from Selective Etching of In-Plane, Chemically Ordered MAX Phases. *Small* **2018**, *14*, 1703676.

(112) Halim, J.; Palisaitis, J.; Lu, J.; Thörnberg, J.; Moon, E. J.; Precner, M.; Eklund, P.; Persson, P. O. Å.; Barsoum, M. W.; Rosen, J. Synthesis of Two-Dimensional $\text{Nb}_{1.33}\text{C}$ (MXene) with Randomly Distributed Vacancies by Etching of the Quaternary Solid Solution $(\text{Nb}_{2/3}\text{Sc}_{1/3})_2\text{AlC}$ Max Phase. *ACS Appl. Nano Mater.* **2018**, *1*, 2455–2460.

(113) Zheng, W.; Halim, J.; Persson, P. O. Å.; Rosen, J.; Barsoum, M. W. Effect of Vacancies on the Electrochemical Behavior of Mo-Based MXenes in Aqueous Supercapacitors. *J. Power Sources* **2022**, *525*, 231064.

(114) Meshkian, R.; Tao, Q.; Dahlqvist, M.; Lu, J.; Hultman, L.; Rosen, J. Theoretical Stability and Materials Synthesis of a Chemically Ordered MAX Phase, $\text{Mo}_2\text{ScAlC}_2$, and Its Two-Dimensional Derivate Mo_2ScC_2 MXene. *Acta Mater.* **2017**, *125*, 476–480.

(115) Hart, J. L.; Hantanasirisakul, K.; Lang, A. C.; Li, Y.; Mehmood, F.; Pachter, R.; Frenkel, A. I.; Gogotsi, Y.; Taheri, M. L. Multimodal Spectroscopic Study of Surface Termination Evolution in $\text{Cr}_2\text{TiC}_2\text{T}_x$ MXene. *Adv. Mater. Interfaces* **2021**, *8*, 2001789.

(116) Hantanasirisakul, K.; Anasori, B.; Nemsak, S.; Hart, J. L.; Wu, J.; Yang, Y.; Chopdekar, R. v.; Shafer, P.; May, A. F.; Moon, E. J.; Zhou, J.; Zhang, Q.; Taheri, M. L.; May, S. J.; Gogotsi, Y. Evidence of a Magnetic Transition in Atomically Thin $\text{Cr}_2\text{TiC}_2\text{T}_x$ MXene. *Nanoscale Horiz* **2020**, *5*, 1557–1565.

(117) Yang, Y.; Hantanasirisakul, K.; Frey, N. C.; Anasori, B.; Green, R. J.; Rogge, P. C.; Waluyo, I.; Hunt, A.; Shafer, P.; Arenholz, E.; Shenoy, V. B.; Gogotsi, Y.; May, S. J. Distinguishing Electronic Contributions of Surface and Sub-Surface Transition Metal Atoms in Ti-Based MXenes. *2d Mater.* **2020**, *7*, 025015.

(118) Mathis, T. S.; Maleski, K.; Goad, A.; Sarycheva, A.; Anayee, M.; Foucher, A. C.; Hantanasirisakul, K.; Shuck, C. E.; Stach, E. A.; Gogotsi, Y. Modified MAX Phase Synthesis for Environmentally Stable and Highly Conductive Ti_3C_2 MXene. *ACS Nano* **2021**, *15*, 6420–6429.

(119) Rigby-Bell, M. T. P.; Natu, V.; Sokol, M.; Kelly, D. J.; Hopkinson, D. G.; Zou, Y.; Bird, J. R. T.; Evitts, L. J.; Smith, M.; Race, C. P.; Frankel, P.; Haigh, S. J.; Barsoum, M. W. Synthesis of New M-Layer Solid-Solution 312 MAX Phases $(\text{Ta}_{1-x}\text{Ti}_x)_3\text{AlC}_2$ ($x = 0.4, 0.62, 0.75, 0.91$ or 0.95), and Their Corresponding MXenes. *RSC Adv.* **2021**, *11*, 3110–3114.

(120) Pinto, D.; Anasori, B.; Avireddy, H.; Shuck, C. E.; Hantanasirisakul, K.; Deysher, G.; Morante, J. R.; Porzio, W.; Alshareef, H. N.; Gogotsi, Y. Synthesis and Electrochemical Properties of 2D Molybdenum Vanadium Carbides – Solid Solution MXenes. *J. Mater. Chem. A Mater.* **2020**, *8*, 8957–8968.

(121) Yang, J.; Naguib, M.; Ghidui, M.; Pan, L. M.; Gu, J.; Nanda, J.; Halim, J.; Gogotsi, Y.; Barsoum, M. W. Two-Dimensional Nb-Based M_4C_3 Solid Solutions (MXenes). *J. Am. Ceram. Soc.* **2016**, *99*, 660–666.

(122) Matthews, K.; Zhang, T.; Shuck, C. E.; Vahidmohammadi, A.; Gogotsi, Y. Guidelines for Synthesis and Processing of Chemically Stable Two-Dimensional V_2CT_x MXene. *Chem. Mater.* **2022**, *34*, 499–509.

(123) Han, M.; Shuck, C. E.; Rakhmanov, R.; Parchment, D.; Anasori, B.; Koo, C. M.; Friedman, G.; Gogotsi, Y. Beyond $\text{Ti}_3\text{C}_2\text{T}_x$: MXenes for Electromagnetic Interference Shielding. *ACS Nano* **2020**, *14*, 5008–5016.

(124) Foucher, A. C.; Han, M.; Shuck, C. E.; Maleski, K.; Gogotsi, Y.; Stach, E. A. Shifts in Valence States in Bimetallic MXenes Revealed by Electron Energy-Loss Spectroscopy (EELS). *2d Mater.* **2022**, *9*, 025004.

(125) Wang, L.; Han, M.; Shuck, C. E.; Wang, X.; Gogotsi, Y. Adjustable Electrochemical Properties of Solid-Solution MXenes. *Nano Energy* **2021**, *88*, 106308.

- (126) Tian, H.; Tice, J.; Fei, R.; Tran, V.; Yan, X.; Yang, L.; Wang, H. Low-Symmetry Two-Dimensional Materials for Electronic and Photonic Applications. *Nano Today* **2016**, *11*, 763–777.
- (127) Gomes, L. C.; Carvalho, A. Electronic and Optical Properties of Low-Dimensional Group-IV Monochalcogenides. *J. Appl. Phys.* **2020**, *128*, 121101.
- (128) Zhou, C.; Lee, Y. K.; Yu, Y.; Byun, S.; Luo, Z. Z.; Lee, H.; Ge, B.; Lee, Y. L.; Chen, X.; Lee, J. Y.; Cojocaru-Mirédin, O.; Chang, H.; Im, J.; Cho, S. P.; Wuttig, M.; Dravid, V. P.; Kanatzidis, M. G.; Chung, I. Polycrystalline SnSe with a Thermoelectric Figure of Merit Greater than the Single Crystal. *Nat. Mater.* **2021**, *20*, 1378–1384.
- (129) Sutter, P.; Komsa, H. P.; Lu, H.; Gruverman, A.; Sutter, E. Few-Layer Tin Sulfide (SnS): Controlled Synthesis, Thickness Dependent Vibrational Properties, and Ferroelectricity. *Nano Today* **2021**, *37*, 101082.
- (130) Singh, A.; Jo, S. S.; Li, Y.; Wu, C.; Li, M.; Jaramillo, R. Refractive Uses of Layered and Two-Dimensional Materials for Integrated Photonics. *ACS Photonics* **2020**, *7*, 3270–3285.
- (131) Littlewood, P. B. The Crystal Structure of IV-VI Compounds. I. Classification and Description. *Journal of Physics C: Solid State Physics* **1980**, *13*, 4855–4873.
- (132) Bao, Y.; Song, P.; Liu, Y.; Chen, Z.; Zhu, M.; Abdelwahab, I.; Su, J.; Fu, W.; Chi, X.; Yu, W.; Liu, W.; Zhao, X.; Xu, Q. H.; Yang, M.; Loh, K. P. Gate-Tunable In-Plane Ferroelectricity in Few-Layer SnS. *Nano Lett.* **2019**, *19*, 5109–5117.
- (133) Zhao, L. D.; Lo, S. H.; Zhang, Y.; Sun, H.; Tan, G.; Uher, C.; Wolverton, C.; Dravid, V. P.; Kanatzidis, M. G. Ultralow Thermal Conductivity and High Thermoelectric Figure of Merit in SnSe Crystals. *Nature* **2014**, *508*, 373–377.
- (134) Mortelmans, W.; Hilse, M.; Song, Q.; Jo, S. S.; Ye, K.; Liu, D.; Samarth, N.; Jaramillo, R. Measuring and Then Eliminating Twin Domains in SnSe Thin Films Using Fast Optical Metrology and Molecular Beam Epitaxy. *ACS Nano* **2022**, *16*, 9472–9478.
- (135) Chang, K.; Küster, F.; Miller, B. J.; Ji, J. R.; Zhang, J. L.; Sessi, P.; Barraza-Lopez, S.; Parkin, S. S. P. Microscopic Manipulation of Ferroelectric Domains in SnSe Monolayers at Room Temperature. *Nano Lett.* **2020**, *20*, 6590–6597.
- (136) Higashitarumizu, N.; Kawamoto, H.; Lee, C. J.; Lin, B. H.; Chu, F. H.; Yonemori, I.; Nishimura, T.; Wakabayashi, K.; Chang, W. H.; Nagashio, K. Purely In-Plane Ferroelectricity in Monolayer SnS at Room Temperature. *Nat. Commun.* **2020**, *11*, 2428.
- (137) Jin, W.; Vishwanath, S.; Liu, J.; Kong, L.; Lou, R.; Dai, Z.; Sadowski, J. T.; Liu, X.; Lien, H. H.; Chaney, A.; Han, Y.; Cao, M.; Ma, J.; Qian, T.; Wang, S.; Dobrowolska, M.; Furdyna, J.; Muller, D. A.; Pohl, K.; Ding, H.; Dadap, J. I.; Xing, H. G.; Osgood, R. M. Electronic Structure of the Metastable Epitaxial Rock-Salt SnSe {111} Topological Crystalline Insulator. *Phys. Rev. X* **2017**, *7*, 041020.
- (138) Wu, M.; Zeng, X. C. Intrinsic Ferroelasticity and/or Multiferroicity in Two-Dimensional Phosphorene and Phosphorene Analogues. *Nano Lett.* **2016**, *16*, 3236–3241.
- (139) Nag, S.; Saini, A.; Singh, R.; Kumar, R. Ultralow Lattice Thermal Conductivity and Anisotropic Thermoelectric Performance of AA Stacked SnSe Bilayer. *Appl. Surf. Sci.* **2020**, *512*, 145640.
- (140) Boscher, N. D.; Carmalt, C. J.; Palgrave, R. G.; Parkin, I. P. Atmospheric Pressure Chemical Vapour Deposition of SnSe and SnSe₂ Thin Films on Glass. *Thin Solid Films* **2008**, *516*, 4750–4757.
- (141) Horide, T.; Murakami, Y.; Hirayama, Y.; Ishimaru, M.; Matsumoto, K. Thermoelectric Property in Orthorhombic-Domained SnSe Film. *ACS Appl. Mater. Interfaces* **2019**, *11*, 27057–27063.
- (142) Zhou, J.; Xu, H.; Li, Y.; Jaramillo, R.; Li, J. Opto-Mechanics Driven Fast Martensitic Transition in Two-Dimensional Materials. *Nano Lett.* **2018**, *18*, 7794–7800.
- (143) Jo, S. S.; Wu, C.; Zhu, L.; Yang, L.; Li, M.; Jaramillo, R. Photonic Platforms Using In-Plane Optical Anisotropy of Tin (II) Selenide and Black Phosphorus. *Adv. Photonics Res.* **2021**, *2*, 2100176.
- (144) Sarkar, A. S.; Stratakis, E. Recent Advances in 2D Metal Monochalcogenides. *Advanced Science* **2020**, *7*, 2001655.
- (145) Xu, H.; Zhou, J.; Wang, H.; Li, J. Giant Photonic Response of Mexican-Hat Topological Semiconductors for Mid-Infrared to Terahertz Applications. *J. Phys. Chem. Lett.* **2020**, *11*, 6119–6126.
- (146) Chen, Z. G.; Shi, X.; Zhao, L. D.; Zou, J. High-Performance SnSe Thermoelectric Materials: Progress and Future Challenge. *Prog. Mater. Sci.* **2018**, *97*, 283–346.
- (147) Zhang, X.; Choudhury, T. H.; Chubarov, M.; Xiang, Y.; Jariwala, B.; Zhang, F.; Alem, N.; Wang, G. C.; Robinson, J. A.; Redwing, J. M. Diffusion-Controlled Epitaxy of Large Area Coalesced WSe₂ Monolayers on Sapphire. *Nano Lett.* **2018**, *18*, 1049–1056.
- (148) Lin, Y. C.; Jariwala, B.; Bersch, B. M.; Xu, K.; Nie, Y.; Wang, B.; Eichfeld, S. M.; Zhang, X.; Choudhury, T. H.; Pan, Y.; Addou, R.; Smyth, C. M.; Li, J.; Zhang, K.; Haque, M. A.; Fölsch, S.; Feenstra, R. M.; Wallace, R. M.; Cho, K.; Fullerton-Shirey, S. K.; Redwing, J. M.; Robinson, J. A. Realizing Large-Scale, Electronic-Grade Two-Dimensional Semiconductors. *ACS Nano* **2018**, *12*, 965–975.
- (149) Li, T.; Guo, W.; Ma, L.; Li, W.; Yu, Z.; Han, Z.; Gao, S.; Liu, L.; Fan, D.; Wang, Z.; Yang, Y.; Lin, W.; Luo, Z.; Chen, X.; Dai, N.; Tu, X.; Pan, D.; Yao, Y.; Wang, P.; Nie, Y.; Wang, J.; Shi, Y.; Wang, X. Epitaxial Growth of Wafer-Scale Molybdenum Disulfide Semiconductor Single Crystals on Sapphire. *Nat. Nanotechnol.* **2021**, *16*, 1201–1207.
- (150) Liu, L.; Li, T.; Ma, L.; Li, W.; Gao, S.; Sun, W.; Dong, R.; Zou, X.; Fan, D.; Shao, L.; Gu, C.; Dai, N.; Yu, Z.; Chen, X.; Tu, X.; Nie, Y.; Wang, P.; Wang, J.; Shi, Y.; Wang, X. Uniform Nucleation and Epitaxy of Bilayer Molybdenum Disulfide on Sapphire. *Nature* **2022**, *605*, 69–75.
- (151) <https://www.mri.psu.edu/2d-crystal-consortium/user-facilities/thin-films/chalcogenide-metalorganic-chemical-vapor> (accessed March 1, 2023).
- (152) Xiang, Y.; Sun, X.; Valdman, L.; Zhang, F.; Choudhury, T. H.; Chubarov, M.; Robinson, J. A.; Redwing, J. M.; Terrones, M.; Ma, Y.; Gao, L.; Washington, M. A.; Lu, T. M.; Wang, G. C. Monolayer MoS₂ on Sapphire: An Azimuthal Reflection High-Energy Electron Diffraction Perspective. *2d Mater.* **2021**, *8*, 025003.
- (153) Chubarov, M.; Choudhury, T. H.; Hickey, D. R.; Bachu, S.; Zhang, T.; Sebastian, A.; Bansal, A.; Zhu, H.; Trainor, N.; Das, S.; Terrones, M.; Alem, N.; Redwing, J. M. Wafer-Scale Epitaxial Growth of Unidirectional WS₂ Monolayers on Sapphire. *ACS Nano* **2021**, *15*, 2532–2541.
- (154) Chen, X.; Huet, B.; Choudhury, T. H.; Redwing, J. M.; Lu, T. M.; Wang, G. C. Orientation Domain Dispersions in Wafer Scale Epitaxial Monolayer WSe₂ on Sapphire. *Appl. Surf. Sci.* **2021**, *567*, 150798.
- (155) McCreary, K. M.; Hanbicki, A. T.; Sivaram, S. v.; Jonker, B. T. A- and B-Exciton Photoluminescence Intensity Ratio as a Measure of Sample Quality for Transition Metal Dichalcogenide Monolayers. *APL Mater.* **2018**, *6*, 111106.
- (156) Sebastian, A.; Pendurthi, R.; Choudhury, T. H.; Redwing, J. M.; Das, S. Benchmarking Monolayer MoS₂ and WS₂ Field-Effect Transistors. *Nat. Commun.* **2021**, *12*, 693.
- (157) Zheng, Y.; Ravichandran, H.; Schranghamer, T. F.; Trainor, N.; Redwing, J. M.; Das, S. Hardware Implementation of Bayesian Network Based on Two-Dimensional Memtransistors. *Nat. Commun.* **2022**, *13*, 5578.
- (158) Sebastian, A.; Pendurthi, R.; Kozhakhmetov, A.; Trainor, N.; Robinson, J. A.; Redwing, J. M.; Das, S. Two-Dimensional Materials-Based Probabilistic Synapses and Reconfigurable Neurons for Measuring Inference Uncertainty Using Bayesian Neural Networks. *Nat. Commun.* **2022**, *13*, 6139.
- (159) Kumar, P.; Lynch, J.; Song, B.; Ling, H.; Barrera, F.; Kisslinger, K.; Zhang, H.; Anantharaman, S. B.; Digani, J.; Zhu, H.; Choudhury, T. H.; McAleese, C.; Wang, X.; Conran, B. R.; Whear, O.; Motala, M. J.; Snure, M.; Muratore, C.; Redwing, J. M.; Glavin, N. R.; Stach, E. A.; Davoyan, A. R.; Jariwala, D. Light–Matter Coupling in Large-Area van Der Waals Superlattices. *Nat. Nanotechnol.* **2022**, *17*, 182–189.
- (160) Jayachandran, D.; Oberoi, A.; Sebastian, A.; Choudhury, T. H.; Shankar, B.; Redwing, J. M.; Das, S. A Low-Power Biomimetic Collision Detector Based on an in-Memory Molybdenum Disulfide Photodetector. *Nat. Electron* **2020**, *3*, 646–655.

- (161) Barton, A. T.; Yue, R.; Walsh, L. A.; Zhou, G.; Cormier, C.; Smyth, C. M.; Addou, R.; Colombo, L.; Wallace, R. M.; Hinkle, C. L. $\text{WSe}_{2-x}\text{Te}_x$ Alloys Grown by Molecular Beam Epitaxy. *2d Mater.* **2019**, *6*, 045027.
- (162) Xia, Y.; Zhang, J.; Yu, Z.; Jin, Y.; Tian, H.; Feng, Y.; Li, B.; Ho, W.; Liu, C.; Xu, H.; Jin, C.; Xie, M. A Shallow Acceptor of Phosphorous Doped in MoSe_2 Monolayer. *Adv. Electron Mater.* **2020**, *6*, 1900830.
- (163) Coelho, P. M.; Komsa, H. P.; Coy Diaz, H.; Ma, Y.; Krashenninnikov, A. v.; Batzill, M. Post-Synthesis Modifications of Two-Dimensional MoSe_2 or MoTe_2 by Incorporation of Excess Metal Atoms into the Crystal Structure. *ACS Nano* **2018**, *12*, 3975–3984.
- (164) Kozhakhmetov, A.; Schuler, B.; Tan, A. M. Z.; Cochrane, K. A.; Nasr, J. R.; El-Sherif, H.; Bansal, A.; Vera, A.; Bojan, V.; Redwing, J. M.; Bassim, N.; Das, S.; Hennig, R. G.; Weber-Bargioni, A.; Robinson, J. A. Scalable Substitutional Re-Doping and Its Impact on the Optical and Electronic Properties of Tungsten Diselenide. *Adv. Mater.* **2020**, *32*, 2005159.
- (165) Kozhakhmetov, A.; Stolz, S.; Tan, A. M. Z.; Pendurthi, R.; Bachu, S.; Turker, F.; Alem, N.; Kachian, J.; Das, S.; Hennig, R. G.; Gröning, O.; Schuler, B.; Robinson, J. A. Controllable P-Type Doping of 2D WSe_2 via Vanadium Substitution. *Adv. Funct. Mater.* **2021**, *31*, 2105252.
- (166) Noh, J. Y.; Kim, H.; Park, M.; Kim, Y. S. Deep-to-Shallow Level Transition of Re and Nb Dopants in Monolayer MoS_2 with Dielectric Environments. *Phys. Rev. B* **2015**, *92*, 115431.
- (167) Gao, H.; Suh, J.; Cao, M. C.; Joe, A. Y.; Mujid, F.; Lee, K. H.; Xie, S.; Poddar, P.; Lee, J. U.; Kang, K.; Kim, P.; Muller, D. A.; Park, J. Tuning Electrical Conductance of MoS_2 Monolayers through Substitutional Doping. *Nano Lett.* **2020**, *20*, 4095–4101.
- (168) Dabral, A.; Lu, A. K. A.; Chiappe, D.; Houssa, M.; Pourtois, G. A Systematic Study of Various 2D Materials in the Light of Defect Formation and Oxidation. *Phys. Chem. Chem. Phys.* **2019**, *21*, 1089–1099.
- (169) Longo, R. C.; Addou, R.; Santosh, K. C.; Noh, J. Y.; Smyth, C. M.; Barrera, D.; Zhang, C.; Hsu, J. W. P.; Wallace, R. M.; Cho, K. Intrinsic Air Stability Mechanisms of Two-Dimensional Transition Metal Dichalcogenide Surfaces: Basal versus Edge Oxidation. *2d Mater.* **2017**, *4*, 025050.
- (170) Chang, Y. R.; Nishimura, T.; Nagashio, K. Thermodynamic Perspective on the Oxidation of Layered Materials and Surface Oxide Amelioration in 2D Devices. *ACS Appl. Mater. Interfaces* **2021**, *13*, 43282–43289.
- (171) Diaz, H. C.; Chaghi, R.; Ma, Y.; Batzill, M. Molecular Beam Epitaxy of the van Der Waals Heterostructure MoTe_2 on MoS_2 : Phase, Thermal, and Chemical Stability. *2d Mater.* **2015**, *2*, 044010.
- (172) Vega-Mayoral, V.; Tian, R.; Kelly, A. G.; Griffin, A.; Harvey, A.; Borrelli, M.; Nisi, K.; Backes, C.; Coleman, J. N. Solvent Exfoliation Stabilizes TiS_2 Nanosheets against Oxidation, Facilitating Lithium Storage Applications. *Nanoscale* **2019**, *11*, 6206–6216.
- (173) Jo, S. S.; Singh, A.; Yang, L.; Tiwari, S. C.; Hong, S.; Krishnamoorthy, A.; Sales, M. G.; Oliver, S. M.; Fox, J.; Cavaleiro, R. L.; Snyder, D. W.; Vora, P. M.; McDonnell, S. J.; Vashishta, P.; Kalia, R. K.; Nakano, A.; Jaramillo, R. Growth Kinetics and Atomistic Mechanisms of Native Oxidation of $\text{ZrS}_x\text{Se}_{2-x}$ and MoS_2 Crystals. *Nano Lett.* **2020**, *20*, 8592–8599.
- (174) Alam, M. H.; Chowdhury, S.; Roy, A.; Wu, X.; Ge, R.; Rodder, M. A.; Chen, J.; Lu, Y.; Stern, C.; Houben, L.; Chrostowski, R.; Burlison, S. R.; Yang, S. J.; Serna, M. I.; Dodabalapur, A.; Mangolini, F.; Naveh, D.; Lee, J. C.; Banerjee, S. K.; Warner, J. H.; Akinwande, D. Wafer-Scalable Single-Layer Amorphous Molybdenum Trioxide. *ACS Nano* **2022**, *16*, 3756–3767.
- (175) Yang, L.; Tiwari, S. C.; Jo, S. S.; Hong, S.; Mishra, A.; Krishnamoorthy, A.; Kalia, R. K.; Nakano, A.; Jaramillo, R.; Vashishta, P. Unveiling Oxidation Mechanism of Bulk ZrS_2 . *MRS Adv.* **2021**, *6*, 303–306.
- (176) Yoon, A.; Kim, J. H.; Yoon, J.; Lee, Y.; Lee, Z. van Der Waals Epitaxial Formation of Atomic Layered $\alpha\text{-MoO}_3$ on MoS_2 by Oxidation. *ACS Appl. Mater. Interfaces* **2020**, *12*, 22029–22036.
- (177) Kim, Y.; Cruz, S. S.; Lee, K.; Alawode, B. O.; Choi, C.; Song, Y.; Johnson, J. M.; Heidelberger, C.; Kong, W.; Choi, S.; Qiao, K.; Almansouri, I.; Fitzgerald, E. A.; Kong, J.; Kolpak, A. M.; Hwang, J.; Kim, J. Remote Epitaxy through Graphene Enables Two-Dimensional Material-Based Layer Transfer. *Nature* **2017**, *544*, 340–343.
- (178) Bae, S. H.; Kum, H.; Kong, W.; Kim, Y.; Choi, C.; Lee, B.; Lin, P.; Park, Y.; Kim, J. Integration of Bulk Materials with Two-Dimensional Materials for Physical Coupling and Applications. *Nat. Mater.* **2019**, *18*, 550–560.
- (179) Ryu, H.; Park, H.; Kim, J.-H.; Ren, F.; Kim, J.; Lee, G.-H.; Pearton, S. J. Two-dimensional material templates for van der Waals epitaxy, remote epitaxy, and intercalation growth. *Appl. Phys. Rev.* **2022**, *9*, 031305.
- (180) Kim, H.; Kim, J. C.; Jeong, Y.; Yu, J.; Lu, K.; Lee, D.; Kim, N.; Jeong, H. Y.; Kim, J.; Kim, S. Role of Transferred Graphene on Atomic Interaction of GaAs for Remote Epitaxy. *J. Appl. Phys.* **2021**, *130*, 174901.
- (181) Wang, P.; Pandey, A.; Gim, J.; Shin, W. J.; Reid, E. T.; Laleyan, D. A.; Sun, Y.; Zhang, D.; Liu, Z.; Zhong, Z.; Hovden, R.; Mi, Z. Graphene-Assisted Molecular Beam Epitaxy of AlN for AlGaN Deep-Ultraviolet Light-Emitting Diodes. *Appl. Phys. Lett.* **2020**, *116*, 171905.
- (182) Kum, H. S.; Lee, H.; Kim, S.; Lindemann, S.; Kong, W.; Qiao, K.; Chen, P.; Irwin, J.; Lee, J. H.; Xie, S.; Subramanian, S.; Shim, J.; Bae, S. H.; Choi, C.; Ranno, L.; Seo, S.; Lee, S.; Bauer, J.; Li, H.; Lee, K.; Robinson, J. A.; Ross, C. A.; Schlom, D. G.; Rzechowski, M. S.; Eom, C. B.; Kim, J. Heterogeneous Integration of Single-Crystalline Complex-Oxide Membranes. *Nature* **2020**, *578*, 75–81.
- (183) Wang, D.; Lu, Y.; Meng, J.; Zhang, X.; Yin, Z.; Gao, M.; Wang, Y.; Cheng, L.; You, J.; Zhang, J. Remote Heteroepitaxy of Atomic Layered Hafnium Disulfide on Sapphire through Hexagonal Boron Nitride. *Nanoscale* **2019**, *11*, 9310–9318.
- (184) Zhou, G.; Younas, R.; Sun, T.; Harden, G.; Li, Y.; Hoffman, A. J.; Hinkle, C. L. Superior Quality Low-Temperature Growth of Three-Dimensional Semiconductors Using Intermediate Two-Dimensional Layers. *ACS Nano* **2022**, *16*, 19385–19392.
- (185) Jeong, J.; Jin, D. K.; Choi, J.; Jang, J.; Kang, B. K.; Wang, Q.; Park, W. I.; Jeong, M. S.; Bae, B.-S.; Yang, W. S.; Kim, M. J.; Hong, Y. J. Transferable, Flexible White Light-Emitting Diodes of GaN p - n Junction Microcrystals Fabricated by Remote Epitaxy. *Nano Energy* **2021**, *86*, 106075.
- (186) Kim, H.; Lu, K.; Liu, Y.; Kum, H. S.; Kim, K. S.; Qiao, K.; Bae, S. H.; Lee, S.; Ji, Y. J.; Kim, K. H.; Paik, H.; Xie, S.; Shin, H.; Choi, C.; Lee, J. H.; Dong, C.; Robinson, J. A.; Lee, J. H.; Ahn, J. H.; Yeom, G. Y.; Schlom, D. G.; Kim, J. Impact of 2D-3D Heterointerface on Remote Epitaxial Interaction through Graphene. *ACS Nano* **2021**, *15*, 10587–10596.
- (187) Zhou, G.; Sun, T.; Younas, R.; Hinkle, C. L. Materials and Device Strategies for Nanoelectronic 3D Heterogeneous Integration. In *IEEE International Conference on Simulation of Semiconductor Processes and Devices; SISPAD*; 2021; pp 163–166.
- (188) Koirala, N.; Brahlek, M.; Salehi, M.; Wu, L.; Dai, J.; Waugh, J.; Nummy, T.; Han, M. G.; Moon, J.; Zhu, Y.; Dessau, D.; Wu, W.; Armitage, N. P.; Oh, S. Record Surface State Mobility and Quantum Hall Effect in Topological Insulator Thin Films via Interface Engineering. *Nano Lett.* **2015**, *15*, 8245–8249.
- (189) Schlenk, T.; Bianchi, M.; Koleini, M.; Eich, A.; Pietzsch, O.; Wehling, T. O.; Frauenheim, T.; Balatsky, A.; Mi, J. L.; Iversen, B. B.; Wiebe, J.; Khajetoorians, A. A.; Hofmann, P.; Wiesendanger, R. Controllable Magnetic Doping of the Surface State of a Topological Insulator. *Phys. Rev. Lett.* **2013**, *110*, 126804.
- (190) Liu, Y.; Acuna, W.; Zhang, H.; Ho, D. Q.; Hu, R.; Wang, Z.; Janotti, A.; Bryant, G.; Davydov, A. v.; Zide, J. M. O.; Law, S. Bi_2Se_3 Growth on (001) GaAs Substrates for Terahertz Integrated Systems. *ACS Appl. Mater. Interfaces* **2022**, *14*, 42683–42691.
- (191) Chen, Y. L.; Analytis, J. G.; Chu, J. H.; Liu, Z. K.; Mo, S. K.; Qi, X. L.; Zhang, H. J.; Lu, P. H.; Dai, X.; Fang, Z.; Zhang, S. C.; Fisher, I. R.; Hussain, Z.; Shen, Z. X. Experimental Realization of a Three-Dimensional Topological Insulator, Bi_2Te_3 . *Science* **2009**, *325*, 178–181.

- (192) Wang, Z.; Law, S. Optimization of the Growth of the van Der Waals Materials Bi_2Se_3 and $(\text{Bi}_{0.5}\text{In}_{0.5})_2\text{Se}_3$ by Molecular Beam Epitaxy. *Cryst. Growth Des.* **2021**, *21*, 6752–6765.
- (193) Taskin, A. A.; Sasaki, S.; Segawa, K.; Ando, Y. Achieving Surface Quantum Oscillations in Topological Insulator Thin Films of Bi_2Se_3 . *Adv. Mater.* **2012**, *24*, 5581–5585.
- (194) Liu, X.; Smith, D. J.; Cao, H.; Chen, Y. P.; Fan, J.; Zhang, Y.-H.; Pimpinella, R. E.; Dobrowolska, M.; Furdyna, J. K. Characterization of Bi_2Te_3 and Bi_2Se_3 Topological Insulators Grown by MBE on (001) GaAs Substrates. *J. Vac. Sci. Technol. B* **2012**, *30*, 02B103.
- (195) Bansal, N.; Kim, Y. S.; Edrey, E.; Brahlek, M.; Horibe, Y.; Iida, K.; Tanimura, M.; Li, G. H.; Feng, T.; Lee, H. D.; Gustafsson, T.; Andrei, E.; Oh, S. Epitaxial Growth of Topological Insulator Bi_2Se_3 Film on Si(111) with Atomically Sharp Interface. *Thin Solid Films* **2011**, *520*, 224–229.
- (196) Jiang, Z.; Katmis, F.; Tang, C.; Wei, P.; Mooder, J. S.; Shi, J. A Comparative Transport Study of Bi_2Se_3 and $\text{Bi}_2\text{Se}_3/\text{Yttrium Iron Garnet}$. *Appl. Phys. Lett.* **2014**, *104*, 222409.
- (197) Bonell, F.; Cuxart, M. G.; Song, K.; Robles, R.; Ordejón, P.; Roche, S.; Mugarza, A.; Valenzuela, S. O. Growth of Twin-Free and Low-Doped Topological Insulators on $\text{BaF}_2(111)$. *Cryst. Growth Des.* **2017**, *17*, 4655–4660.
- (198) Richardella, A.; Kandala, A.; Lee, J. S.; Samarth, N. Characterizing the Structure of Topological Insulator Thin Films. *APL Mater.* **2015**, *3*, 083303.
- (199) Levy, I.; Garcia, T. A.; Shafique, S.; Tamargo, M. C. Reduced Twinning and Surface Roughness of Bi_2Se_3 and Bi_2Te_3 Layers Grown by Molecular Beam Epitaxy on Sapphire Substrates. *J. Vac. Sci. Technol. B* **2018**, *36*, 02D107.
- (200) Wang, Z. Y.; Li, H. D.; Guo, X.; Ho, W. K.; Xie, M. H. Growth Characteristics of Topological Insulator Bi_2Se_3 Films on Different Substrates. *J. Cryst. Growth* **2011**, *334*, 96–102.
- (201) Schwoebel, R. L.; Shipsey, E. J. Step Motion on Crystal Surfaces. *J. Appl. Phys.* **1966**, *37*, 3682–3686.
- (202) Ehrlich, G.; Hudda, F. G. Atomic View of Surface Self-Diffusion: Tungsten on Tungsten. *J. Chem. Phys.* **1966**, *44*, 1039–1049.
- (203) Li, S. C.; Han, Y.; Jia, J. F.; Xue, Q. K.; Liu, F. Determination of the Ehrlich-Schwobell Barrier in Epitaxial Growth of Thin Films. *Phys. Rev. B* **2006**, *74*, 195428.
- (204) Strosio, J. A.; Pierce, D. T.; Stiles, M. D.; Zangwill, A.; Sander, L. M. Coarsening of Unstable Surface Features during Fe(001) Homoepitaxy. *Phys. Rev. Lett.* **1995**, *75* (23), 4246–4249.
- (205) Politi, P.; Grenet, G.; Marty, A.; Ponchet, A.; Villain, J. Instabilities in Crystal Growth by Atomic or Molecular Beams. *Phys. Rep.* **2000**, *324*, 271–404.
- (206) Burton, W. K.; Cabrera, N.; Frank, F. C. The Growth of Crystals and the Equilibrium Structure of Their Surfaces. *Philosophical Transactions of the Royal Society A: Mathematical, Physical and Engineering Sciences* **1951**, *243*, 299–358.
- (207) Liu, Y.; Weinert, M.; Li, L. Spiral Growth without Dislocations: Molecular Beam Epitaxy of the Topological Insulator Bi_2Se_3 on Epitaxial Graphene/SiC(0001). *Phys. Rev. Lett.* **2012**, *108*, 115501.
- (208) Ginley, T. P.; Law, S. Growth of Bi_2Se_3 Topological Insulator Films Using a Selenium Cracker Source. *J. Vac. Sci. Technol. B* **2016**, *34*, 02L105.
- (209) Dai, J.; Wang, W.; Brahlek, M.; Koirala, N.; Salehi, M.; Oh, S.; Wu, W. Restoring Pristine Bi_2Se_3 Surfaces with an Effective Se Decapping Process. *Nano Res.* **2015**, *8*, 1222–1228.
- (210) Wang, Y.; Ginley, T. P.; Law, S. Growth of High-Quality Bi_2Se_3 Topological Insulators Using $(\text{Bi}_{1-x}\text{In}_x)_2\text{Se}_3$ Buffer Layers Growth of High-Quality Bi_2Se_3 Topological Insulators Using $(\text{Bi}_{1-x}\text{In}_x)_2\text{Se}_3$ Buffer Layers. *Journal of Vacuum Science & Technology B* **2018**, *36*, 02D101.
- (211) Tsoutsou, D.; Xenogiannopoulou, E.; Golias, E.; Tsipas, P.; Dimoulas, A. Evidence for Hybrid Surface Metallic Band in (4×4) Silicene on Ag(111). *Appl. Phys. Lett.* **2013**, *103*, 231604.
- (212) Deng, J.; Xia, B.; Ma, X.; Chen, H.; Shan, H.; Zhai, X.; Li, B.; Zhao, A.; Xu, Y.; Duan, W.; Zhang, S. C.; Wang, B.; Hou, J. G. Epitaxial Growth of Ultraflat Stanene with Topological Band Inversion. *Nat. Mater.* **2018**, *17*, 1081–1086.
- (213) Shi, Z.-Q.; Li, H.; Yuan, Q.-Q.; Song, Y.-H.; Lv, Y.-Y.; Shi, W.; Jia, Z.-Y.; Gao, L.; Chen, Y.-B.; Zhu, W.; Li, S.-C. Van Der Waals Heteroepitaxial Growth of Monolayer Sb in a Puckered Honeycomb Structure. *Adv. Mater.* **2019**, *31*, 1806130.
- (214) Chen, M. W.; Ovchinnikov, D.; Lazar, S.; Pizzochero, M.; Whitwick, M. B.; Surrente, A.; Baranowski, M.; Sanchez, O. L.; Gillet, P.; Plochocka, P.; Yazyev, O. v.; Kis, A. Highly Oriented Atomically Thin Ambipolar MoSe_2 Grown by Molecular Beam Epitaxy. *ACS Nano* **2017**, *11*, 6355–6361.
- (215) Nakano, M.; Wang, Y.; Kashiwabara, Y.; Matsuoka, H.; Iwasa, Y. Layer-by-Layer Epitaxial Growth of Scalable WSe_2 on Sapphire by Molecular Beam Epitaxy. *Nano Lett.* **2017**, *17*, 5595–5599.
- (216) Wang, Z.; Ginley, T. P.; Mambakkam, S. V.; Chandan, G.; Zhang, Y.; Ni, C.; Law, S. Plasmon Coupling in Topological Insulator Multilayers. *Phys. Rev. Mater.* **2020**, *4*, 115202.
- (217) Mleczko, M. J.; Zhang, C.; Lee, H. R.; Kuo, H. H.; Magyari-Köpe, B.; Moore, R. G.; Shen, Z. X.; Fisher, I. R.; Nishi, Y.; Pop, E. HfSe_2 and ZrSe_2 : Two-Dimensional Semiconductors with Native High- κ Oxides. *Sci. Adv.* **2017**, *3*, e170048.
- (218) Mermin, N. D.; Wagner, H. Absence of Ferromagnetism or Antiferromagnetism in One- or Two-Dimensional Isotropic Heisenberg Models. *Phys. Rev. Lett.* **1966**, *17*, 1133.
- (219) Huang, B.; Clark, G.; Navarro-Moratalla, E.; Klein, D. R.; Cheng, R.; Seyler, K. L.; Zhong, D.; Schmidgall, E.; McGuire, M. A.; Cobden, D. H.; Yao, W.; Xiao, D.; Jarillo-Herrero, P.; Xu, X. Layer-Dependent Ferromagnetism in a van Der Waals Crystal down to the Monolayer Limit. *Nature* **2017**, *546*, 270–273.
- (220) Gong, C.; Li, L.; Li, Z.; Ji, H.; Stern, A.; Xia, Y.; Cao, T.; Bao, W.; Wang, C.; Wang, Y.; Qiu, Z. Q.; Cava, R. J.; Louie, S. G.; Xia, J.; Zhang, X. Discovery of Intrinsic Ferromagnetism in Two-Dimensional van Der Waals Crystals. *Nature* **2017**, *546*, 265–269.
- (221) Wang, Q. H.; Bedoya-Pinto, A.; Blei, M.; Dismukes, A. H.; Hamo, A.; Jenkins, S.; Koperski, M.; Liu, Y.; Sun, Q. C.; Telford, E. J.; Kim, H. H.; Augustin, M.; Vool, U.; Yin, J. X.; Li, L. H.; Falin, A.; Dean, C. R.; Casanova, F.; Evans, R. F. L.; Chshiev, M.; Mishchenko, A.; Petrovic, C.; He, R.; Zhao, L.; Tsen, A. W.; Gerardot, B. D.; Brotons-Gisbert, M.; Guguchia, Z.; Roy, X.; Tongay, S.; Wang, Z.; Hasan, M. Z.; Wrachtrup, J.; Yacoby, A.; Fert, A.; Parkin, S.; Novoselov, K. S.; Dai, P.; Balicas, L.; Santos, E. J. G. The Magnetic Genome of Two-Dimensional van Der Waals Materials. *ACS Nano* **2022**, *16*, 6960–7079.
- (222) Xu, Y.; Ray, A.; Shao, Y. T.; Jiang, S.; Lee, K.; Weber, D.; Goldberger, J. E.; Watanabe, K.; Taniguchi, T.; Muller, D. A.; Mak, K. F.; Shan, J. Coexisting Ferromagnetic-Antiferromagnetic State in Twisted Bilayer CrI_3 . *Nat. Nanotechnol.* **2022**, *17*, 143–147.
- (223) Wu, Y.; Zhang, S.; Zhang, J.; Wang, W.; Zhu, Y. L.; Hu, J.; Yin, G.; Wong, K.; Fang, C.; Wan, C.; Han, X.; Shao, Q.; Taniguchi, T.; Watanabe, K.; Zang, J.; Mao, Z.; Zhang, X.; Wang, K. L. Néel-Type Skyrmion in $\text{WTe}_2/\text{Fe}_3\text{GeTe}_2$ van Der Waals Heterostructure. *Nat. Commun.* **2020**, *11*, 3860.
- (224) Sierra, J. F.; Fabian, J.; Kawakami, R. K.; Roche, S.; Valenzuela, S. O. Van Der Waals Heterostructures for Spintronics and Opto-Spintronics. *Nat. Nanotechnol.* **2021**, *16*, 856–868.
- (225) Kurebayashi, H.; Garcia, J. H.; Khan, S.; Sinova, J.; Roche, S. Magnetism, Symmetry and Spin Transport in van Der Waals Layered Systems. *Nature Reviews Physics* **2022**, *4*, 150–166.
- (226) Shcherbakov, D.; Stepanov, P.; Weber, D.; Wang, Y.; Hu, J.; Zhu, Y.; Watanabe, K.; Taniguchi, T.; Mao, Z.; Windl, W.; Goldberger, J.; Bockrath, M.; Lau, C. N. Raman Spectroscopy, Photocatalytic Degradation, and Stabilization of Atomically Thin Chromium Tri-Iodide. *Nano Lett.* **2018**, *18*, 4214–4219.
- (227) Bonilla, M.; Kolekar, S.; Ma, Y.; Diaz, H. C.; Kalappattil, V.; Das, R.; Eggers, T.; Gutierrez, H. R.; Phan, M. H.; Batzill, M. Strong Room-Temperature Ferromagnetism in VSe_2 Monolayers on van Der Waals Substrates. *Nat. Nanotechnol.* **2018**, *13*, 289–293.
- (228) Sun, X.; Li, W.; Wang, X.; Sui, Q.; Zhang, T.; Wang, Z.; Liu, L.; Li, D.; Feng, S.; Zhong, S.; Wang, H.; Bouchiat, V.; Nunez Regueiro, M.; Rougemaille, N.; Coraux, J.; Purbawati, A.; Hadj-Azzem, A.; Wang, Z.; Dong, B.; Wu, X.; Yang, T.; Yu, G.; Wang, B.; Han, Z.; Han, X.

Zhang, Z. Room Temperature Ferromagnetism in Ultra-Thin van Der Waals Crystals of 1T-CrTe₂. *Nano Res.* **2020**, *13*, 3358–3363.

(229) Ribeiro, M.; Gentile, G.; Marty, A.; Dosenovic, D.; Okuno, H.; Vergnaud, C.; Jacquot, J. F.; Jalabert, D.; Longo, D.; Ohresser, P.; Hallal, A.; Chshiev, M.; Boulle, O.; Bonell, F.; Jamet, M. Large-Scale Epitaxy of Two-Dimensional van Der Waals Room-Temperature Ferromagnet Fe₃GeTe₂. *NPJ. 2D Mater. Appl.* **2022**, *6*, 10.

(230) Chua, R.; Yang, J.; He, X.; Yu, X.; Yu, W.; Bussolotti, F.; Wong, P. K. J.; Loh, K. P.; Breese, M. B. H.; Goh, K. E. J.; Huang, Y. L.; Wee, A. T. S. Can Reconstructed Se-Deficient Line Defects in Monolayer VSe₂ Induce Magnetism? *Adv. Mater.* **2020**, *32*, 2000693.

(231) Heilmann, M.; Deinhart, V.; Tahraoui, A.; Höflich, K.; Lopes, J. M. J. Spatially Controlled Epitaxial Growth of 2D Heterostructures via Defect Engineering Using a Focused He Ion Beam. *NPJ. 2D Mater. Appl.* **2021**, *5*, 70.

(232) Yu, W.; Li, J.; Herng, T. S.; Wang, Z.; Zhao, X.; Chi, X.; Fu, W.; Abdelwahab, I.; Zhou, J.; Dan, J.; Chen, Z.; Chen, Z.; Li, Z.; Lu, J.; Pennycook, S. J.; Feng, Y. P.; Ding, J.; Loh, K. P. Chemically Exfoliated VSe₂ Monolayers with Room-Temperature Ferromagnetism. *Adv. Mater.* **2019**, *31*, 1903779.

(233) Purbawati, A.; Coraux, J.; Vogel, J.; Hadj-Azzem, A.; Wu, N. J.; Bendiab, N.; Jegouso, D.; Renard, J.; Marty, L.; Bouchiat, V.; Sulpice, A.; Aballe, L.; Foerster, M.; Genuzio, F.; Locatelli, A.; Mentes, T. O.; Han, Z. V.; Sun, X.; Núñez-Regueiro, M.; Rougemaille, N. In-Plane Magnetic Domains and Néel-like Domain Walls in Thin Flakes of the Room Temperature CrTe₂ van Der Waals Ferromagnet. *ACS Appl. Mater. Interfaces* **2020**, *12*, 30702–30710.

(234) Zhang, X.; Lu, Q.; Liu, W.; Niu, W.; Sun, J.; Cook, J.; Vaninger, M.; Miceli, P. F.; Singh, D. J.; Lian, S. W.; Chang, T. R.; He, X.; Du, J.; He, L.; Zhang, R.; Bian, G.; Xu, Y. Room-Temperature Intrinsic Ferromagnetism in Epitaxial CrTe₂ Ultrathin Films. *Nat. Commun.* **2021**, *12*, 2492.

(235) Meng, L.; Zhou, Z.; Xu, M.; Yang, S.; Si, K.; Liu, L.; Wang, X.; Jiang, H.; Li, B.; Qin, P.; Zhang, P.; Wang, J.; Liu, Z.; Tang, P.; Ye, Y.; Zhou, W.; Bao, L.; Gao, H. J.; Gong, Y. Anomalous Thickness Dependence of Curie Temperature in Air-Stable Two-Dimensional Ferromagnetic 1T-CrTe₂ Grown by Chemical Vapor Deposition. *Nat. Commun.* **2021**, *12*, 809.

(236) Saha, R.; Meyerheim, H. L.; Göbel, B.; Hazra, B. K.; Deniz, H.; Mohseni, K.; Antonov, V.; Ernst, A.; Knyazev, D.; Bedoya-Pinto, A.; Mertig, I.; Parkin, S. S. P. Observation of Néel-Type Skyrmions in Acentric Self-Intercalated Cr_{1+x}Te₂. *Nat. Commun.* **2022**, *13*, 3965.

(237) Seo, J.; Kim, D. Y.; An, E. S.; Kim, K.; Kim, G.-Y.; Hwang, S.-Y.; Kim, D. W.; Jang, B. G.; Kim, H.; Eom, G.; Seo, S. Y.; Stanina, R.; Muntwiler, M.; Lee, J.; Watanabe, K.; Taniguchi, T.; Jo, Y. J.; Lee, J.; Min, B. I.; Jo, M. H.; Yeom, H. W.; Choi, S.-Y.; Shim, J. H.; Kim, J. S. Nearly Room Temperature Ferromagnetism in a Magnetic Metal-Rich van Der Waals Metal. *Sci. Adv.* **2020**, *6*, eaay8912.

(238) Lopes, J. M. J.; Czubak, D.; Zallo, E.; Figueroa, A. I.; Guillemard, C.; Valvidares, M.; Rubio-Zuazo, J.; López-Sánchez, J.; Valenzuela, S. O.; Hanke, M.; Ramsteiner, M. Large-Area van Der Waals Epitaxy and Magnetic Characterization of Fe₃GeTe₂ Films on Graphene. *2d Mater.* **2021**, *8*, 041001.

(239) Roemer, R.; Liu, C.; Zou, K. Robust Ferromagnetism in Wafer-Scale Monolayer and Multilayer Fe₃GeTe₂. *NPJ. 2D Mater. Appl.* **2020**, *4*, 33.

(240) Deng, Y.; Yu, Y.; Song, Y.; Zhang, J.; Wang, N. Z.; Sun, Z.; Yi, Y.; Wu, Y. Z.; Wu, S.; Zhu, J.; Wang, J.; Chen, X. H.; Zhang, Y. Gate-Tunable Room-Temperature Ferromagnetism in Two-Dimensional Fe₃GeTe₂. *Nature* **2018**, *563*, 94–99.

(241) Chen, X.; Shao, Y. T.; Chen, R.; Susarla, S.; Hogan, T.; He, Y.; Zhang, H.; Wang, S.; Yao, J.; Ercius, P.; Muller, D. A.; Ramesh, R.; Birgeneau, R. J. Pervasive beyond Room-Temperature Ferromagnetism in a Doped van Der Waals Magnet. *Phys. Rev. Lett.* **2022**, *128*, 217203.

(242) Liu, S.; Yuan, X.; Zou, Y.; Sheng, Y.; Huang, C.; Zhang, E.; Ling, J.; Liu, Y.; Wang, W.; Zhang, C.; Zou, J.; Wang, K.; Xiu, F. Wafer-Scale Two-Dimensional Ferromagnetic Fe₃GeTe₂ Thin Films Grown by Molecular Beam Epitaxy. *NPJ. 2D Mater. Appl.* **2017**, *1*, 30.

(243) May, A. F.; Ovchinnikov, D.; Zheng, Q.; Hermann, R.; Calder, S.; Huang, B.; Fei, Z.; Liu, Y.; Xu, X.; McGuire, M. A. Ferromagnetism Near Room Temperature in the Cleavable van Der Waals Crystal Fe₃GeTe₂. *ACS Nano* **2019**, *13*, 4436–4442.

(244) Jiang, X.; Liu, Q.; Xing, J.; Liu, N.; Guo, Y.; Liu, Z.; Zhao, J. Recent Progress on 2D Magnets: Fundamental Mechanism, Structural Design and Modification. *Appl. Phys. Rev.* **2021**, *8*, 031305.

(245) Lasek, K.; Li, J.; Kolekar, S.; Coelho, P. M.; Guo, L.; Zhang, M.; Wang, Z.; Batzill, M. Synthesis and Characterization of 2D Transition Metal Dichalcogenides: Recent Progress from a Vacuum Surface Science Perspective. *Surf. Sci. Rep.* **2021**, *76*, 100523.

(246) Cortie, D. L.; Causer, G. L.; Rule, K. C.; Fritzsche, H.; Kreuzpaintner, W.; Klose, F. Two-Dimensional Magnets: Forgotten History and Recent Progress towards Spintronic Applications. *Adv. Funct. Mater.* **2020**, *30*, 1901414.

(247) Bonilla, M.; Kolekar, S.; Ma, Y.; Diaz, H. C.; Kalappattil, V.; Das, R.; Eggers, T.; Gutierrez, H. R.; Phan, M. H.; Batzill, M. Strong Room-Temperature Ferromagnetism in VSe₂ Monolayers on van Der Waals Substrates. *Nat. Nanotechnol.* **2018**, *13*, 289–293.

(248) Duvjir, G.; Choi, B. K.; Jang, I.; Ulstrup, S.; Kang, S.; Thi Ly, T.; Kim, S.; Choi, Y. H.; Jozwiak, C.; Bostwick, A.; Rotenberg, E.; Park, J. G.; Sankar, R.; Kim, K. S.; Kim, J.; Chang, Y. J. Emergence of a Metal-Insulator Transition and High-Temperature Charge-Density Waves in VSe₂ at the Monolayer Limit. *Nano Lett.* **2018**, *18*, 5432–5438.

(249) Chua, R.; Yang, J.; He, X.; Yu, X.; Yu, W.; Bussolotti, F.; Wong, P. K. J.; Loh, K. P.; Breese, M. B. H.; Goh, K. E. J.; Huang, Y. L.; Wee, A. T. S. Can Reconstructed Se-Deficient Line Defects in Monolayer VSe₂ Induce Magnetism? *Adv. Mater.* **2020**, *32*, 2000693.

(250) Wong, P. K. J.; Zhang, W.; Bussolotti, F.; Yin, X.; Herng, T. S.; Zhang, L.; Huang, Y. L.; Vinai, G.; Krishnamurthi, S.; Bukhvalov, D. W.; Zheng, Y. J.; Chua, R.; N'Diaye, A. T.; Morton, S. A.; Yang, C. Y.; Ou Yang, K. H.; Torelli, P.; Chen, W.; Goh, K. E. J.; Ding, J.; Lin, M. T.; Brocks, G.; de Jong, M. P.; Castro Neto, A. H.; Wee, A. T. S. Evidence of Spin Frustration in a Vanadium Diselenide Monolayer Magnet. *Adv. Mater.* **2019**, *31*, 1901185.

(251) Feng, J.; Biswas, D.; Rajan, A.; Watson, M. D.; Mazzola, F.; Clark, O. J.; Underwood, K.; Marković, I.; McLaren, M.; Hunter, A.; Burn, D. M.; Duffy, L. B.; Barua, S.; Balakrishnan, G.; Bertran, F.; Le Fèvre, P.; Kim, T. K.; Van Der Laan, G.; Hesjedal, T.; Wahl, P.; King, P. D. C. Electronic Structure and Enhanced Charge-Density Wave Order of Monolayer VSe₂. *Nano Lett.* **2018**, *18*, 4493–4499.

(252) Coelho, P. M.; Nguyen Cong, K.; Bonilla, M.; Kolekar, S.; Phan, M. H.; Avila, J.; Asensio, M. C.; Oleynik, I. I.; Batzill, M. Charge Density Wave State Suppresses Ferromagnetic Ordering in VSe₂ Monolayers. *J. Phys. Chem. C* **2019**, *123*, 14089–14096.

(253) Fumega, A. O.; Gobbi, M.; Dreher, P.; Wan, W.; González-Orellana, C.; Peña-Díaz, M.; Rogero, C.; Herrero-Martín, J.; Gargiani, P.; Ilyn, M.; Ugeda, M. M.; Pardo, V.; Blanco-Canosa, S. Absence of Ferromagnetism in VSe₂ Caused by Its Charge Density Wave Phase. *J. Phys. Chem. C* **2019**, *123*, 27802–27810.

(254) Zhao, X.; Fu, D.; Ding, Z.; Zhang, Y. Y.; Wan, D.; Tan, S. J. R.; Chen, Z.; Leng, K.; Dan, J.; Fu, W.; Geng, D.; Song, P.; Du, Y.; Venkatesan, T.; Pantelides, S. T.; Pennycook, S. J.; Zhou, W.; Loh, K. P. Mo-Terminated Edge Reconstructions in Nanoporous Molybdenum Disulfide Film. *Nano Lett.* **2018**, *18*, 482–490.

(255) Radhakrishnan, S.; Das, D.; Samanta, A.; de Los Reyes, C. A.; Deng, L.; Alemany, L. B.; Weldeghiorghis, T. K.; Khabashesku, V. N.; Kochat, V.; Jin, Z.; Sudeep, P. M.; Martí, A. A.; Chu, C. W.; Roy, A.; Tiwari, C. S.; Singh, A. K.; Ajayan, P. M. Fluorinated H-BN As a Magnetic Semiconductor. *Sci. Adv.* **2017**, *3*, e170084.

(256) Yun, S. J.; Cho, B. W.; Dinesh, T.; Yang, D. H.; Kim, Y. I.; Jin, J. W.; Yang, S.-H.; Nguyen, T. D.; Kim, Y.-M.; Kim, K. K.; Duong, D. L.; Kim, S.-G.; Lee, Y. H. Escalating Ferromagnetic Order via Se-Vacancies Near Vanadium in WSe₂ Monolayers. *Adv. Mater.* **2022**, *34*, 2106551.

(257) Tiwari, S.; Van de Put, M. L.; Sorée, B.; Vandenberghe, W. G. Magnetic Order and Critical Temperature of Substitutionally Doped Transition Metal Dichalcogenide Monolayers. *NPJ. 2D Mater. Appl.* **2021**, *5*, 1–7.

- (258) Yun, S. J.; Duong, D. L.; Ha, D. M.; Singh, K.; Phan, T. L.; Choi, W.; Kim, Y.-M.; Lee, Y. H. Ferromagnetic Order at Room Temperature in Monolayer WSe₂ Semiconductor via Vanadium Dopant. *Advanced Science* **2020**, *7*, 1903076.
- (259) Pham, Y. T. H.; Liu, M.; Jimenez, V. O.; Yu, Z.; Kalappattil, V.; Zhang, F.; Wang, K.; Williams, T.; Terrones, M.; Phan, M.-H. Tunable Ferromagnetism and Thermally Induced Spin Flip in Vanadium-Doped Tungsten Diselenide Monolayers at Room Temperature. *Adv. Mater.* **2020**, *32*, 2003607.
- (260) Zheng, H.; Cao, A.; Weinberger, C. R.; Huang, J. Y.; Du, K.; Wang, J.; Ma, Y.; Xia, Y.; Mao, S. X. Discrete Plasticity in Sub-10-nm-Sized Gold Crystals. *Nat. Commun.* **2010**, *1*, 144.
- (261) Lee, C.; Wei, X.; Kysar, J. W.; Hone, J. Measurement of the Elastic Properties and Intrinsic Strength of Monolayer Graphene. *Science* **2008**, *321*, 385–388.
- (262) Pérez Garza, H. H.; Kievit, E. W.; Schneider, G. F.; Staufer, U. Controlled, Reversible, and Nondestructive Generation of Uniaxial Extreme Strains (>10%) in Graphene. *Nano Lett.* **2014**, *14*, 4107–4113.
- (263) Bertolazzi, S.; Brivio, J.; Kis, A. Stretching and Breaking of Ultrathin MoS₂. *ACS Nano* **2011**, *5*, 9703–9709.
- (264) Shu, L.; Ke, S.; Fei, L.; Huang, W.; Wang, Z.; Gong, J.; Jiang, X.; Wang, L.; Li, F.; Lei, S.; Rao, Z.; Zhou, Y.; Zheng, R. K.; Yao, X.; Wang, Y.; Stengel, M.; Catalan, G. Photoflexoelectric Effect in Halide Perovskites. *Nat. Mater.* **2020**, *19*, 605–609.
- (265) Castellanos-Gomez, A.; Roldán, R.; Cappelluti, E.; Buscema, M.; Guinea, F.; van der Zant, H. S. J.; Steele, G. A. Local Strain Engineering in Atomically Thin MoS₂. *Nano Lett.* **2013**, *13*, 5361–5366.
- (266) da Cunha Rodrigues, G.; Zelenovskiy, P.; Romanyuk, K.; Luchkin, S.; Kopelevich, Y.; Kholkin, A. Strong Piezoelectricity in Single-Layer Graphene Deposited on SiO₂ Grating Substrates. *Nat. Commun.* **2015**, *6*, 7572.
- (267) Li, H.; Contryman, A. W.; Qian, X.; Ardakani, S. M.; Gong, Y.; Wang, X.; Weisse, J. M.; Lee, C. H.; Zhao, J.; Ajayan, P. M.; Li, J.; Manoharan, H. C.; Zheng, X. Optoelectronic Crystal of Artificial Atoms in Strain-Textured Molybdenum Disulphide. *Nat. Commun.* **2015**, *6*, 7381.
- (268) Niehues, I.; Schmidt, R.; Drüppel, M.; Marauhn, P.; Christiansen, D.; Selig, M.; Berghäuser, G.; Wigger, D.; Schneider, R.; Braasch, L.; Koch, R.; Castellanos-Gomez, A.; Kuhn, T.; Knorr, A.; Malic, E.; Rohlfing, M.; Michaelis De Vasconcellos, S.; Bratschkitsch, R. Strain Control of Exciton-Phonon Coupling in Atomically Thin Semiconductors. *Nano Lett.* **2018**, *18*, 1751–1757.
- (269) Liang, J.; Zhang, J.; Li, Z.; Hong, H.; Wang, J.; Zhang, Z.; Zhou, X.; Qiao, R.; Xu, J.; Gao, P.; Liu, Z.; Liu, Z.; Sun, Z.; Meng, S.; Liu, K.; Yu, D. Monitoring Local Strain Vector in Atomic-Layered MoSe₂ by Second-Harmonic Generation. *Nano Lett.* **2017**, *17*, 7539–7543.
- (270) Maiti, R.; Patil, C.; Saadi, M. A. S. R.; Xie, T.; Azadani, J. G.; Uluutku, B.; Amin, R.; Briggs, A. F.; Miscuglio, M.; van Thourhout, D.; Solares, S. D.; Low, T.; Agarwal, R.; Bank, S. R.; Sorger, V. J. Strain-Engineered High-Responsivity MoTe₂ Photodetector for Silicon Photonic Integrated Circuits. *Nat. Photonics* **2020**, *14*, 578–584.
- (271) Hou, W.; Azizmanesh, A.; Sewaket, A.; Peña, T.; Watson, C.; Liu, M.; Askari, H.; Wu, S. M. Strain-Based Room-Temperature Non-Volatile MoTe₂ Ferroelectric Phase Change Transistor. *Nat. Nanotechnol.* **2019**, *14*, 668–673.
- (272) Aslan, O. B.; Datye, I. M.; Mleczko, M. J.; Sze Cheung, K.; Krylyuk, S.; Bruma, A.; Kalish, I.; Davydov, A. v.; Pop, E.; Heinz, T. F. Probing the Optical Properties and Strain-Tuning of Ultrathin Mo_{1-x}W_xTe₂. *Nano Lett.* **2018**, *18*, 2485–2491.
- (273) Harats, M. G.; Kirchhof, J. N.; Qiao, M.; Greben, K.; Bolotin, K. I. Dynamics and Efficient Conversion of Excitons to Trions in Non-Uniformly Strained Monolayer WS₂. *Nat. Photonics* **2020**, *14*, 324–329.
- (274) Wang, Y.; Cong, C.; Yang, W.; Shang, J.; Peimyo, N.; Chen, Y.; Kang, J.; Wang, J.; Huang, W.; Yu, T. Strain-Induced Direct–Indirect Bandgap Transition and Phonon Modulation in Monolayer WS₂. *Nano Res.* **2015**, *8*, 2562–2572.
- (275) Moon, H.; Grosso, G.; Chakraborty, C.; Peng, C.; Taniguchi, T.; Watanabe, K.; Englund, D. Dynamic Exciton Funneling by Local Strain Control in a Monolayer Semiconductor. *Nano Lett.* **2020**, *20*, 6791–6797.
- (276) Desai, S. B.; Seol, G.; Kang, J. S.; Fang, H.; Battaglia, C.; Kapadia, R.; Ager, J. W.; Guo, J.; Javey, A. Strain-Induced Indirect to Direct Bandgap Transition in Multilayer WSe₂. *Nano Lett.* **2014**, *14*, 4592–4597.
- (277) Zhao, C.; Hu, M.; Qin, J.; Xia, B.; Liu, C.; Wang, S.; Guan, D. D.; Li, Y.; Zheng, H.; Liu, J.; Jia, J. Strain Tunable Semimetal-Topological-Insulator Transition in Monolayer 1 T'-WTe₂. *Phys. Rev. Lett.* **2020**, *125*, 046801.
- (278) Yang, S.; Wang, C.; Sahin, H.; Chen, H.; Li, Y.; Li, S. S.; Suslu, A.; Peeters, F. M.; Liu, Q.; Li, J.; Tongay, S. Tuning the Optical, Magnetic, and Electrical Properties of ReSe₂ by Nanoscale Strain Engineering. *Nano Lett.* **2015**, *15*, 1660–1666.
- (279) Flötotto, D.; Bai, Y.; Chan, Y. H.; Chen, P.; Wang, X.; Rossi, P.; Xu, C. Z.; Zhang, C.; Hlevyack, J. A.; Denlinger, J. D.; Hong, H.; Chou, M. Y.; Mittemeijer, E. J.; Eckstein, J. N.; Chiang, T. C. In Situ Strain Tuning of the Dirac Surface States in Bi₂Se₃ Films. *Nano Lett.* **2018**, *18*, 5628–5632.
- (280) Kim, H.; Uddin, S. Z.; Lien, D. H.; Yeh, M.; Azar, N. S.; Balendhran, S.; Kim, T.; Gupta, N.; Rho, Y.; Grigoropoulos, C. P.; Crozier, K. B.; Javey, A. Actively Variable-Spectrum Optoelectronics with Black Phosphorus. *Nature* **2021**, *596*, 232–237.
- (281) Tao, J.; Shen, W.; Wu, S.; Liu, L.; Feng, Z.; Wang, C.; Hu, C.; Yao, P.; Zhang, H.; Pang, W.; Duan, X.; Liu, J.; Zhou, C.; Zhang, D. Mechanical and Electrical Anisotropy of Few-Layer Black Phosphorus. *ACS Nano* **2015**, *9*, 11362–11370.
- (282) Cenker, J.; Sivakumar, S.; Xie, K.; Miller, A.; Thijssen, P.; Liu, Z.; Dismukes, A.; Fonseca, J.; Anderson, E.; Zhu, X.; Roy, X.; Xiao, D.; Chu, J. H.; Cao, T.; Xu, X. Reversible Strain-Induced Magnetic Phase Transition in a van Der Waals Magnet. *Nat. Nanotech* **2022**, *17*, 256–261.
- (283) Wang, Y.; Wang, C.; Liang, S.-J.; Ma, Z.; Xu, K.; Liu, X.; Zhang, L.; Admasu, A. S.; Cheong, S.-W.; Wang, L.; Chen, M.; Liu, Z.; Cheng, B.; Ji, W.; Miao, F. Strain-Sensitive Magnetization Reversal of a van Der Waals Magnet. *Adv. Mater.* **2020**, *32*, 2004533.
- (284) Wang, Y.; Sun, Y. Y.; Zhang, S.; Lu, T. M.; Shi, J. Band Gap Engineering of a Soft Inorganic Compound PbI₂ by Incommensurate van Der Waals Epitaxy. *Appl. Phys. Lett.* **2016**, *108*, 013105.
- (285) Jiang, J.; Chen, Z.; Hu, Y.; Xiang, Y.; Zhang, L.; Wang, Y.; Wang, G. C.; Shi, J. Flexo-Photovoltaic Effect in MoS₂. *Nat. Nanotech* **2021**, *16*, 894–901.
- (286) Guo, R.; You, L.; Lin, W.; Abdelsamie, A.; Shu, X.; Zhou, G.; Chen, S.; Liu, L.; Yan, X.; Wang, J.; Chen, J. Continuously Controllable Photoconductance in Freestanding BiFeO₃ by the Macroscopic Flexoelectric Effect. *Nat. Commun.* **2020**, *11*, 2571.
- (287) Yang, M. M.; Kim, D. J.; Alexe, M. Flexo-Photovoltaic Effect. *Science* **2018**, *360*, 904–907.
- (288) Xiao, D.; Chang, M. C.; Niu, Q. Berry Phase Effects on Electronic Properties. *Rev. Mod. Phys.* **2010**, *82*, 1959–2007.
- (289) Conley, H. J.; Wang, B.; Ziegler, J. I.; Haglund, R. F.; Pantelides, S. T.; Bolotin, K. I. Bandgap Engineering of Strained Monolayer and Bilayer MoS₂. *Nano Lett.* **2013**, *13*, 3626–3630.
- (290) Feng, J.; Qian, X.; Huang, C. W.; Li, J. Strain-Engineered Artificial Atom as a Broad-Spectrum Solar Energy Funnel. *Nat. Photonics* **2012**, *6*, 866–872.
- (291) Branny, A.; Kumar, S.; Proux, R.; Gerardot, B. D. Deterministic Strain-Induced Arrays of Quantum Emitters in a Two-Dimensional Semiconductor. *Nat. Commun.* **2017**, *8*, 15053.
- (292) Palacios-Berraquero, C.; Kara, D. M.; Montblanch, A. R. P.; Barbone, M.; Latawiec, P.; Yoon, D.; Ott, A. K.; Loncar, M.; Ferrari, A. C.; Atatüre, M. Large-Scale Quantum-Emitter Arrays in Atomically Thin Semiconductors. *Nat. Commun.* **2017**, *8*, 15093.
- (293) Song, S.; Keum, D. H.; Cho, S.; Perello, D.; Kim, Y.; Lee, Y. H. Room Temperature Semiconductor-Metal Transition of MoTe₂ Thin Films Engineered by Strain. *Nano Lett.* **2016**, *16*, 188–193.

- (294) Wu, W.; Wang, L.; Li, Y.; Zhang, F.; Lin, L.; Niu, S.; Chenet, D.; Zhang, X.; Hao, Y.; Heinz, T. F.; Hone, J.; Wang, Z. L. Piezoelectricity of Single-Atomic-Layer MoS₂ for Energy Conversion and Piezotronics. *Nature* **2014**, *514*, 470–474.
- (295) Wang, Y.; Sun, Y. Y.; Zhang, S.; Lu, T. M.; Shi, J. Band Gap Engineering of a Soft Inorganic Compound PbI₂ by Incommensurate van Der Waals Epitaxy. *Appl. Phys. Lett.* **2016**, *108*, 013105.
- (296) Abudurusuli, A.; Li, J.; Pan, S. A Review on the Recently Developed Promising Infrared Nonlinear Optical Materials. *Dalton Transactions* **2021**, *50*, 3155–3160.
- (297) You, J. W.; Bongu, S. R.; Bao, Q.; Panoiu, N. C. Nonlinear Optical Properties and Applications of 2D Materials: Theoretical and Experimental Aspects. *Nanophotonics* **2018**, *8*, 63–97.
- (298) Li, Y.; Rao, Y.; Mak, K. F.; You, Y.; Wang, S.; Dean, C. R.; Heinz, T. F. Probing Symmetry Properties of Few-Layer MoS₂ and h-BN by Optical Second-Harmonic Generation. *Nano Lett.* **2013**, *13*, 3329–3333.
- (299) Yin, X.; Ye, Z.; Chenet, D. A.; Ye, Y.; O'Brien, K.; Hone, J. C.; Zhang, X. Edge Nonlinear Optics on a MoS₂ Atomic Monolayer. *Science* **2014**, *344*, 488–490.
- (300) Carvalho, B. R.; Wang, Y.; Fujisawa, K.; Zhang, T.; Kahn, E.; Bilgin, I.; Ajayan, P. M.; de Paula, A. M.; Pimenta, M. A.; Kar, S.; Crespi, V. H.; Terrones, M.; Malard, L. M. Nonlinear Dark-Field Imaging of One-Dimensional Defects in Monolayer Dichalcogenides. *Nano Lett.* **2020**, *20*, 284–291.
- (301) Lin, K. I.; Ho, Y. H.; Liu, S. B.; Ciou, J. J.; Huang, B. T.; Chen, C.; Chang, H. C.; Tu, C. L.; Chen, C. H. Atom-Dependent Edge-Enhanced Second-Harmonic Generation on MoS₂ Monolayers. *Nano Lett.* **2018**, *18*, 793–797.
- (302) Kumar, N.; Najmaei, S.; Cui, Q.; Ceballos, F.; Ajayan, P. M.; Lou, J.; Zhao, H. Second Harmonic Microscopy of Monolayer MoS₂. *Phys. Rev. B* **2013**, *87*, 161403.
- (303) Zhou, X.; Cheng, J.; Zhou, Y.; Cao, T.; Hong, H.; Liao, Z.; Wu, S.; Peng, H.; Liu, K.; Yu, D. Strong Second-Harmonic Generation in Atomic Layered GaSe. *J. Am. Chem. Soc.* **2015**, *137*, 7994–7997.
- (304) Zhou, J.; Shi, J.; Zeng, Q.; Chen, Y.; Niu, L.; Liu, F.; Yu, T.; Suenaga, K.; Liu, X.; Lin, J.; Liu, Z. InSe Monolayer: Synthesis, Structure and Ultra-High Second-Harmonic Generation. *2d Mater.* **2018**, *5*, 025019.
- (305) Clark, D. J.; Senthilkumar, V.; Le, C. T.; Weerawarne, D. L.; Shim, B.; Jang, J. I.; Shim, J. H.; Cho, J.; Sim, Y.; Seong, M.-J.; Rhim, S. H.; Freeman, A. J.; Chung, K.-H.; Kim, Y. S. Strong Optical Nonlinearity of CVD-Grown MoS₂ Monolayer as Probed by Wavelength-Dependent Second-Harmonic Generation. *Phys. Rev. B* **2014**, *90*, 121409.
- (306) Clark, D. J.; Senthilkumar, V.; Le, C. T.; Weerawarne, D. L.; Shim, B.; Jang, J. I.; Shim, J. H.; Cho, J.; Sim, Y.; Seong, M.-J.; Rhim, S. H.; Freeman, A. J.; Chung, K.-H.; Kim, Y. S. Erratum: Strong Optical Nonlinearity of CVD-Grown MoS₂ Monolayer as Probed by Wavelength-Dependent Second-Harmonic Generation [Phys. Rev. B **90**, 121409(R) (2014)]. *Phys. Rev. B* **2015**, *92*, 159901.
- (307) Attacalite, C.; Palummo, M.; Cannuccia, E.; Grüning, M. Second-Harmonic Generation in Single-Layer Monochalcogenides: A Response from First-Principles Real-Time Simulations. *Phys. Rev. Mater.* **2019**, *3*, 074003.
- (308) Ribeiro-Soares, J.; Janisch, C.; Liu, Z.; Elías, A. L.; Dresselhaus, M. S.; Terrones, M.; Cançado, L. G.; Jorio, A. Second Harmonic Generation in WSe₂. *2d Mater.* **2015**, *2*, 045015.
- (309) Janisch, C.; Wang, Y.; Ma, D.; Mehta, N.; Elías, A. L.; Perea-López, N.; Terrones, M.; Crespi, V.; Liu, Z. Extraordinary Second Harmonic Generation in Tungsten Disulfide Monolayers. *Sci. Rep.* **2014**, *4*, 5530.
- (310) Jackson, A. G.; Ohmer, M. C.; LeClair, S. R. Relationship of the Second Order Nonlinear Optical Coefficient to Energy Gap in Inorganic Non-Centrosymmetric Crystals. *Infrared Phys. Technol.* **1997**, *38*, 233–244.
- (311) Taghizadeh, A.; Thygesen, K. S.; Pedersen, T. G. Two-Dimensional Materials with Giant Optical Nonlinearities near the Theoretical Upper Limit. *ACS Nano* **2021**, *15*, 7155–7167.
- (312) Steves, M. A.; Wang, Y.; Briggs, N.; Zhao, T.; El-Sherif, H.; Bersch, B. M.; Subramanian, S.; Dong, C.; Bowen, T.; Fuente Duran, A. D. L.; Nisi, K.; Lassauniere, M.; Wurstbauer, U.; Bassim, N. D.; Fonseca, J.; Robinson, J. T.; Crespi, V. H.; Robinson, J.; Knappenberger Jr, K. L. Unexpected Near-Infrared to Visible Nonlinear Optical Properties from 2-D Polar Metals. *Nano Lett.* **2020**, *20*, 8312–8318.
- (313) He, J.; Lee, S. H.; Naccarato, F.; Brunin, G.; Zu, R.; Wang, Y.; Miao, L.; Wang, H.; Alem, N.; Hautier, G.; Rignanese, G. M.; Mao, Z.; Gopalan, V. SnP₂S₆: A Promising Infrared Nonlinear Optical Crystal with Strong Nonresonant Second Harmonic Generation and Phase-Matchability. *ACS Photonics* **2022**, *9*, 1724–1732.
- (314) Steves, M. A.; Jawaid, A.; Struzyk, A.; Torsi, R.; Robinson, J. A.; Vaia, R. A.; Knappenberger, K. L. Tenth-Order Multiphoton Excitation and Saturable Second Harmonic Generation in Polyoxometalate-Exfoliated Molybdenum Disulfide. *J. Phys. Chem. C* **2022**, *126*, 18036–18046.
- (315) Cao, Y.; Fatemi, V.; Fang, S.; Watanabe, K.; Taniguchi, T.; Kaxiras, E.; Jarillo-Herrero, P. Unconventional Superconductivity in Magic-Angle Graphene Superlattices. *Nature* **2018**, *556*, 43–50.
- (316) Zhang, K.; Guo, Y.; Ji, Q.; Lu, A. Y.; Su, C.; Wang, H.; Puzetky, A. A.; Geohegan, D. B.; Qian, X.; Fang, S.; Kaxiras, E.; Kong, J.; Huang, S. Enhancement of van Der Waals Interlayer Coupling through Polar Janus MoSSe. *J. Am. Chem. Soc.* **2020**, *142*, 17499–17507.
- (317) Zhang, K.; Guo, Y.; Larson, D. T.; Zhu, Z.; Fang, S.; Kaxiras, E.; Kong, J.; Huang, S. Spectroscopic Signatures of Interlayer Coupling in Janus MoSSe/MoS₂ Heterostructures. *ACS Nano* **2021**, *15*, 14394–14403.
- (318) Hu, T.; Jia, F.; Zhao, G.; Wu, J.; Stroppa, A.; Ren, W. Intrinsic and Anisotropic Rashba Spin Splitting in Janus Transition-Metal Dichalcogenide Monolayers. *Phys. Rev. B* **2018**, *97*, 235404.
- (319) Maniyara, R. A.; Rodrigo, D.; Yu, R.; Canet-Ferrer, J.; Ghosh, D. S.; Yongsunthorn, R.; Baker, D. E.; Rezikyan, A.; García de Abajo, F. J.; Pruneri, V. Tunable Plasmons in Ultrathin Metal Films. *Nat. Photonics* **2019**, *13*, 328–333.
- (320) Liu, Y.; Wang, Z.; Zhang, X.; Liu, C.; Liu, Y.; Zhou, Z.; Wang, J.; Wang, Q.; Liu, Y.; Xi, C.; Tian, M.; Liu, H.; Feng, J.; Xie, X. C.; Wang, J. Interface-Induced Zeeman-Protected Superconductivity in Ultrathin Crystalline Lead Films. *Phys. Rev. X* **2018**, *8*, 021002.
- (321) Wang, T.; Park, M.; Yu, Q.; Zhang, J.; Yang, Y. Stability and Synthesis of 2D Metals and Alloys: A Review. *Mater. Today Adv.* **2020**, *8*, 100092.
- (322) Riedl, C.; Coletti, C.; Iwasaki, T.; Zakharov, A. A.; Starke, U. Quasi-Free-Standing Epitaxial Graphene on SiC Obtained by Hydrogen Intercalation. *Phys. Rev. Lett.* **2009**, *103*, 246804.
- (323) Nisi, K.; Subramanian, S.; He, W.; Ulman, K. A.; El-Sherif, H.; Sigger, F.; Lassauniere, M.; Wetherington, M. T.; Briggs, N.; Gray, J.; Holleitner, A. W.; Bassim, N.; Quek, S. Y.; Robinson, J. A.; Wurstbauer, U. Light–Matter Interaction in Quantum Confined 2D Polar Metals. *Adv. Funct. Mater.* **2021**, *31*, 2005977.
- (324) Steves, M. A.; Rajabpour, S.; Wang, K.; Dong, C.; He, W.; Quek, S. Y.; Robinson, J. A.; Knappenberger, K. L. Atomic-Level Structure Determines Electron-Phonon Scattering Rates in 2-D Polar Metal Heterostructures. *ACS Nano* **2021**, *15*, 17780–17789.
- (325) Chang, L.; Pfeiffer, M. H. P.; Volet, N.; Zervas, M.; Peters, J. D.; Manganelli, C. L.; Stanton, E. J.; Li, Y.; Kippenberg, T. J.; Bowers, J. E. Heterogeneous Integration of Lithium Niobate and Silicon Nitride Waveguides for Wafer-Scale Photonic Integrated Circuits on Silicon. *Opt. Lett.* **2017**, *42*, 803.
- (326) Steves, M. A.; Knappenberger, K. L. Achieving Sub-Diffraction Spatial Resolution Using Combined Fourier Transform Spectroscopy and Nonlinear Optical Microscopy. *J. Chem. Phys.* **2022**, *156*, 021101.
- (327) Steves, M. A.; Knappenberger, K. L., Jr. Improving Spectral, Spatial, and Mechanistic Resolution Using Fourier Transform Nonlinear Optics: A Tutorial Review. *ACS Phys. Chem. Au* **2023**, *3*, 130–142.
- (328) Silver, A.; Kitadai, H.; Liu, H.; Granzier-Nakajima, T.; Terrones, M.; Ling, X.; Huang, S. Chemical and Bio Sensing Using Graphene-Enhanced Raman Spectroscopy. *Nanomaterials* **2019**, *9*, 516.

- (329) Ignatova, T.; Pourianejad, S.; Li, X.; Schmidt, K.; Aryeetey, F.; Aravamudan, S.; Rotkin, S. v. Multidimensional Imaging Reveals Mechanisms Controlling Multimodal Label-Free Biosensing in Vertical 2D-Heterostructures. *ACS Nano* **2022**, *16*, 2598–2607.
- (330) Ranasinghe, J. C.; Jain, A.; Wu, W.; Zhang, K.; Wang, Z.; Huang, S. Engineered 2D Materials for Optical Bioimaging and Path toward Therapy and Tissue Engineering. *J. Mater. Res.* **2022**, *37*, 1689–1713.
- (331) Jain, S.; Nehra, M.; Kumar, R.; Dilbaghi, N.; Hu, T.; Kumar, S.; Kaushik, A.; Li, C.-Z. Internet of Medical Things (IoMT)-Integrated Biosensors for Point-of-Care Testing of Infectious Diseases. *Biosens. Bioelectron* **2021**, *179*, 113074.
- (332) Humpel, C. Identifying and Validating Biomarkers for Alzheimer's Disease. *Trends Biotechnol* **2011**, *29*, 26–32.
- (333) Ling, X.; Huang, S.; Deng, S.; Mao, N.; Kong, J.; Dresselhaus, M. S.; Zhang, J. Lighting Up the Raman Signal of Molecules in the Vicinity of Graphene Related Materials. *Acc. Chem. Res.* **2015**, *48*, 1862–1870.
- (334) Huang, S.; Ling, X.; Liang, L.; Song, Y.; Fang, W.; Zhang, J.; Kong, J.; Meunier, V.; Dresselhaus, M. S. Molecular Selectivity of Graphene-Enhanced Raman Scattering. *Nano Lett.* **2015**, *15*, 2892–2901.
- (335) Kitadai, H.; Wang, X.; Mao, N.; Huang, S.; Ling, X. Enhanced Raman Scattering on Nine 2D van Der Waals Materials. *J. Phys. Chem. Lett.* **2019**, *10*, 3043–3050.
- (336) Tao, L.; Chen, K.; Chen, Z.; Cong, C.; Qiu, C.; Chen, J.; Wang, X.; Chen, H.; Yu, T.; Xie, W.; Deng, S.; Xu, J.-B. 1T' Transition Metal Telluride Atomic Layers for Plasmon-Free SERS at Femtomolar Levels. *J. Am. Chem. Soc.* **2018**, *140*, 8696–8704.
- (337) Ye, J.; Yeh, Y.-T.; Xue, Y.; Wang, Z.; Zhang, N.; Liu, H.; Zhang, K.; Ricker, R.; Yu, Z.; Roder, A.; Perea Lopez, N.; Organtini, L.; Greene, W.; Hafenstein, S.; Lu, H.; Ghedin, E.; Terrones, M.; Huang, S.; Huang, S. X. Accurate Virus Identification with Interpretable Raman Signatures by Machine Learning. *Proc. Natl. Acad. Sci. U. S. A.* **2022**, *119*, e2118836119.
- (338) Wang, Z.; Ye, J.; Zhang, K.; Ding, L.; Granzier-Nakajima, T.; Ranasinghe, J. C.; Xue, Y.; Sharma, S.; Biase, I.; Terrones, M.; Choi, S. H.; Ran, C.; Tanzi, R. E.; Huang, S. X.; Zhang, C.; Huang, S. Rapid Biomarker Screening of Alzheimer's Disease by Interpretable Machine Learning and Graphene-Assisted Raman Spectroscopy. *ACS Nano* **2022**, *16*, 6426–6436.
- (339) Ranc, V.; Markova, Z.; Hajdich, M.; Prucek, R.; Kvitek, L.; Kaslik, J.; Safarova, K.; Zboril, R. Magnetically Assisted Surface-Enhanced Raman Scattering Selective Determination of Dopamine in an Artificial Cerebrospinal Fluid and a Mouse Striatum Using Fe₃O₄/Ag Nanocomposite. *Anal. Chem.* **2014**, *86*, 2939–2946.
- (340) Huang, S.; Pandey, R.; Barman, I.; Kong, J.; Dresselhaus, M. Raman Enhancement of Blood Constituent Proteins Using Graphene. *ACS Photonics* **2018**, *5*, 2978–2982.
- (341) Wen, W.; Song, Y.; Yan, X.; Zhu, C.; Du, D.; Wang, S.; Asiri, A. M.; Lin, Y. Recent Advances in Emerging 2D Nanomaterials for Biosensing and Bioimaging Applications. *Mater. Today* **2018**, *21*, 164–177.
- (342) Dubey, N.; Bentini, R.; Islam, I.; Cao, T.; Castro Neto, A. H.; Rosa, V. Graphene: A Versatile Carbon-Based Material for Bone Tissue Engineering. *Stem Cells Int.* **2015**, *2015*, 804213.
- (343) Li, B. L.; Setyawati, M. I.; Chen, L.; Xie, J.; Ariga, K.; Lim, C. T.; Garaj, S.; Leong, D. T. Directing Assembly and Disassembly of 2D MoS₂ Nanosheets with DNA for Drug Delivery. *ACS Appl. Mater. Interfaces* **2017**, *9*, 15286–15296.
- (344) Welch, N. L.; Zhu, M.; Hua, C.; Weller, J.; Mirhashemi, M. E.; Nguyen, T. G.; Mantena, S.; Bauer, M. R.; Shaw, B. M.; Ackerman, C. M.; Thakku, S. G.; Tse, M. W.; Kehe, J.; Uwera, M. M.; Eversley, J. S.; Bielwaski, D. A.; McGrath, G.; Braidt, J.; Johnson, J.; Cerrato, F.; Moreno, G. K.; Krasilnikova, L. A.; Petros, B. A.; Gionet, G. L.; King, E.; Huard, R. C.; Jalbert, S. K.; Cleary, M. L.; Fitzgerald, N. A.; Gabriel, S. B.; Gallagher, G. R.; Smole, S. C.; Madoff, L. C.; Brown, C. M.; Keller, M. W.; Wilson, M. M.; Kirby, M. K.; Barnes, J. R.; Park, D. J.; Siddle, K. J.; Happei, C. T.; Hung, D. T.; Springer, M.; MacInnis, B. L.; Lemieux, J. E.; Rosenberg, E.; Branda, J. A.; Blainey, P. C.; Sabeti, P. C.; Myhrvold, C. Multiplexed CRISPR-Based Microfluidic Platform for Clinical Testing of Respiratory Viruses and Identification of SARS-CoV-2 Variants. *Nat. Med.* **2022**, *28*, 1083–1094.
- (345) Aryeetey, F.; Ignatova, T.; Aravamudan, S. Quantification of Defects Engineered in Single Layer MoS₂. *RSC Adv.* **2020**, *10*, 22996–23001.
- (346) Ayodele, O. O.; Pourianejad, S.; Trofe, A.; Prokofjevs, A.; Ignatova, T. Application of Soxhlet Extractor for Ultra-Clean Graphene Transfer. *ACS Omega* **2022**, *7*, 7297–7303.
- (347) Neumann, C.; Reichardt, S.; Venezuela, P.; Drögeler, M.; Banszerus, L.; Schmitz, M.; Watanabe, K.; Taniguchi, T.; Mauri, F.; Beschoten, B.; Rotkin, S. v.; Stampfer, C. Raman Spectroscopy as Probe of Nanometre-Scale Strain Variations in Graphene. *Nat. Commun.* **2015**, *6*, 8429.
- (348) Mueller, N. S.; Heeg, S.; Alvarez, M. P.; Kusch, P.; Wassertho, S.; Clark, N.; Schedin, F.; Parthenios, J.; Papagelis, K.; Galiotis, C.; Kalbáč, M.; Vijayaraghavan, A.; Huebner, U.; Gorbachev, R.; Frank, O.; Reich, S. Evaluating Arbitrary Strain Configurations and Doping in Graphene with Raman Spectroscopy. *2d Mater.* **2018**, *5*, 015016.
- (349) Liu, Y.; Huang, Y.; Duan, X. Van Der Waals Integration before and beyond Two-Dimensional Materials. *Nature* **2019**, *567*, 323–333.
- (350) Wang, Z.; Hu, T.; Liang, R.; Wei, M. Application of Zero-Dimensional Nanomaterials in Biosensing. *Front. Chem.* **2020**, *8*, 320.
- (351) Mohanty, B.; Jena, B. K.; Basu, S. Single Atom on the 2D Matrix: An Emerging Electrocatalyst for Energy Applications. *ACS Omega* **2020**, *5*, 1287–1295.
- (352) Lei, Y.; Butler, D.; Lucking, M. C.; Zhang, F.; Xia, T.; Fujisawa, K.; Granzier-Nakajima, T.; Cruz-Silva, R.; Endo, M.; Terrones, H.; Terrones, M.; Ebrahimi, A. Single-Atom Doping of MoS₂ with Manganese Enables Ultrasensitive Detection of Dopamine: Experimental and Computational Approach. *Sci. Adv.* **2020**, *6*, eabc4250.
- (353) Kolli, C. S. R.; Selamneni, V.; Muñoz Martínez, B. A.; Fest Carreno, A.; Emanuel Sanchez, D.; Terrones, M.; Strupiechonski, E.; de Luna Bugallo, A.; Sahatiya, P. Broadband, Ultra-High-Responsive Monolayer MoS₂/SnS₂ Quantum-Dot-Based Mixed-Dimensional Photodetector. *ACS Appl. Mater. Interfaces* **2022**, *14*, 15415–15425.
- (354) Yin, Y.; Shi, L.; Zhang, S.; Duan, X.; Zhang, J.; Sun, H.; Wang, S. Two-dimensional Nanomaterials Confined Single Atoms: New Opportunities for Environmental Remediation. *Nano Materials Science* **2022**, *5* (1), 15–38.
- (355) Gao, Y.; Chen, X.; Zhang, J.; Asakura, H.; Tanaka, T.; Teramura, K.; Ma, D.; Yan, N. Popping of Graphite Oxide: Application in Preparing Metal Nanoparticle Catalysts. *Adv. Mater.* **2015**, *27*, 4688–4694.
- (356) Lin, Y.-C.; Dumcenco, D. O.; Komsa, H.-P.; Niimi, Y.; Krashenninnikov, A. V.; Huang, Y.-S.; Suenaga, K. Properties of Individual Dopant Atoms in Single-Layer MoS₂: Atomic Structure, Migration, and Enhanced Reactivity. *Adv. Mater.* **2014**, *26*, 2857–2861.
- (357) Liu, H.; Grasseschi, D.; Dodda, A.; Fujisawa, K.; Olson, D.; Kahn, E.; Zhang, F.; Zhang, T.; Lei, Y.; Nogueira Branco, R. B.; Elías, A. L.; Silva, R. C.; Yeh, Y. T.; Maroneze, C. M.; Seixas, L.; Hopkins, P.; Das, S.; de Matos, C. J. S.; Terrones, M. Spontaneous Chemical Functionalization via Coordination of Au Single Atoms on Monolayer MoS₂. *Sci. Adv.* **2020**, *6*, eabc9308.
- (358) Liu, H.; Silva, W. C.; Santana Gonçalves de Souza, L.; Veiga, A. G.; Seixas, L.; Fujisawa, K.; Kahn, E.; Zhang, T.; Zhang, F.; Yu, Z.; Thompson, K.; Lei, Y.; de Matos, C. J. S.; Rocco, M. L. M.; Terrones, M.; Grasseschi, D. 3d Transition Metal Coordination on Monolayer MoS₂: A Facile Doping Method to Functionalize Surfaces. *Nanoscale* **2022**, *14*, 10801–10815.
- (359) Jariwala, D.; Marks, T. J.; Hersam, M. C. Mixed-Dimensional van Der Waals Heterostructures. *Nat. Mater.* **2017**, *16*, 170–181.
- (360) Liu, Y.; Huang, Y.; Duan, X. Van Der Waals Integration before and beyond Two-Dimensional Materials. *Nature* **2019**, *567*, 323–333.
- (361) Qi, D.; Han, C.; Rong, X.; Zhang, X. W.; Chhowalla, M.; Wee, A. T. S.; Zhang, W. Continuously Tuning Electronic Properties of Few-Layer Molybdenum Ditelluride with *in Situ* Aluminum Modification toward Ultrahigh Gain Complementary Inverters. *ACS Nano* **2019**, *13*, 9464–9472.

- (362) Xiang, D.; Han, C.; Wu, J.; Zhong, S.; Liu, Y.; Lin, J.; Zhang, X. A.; Ping Hu, W.; Özyilmaz, B.; Neto, A. H. C.; Wee, A. T. S.; Chen, W. Surface Transfer Doping Induced Effective Modulation on Ambipolar Characteristics of Few-Layer Black Phosphorus. *Nat. Commun.* **2015**, *6*, 6485.
- (363) Zhou, C.; Chai, Y. Ferroelectric-Gated Two-Dimensional-Material-Based Electron Devices. *Adv. Electron Mater.* **2017**, *3*, 1600400.
- (364) Lu, H.; Seabaugh, A. Tunnel Field-Effect Transistors: State-of-the-Art. *IEEE Journal of the Electron Devices Society* **2014**, *2*, 44–49.
- (365) Duong, N. T.; Park, C.; Nguyen, D. H.; Nguyen, P. H.; Tran, T. U.; Park, D. Y.; Lee, J.; Nguyen, D. A.; Oh, J. H.; Yu, Y. S.; Jeong, M. S. Gate-Controlled MoTe₂ Homojunction for Sub-Thermionic Subthreshold Swing Tunnel Field-Effect Transistor. *Nano Today* **2021**, *40*, 101263.
- (366) Miao, J.; Leblanc, C.; Wang, J.; Gu, Y.; Liu, X.; Song, B.; Zhang, H.; Krylyuk, S.; Hu, W.; Davydov, A. v.; Back, T.; Glavin, N.; Jariwala, D. Heterojunction Tunnel Triodes Based on Two-Dimensional Metal Selenide and Three-Dimensional Silicon. *Nat. Electron* **2022**, *5*, 744–751.
- (367) Shin, G. H.; Koo, B.; Park, H.; Woo, Y.; Lee, J. E.; Choi, S. Y. Vertical-Tunnel Field-Effect Transistor Based on a Silicon-MoS₂ Three-Dimensional-Two-Dimensional Heterostructure. *ACS Appl. Mater. Interfaces* **2018**, *10*, 40212–40218.
- (368) Sarkar, D.; Xie, X.; Liu, W.; Cao, W.; Kang, J.; Gong, Y.; Kraemer, S.; Ajayan, P. M.; Banerjee, K. A Subthermionic Tunnel Field-Effect Transistor with an Atomically Thin Channel. *Nature* **2015**, *526*, 91–95.
- (369) Si, M.; Su, C. J.; Jiang, C.; Conrad, N. J.; Zhou, H.; Maize, K. D.; Qiu, G.; Wu, C. T.; Shakouri, A.; Alam, M. A.; Ye, P. D. Steep-Slope Hysteresis-Free Negative Capacitance MoS₂ Transistors. *Nat. Nanotechnol* **2018**, *13*, 24–28.
- (370) Salahuddin, S.; Datta, S. Use of Negative Capacitance to Provide Voltage Amplification for Low Power Nanoscale Devices. *Nano Lett.* **2008**, *8*, 405–410.
- (371) Pang, C. S.; Thakuria, N.; Gupta, S. K.; Chen, Z. First Demonstration of WSe₂ Based CMOS-SRAM. In *2018 IEEE International Electron Devices Meeting (IEDM)*; IEEE, 2018; pp 22.2.1–22.2.4.
- (372) Wang, H.; Yu, L.; Lee, Y. H.; Shi, Y.; Hsu, A.; Chin, M. L.; Li, L. J.; Dubey, M.; Kong, J.; Palacios, T. Integrated Circuits Based on Bilayer MoS₂ Transistors. *Nano Lett.* **2012**, *12*, 4674–4680.
- (373) Si, M.; Zhang, Z.; Chang, S. C.; Haratipour, N.; Zheng, D.; Li, J.; Avci, U. E.; Ye, P. D. Asymmetric Metal/ α -In₂Se₃/Si Crossbar Ferroelectric Semiconductor Junction. *ACS Nano* **2021**, *15*, 5689–5695.
- (374) Migliato Marega, G.; Zhao, Y.; Avsar, A.; Wang, Z.; Tripathi, M.; Radenovic, A.; Kis, A. Logic-in-Memory Based on an Atomically Thin Semiconductor. *Nature* **2020**, *587*, 72–77.
- (375) Liu, X.; Wang, D.; Kim, K. H.; Katti, K.; Zheng, J.; Musavigharavi, P.; Miao, J.; Stach, E. A.; Olsson, R. H.; Jariwala, D. Post-CMOS Compatible Aluminum Scandium Nitride/2D Channel Ferroelectric Field-Effect-Transistor Memory. *Nano Lett.* **2021**, *21*, 3753–3761.
- (376) Si, M.; Saha, A. K.; Gao, S.; Qiu, G.; Qin, J.; Duan, Y.; Jian, J.; Niu, C.; Wang, H.; Wu, W.; Gupta, S. K.; Ye, P. D. A Ferroelectric Semiconductor Field-Effect Transistor. *Nat. Electron* **2019**, *2*, 580–586.
- (377) Akinwande, D.; Huyghebaert, C.; Wang, C. H.; Serna, M. I.; Goossens, S.; Li, L. J.; Wong, H. S. P.; Koppens, F. H. L. Graphene and Two-Dimensional Materials for Silicon Technology. *Nature* **2019**, *573*, 507–518.
- (378) Moll, J. L.; Tarui, Y. A New Solid State Memory Resistor. *IEEE Trans. Electron Devices* **1963**, *10*, 338.
- (379) Ma, T. P.; Han, J.-P. Why Is Nonvolatile Ferroelectric Memory Field-Effect Transistor Still Elusive? *IEEE Electron Device Lett.* **2002**, *23*, 386–388.
- (380) Wang, D.; Musavigharavi, P.; Zheng, J.; Esteves, G.; Liu, X.; Fiagbenu, M. M. A.; Stach, E. A.; Jariwala, D.; Olsson, R. H. Sub-Microsecond Polarization Switching in (Al,Sc)N Ferroelectric Capacitors Grown on Complementary Metal–Oxide–Semiconductor-Compatible Aluminum Electrodes. *Phys. Rapid Res. Lett.* **2021**, *15*, 2000575.
- (381) Liu, X.; Zheng, J.; Wang, D.; Musavigharavi, P.; Stach, E. A.; Olsson, R.; Jariwala, D. Aluminum Scandium Nitride-Based Metal–Ferroelectric–Metal Diode Memory Devices with High on/off Ratios. *Appl. Phys. Lett.* **2021**, *118*, 202901.
- (382) Ge, R.; Wu, X.; Kim, M.; Shi, J.; Sonde, S.; Tao, L.; Zhang, Y.; Lee, J. C.; Akinwande, D. Atomristor: Nonvolatile Resistance Switching in Atomic Sheets of Transition Metal Dichalcogenides. *Nano Lett.* **2018**, *18*, 434–441.
- (383) Ge, R.; Wu, X.; Liang, L.; Hus, S. M.; Gu, Y.; Okogbue, E.; Chou, H.; Shi, J.; Zhang, Y.; Banerjee, S. K.; Jung, Y.; Lee, J. C.; Akinwande, D. A Library of Atomically Thin 2D Materials Featuring the Conductive-Point Resistive Switching Phenomenon. *Adv. Mater.* **2021**, *33*, 2007792.
- (384) Xu, R.; Jang, H.; Lee, M. H.; Amanov, D.; Cho, Y.; Kim, H.; Park, S.; Shin, H. J.; Ham, D. Vertical MoS₂ Double-Layer Memristor with Electrochemical Metallization as an Atomic-Scale Synapse with Switching Thresholds Approaching 100 mV. *Nano Lett.* **2019**, *19*, 2411–2417.
- (385) Wu, X.; Ge, R.; Chen, P.-A.; Chou, H.; Zhang, Z.; Zhang, Y.; Banerjee, S.; Chiang, M.-H.; Lee, J. C.; Akinwande, D. Thinnest Nonvolatile Memory Based on Monolayer h-BN. *Adv. Mater.* **2019**, *31*, 1806790.
- (386) Hus, S. M.; Ge, R.; Chen, P. A.; Liang, L.; Donnelly, G. E.; Ko, W.; Huang, F.; Chiang, M. H.; Li, A. P.; Akinwande, D. Observation of Single-Defect Memristor in an MoS₂ Atomic Sheet. *Nat. Nanotechnol* **2021**, *16*, 58–62.
- (387) Wu, X.; Gu, Y.; Ge, R.; Serna, M. I.; Huang, Y.; Lee, J. C.; Akinwande, D. Electron Irradiation-Induced Defects for Reliability Improvement in Monolayer MoS₂-Based Conductive-Point Memory Devices. *NPJ. 2D Mater. Appl.* **2022**, *6*, 31.
- (388) Pan, C.; Ji, Y.; Xiao, N.; Hui, F.; Tang, K.; Guo, Y.; Xie, X.; Puglisi, F. M.; Larcher, L.; Miranda, E.; Jiang, L.; Shi, Y.; Valov, I.; McIntyre, P. C.; Waser, R.; Lanza, M. Coexistence of Grain-Boundaries-Assisted Bipolar and Threshold Resistive Switching in Multilayer Hexagonal Boron Nitride. *Adv. Funct. Mater.* **2017**, *27*, 1604811.
- (389) Zhang, F.; Zhang, H.; Krylyuk, S.; Milligan, C. A.; Zhu, Y.; Zemlyanov, D. Y.; Bendersky, L. A.; Burton, B. P.; Davydov, A. v.; Appenzeller, J. Electric-Field Induced Structural Transition in Vertical MoTe₂- and Mo_{1-x}W_xTe₂-Based Resistive Memories. *Nat. Mater.* **2019**, *18*, 55–61.
- (390) Mitra, S.; Kabiraj, A.; Mahapatra, S. Theory of Nonvolatile Resistive Switching in Monolayer Molybdenum Disulfide with Passive Electrodes. *NPJ. 2D Mater. Appl.* **2021**, *5*, 33.
- (391) Li, X.-D.; Chen, N.-K.; Wang, B.-Q.; Li, X.-B. Conductive Mechanism in Memristor at the Thinnest Limit: The Case Based on Monolayer Boron Nitride. *Appl. Phys. Lett.* **2022**, *121*, 073505.
- (392) Chen, S.; Mahmoodi, M. R.; Shi, Y.; Mahata, C.; Yuan, B.; Liang, X.; Wen, C.; Hui, F.; Akinwande, D.; Strukov, D. B.; Lanza, M. Wafer-Scale Integration of Two-Dimensional Materials in High-Density Memristive Crossbar Arrays for Artificial Neural Networks. *Nat. Electron* **2020**, *3*, 638–645.
- (393) Zhao, H.; Dong, Z.; Tian, H.; DiMarzi, D.; Han, M.-G.; Zhang, L.; Yan, X.; Liu, F.; Shen, L.; Han, S.-J.; Cronin, S.; Wu, W.; Tice, J.; Guo, J.; Wang, H. Atomically Thin Femtojoule Memristive Device. *Adv. Mater.* **2017**, *29*, 1703232.
- (394) Krishnaprasad, A.; Choudhary, N.; Das, S.; Dev, D.; Kalita, H.; Chung, H. S.; Aina, O.; Jung, Y.; Roy, T. Electronic Synapses with Near-Linear Weight Update Using MoS₂/Graphene Memristors. *Appl. Phys. Lett.* **2019**, *115*, 103104.
- (395) Kim, M.; Pallecchi, E.; Ge, R.; Wu, X.; Ducournau, G.; Lee, J. C.; Happy, H.; Akinwande, D. Analogue Switches Made from Boron Nitride Monolayers for Application in 5G and Terahertz Communication Systems. *Nat. Electron* **2020**, *3*, 479–485.
- (396) Wang, M.; Cai, S.; Pan, C.; Wang, C.; Lian, X.; Zhuo, Y.; Xu, K.; Cao, T.; Pan, X.; Wang, B.; Liang, S.-J.; Yang, J. J.; Wang, P.; Miao, F.

Robust Memristors Based on Layered Two-Dimensional Materials. *Nat. Electron* **2018**, *1*, 130–136.

(397) Kim, M.; Ducournau, G.; Skrzypczak, S.; Yang, S. J.; Szriftgiser, P.; Wainstein, N.; Stern, K.; Happy, H.; Yalon, E.; Palleschi, E.; Akinwande, D. Monolayer Molybdenum Disulfide Switches for 6G Communication Systems. *Nat. Electron* **2022**, *5*, 367–373.

(398) Tokura, Y.; Yasuda, K.; Tsukazaki, A. Magnetic Topological Insulators. *Nature Reviews Physics* **2019**, *1*, 126–143.

(399) Chang, C. Z.; Zhang, J.; Feng, X.; Shen, J.; Zhang, Z.; Guo, M.; Li, K.; Ou, Y.; Wei, P.; Wang, L. L.; Ji, Z. Q.; Feng, Y.; Ji, S.; Chen, X.; Jia, J.; Dai, X.; Fang, Z.; Zhang, S. C.; He, K.; Wang, Y.; Lu, L.; Ma, X. C.; Xue, Q. K. Experimental Observation of the Quantum Anomalous Hall Effect in a Magnetic Topological Insulator. *Science* **2013**, *340*, 167–170.

(400) Mogi, M.; Yoshimi, R.; Tsukazaki, A.; Yasuda, K.; Kozuka, Y.; Takahashi, K. S.; Kawasaki, M.; Tokura, Y. Magnetic Modulation Doping in Topological Insulators toward Higher-Temperature Quantum Anomalous Hall Effect. *Appl. Phys. Lett.* **2015**, *107*, 182401.

(401) Otrokov, M. M.; Klimovskikh, I. I.; Bentmann, H.; Estyunin, D.; Zeugner, A.; Aliev, Z. S.; Gaß, S.; Wolter, A. U. B.; Koroleva, A. v.; Shikin, A. M.; Blanco-Rey, M.; Hoffmann, M.; Rusinov, I. P.; Vyazovskaya, A. Y.; Ereemeev, S. v.; Koroteev, Y. M.; Kuznetsov, V. M.; Freyre, F.; Sánchez-Barriga, J.; Amirasanov, I. R.; Babanly, M. B.; Mamedov, N. T.; Abdullayev, N. A.; Zverev, V. N.; Alfonsov, A.; Kataev, V.; Büchner, B.; Schwier, E. F.; Kumar, S.; Kimura, A.; Petaccia, L.; di Santo, G.; Vidal, R. C.; Schatz, S.; Kißner, K.; Ünzelmann, M.; Min, C. H.; Moser, S.; Peixoto, T. R. F.; Reinert, F.; Ernst, A.; Echenique, P. M.; Isaeva, A.; Chulkov, E. v. Prediction and Observation of an Antiferromagnetic Topological Insulator. *Nature* **2019**, *576*, 416–422.

(402) Zhang, D.; Shi, M.; Zhu, T.; Xing, D.; Zhang, H.; Wang, J. Topological Axion States in the Magnetic Insulator MnBi_2Te_4 with the Quantized Magnetoelectric Effect. *Phys. Rev. Lett.* **2019**, *122*, 206401.

(403) Wu, J.; Liu, F.; Sasase, M.; Ienaga, K.; Obata, Y.; Yukawa, R.; Horiba, K.; Kumigashira, H.; Okuma, S.; Inoshita, T.; Hosono, H. Natural van Der Waals Heterostructural Single Crystals with Both Magnetic and Topological Properties. *Sci. Adv.* **2019**, *5*, eaax9989.

(404) Lee, S. H.; Zhu, Y.; Wang, Y.; Miao, L.; Pillsbury, T.; Yi, H.; Kempinger, S.; Hu, J.; Heikes, C. A.; Quarterman, P.; Ratcliff, W.; Borchers, J. A.; Zhang, H.; Ke, X.; Graf, D.; Alem, N.; Chang, C. Z.; Samarth, N.; Mao, Z. Spin Scattering and Noncollinear Spin Structure-Induced Intrinsic Anomalous Hall Effect in Antiferromagnetic Topological Insulator MnBi_2Te_4 . *Phys. Rev. Res.* **2019**, *1*, 012011.

(405) Yan, J. Q.; Zhang, Q.; Heitmann, T.; Huang, Z.; Chen, K. Y.; Cheng, J. G.; Wu, W.; Vaknin, D.; Sales, B. C.; McQueeney, R. J. Crystal Growth and Magnetic Structure of MnBi_2Te_4 . *Phys. Rev. Mater.* **2019**, *3*, 064202.

(406) Deng, Y.; Yu, Y.; Shi, M. Z.; Guo, Z.; Xu, Z.; Wang, J.; Chen, X. H.; Zhang, Y. Quantum Anomalous Hall Effect in Intrinsic Magnetic Topological Insulator MnBi_2Te_4 . *Science* **2020**, *367*, 895–900.

(407) Liu, C.; Wang, Y.; Li, H.; Wu, Y.; Li, Y.; Li, J.; He, K.; Xu, Y.; Zhang, J.; Wang, Y. Robust Axion Insulator and Chern Insulator Phases in a Two-Dimensional Antiferromagnetic Topological Insulator. *Nat. Mater.* **2020**, *19*, 522–527.

(408) Ge, J.; Liu, Y.; Li, J.; Li, H.; Luo, T.; Wu, Y.; Xu, Y.; Wang, J. High-Chern-Number and High-Temperature Quantum Hall Effect without Landau Levels. *Natl. Sci. Rev.* **2020**, *7*, 1280–1287.

(409) Gao, A.; Liu, Y. F.; Hu, C.; Qiu, J. X.; Tzschaschel, C.; Ghosh, B.; Ho, S. C.; Bérubé, D.; Chen, R.; Sun, H.; Zhang, Z.; Zhang, X. Y.; Wang, Y. X.; Wang, N.; Huang, Z.; Felser, C.; Agarwal, A.; Ding, T.; Tien, H. J.; Akey, A.; Gardener, J.; Singh, B.; Watanabe, K.; Taniguchi, T.; Burch, K. S.; Bell, D. C.; Zhou, B. B.; Gao, W.; Lu, H. Z.; Bansil, A.; Lin, H.; Chang, T. R.; Fu, L.; Ma, Q.; Ni, N.; Xu, S. Y. Layer Hall Effect in a 2D Topological Axion Antiferromagnet. *Nature* **2021**, *595*, 521–525.

(410) Lee, S. H.; Graf, D.; Min, L.; Zhu, Y.; Yi, H.; Ciocys, S.; Wang, Y.; Choi, E. S.; Basnet, R.; Fereidouni, A.; Wegner, A.; Zhao, Y. F.; Verlinde, K.; He, J.; Redwing, R.; Gopalan, V.; Churchill, H. O. H.; Lanzara, A.; Samarth, N.; Chang, C. Z.; Hu, J.; Mao, Z. Q. Evidence for a Magnetic-Field-Induced Ideal Type-II Weyl State in Antiferromag-

netic Topological Insulator $\text{Mn}(\text{Bi}_{1-x}\text{Sb}_x)_2\text{Te}_4$. *Phys. Rev. X* **2021**, *11*, 031032.

(411) Chen, Y.; Chuang, Y. W.; Lee, S. H.; Zhu, Y.; Honz, K.; Guan, Y.; Wang, Y.; Wang, K.; Mao, Z.; Zhu, J.; Heikes, C.; Quarterman, P.; Zajdel, P.; Borchers, J. A.; Ratcliff, W. Ferromagnetism in van Der Waals Compound $\text{MnSb}_{1.8}\text{Bi}_{0.2}\text{Te}_4$. *Phys. Rev. Mater.* **2020**, *4*, 064411.

(412) Wang, P.; Ge, J.; Li, J.; Liu, Y.; Xu, Y.; Wang, J. Intrinsic Magnetic Topological Insulators. *Innovation* **2021**, *2*, 100098.

(413) Chen, B.; Fei, F.; Zhang, D.; Zhang, B.; Liu, W.; Zhang, S.; Wang, P.; Wei, B.; Zhang, Y.; Zuo, Z.; Guo, J.; Liu, Q.; Wang, Z.; Wu, X.; Zong, J.; Xie, X.; Chen, W.; Sun, Z.; Wang, S.; Zhang, Y.; Zhang, M.; Wang, X.; Song, F.; Zhang, H.; Shen, D.; Wang, B. Intrinsic Magnetic Topological Insulator Phases in the Sb Doped MnBi_2Te_4 Bulks and Thin Flakes. *Nat. Commun.* **2019**, *10*, 4469.

(414) Yan, J. Q.; Okamoto, S.; McGuire, M. A.; May, A. F.; McQueeney, R. J.; Sales, B. C. Evolution of Structural, Magnetic, and Transport Properties in $\text{MnBi}_{2-x}\text{Sb}_x\text{Te}_4$. *Phys. Rev. B* **2019**, *100*, 104409.

(415) Lee, S. H.; Graf, D.; Robinson, R.; Singleton, J.; Palmstrom, J. C.; Mao, Z. Evidence of magnetic fluctuation induced Weyl semimetal state in the antiferromagnetic topological insulator $\text{Mn}(\text{Bi}_{1-x}\text{Sb}_x)_2\text{Te}_4$. *Phys. Rev. B* **2023**, *107*, 205105.

(416) Murakami, T.; Nambu, Y.; Koretsune, T.; Xiangyu, G.; Yamamoto, T.; Brown, C. M.; Kageyama, H. Realization of Interlayer Ferromagnetic Interaction in MnSb_2Te_4 toward the Magnetic Weyl Semimetal State. *Phys. Rev. B* **2019**, *100*, 195103.

(417) Liu, Y.; Wang, L. L.; Zheng, Q.; Huang, Z.; Wang, X.; Chi, M.; Wu, Y.; Chakoumakos, B. C.; McGuire, M. A.; Sales, B. C.; Wu, W.; Yan, J. Site Mixing for Engineering Magnetic Topological Insulators. *Phys. Rev. X* **2021**, *11*, 021033.

(418) Riberolles, S. X. M.; Zhang, Q.; Gordon, E.; Butch, N. P.; Ke, L.; Yan, J. Q.; McQueeney, R. J. Evolution of Magnetic Interactions in Sb-Substituted MnBi_2Te_4 . *Phys. Rev. B* **2021**, *104*, 064401.

(419) Oe, T.; Rigosi, A. F.; Kruskopf, M.; Wu, B. Y.; Lee, H. Y.; Yang, Y.; Elmquist, R. E.; Kaneko, N. H.; Jarrett, D. G. Comparison between NIST Graphene and AIST GaAs Quantized Hall Devices. *IEEE Trans Instrum Meas* **2020**, *69*, 3103–3108.

(420) Chen, Y. L.; Chu, J. H.; Analytis, J. G.; Liu, Z. K.; Igarashi, K.; Kuo, H. H.; Qi, X. L.; Mo, S. K.; Moore, R. G.; Lu, D. H.; Hashimoto, M.; Sasagawa, T.; Zhang, S. C.; Fisher, I. R.; Hussain, Z.; Shen, Z. X. Massive Dirac Fermion on the Surface of a Magnetically Doped Topological Insulator. *Science* **2010**, *329*, 659–662.

(421) Checkelsky, J. G.; Ye, J.; Onose, Y.; Iwasa, Y.; Tokura, Y. Dirac-Fermion-Mediated Ferromagnetism in a Topological Insulator. *Nat. Phys.* **2012**, *8*, 729–733.

(422) Yu, R.; Zhang, W.; Zhang, H. J.; Zhang, S. C.; Dai, X.; Fang, Z. Quantized Anomalous Hall Effect in Magnetic Topological Insulators. *Science* **2010**, *329*, 61–64.

(423) Götz, M.; Fijalkowski, K. M.; Pesel, E.; Hartl, M.; Schreyeck, S.; Winnerlein, M.; Grauer, S.; Scherer, H.; Brunner, K.; Gould, C.; Ahlers, F. J.; Molenkamp, L. W. Precision Measurement of the Quantized Anomalous Hall Resistance at Zero Magnetic Field. *Appl. Phys. Lett.* **2018**, *112*, 072102.

(424) Okazaki, Y.; Oe, T.; Kawamura, M.; Yoshimi, R.; Nakamura, S.; Takada, S.; Mogi, M.; Takahashi, K. S.; Tsukazaki, A.; Kawasaki, M.; Tokura, Y.; Kaneko, N. H. Quantum Anomalous Hall Effect with a Permanent Magnet Defines a Quantum Resistance Standard. *Nat. Phys.* **2022**, *18*, 25–29.

(425) Fox, E. J.; Rosen, I. T.; Yang, Y.; Jones, G. R.; Elmquist, R. E.; Kou, X.; Pan, L.; Wang, K. L.; Goldhaber-Gordon, D. Part-per-Million Quantization and Current-Induced Breakdown of the Quantum Anomalous Hall Effect. *Phys. Rev. B* **2018**, *98*, 075145.

(426) Kou, X.; Fan, Y.; Lang, M.; Upadhyaya, P.; Wang, K. L. Magnetic Topological Insulators and Quantum Anomalous Hall Effect. *Solid State Commun.* **2015**, *215–216*, 34–53.

(427) Zhang, D.; Richardella, A.; Rench, D. W.; Xu, S. Y.; Kandala, A.; Flanagan, T. C.; Beidenkopf, H.; Yeats, A. L.; Buckley, B. B.; Klimov, P. v.; Awschalom, D. D.; Yazdani, A.; Schiffer, P.; Hasan, M. Z.; Samarth, N. Interplay between Ferromagnetism, Surface States, and Quantum

Corrections in a Magnetically Doped Topological Insulator. *Phys. Rev. B* **2012**, *86*, 205127.

(428) Rodenbach, L. K.; Panna, A. R.; Payagala, S. U.; Rosen, I. T.; Andersen, M. P.; Zhang, P.; Tai, L.; Wang, K. L.; Jarrett, D. G.; Elmquist, R. E.; Newell, D. B.; Goldhaber-Gordon, D.; Rigosi, A. F. Metrological Assessment of Quantum Anomalous Hall Properties. *Phys. Rev. Appl.* **2022**, *18*, 034008.

(429) Fijalkowski, K. M.; Liu, N.; Mandal, P.; Schreyeck, S.; Brunner, K.; Gould, C.; Molenkamp, L. W. Quantum Anomalous Hall Edge Channels Survive up to the Curie Temperature. *Nat. Commun.* **2021**, *12*, 5599.

(430) Matthias, B. T.; Suhl, H.; Corenzwit, E. Spin Exchange in Superconductors. *Phys. Rev. Lett.* **1958**, *1*, 92.

(431) Anderson, P. W. Theory of Dirty Superconductors. *J. Phys. Chem. Solids* **1959**, *11*, 26–30.

(432) Dikin, D. A.; Mehta, M.; Bark, C. W.; Folkman, C. M.; Eom, C. B.; Chandrasekhar, V. Coexistence of Superconductivity and Ferromagnetism in Two Dimensions. *Phys. Rev. Lett.* **2011**, *107*, 056802.

(433) Li, L.; Richter, C.; Mannhart, J.; Ashoori, R. C. Coexistence of Magnetic Order and Two-Dimensional Superconductivity at LaAlO₃/SrTiO₃ Interfaces. *Nat. Phys.* **2011**, *7*, 762–766.

(434) Bert, J. A.; Kalisky, B.; Bell, C.; Kim, M.; Hikita, Y.; Hwang, H. Y.; Moler, K. A. Direct Imaging of the Coexistence of Ferromagnetism and Superconductivity at the LaAlO₃/SrTiO₃ Interface. *Nat. Phys.* **2011**, *7*, 767–771.

(435) Ando, F.; Miyasaka, Y.; Li, T.; Ishizuka, J.; Arakawa, T.; Shiota, Y.; Moriyama, T.; Yanase, Y.; Ono, T. Observation of Superconducting Diode Effect. *Nature* **2020**, *584*, 373–376.

(436) Pal, B.; Chakraborty, A.; Sivakumar, P. K.; Davydova, M.; Gopi, A. K.; Pandeya, A. K.; Krieger, J. A.; Zhang, Y.; Date, M.; Ju, S.; Yuan, N.; Schröter, N. B. M.; Fu, L.; Parkin, S. S. P. Josephson Diode Effect from Cooper Pair Momentum in a Topological Semimetal. *Nat. Phys.* **2022**, *18*, 1228–1233.

(437) Narita, H.; Ishizuka, J.; Kawarazaki, R.; Kan, D.; Shiota, Y.; Moriyama, T.; Shimakawa, Y.; Ognev, A. v.; Samardak, A. S.; Yanase, Y.; Ono, T. Field-Free Superconducting Diode Effect in Noncentrosymmetric Superconductor/Ferromagnet Multilayers. *Nat. Nanotechnol.* **2022**, *17*, 823–828.

(438) Hou, Y.; Nichele, F.; Chi, H.; Lodesani, A.; Wu, Y.; Ritter, M. F.; Haxell, D. Z.; Davydova, M.; Ilić, S.; Bergeret, F. S.; Kamra, A.; Fu, L.; Lee, P. A.; Moodera, J. S. Ubiquitous Superconducting Diode Effect in Superconductor Thin Films. *arXiv* **2022**, 2205.09276. DOI: 10.48550/arXiv.2205.09276 (accessed March 1, 2023).

(439) Wu, H.; Wang, Y.; Xu, Y.; Sivakumar, P. K.; Pasco, C.; Filippozzi, U.; Parkin, S. S. P.; Zeng, Y. J.; McQueen, T.; Ali, M. N. The Field-Free Josephson Diode in a van Der Waals Heterostructure. *Nature* **2022**, *604*, 653–656.

(440) Baumgartner, C.; Fuchs, L.; Costa, A.; Reinhardt, S.; Gronin, S.; Gardner, G. C.; Lindemann, T.; Manfra, M. J.; Faria Junior, P. E.; Kochan, D.; Fabian, J.; Paradiso, N.; Strunk, C. Supercurrent Rectification and Magnetochiral Effects in Symmetric Josephson Junctions. *Nat. Nanotechnol.* **2022**, *17*, 39–44.

(441) Lin, J. X.; Siriviboon, P.; Scammell, H. D.; Liu, S.; Rhodes, D.; Watanabe, K.; Taniguchi, T.; Hone, J.; Scheurer, M. S.; Li, J. I. A. Zero-Field Superconducting Diode Effect in Small-Twist-Angle Trilayer Graphene. *Nat. Phys.* **2022**, *18*, 1221–1227.

(442) Christos, M.; Sachdev, S.; Scheurer, M. S. Correlated Insulators, Semimetals, and Superconductivity in Twisted Trilayer Graphene. *Phys. Rev. X* **2022**, *12*, 021018.

(443) Giamarchi, T. *Quantum Physics in One Dimension*; Oxford University Press: Oxford, UK, 2003.

(444) Haldane, F. D. M. “Luttinger Liquid Theory” of One-Dimensional Quantum Fluids. I. Properties of the Luttinger Model and Their Extension to the General 1D Interacting Spinless Fermi Gas. *Journal of Physics C: Solid State Physics* **1981**, *14*, 2585.

(445) Anderson, P. W. “Luttinger-Liquid” Behavior of the Normal Metallic State of the 2D Hubbard Model. *Phys. Rev. Lett.* **1990**, *64*, 1839.

(446) Wen, X. G. Metallic Non-Fermi-Liquid Fixed Point in Two and Higher Dimensions. *Phys. Rev. B* **1990**, *42*, 6623.

(447) Vishwanath, A.; Carpentier, D. Two-Dimensional Anisotropic Non-Fermi-Liquid Phase of Coupled Luttinger Liquids. *Phys. Rev. Lett.* **2001**, *86*, 676.

(448) Mukhopadhyay, R.; Kane, C. L.; Lubensky, T. C. Sliding Luttinger Liquid Phases. *Phys. Rev. B* **2001**, *64*, 045120.

(449) Emery, V. J.; Fradkin, E.; Kivelson, S. A.; Lubensky, T. C. Quantum Theory of the Smectic Metal State in Stripe Phases. *Phys. Rev. Lett.* **2000**, *85*, 2160.

(450) Sondhi, S. L.; Yang, K. Sliding Phases via Magnetic Fields. *Phys. Rev. B* **2001**, *63*, 054430.

(451) Kane, C. L.; Mukhopadhyay, R.; Lubensky, T. C. Fractional Quantum Hall Effect in an Array of Quantum Wires. *Phys. Rev. Lett.* **2002**, *88*, 036401.

(452) Teo, J. C. Y.; Kane, C. L. From Luttinger Liquid to Non-Abelian Quantum Hall States. *Phys. Rev. B* **2014**, *89*, 085101.

(453) Patel, A. A.; Chowdhury, D. Two-Dimensional Spin Liquids with Z₂ Topological Order in an Array of Quantum Wires. *Phys. Rev. B* **2016**, *94*, 195130.

(454) Wang, P.; Yu, G.; Kwan, Y. H.; Jia, Y.; Lei, S.; Klemen, S.; Cevallos, F. A.; Singha, R.; Devakul, T.; Watanabe, K.; Taniguchi, T.; Sondhi, S. L.; Cava, R. J.; Schoop, L. M.; Parameswaran, S. A.; Wu, S. One-Dimensional Luttinger Liquids in a Two-Dimensional Moiré Lattice. *Nature* **2022**, *605*, 57–62.

(455) Qian, X.; Liu, J.; Fu, L.; Li, J. Quantum Spin Hall Effect in Two-Dimensional Transition Metal Dichalcogenides. *Science* **2014**, *346*, 1344–1347.

(456) Wu, S.; Fatemi, V.; Gibson, Q. D.; Watanabe, K.; Taniguchi, T.; Cava, R. J.; Jarillo-Herrero, P. Observation of the Quantum Spin Hall Effect up to 100 K in a Monolayer Crystal. *Science* **2018**, *359*, 76–79.

(457) Fei, Z.; Palomaki, T.; Wu, S.; Zhao, W.; Cai, X.; Sun, B.; Nguyen, P.; Finney, J.; Xu, X.; Cobden, D. H. Edge Conduction in Monolayer WTe₂. *Nat. Phys.* **2017**, *13*, 677–682.

(458) Fatemi, V.; Wu, S.; Cao, Y.; Bretheau, L.; Gibson, Q. D.; Watanabe, K.; Taniguchi, T.; Cava, R. J.; Jarillo-Herrero, P. Electrically Tunable Low-Density Superconductivity in a Monolayer Topological Insulator. *Science* **2018**, *362*, 926–929.

(459) Sajadi, E.; Palomaki, T.; Fei, Z.; Zhao, W.; Bement, P.; Olsen, C.; Luescher, S.; Xu, X.; Folk, J. A.; Cobden, D. H. Gate-Induced Superconductivity in a Monolayer Topological Insulator. *Science* **2018**, *362*, 922–925.

(460) Wang, P.; Yu, G.; Jia, Y.; Onyszczak, M.; Cevallos, F. A.; Lei, S.; Klemen, S.; Watanabe, K.; Taniguchi, T.; Cava, R. J.; Schoop, L. M.; Wu, S. Landau Quantization and Highly Mobile Fermions in an Insulator. *Nature* **2021**, *589*, 225–229.

(461) Jia, Y.; Wang, P.; Chiu, C. L.; Song, Z.; Yu, G.; Jäck, B.; Lei, S.; Klemen, S.; Cevallos, F. A.; Onyszczak, M.; Fishchenko, N.; Liu, X.; Farahi, G.; Xie, F.; Xu, Y.; Watanabe, K.; Taniguchi, T.; Bernevig, B. A.; Cava, R. J.; Schoop, L. M.; Yazdani, A.; Wu, S. Evidence for a Monolayer Excitonic Insulator. *Nat. Phys.* **2022**, *18*, 87–93.

(462) Iadecola, T.; Neupert, T.; Chamon, C.; Mudry, C. Wire Constructions of Abelian Topological Phases in Three or More Dimensions. *Phys. Rev. B* **2016**, *93*, 195136.

(463) Meng, T.; Neupert, T.; Greiter, M.; Thomale, R. Coupled-Wire Construction of Chiral Spin Liquids. *Phys. Rev. B* **2015**, *91*, 241106.

(464) Kennes, D. M.; Xian, L.; Claassen, M.; Rubio, A. One-Dimensional Flat Bands in Twisted Bilayer Germanium Selenide. *Nat. Commun.* **2020**, *11*, 1124.

(465) Frey, N. C.; Wang, J.; Vega Bellido, G. I.; Anasori, B.; Gogotsi, Y.; Shenoy, V. B. Prediction of Synthesis of 2D Metal Carbides and Nitrides (MXenes) and Their Precursors with Positive and Unlabeled Machine Learning. *ACS Nano* **2019**, *13*, 3031–3041.

(466) Tan, T. L.; Jin, H. M.; Sullivan, M. B.; Anasori, B.; Gogotsi, Y. High-Throughput Survey of Ordering Configurations in MXene Alloys Across Compositions and Temperatures. *ACS Nano* **2017**, *11*, 4407–4418.

(467) Dong, L.; Kumar, H.; Anasori, B.; Gogotsi, Y.; Shenoy, V. B. Rational Design of Two-Dimensional Metallic and Semiconducting

Spintronic Materials Based on Ordered Double-Transition-Metal MXenes. *J. Phys. Chem. Lett.* **2017**, 8, 422–428.

(468) Frey, N. C.; Bandyopadhyay, A.; Kumar, H.; Anasori, B.; Gogotsi, Y.; Shenoy, V. B. Surface-Engineered MXenes: Electric Field Control of Magnetism and Enhanced Magnetic Anisotropy. *ACS Nano* **2019**, 13, 2831–2839.

(469) Liu, Q.; Xing, J.; Jiang, Z.; Guo, Y.; Jiang, X.; Qi, Y.; Zhao, J. Layer-Dependent Magnetic Phase Diagram in Fe_nGeTe_2 ($3 \leq n \leq 7$) Ultrathin Films. *Commun. Phys.* **2022**, 5, 140.

(470) Zhou, X.; Jiang, Z.; Zhang, K.; Yao, W.; Yan, M.; Zhang, H.; Duan, W.; Zhou, S. Electronic Structure of Molecular Beam Epitaxy Grown -MoTe_2 Film and Strain Effect. *Chinese Physics B* **2019**, 28, 107307.

(471) Zhao, C.; Hu, M.; Qin, J.; Xia, B.; Liu, C.; Wang, S.; Guan, D. D.; Li, Y.; Zheng, H.; Liu, J.; Jia, J. Strain Tunable Semimetal-Topological-Insulator Transition in Monolayer $1\text{T}'\text{-WTe}_2$. *Phys. Rev. Lett.* **2020**, 125, 046801.

(472) Naccarato, F.; Ricci, F.; Suntivich, J.; Hautier, G.; Wirtz, L.; Rignanese, G.-M. Searching for Materials with High Refractive Index and Wide Band Gap: A First-Principles High-Throughput Study. *Phys. Rev. Mater.* **2019**, 3, 044602.

(473) Rondinelli, J. M.; Kioupakis, E. Predicting and Designing Optical Properties of Inorganic Materials. *Annu. Rev. Mater. Res.* **2015**, 45, 491–518.

(474) Brun-Picard, J.; Djordjevic, S.; Leprat, D.; Schopfer, F.; Poirier, W. Practical Quantum Realization of the Ampere from the Elementary Charge. *Phys. Rev. X* **2016**, 6, 041051.

Recommended by ACS

Database Construction of Two-Dimensional Charged Building Blocks for Functional-Oriented Material Design

Jun Deng, Shixuan Du, *et al.*

MAY 05, 2023
NANO LETTERS

READ 

Complex Strain Scapes in Reconstructed Transition-Metal Dichalcogenide Moiré Superlattices

Álvaro Rodríguez, Otakar Frank, *et al.*

APRIL 06, 2023
ACS NANO

READ 

Gate and Temperature Driven Phase Transitions in Few-Layer MoTe_2

Hugo Kowalczyk, Abhay Shukla, *et al.*

MARCH 27, 2023
ACS NANO

READ 

Traversing Double-Well Potential Energy Surfaces: Photoinduced Concurrent Intralayer and Interlayer Structural Transitions in XTe_2 ($\text{X} = \text{Mo}, \text{W}$)

Yingpeng Qi, Ralph Ernstorfer, *et al.*

JULY 06, 2022
ACS NANO

READ 

Get More Suggestions >